AD-A137 740 STUDIES OF AERODYNAMIC DRAG(U) CAMBRIDGE UNIV (ENGLAND) CAVENDISH LAB W A WILBY ET AL. DEC 82 AFOSR-TR-84-0071 AFOSR-79-0057 1/3

UNCLASSIFIED F/G 20/4 NL

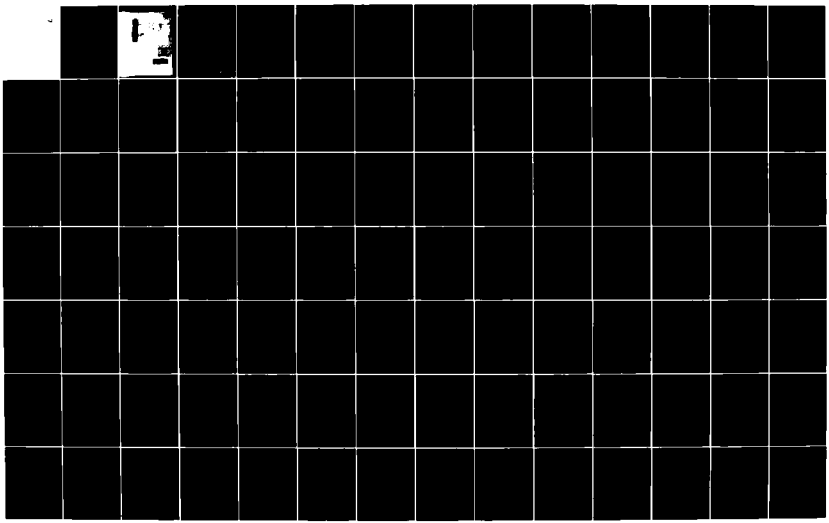

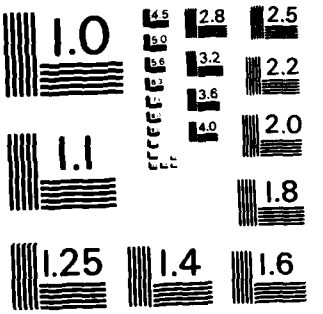

MICROCOPY RESOLUTION TEST CHART
NATIONAL BUREAU OF STANDARDS - 1963 - A

AD A137740

UNCLASSIFIED

REPORT DOCUMENTATION PAGE		READ INSTRUCTIONS BEFORE COMPLETING FORM
1. Report Number AFOSR-TR- 84-0071	2. Govt Accession No. AD-A137	3. Recipient's Catalog Number 740
4. Title (and Subtitle) Studies of Aerodynamic Drag		5. Type of Report & Period Covered Final Report 79 April 01 - 82 Sept 30
		6. Performing Org. Report Number
7. Author(s) W.A. Wilby J.E. Field		8. Contract or Grant Number AFOSR-79-0057
9. Performing Organization Name and Address Cavendish Laboratory, University of Cambridge Madingley Road, Cambridge CB3 OHE England		10. Program Element, Project, Task Area & Work Unit Numbers 61102F 2307/A2
11. Controlling Office Name and Address Air Force Office of Scientific Research/NA Bolling AFB, DC 20332		12. Report Date December 1982
		13. Number of Pages 265
14. Monitoring Agency Name and Address European Office of Aerospace Research and Development, Box 14, 223/231 Old Marylebone Road, London NW1 5TH, England		15. Security Class (of this report) UNCLASSIFIED

16. & 17. Distribution Statement

Approved for public release; distribution unlimited.

18. Supplementary Notes

19. Key Words

Aerodynamics, Turbulence, Viscosity, Molecular Aerodynamics, Electromagnetic Radiation

20. Abstract Earlier workers ~~have~~ reported that the viscosity of gases can be changed appreciablyby radioactive irradiation, offering a possible means of achieving drag reduction in flight. A precision skin friction drag balance and torsion disc viscometer were developed ~~in order~~ to investigate this effect. It is shown that, with practical radiation levels, irradiation has a negligibly small effect on viscosity and skin friction drag (both laminar and turbulent). This is in agreement with theoretical estimates of the change in viscosity due to ionisation. A critical analysis of the earlier work highlights various inadequacies, and the present work is considered to be the most reliable to date.

It has also been reported that turbulent gas flows align polar or polarisable molecules, whose motion then gives rise to detectable electromagnetic radiation. A study was made of this phenomenon, with a view to applications in monitoring the structure of turbulent gas glows during drag reduction experiments. It is concluded that the previous interpretation was erroneous and that the probes used

FORM 1473

UNCLASSIFIED

UNCLASSIFIED

were responding to vibration rather than to electromagnetic radiation. Calculations suggest that any electromagnetic signal will be at least 120 dB below the background noise level.

The equipment and electronics developed in the course of the research can be used for accurate, relative, measurements of skin friction drag and viscosity. The operation of the viscometer is particularly simple, with the logarithmic decrement being determined automatically. The relative viscosity is calculated using a simple formula, derived from earlier thoeretical work. Some suggestions are made for improving the theory of the torsion disc viscometer, so as to permit accurate, absolute, measurements of viscosity with this type of instrument.

The results obtained with the viscometer and drag balance show that radioactive irradiation does not offer a practical means of reducing drag in flight.

Accession For
NTIS GRA&I ☑
DTIC TAB ☐
Unannounced ☐
Justification
By
Distribution/
Availability Codes
Dist | Avail and/or Special
A-1

DTIC COPY INSPECTED

UNCLASSIFIED

INTRODUCTION

1.1 Introduction

As a result of soaring fuel prices, the problem of reducing the drag on a body moving through a fluid has assumed increasing importance in recent years. The drag has two components, pressure or form drag, resulting essentially from the cross sectional area presented to the flow, and viscous or skin friction drag arising from the shear stresses at the surface of the body*. Since the skin friction drag can account for up to one half of the total drag of an aircraft, there is a strong incentive to achieve greater efficiency and performance by reducing the surface shear stress. The region of the fluid in which shear stresses become important is generally restricted to a thin layer on the surface of the body, the boundary layer, in which the relative fluid velocity rises from zero at the surface ("no slip" condition) to the free stream value. It follows that the properties of this boundary layer, and of the surface, are of paramount importance in determining the skin friction drag. Hitherto, most approaches to aerodynamic drag reduction have involved laminar flow or boundary layer control, where the transition to turbulence or the separation of the boundary layer is delayed. However, it has become apparent that a closer understanding of the boundary layer-surface interaction at the molecular level is called for. Considerable effort in this direction has been invested in the field of hydrodynamics, where the addition of small quantities of long chain polymers to turbulent liquids results in large drag

* in the presence of another body or surface there can be an extra component of drag, the induced drag.

reductions. This dissertation describes research into the effect of changing gas properties at the molecular level. The work was inspired by the results of experiments by Clark, Kestin and Shah (Clark et al 1977, Kestin & Shah 1968) and by August (1972; see also August 1967,1969) in which changes in gas viscosity or drag were obtained by radioactive irradiation of the gas.

An investigation has also been made of an effect reported by Clark (1958, 1975, 1980a, 1981), who detected signals from turbulent gas flows and shock waves using sensitive electric and magnetic probes. It was thought that this effect might have been of use in studying changes induced in the structure of turbulent gas flows during drag reduction experiments.

1.2 Fluid Dynamic Drag

To consider the origins of fluid dynamic drag forces let us start with the equations of motion of an ideal, i.e. incompressible and inviscid, fluid. The equation of continuity is

$$\text{div} \quad \underline{u} = 0$$

and the equivalent of Newton's second law is

$$- \underline{\nabla} p = \rho \frac{D\underline{u}}{Dt}$$

where p, ρ and $\underline{u}$ are the pressure, density and velocity of the fluid, and $\frac{D}{Dt}$ is the substantive derivative (i.e. we are looking at a particle of fluid)

Since $\delta u_i = \frac{\partial u_i}{\partial t} \delta t + \sum_j \frac{\partial u_i}{\partial x_j} \delta x_j$

AIR FO[illegible] (AFSC
NOTIC[illegible]
This [illegible] is
appr[illegible] 2.
Distr[illegible] unlimited.
MATTHE[illegible]ER
Chief, Technical Information Division

we can write $\frac{D\underline{u}}{Dt} = \frac{\partial \underline{u}}{\partial t} + (\underline{u}.\ \underline{\nabla})\underline{u}$

and hence

$$\frac{\partial \underline{u}}{\partial t} + (\underline{u}.\ \underline{\nabla})\underline{u} = -\frac{1}{\rho}\underline{\nabla}\, p \qquad \text{(Euler's Equation).}$$

From Euler's Equation and the continuity equation it can be shown that

$$\oint \underline{u}.\underline{dl} = \Gamma = \text{constant} \qquad \text{(Kelvin's Circulation Theorem)}$$

(on a path following the particle)

and if $\Gamma = 0$ initially (irrotational flow) then curl $\underline{u} = 0$.

Since curl grad $\phi \equiv 0$ for all ϕ we can define a flow potential by

$$\underline{u} = \text{grad}\ \phi$$

From the continuity equation ϕ must satisfy Laplace's Equation

$$\nabla^2\phi = 0$$

If we now consider a steady state flow and integrate Euler's Equation along a streamline (a continuous line whose tangent at any point is in the direction of the fluid velocity at that point) we get Bernoulli's Theorem,

$$\tfrac{1}{2}\, u^2 + \frac{p}{\rho} = \text{constant}$$

If we apply this result to the potential flow solutions for flow around an obstacle, with the boundary condition $u_\perp = 0$ at the surface of the (impenetrable) obstacle, it can be shown that the drag (integral of pressure forces parallel to the mean flow

direction) is zero. This is known as d'Alembertps Paradox. (There is, however, a lift, given by $L = -\rho\mu_o\Gamma$ where μ_o is the ambient flow speed:- this is the Kutta-Zhukovksii theorem).
It is contrary to our everyday experience and might suggest that the idea of a potential flow is not particularly helpful. However, we shall see that it is a useful idea for the flow at some distance from a body in the fluid. (A drag can in fact arise in an ideal fluid if there is a surface along which waves can transport energy away from the body(see Landau & Lifshitz (1959a) for example). or if another body or boundary is present.

An obvious modification to the theory, however, is the introduction of viscosity. By considering a fluid from the molecular viewpoint, we can see that on average there will be a transfer of momentum between molecules from regions with different mean velocities. The coefficient of viscosity, μ, can be defined in terms of the shear stress necessary to sustain momentum transport along a velocity gradient.* If $\underline{u}$ is parallel to the x direction and varies in the y direction, the shear is

$$\tau = \mu \frac{\partial u}{\partial y} \tag{1.1}$$

For a dilute gas, kinetic theory gives the result $\mu = \frac{1}{3}mn\bar{c}\lambda$, where λ is the mean free path. This is a fair approximation to observed behaviour (see Reif (1965) for example). Within the fluid there can not be any discontinuity in velocity, since this would imply an infinite velocity gradient (which would give an infinite shear stress, acting to remove the discontinuity in an infinitesimal time). If we assume that the forces between the molecules of the fluid and those of a body in the fluid are similar, then it follows that the relative fluid velocity must

* It will be assumed that the fluid is incompressible, i.e. of constant density, so that the second coefficient of viscosity need not be considered explicitly.

drop to zero at the surface, i.e. $u_{||} = 0$. This new boundary condition is known as the "no slip" condition, and holds provided that the mean free path is very much smaller than the length scale of the body.

When this condition is not satisfied (e.g. at very low gas pressures) the gas can often still be treated as a continuum, but with the introduction of a slip velocity at the wall (see Kennard (1938) for example).

The shear at the wall,

$$\tau_o = \mu \left.\frac{\partial u}{\partial y}\right|_{y=o} \tag{1.2}$$

where y is the distance from the wall, allows for a drag force on the body. The flow pattern also changes, usually most markedly behind the body with the introduction of a wake. This causes a change in the pressure distribution which will also contribute to the drag. The effects of viscosity are generally only important in a thin layer, the boundary layer, on the surface of the body. This observation was first made by Prandtl in 1904 and marked the beginning of boundary layer theory. Outside of the boundary layer the flow remains essentially potential. Considerable information on the drag can therefore be obtained by studying the flow in the boundary layer.

To go into more detail, let us look at the equations of motion of the fluid. With the introduction of viscosity, Euler's Equation takes the form

$$\frac{\partial \underline{u}}{\partial t} + (\underline{u}.\underline{\nabla})\underline{u} = -\frac{1}{\rho}\,\underline{\nabla}\,p + \nu\,\nabla^2\,\underline{u} \tag{1.3}$$

where $\nu = \mu/\rho$ (kinematic viscosity)

This is the Navier-Stokes equation and the inherent mathematical difficulty of many fluid dynamic problems may be traced to the non-linearity of this equation. We can get an idea of the boundary layer thickness, δ, by observing that inertial forces must dominate outside of the boundary layer, while inside the boundary layer the inertial and viscous forces will have comparable magnitudes. Therefore, if U is the free stream velocity and L a characteristic dimension of the body, the Navier-Stokes equation implies that

$$\frac{\rho U^2}{L} \sim \frac{\mu U}{\delta^2}$$

and hence $\frac{\delta}{L} \sim (\frac{UL}{\nu})^{-\frac{1}{2}} = Re^{-\frac{1}{2}}$ where Re is the Reynolds Number. This justifies the idea of a thin boundary layer except when the Reynolds Number is small.

Of course, the definition of the boundary layer thickness has to be arbitrary to some extent, as the flow velocity will generally increase asymptotically to the free stream value. The conventional approach is to take the boundary layer as extending to the point where

$$u = 0.99\ U$$

Let us take a specific example by way of illustration and consider a flat plate in a uniform flow (this will be of use later). Let us take $\underline{u}$ to have cartesian components u,v,w and take x along the surface, parallel to the flow direction, y

perpendicular to the surface, and $w = 0$. Then for a thin boundary layer the Navier-Stokes equations simplify to

$$\frac{\partial u}{\partial t} + u \frac{\partial u}{\partial x} + v \frac{\partial u}{\partial y} = - \frac{1}{\rho} \frac{\partial p}{\partial x} + \nu \frac{\partial^2 u}{\partial y^2} \qquad (1.4)$$

The boundary conditions are

$u = v = 0$ at $y = 0$

$u = U(x,t)$ at $y = \infty$

where U is the potential flow solution. The continuity equation is

$$\frac{\partial u}{\partial x} + \frac{\partial v}{\partial y} = 0$$

These equations are Prandtl's Boundary Layer Equations.

A further simplification can be made by observing that the continuity equation can be automatically satisfied by the introduction of a stream function ψ satisfying

$$u = \frac{\partial \psi}{\partial y} \qquad v = \frac{-\partial \psi}{\partial x}$$

The boundary layer equation is then

$$\frac{\partial^2 \psi}{\partial y \partial t} + \frac{\partial \psi}{\partial y} \frac{\partial^2 \psi}{\partial x \partial y} - \frac{\partial \psi}{\partial x} \frac{\partial^2 \psi}{\partial y^2} = - \frac{1}{\rho} \frac{\partial p}{\partial x} + \nu \frac{\partial^3 \psi}{\partial y^3}$$

For a flat plate (figure 1.1) with no pressure gradient and with steady flow we can write $\psi = \sqrt{\nu x u_\infty}\, f(\eta)$, where f is the dimensionless stream function and $\eta = y\sqrt{\frac{u_\infty}{\nu x}}$. Then $u = u_\infty f'(\eta)$ and $v = \frac{1}{2}\sqrt{\frac{\nu u_\infty}{x}}\,(\eta f' - f)$. Substitution into the boundary layer equation and simplification leads to the ordinary differential

equation

$$ff'' + 2f''' = 0 \qquad \text{(Blasius Equation)}$$

with the boundary conditions $f, f' = 0$ at $\eta = 0$

$f = 1$ at $\eta = \infty$

This can be solved numerically and the boundary layer thickness, defined as above, becomes

$$\delta = 5.0\sqrt{\frac{\nu x}{u_\infty}} \tag{1.5}$$

We see that $\frac{\delta}{x} \propto Re^{-\frac{1}{2}}$ as expected.

The skin friction is

$$\tau_o(x) = \mu \left.\frac{\partial u}{\partial y}\right|_{y=o} = 0.332\, \mu u_\infty \sqrt{\frac{u_\infty}{\nu X}} \tag{1.6}$$

or, in terms of a dimensionless drag coefficient,

$$C_f(x) = \frac{\tau_o(x)}{\frac{1}{2}\rho u_\infty^2} = \frac{0.664}{\sqrt{R_x}} \tag{1.7}$$

(Blasius skin friction law for a flat plate; R_x is the Reynolds number based on the distance from the front of the plate)

Behind a flat plate we would expect to see a wake defined by a continuation of the boundary layers. In a more realistic case, with a body of finite thickness, the wake will consist of a region of eddying, rotational fluid moving downstream and bounded by boundary layers which have separated from the surface (figure 1.2). We can understand the phenomenon of boundary layer separation on such a body by considering the pressure gradient

along the surface. The fluid is initially accelerated along the surface, and then decelerated, moving into a region of higher static pressure towards the rear of the body. If this adverse pressure gradient is high enough, then a reversed flow is set up and the boundary layer separates. The wake originates with this reversed flow, and the lower pressure in the wake, compared with that at the front of the body, leads to the pressure or form drag on the body. For bluff bodies this is the major component of the drag and it follows from dimensional arguments that the drag coefficient

$$C_d = \frac{D}{\frac{1}{2}\rho u_\infty^2 A} \qquad \text{(where D is the drag force and A the cross sectional area)} \qquad (1.7)$$

will be relatively insensitive to the Reynolds number. The importance of streamlining is now obvious, since if the body tapers towards the rear, separation occurs at a narrower section and the wake width and drag are reduced.

At higher flow speeds the boundary layer on the body becomes turbulent, the initially smooth flow breaking up into an eddying, fluctuating, three dimensional motion. This leads to an extra (Reynolds) stress; for a boundary layer the shear stress becomes

$$\left(\mu \frac{\partial U}{\partial y} - \rho\, \overline{uv}\right)$$

where U is now the mean flow speed, u,v the velocity fluctuations in the x and y directions and $\overline{}$ denotes a time average.

However, these higher shear stresses need not necessarily lead to higher net drags as turbulent boundary layers are more resistant to separation. In the well known case of a sphere, the delay in separation with a turbulent boundary layer gives a lower drag

due to the narrowing of the wake. This effect has often been exploited, for example with golf balls where the dimpling ensures a turbulent boundary layer.

The transition to turbulence occurs as a result of the dynamical instability of the sheared flow. Transition can be analysed most simply by linear stability theory, in which the stability to infinitely small disturbances is considered. In this case a disturbance can be described in terms of its Fourier components, i.e. we can consider a stream function $\psi = \phi(y)e^{i(\alpha x-\beta t)}$ which satisfies the Navier-Stokes equations with quadratic terms in the fluctuating velocities neglected. The differential equation describing the disturbance, known as the Orr-Sommerfeld equation, is then

$$(U - c)(\phi'' - \alpha^2\phi) - U''\phi = -\frac{i}{\alpha Re}(\phi'''' - 2\alpha^2\phi'' + \alpha^4\phi)$$

when the basic flow is almost parallel,
where c, the (complex) wave velocity, is

$c = \frac{\beta}{\alpha}$ and U is the velocity of the base flow which in general will be a function of the transverse co-ordinate.

Solutions of this eigenvalue equation with $Im(c)<0$ correspond to damped waves and those with $Im(c)>0$ to amplified (unstable) waves. This forms a basis for stability analysis. The solutions generally show that above a critical Reynolds number the flow will be unstable only to disturbances within a certain range of frequencies. This has been confined experimentally, for example by introducing a controlled periodic disturbance (e.g. a vibrating ribbon) and observing which frequencies result in amplification of the resultant wave (Polymeropoulos & Gebhart

1967). These waves are known as Tollmien-Schlichting waves. Although these mechanisms are expected to operate in spontaneous or natural transition, Tollmien-Schlichting waves are not always observed. This is presumably because the critical amplitude for full transition has been reached before the frequency selection process implied by linear stability theory has proceeded far enough for a particular wavelength to dominate. (Transitions at lower Reynolds numbers could also be observed, as linear stability theory does not consider the effect of finite disturbances on the flow). Some striking photographs of the growth of turbulent regions in laminar boundary layers have been obtained by Gad-el-Hak et al (1981).

The resulting turbulent flow is characterised by an irregular eddying motion, whose detailed motion is not reproducible but which has important statistical and structural properties.

The turbulent boundary layer is generally considered as consisting of two main regions. From the boundary conditions at the wall we can see that the Reynolds stress must drop to zero near the wall and that the viscous stress will dominate. This region is known as the laminar sub-boundary layer. Taking the total stress

$$\tau = \mu\frac{\partial U}{\partial y} - \rho\overline{uv} \qquad (1.8)$$

as constant, it follows that the velocity will be linear near the wall. Characterising the velocity scale near the wall by the shear velocity

$$u_\tau = \sqrt{\frac{\tau_w}{\rho}} \qquad (1.9)$$

we can write

$$\frac{U}{u_\tau} = \frac{yu_\tau}{\nu} \tag{1.10}$$

In the outer boundary layer we expect the mean velocity gradient to be independent of viscosity, i.e.

$$\frac{\partial U}{\partial y} = f(u_\tau, y)$$

and, on dimensional grounds,

$$\frac{\partial U}{\partial y} = \frac{u_\tau}{Ky}$$

K is von Kármán's universal constant, found to be 0.41 experimentally. Integration gives the well known logarithmic velocity profile

$$\frac{U}{u_\tau} = \frac{1}{K}\left[\ln\left(\frac{yu_\tau}{\nu}\right) + A\right] \tag{1.11}$$

where $\frac{yu_\tau}{\nu} = y^+$, the dimensionless distance from the wall. In the intermediate (buffer) region large velocity fluctuations and Reynolds stresses are observed, with high rates of energy production and dissipation. The stresses are associated with large scale motions in the boundary layer. Low speed fluid in the sub-boundary layer erupts intermittently, or "bursts", into the outer boundary layer, while regions of higher speed fluid rush in towards the wall. These motions interact with the large scale eddies in the boundary layer and dominate the process of turbulent stress production. The logarithmic region of the boundary layer extends to the point where the large scale eddies

are influenced by the outer regions of the flow, typically at $\frac{y}{\delta} \sim 0.2$. Figure 1.3 shows an example of a turbulent boundary layer mean velocity profile.

This brief discussion provides a framework for the consideration of the various methods of drag reduction to be discussed in the next section. For more detailed descriptions of boundary layer theory and turbulent shear flows see, for example, Schlichting (1979), Tritton (1977), Townsend (1976), Bradshaw (1971) and Phillips (1969).

1.3 Drag Reduction

In the light of the discussion of the previous section let us now consider the methods by which skin friction drag can be reduced. We can take two different approaches; boundary layer control, where the transition to turbulence or the separation of the boundary layer is delayed, or turbulence suppression, where the flow remains turbulent but the turbulent stresses are somehow reduced.

Prevention of separation, generally increasing lift as well as decreasing drag, can be achieved by boundary layer suction or blowing. The former holds the boundary layer onto a porous aerodynamic surface by suction. In the latter method, high speed fluid is ejected into the flow in such a way as to accelerate the boundary layer along the surface and through regions of adverse pressure gradient.

A reduction in fluid viscosity near the wall increases the curvature of the velocity profile and increases the stability

of the boundary layer. It follows that boundary layer heating in liquids and boundary layer cooling in gases increases the transition Reynolds number (Barker & Gile 1981, Schlichting 1979). Boundary layer cooling has not been important for aircraft, but may become so in the event of a replacement of conventional fuels by cryogenic fuels such as LH_2 and LCH_4. Cooling has been considered in the economics of cryo-fuelled aircraft by Reshotko (1979). It is suggested that drag reductions of up to 20% in cruise might be achieved for a conventional transport, and that this would make cryo-fuelled aircraft competitive with present aircraft.

The introduction of dust to a gas has been observed both to delay transition and to reduce turbulent shear stresses (Saffman 1962, Boothroyd 1966, Rossetti & Pfeffer 1972). Qualitatively, the increased inertia of the particles resists small scale velocity fluctuations in the gas and provides an additional means of energy dissipation. The application of this effect to aircraft has been considered by Davey and Melcher (1980).

A disadvantage of these methods is the associated weight and maintenance penalty of the equipment which must be carried by the aircraft. This highlights the attractiveness of methods which use some kind of modification of the surface.

Examples are surface waviness and skin compliance (Cary et al 1980, Blick 1969). The problem with the former is that most configurations cause an increased pressure drag which can negate the skin friction reductions. Skin compliance effects

are particularly effective in hydrodynamics, and are thought to be responsible for the dolphin's speed.

An approach of current interest is the use of "turbulence manipulators" or "large eddy break-up" (LEBU) devices to modify the turbulent boundary layer. Such devices consist of one or more flat plates, inserted into the flow at appropriate distances from the surface so as to interfere with the large scale motions in the boundary layer (Corke et al 1981, Hefner 1980). The results suggest that significant skin friction drag reductions can be obtained in this manner. The exact mechanism is not understood, but the plates appear to remove the large scale eddies and also to interfere with the bursting process. However, if the device drag is included, no net drag reductions have yet been obtained. These devices are at present the subject of an investigation by the Fluid Dynamics Group at the Cavendish Laboratory.

Finally, a discussion of long-chain polymer additives is in order. The effect of long chain polymers in liquid flows was discovered some time ago by Toms (1948) and, independently, by Mysels (1949). This is possibly the most dramatic method of drag reduction, up to 80% drag reductions being attainable with only tens of ppm by weight of polymer additive. A popular additive is the polymer polyethylene oxide ("polyox"), which has random-coiling linear chains of molecular weight $\sim 10^5 - 10^6$. As with skin compliance, the effect has been exploited by nature. The hogchoker fish, for example, has a mucous coating containing long chain glycoprotein molecules which diffuse into the

boundary layer to give significant drag reductions (Ling & Ling 1974). The mechanism of this effect is still not entirely clear. Long chain polymers do not delay transition, but are effective in reducing turbulent shear stresses. The onset of drag reduction occurs at a well defined shear stress and there is a maximum drag reduction asymptote which appears to be independent of the polymer variables. Figure 1.4 shows the velocity profile near the wall during drag reduction. The polymer molecules are active at the edge of the sub-boundary layer, at $y^+ \sim 15$. The length scales involved might appear to be important (see Virk et al 1967) but the radius of gyration of a random-coiled polymer molecule is typically 10^{-3} times the scale of the smallest bursts. In fact, the onset of drag reduction seems to occur when the relaxation time of the long chain polymer molecules is of the order of the turbulence production time scale. This suggests that the storage of energy in extended chains is of importance in inhibiting the bursting and stress production process. The subject has been reviewed by Virk (1975) and the effect of the polymer molecular variables and the time scale discussed by Zakin & Hunston (1980). Malkus (1978) has considered the structure of turbulent velocity profiles from stability criteria, using the hypothesis of spectral "smoothness" in the momentum transport. The change in velocity profile with drag reduction then corresonds to a reduction in the tail of the momentum transport spectrum. Gad-el-Hak et al (1981) also observed a suppression of small scale turbulent structures due to polymer additives in the growth of turbulent regions in laminar boundary

layers.

Applications of this effect have mainly been limited to pipe flows, where larger volume flows can be realised without excessive driving pressures. This could be useful for the transport of oil through pipelines, for fire fighting and for irrigation. Such applications have been discussed by Frenkiel et al (1977); see also Leuchtag (1978).

1.4 The Effect of Irradiation

We now come to the main topic of this thesis, the effect of boundary layer irradiation on the drag due to a gas. To investigate the possibility that long range Coulomb forces might alter the "no slip" condition, and provide a means of reducing drag in flight, Clark, Kestin and Shah (Clark et al 1977, Kestin & Shah 1968) used a torsion disc viscometer to measure the apparent viscosities of several gases with radioactive irradiation providing significant concentrations of ions. The changes in viscosity were generally small, but significant decreases of 0.25 % and 7.6 % were observed for air (at 1 atmosphere and 1 mmHg pressure respectively) and an increase of 5.25 % for argon at atmospheric pressure. The changes could not be explained directly by ionisation of the gas.

Experiments on turbulent air flow by August (1972) gave drag reductions from 0% at atmospheric pressure up to 80% at 0.1 atmosphere. No detailed information was given on the test conditions. The results were explained in terms of an analogy

between long-chain polymers in liquids and α - particle tracks in air.

In both sets of experiments significant changes were reported using relatively low levels of radioactivity, $\sim$ 1m Ci cm^{-2} of an α emitter (the level quoted by Clark, Kestin & Shah was probably too high (Clark 1980b); they also used a strong, i.e. 97.5 Ci, ^{137}Cs γ source).

This dissertation describes a further investigation of this effect. A skin friction drag balance was used with flow conditions more characteristic of aircraft flight, with a view to identifying any potential aerodynamic applications. A torsion disc viscometer was used to obtain results with near static gases for a range of pressures and compositions, with a view to elucidating the physics of the effect.

While the use of radioactive irradiation may not be a particularly practical approach to drag reduction, despite the low activity of the source, it was hoped that an understanding of irradiation effects might indicate possible new approaches to aerodynamic skin friction drag reduction.

Figure 1·1. Flow Past a Flat Plate.

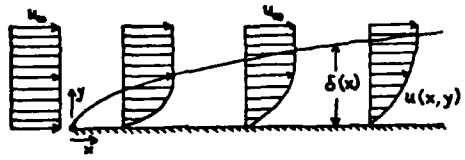

Figure 1·2. Boundary Layer Separation -

a) schematic representation of flow.

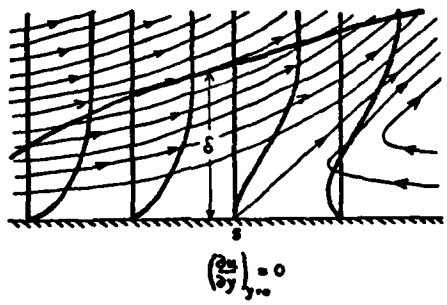

b) on an aerofoil at large angle of attack.

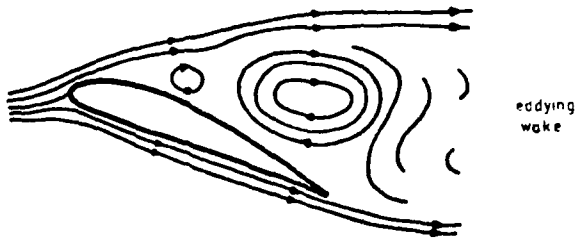

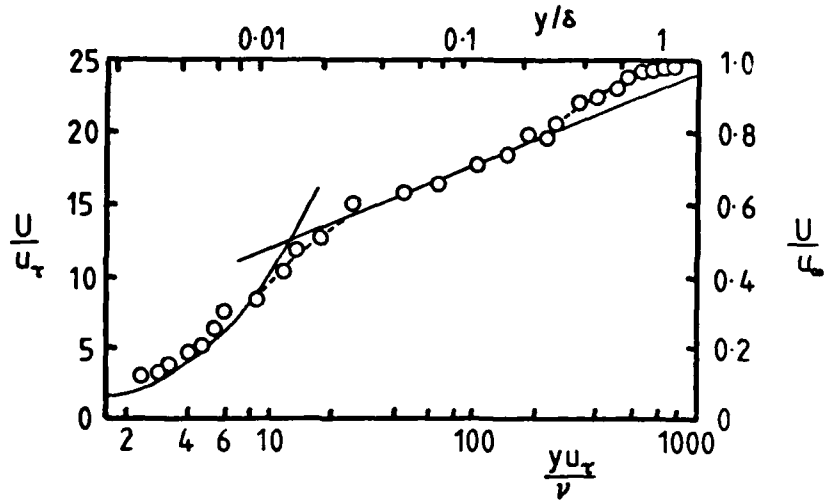

Figure 1·3. Example of a Turbulent Boundary Layer Mean Velocity Profile (after Tritton 1977, solid lines equations 1.10 & 1·11).

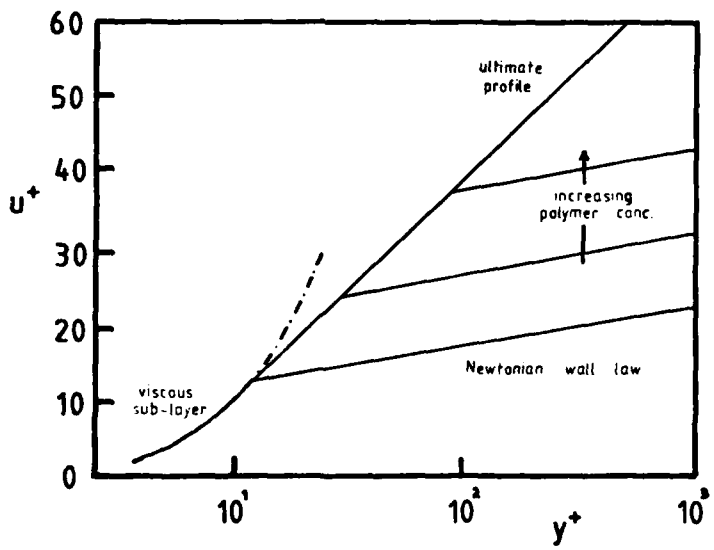

Figure 1·4. Idealised Mean Velocity Profiles during Polymer Drag Reduction (after Virk 1975).

STUDIES OF TURBULENT GAS FLOWS USING MAGNETIC PROBES

2.1 Introduction

Clark (1958, 1975, 1980a, 1981) has reported that turbulent gas flows and shock waves radiate low level electromagnetic fields. Signals were detected using specially designed magnetometer and electrometer probes. Clark suggested that the signals were generated by the motion of polar or polarisable molecules, aligned in regions of shear flow. The possibility of using this remote sensing technique to monitor the structure of turbulent gas flows was of obvious interest and an investigation of the effect is described in this chapter. This work has also been summarised elsewhere (Wilby et al 1982).

2.2 Experimental

The probes used by Clark were a coil magnetometer wound on a ferrite core and an electrometer consisting of a cylindrical electrode connected to a very high input impedence amplifier. Signals from gaseous and liquid oxygen flow were obtained with the probes immersed in the turbulent fluid downstream of a butterfly valve (Clark 1958). In further experiments (Clark 1975) a magnetometer was placed in an open return windtunnel, downstream of a sharp edged strip shedding vortices. Measurements were also made on nozzle flows with a Mach disc. In recent experiments performed by Clark at Cambridge (Clark 1980a) the standard test configuration was a small perspex (PMMA) windtunnel with a 1.63 mm diameter brass cylinder spanning the 5mm x 20 mm test section. A 1000 turn magnetometer wound on a ferrite core (∿ 20 mm x 2 mm

dia.) was cemented into the windtunnel wall above the cylinder so as to detect the vortices shedding from the cylinder. Signals were analysed using a Marconi Instruments TF2370 Spectrum Analyser (see figure 2.1). The frequency response of the magnetometer and circuitry was linear from 0.3 - 100 kHz. Typical spectra contained a peak at the vortex shedding frequency with an amplitude of 10^{-8} - 10^{-9}T. The background noise level was 10^{-10} - 10^{-11}T. Figure 2.2 shows spectra and background traces for a flow velocity of 145 m s^{-1}. The shedding frequency was 17.5 kHz. In a series of experiments with different gases Clark (1980a) found that the signal strength at constant velocity appeared to be a function of the polarisability of the gas molecules. Figure 2.3 shows the results for a flow velocity of 100 m s^{-1}.

Separate experiments involved an overblown whistle producing edge tones of approximately 7 kHz in frequency, with a magnetometer about 20 cm away. The sound level at the magnetometer was $\gtrsim$ 130 dB, and the magnitude of the signal was about 20 dB above the background noise level.

In attempts to understand the mechanism of the effect magnets were placed near the magnetometer. This had the effect of increasing the sensitivity by about 20 dB. To investigate the effect of electric fields high potentials were applied to the cylinder in the windtunnel test section. No change in signal was observed, even for field strengths just short of breakdown between the cylinder and the wall (figure 2.4). This result seemed in complete conflict with the hypothesis of Clark, since

high electric field strengths would be expected to affect any signal from aligned dipoles. This, together with other observations (for example, tapping the magnetometer gave a signal, the maximum signal strength corresponded to a perceptible windtunnel vibration and the coaxial lead to the probe responded to the whistle), suggested that an alternative mechanism might be operating. Although Clark reported having tested for, and not found, a significant vibration response (Clark 1980c), this seemed the most likely hypothesis, and such a response was conclusively demonstrated by vibrating the windtunnel with a tuning fork. With the fork pressed onto the end of the windtunnel test section, signals comparable with those from gas flows could be obtained (figure 2.5). The importance of vibration signals was established in the following experiments, performed with the assistance of Mr. W.G. Rees.

(i) The mechanical contact between the magnetometer and the windtunnel wall was broken. Signals were reduced, typically by $\sim$ 40 dB. By resting the coil on foam the signal could be further reduced to the background noise level.

(ii) Two identical magnetometers were excited by a 7.4 kHz tone from the whistle. By measuring the phase difference of the signals as a function of the separation of the magnetometers, it was possible to determine the wavelength of the exciting signal. The results are shown in figure 2.6. The calculated wavelength, assuming acoustic radiation and an air temperature of 20°C, is 4.64 ± 0.03 cm. The observed value was 4.65 ± 0.03 cm. In a control experiment, with an electromagnetic source of the same

frequency, no phase variation was observed. This is as expected as the electromagnetic wavelength is about 40 km at this frequency.

(iii) The magnetometer was acoustically isolated from the whistle using a glass container. The signal was reduced by $\sim$ 20 dB to the background noise level. No attenuation was observed in a control experiment. With the magnetometer just touching the inside of the glass a signal could again be obtained. It follows that the signal cannot be due to an electromagnetic field generated at the whistle or by the acoustic waves near the magnetometer.

2.3 Discussion +

The experiments described above show that when the magnetometer is isolated from sources of vibration there is no detectable radiation signal from the gas flow. In view of these results, the conclusions of Clark (1958, 1975, 1980a, 1981) are unlikely to be correct, as no isolation from flow induced vibration or shock waves was provided.

The dependence of signal strength on gas polarisability can be interpreted as a dependence on gas density, relating to the polarisability through the molecular volume. A plot of signal strength against gas impact pressure reduces Clark's data for all of the gases to a single curve (figure 2.7), consistent with a vibration signal. (Some data for He and H_2 have been rejected as the signal strengths were anomalous in both cases. For these light gases the signal strengths were very low and the peaks in the spectrum not easily identifiable. The recorded shedding

+ I would like to acknowledge the assistance of Mr. W.G. Rees and the suggestions of Dr. J.C. Mumford in the analysis of the vibration response.

frequencies were also inconsistent, further suggesting that the results may have been erroneous).

The vibration response can be simply explained by vibration of the magnetometer in an inhomogenous magnetic field, or by torsional vibration of the magnetometer in a uniform field. We can get an idea of the likely sensitivity to vibration if we take the earths field in the laboratory to be $\sim 5 \times 10^{-5}$T with inhomogeneities of $\sim 10^{-4}$ Tm^{-1} (Chapman & Bartels 1940). To get an apparent radiation level of 10^{-9}T we would then need displacement amplitudes of $\sim$ 10μm, or torsional amplitudes of $\sim 2 \times 10^{-5}$ radians, corresponding to a relative displacement of the ends of the coil of $\sim \frac{1}{2}$ μm (assuming a field perpendicular to the coil axis). These estimates are in agreement with shaker experiments, which demonstrated a response to vibration amplitudes of a few μm.

To investigate the effect of partly shielding the field of the earth, cylindrical mu-metal screens were used to surround the windtunnel test section. The transverse component of the field of the earth was reduced by a factor of 20, while that perpendicular to the coil was relatively unchanged. As the vibration response and the signal from gas flows were unchanged, it appears that the torsional motion is the more important. It seems, therefore, that the signals reported, and the effect of external magnetic and electric fields on the magnetometer, can be readily explained by the effect of probe vibrations of quite small amplitudes. A similar analysis can be applied to the signals from the electrometer probes (Clark 1981). The signals

correspond to fluctuations of $\sim$ 1 mV in the potential of the probe tip. For a vibration amplitude of 1 μm an electric field of 10^3 Vm^{-1} is necessary to explain the response, of the order of the vertical field of the earth in open space (Chalmers 1949). Fields in a laboratory environment could well be greater.

It is instructive to estimate the magnitude of any electromagnetic signal which might be radiated from turbulent gas flows. While it is well known that shear gradients can cause optical birefringence in gases, resulting from a tensor polarisation of the angular momenta of the gas molecules (Boas 1971), no alignment would be expected for symmetric molecules such as Ar or Ne since the frequency of dipole fluctuations is much greater than the vortex frequency. The effect for other gases would also be expected to be small; for air at atmospheric pressure Boyer et al (1975) found a birefringence of $\Delta n \sim 5 \times 10^{-15}$ G, where G is the velocity gradient, giving $\Delta n \sim 5 \times 10^{-9}$ for the vortices in the windtunnel. However, if we assume that a resonable degree of alignment does exist for a polar gas, we can estimate the maximum credible intensity of radiation by treating the dipole as a Hertzian dipole of frequency given by the vortex shedding frequency. Dipole motions must be poorly correlated on a microscopic scale due to the thermal motion of the molecules, and so the total radiation intensity from N dipoles would be N times the individual radiation intensities,

i.e. $B_{tot} = \sqrt{N}\ B_i$

In the induction zone of a Hertzian dipole

$$B_i = \frac{\mu_0 \omega p}{4\pi r^2}$$

If we take $\omega \sim 10^5\ s^{-1}$, $r^2 \sim 10^{-5} m^2$, $p \sim 10^{-29}$ Cm we get

$$B_i \sim 10^{-26} T$$

The gas volume involved in the process is $\sim 5 \times 10^{-7} m^3$ giving $N \sim 10^{19}$, and hence

$$B_{tot} \sim 10^{-17}\ T \qquad (2.1)$$

At this level a contribution from free charges in the flow might also be expected. For $\sim 10^3$ ions cm^{-3} and a flow velocity of $\sim 100\ m\ s^{-1}$, we get a current flow of 10^7 ions s^{-1}. Treating this as a current loop around the cylinder

$$B = \frac{\mu_0}{4\pi} \frac{2IdS}{r^3} \sim 10^{-17}\ T. \qquad (2.2)$$

Such small signals would be very difficult to detect in the background magnetic noise, and it seems certain that the signals reported by Clark must have been due to vibration.

The extreme sensitivity to vibration suggested possible applications to vibration studies, and, in fact, a similar method has been described elsewhere (Hoffman et al 1976).

The experiments on signals from vortices in the windtunnel stimulated an interest in the effect of flow confinement on vortex shedding frequencies. The following chapter describes an investigation of the problem using a magnetometer and a hot wire

anemometer, illustrating the use of the magnetometer for vibration analysis as well as providing some information on an area of fluid dynamics in which there is still inadequate experimental data.

2.4 Conclusions

In all experiments in which probe vibration was eliminated, no signals could be detected above the background noise level. This places an upper experimental limit of $\sim 10^{-11}$ T on the strength of any radiation signal from the gas flow. Calculations suggest a limit of $\sim 10^{-17}$ T for radiation from this scale of non-ionised gas flow.

The signals reported by Clark are considered to be a consequence of probe vibration, caused either by acoustic radiation or by the flow near the probe. The vibration response seems to be adequately explained in terms of the static magnetic or electric environment of the probes.

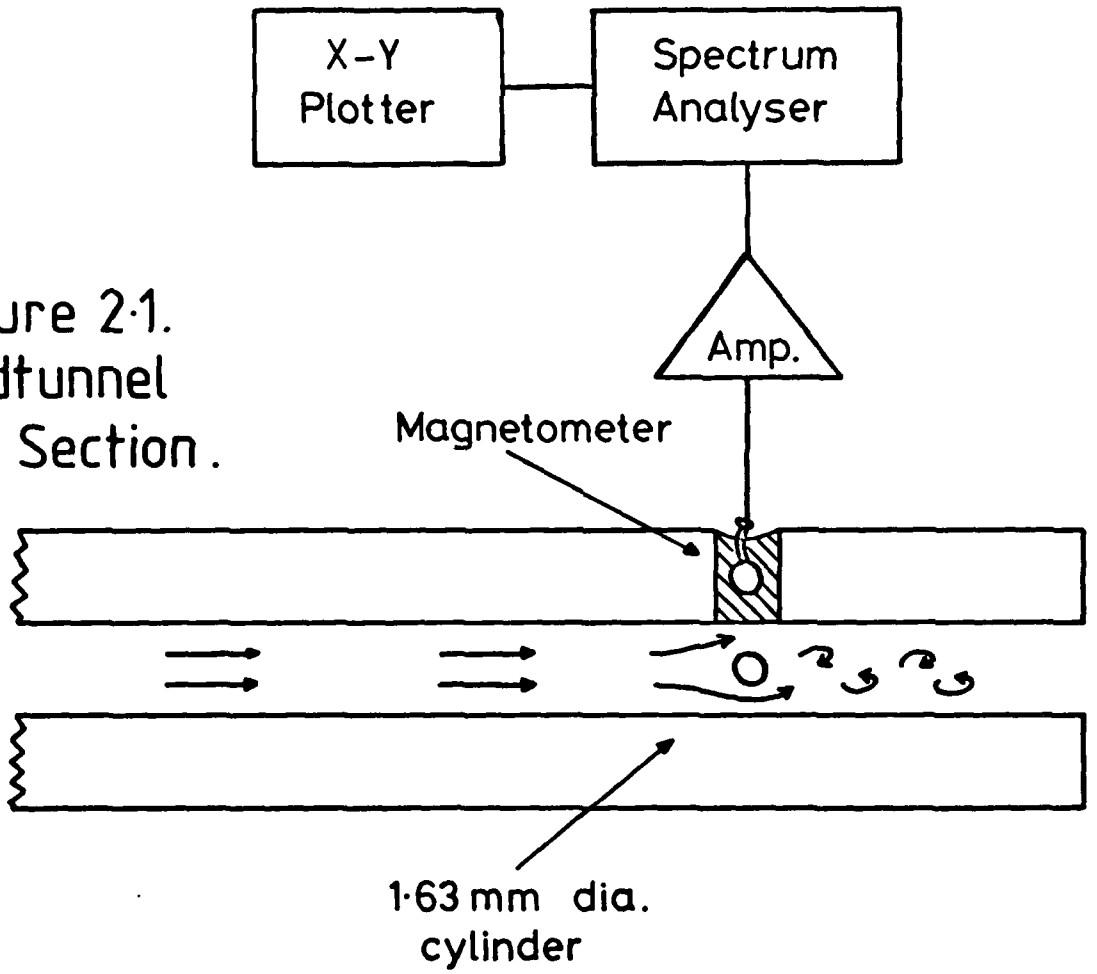

Figure 2·1.
Windtunnel
Test Section.

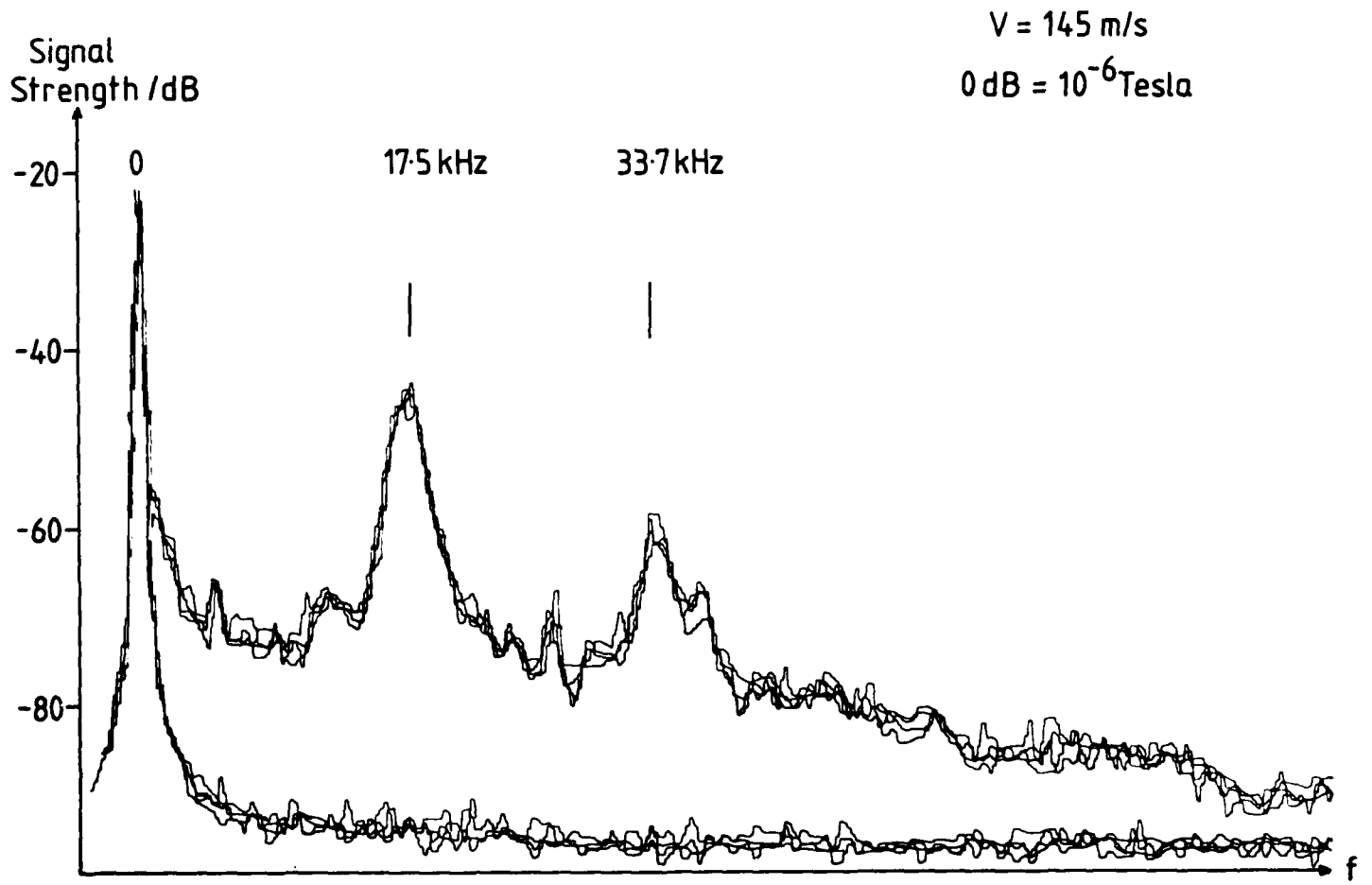

Figure 2·2. Magnetic Spectrum from Air Flow.

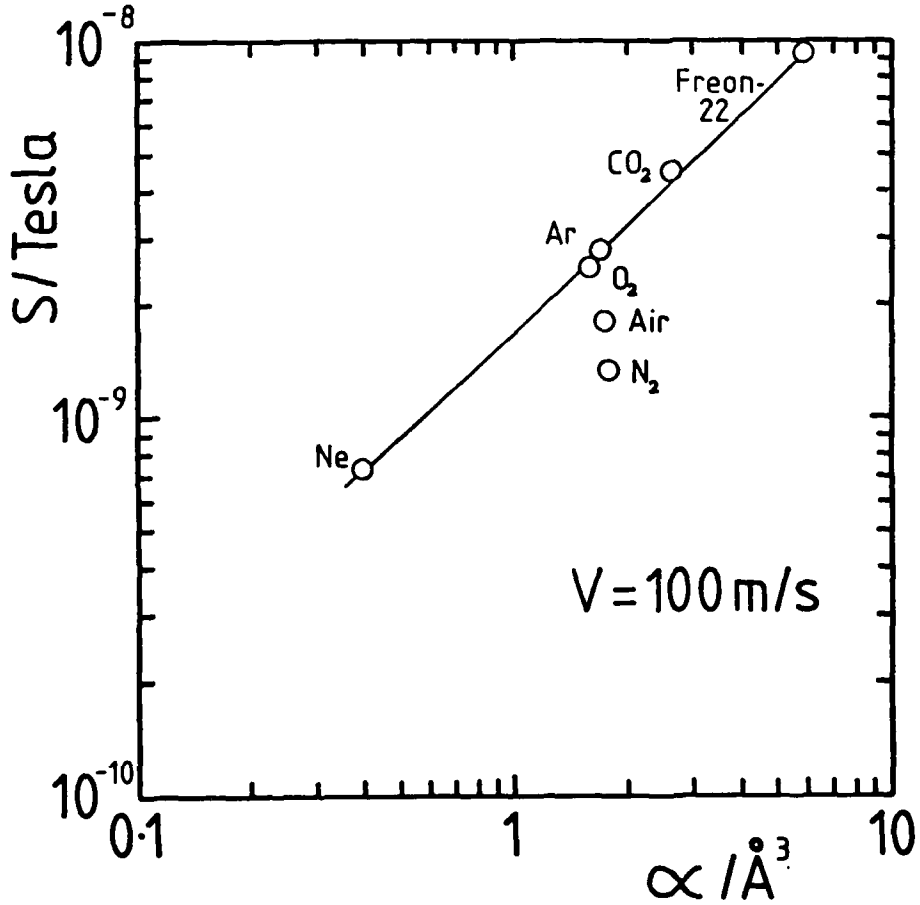

Figure 2·3. Signal Strength vs Polarisability (after Clark 1980a).

Figure 2.4 . Effect of Cylinder Potential.

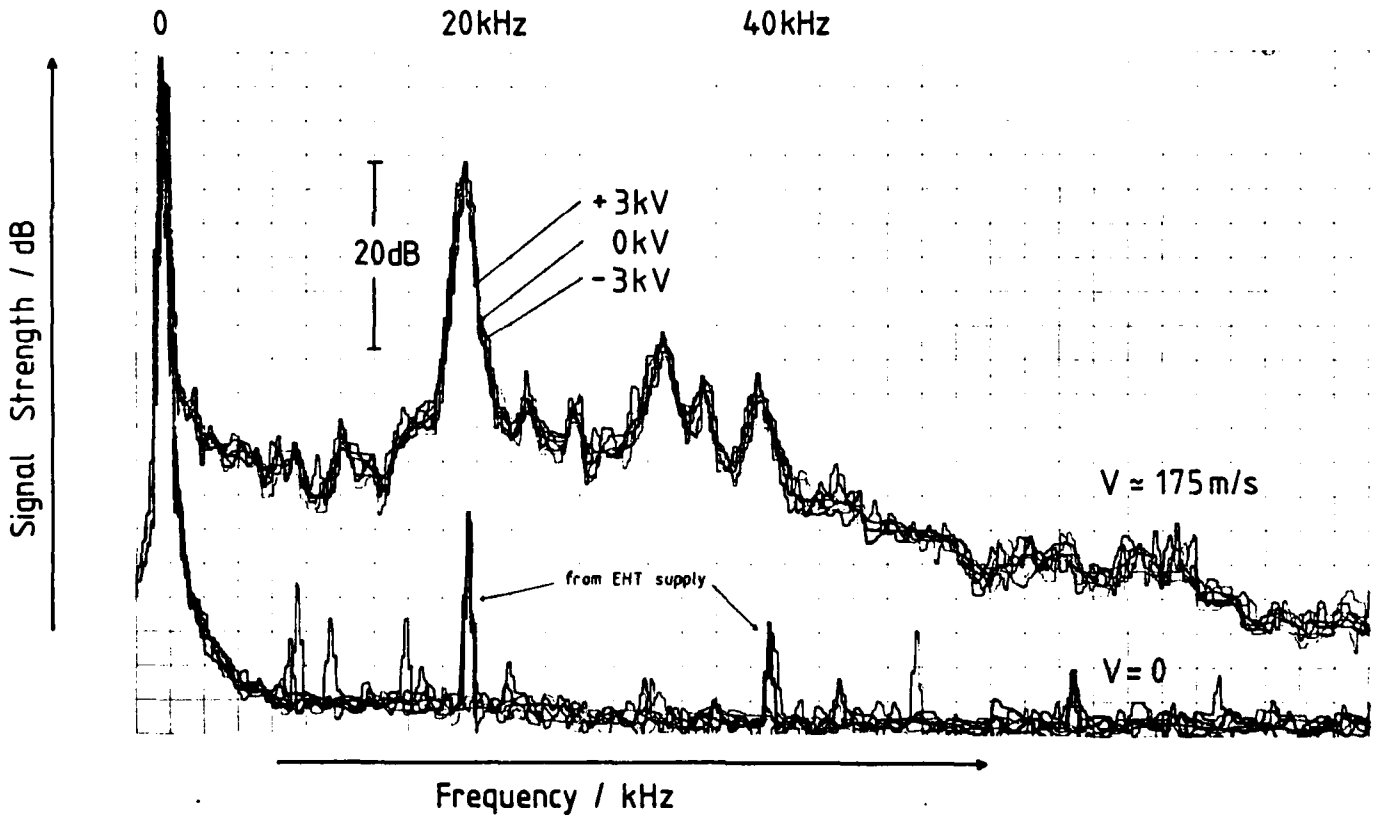

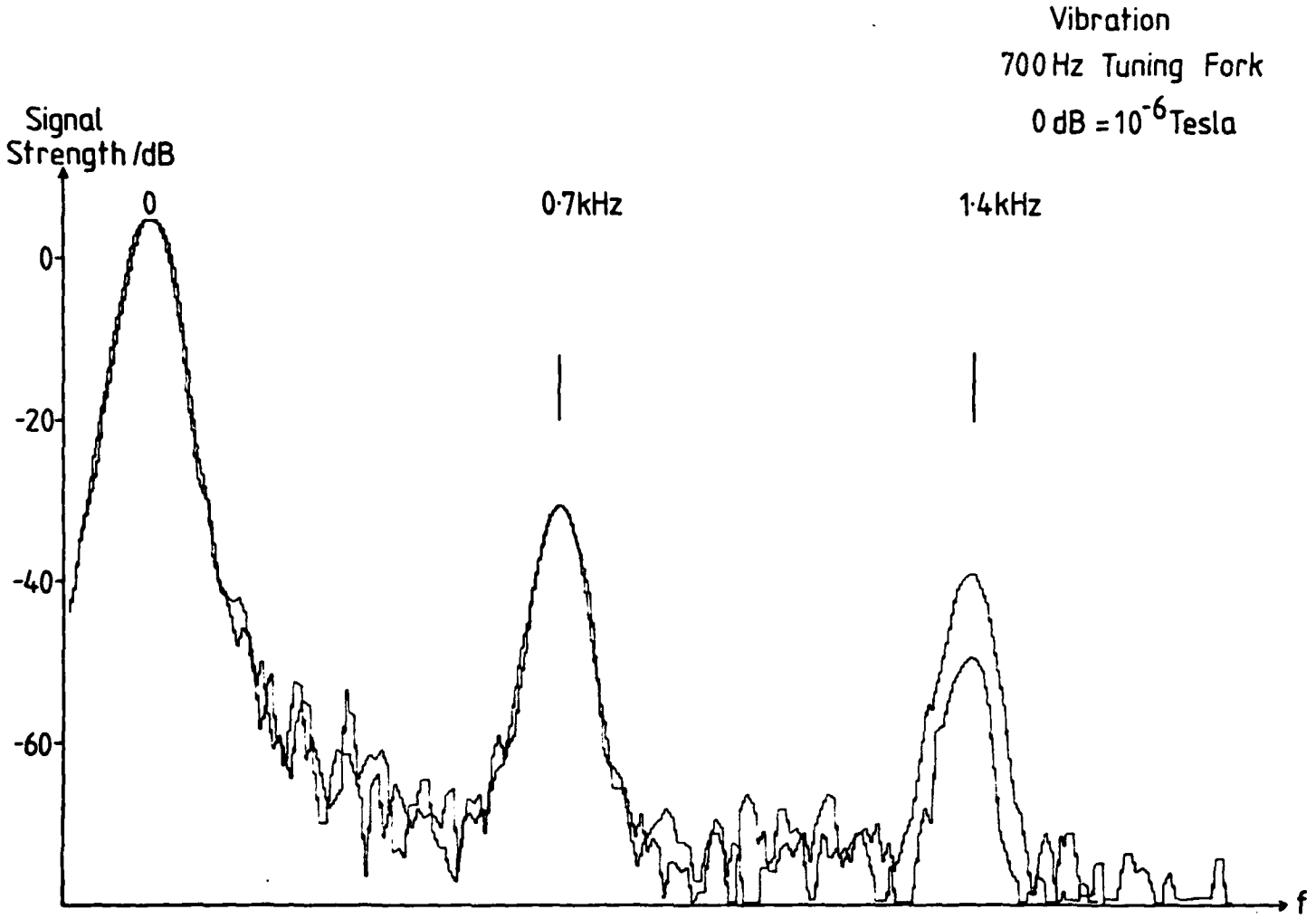

Figure 2·5. Vibration Signal.

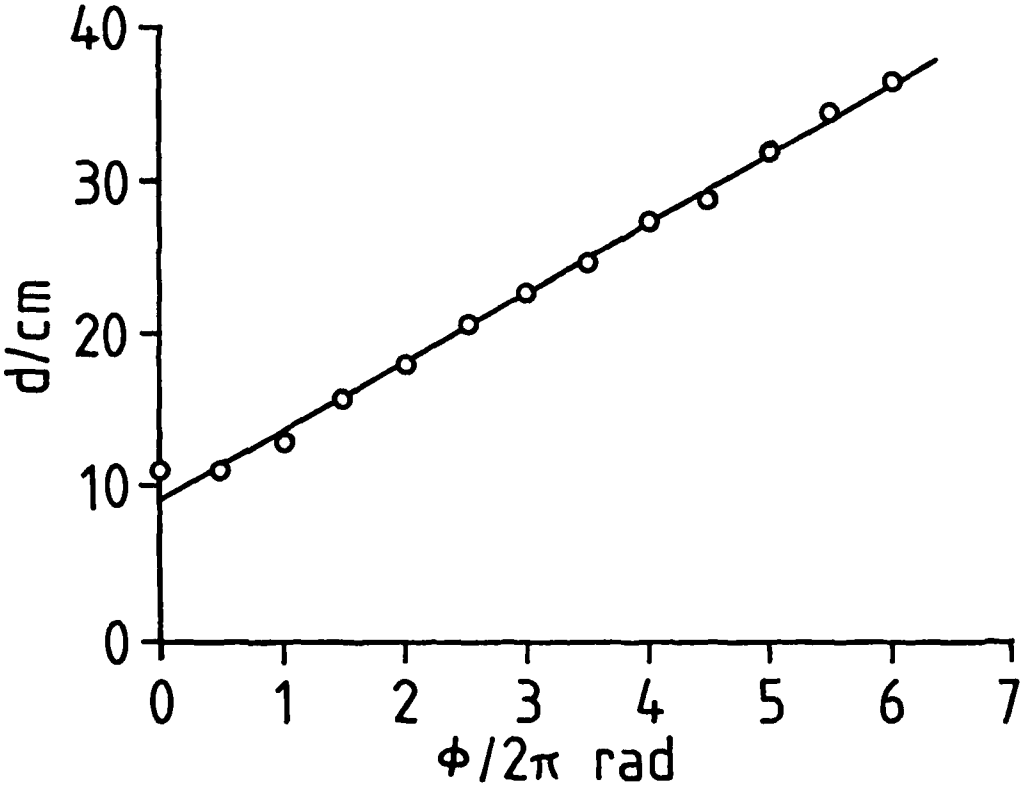

Figure 2·6. Magnetometer Separation vs Phase Difference.

Figure 2·7. Signal Strength vs Gas Impact Pressure (after Clark 1980a).

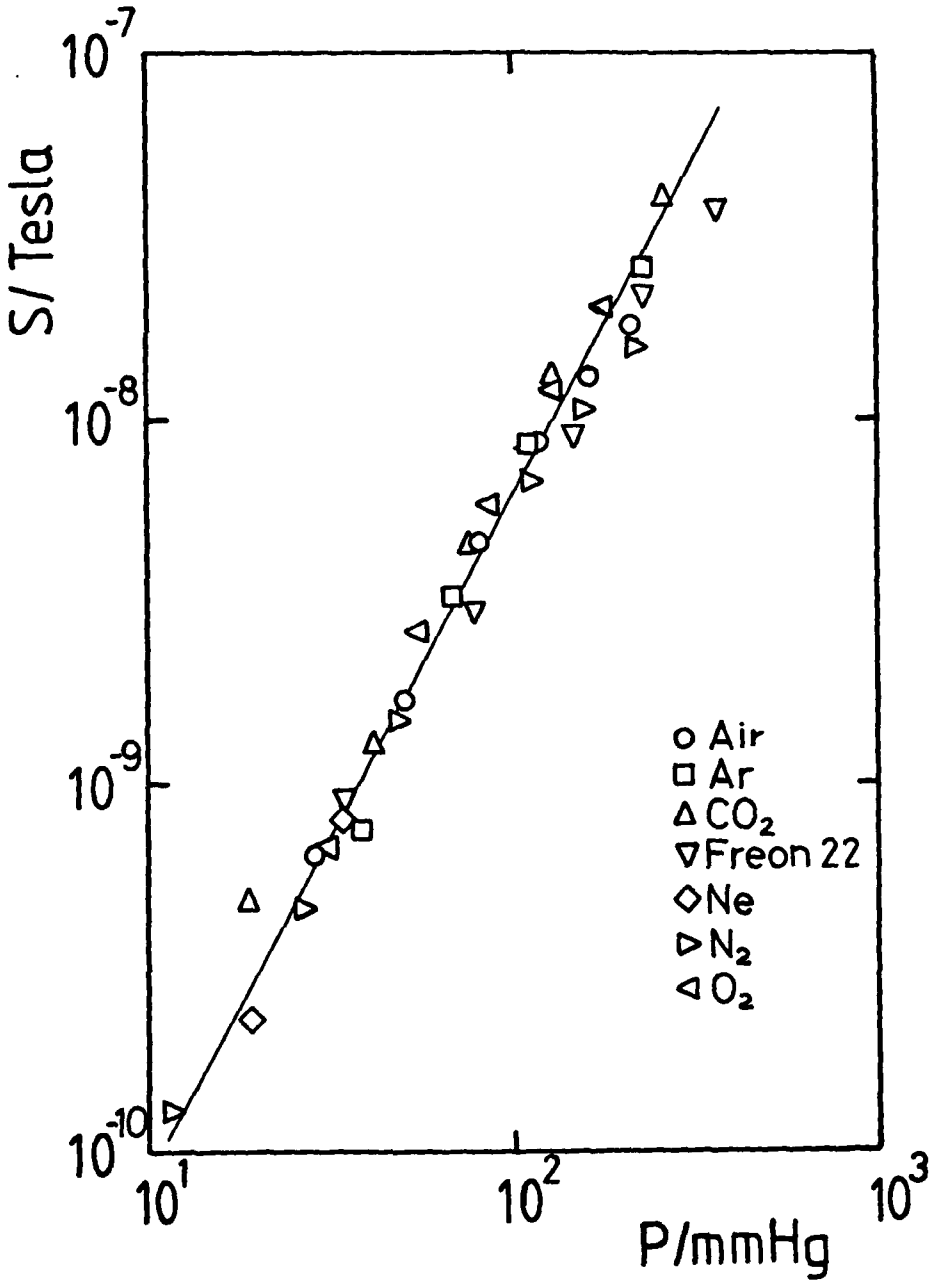

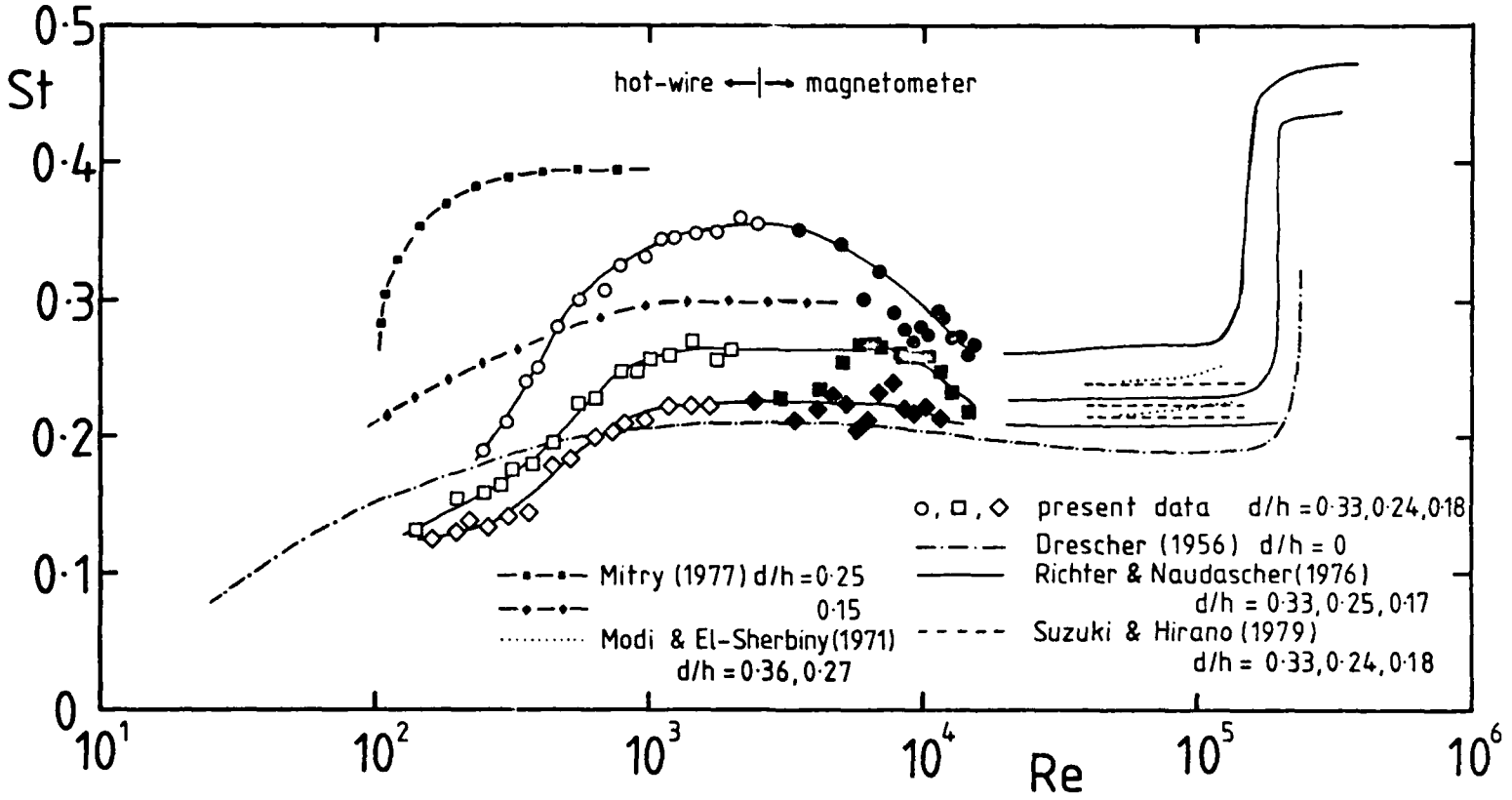

Figure 3·1. Strouhal number vs Reynolds number - Effect of Windtunnel Blockage.

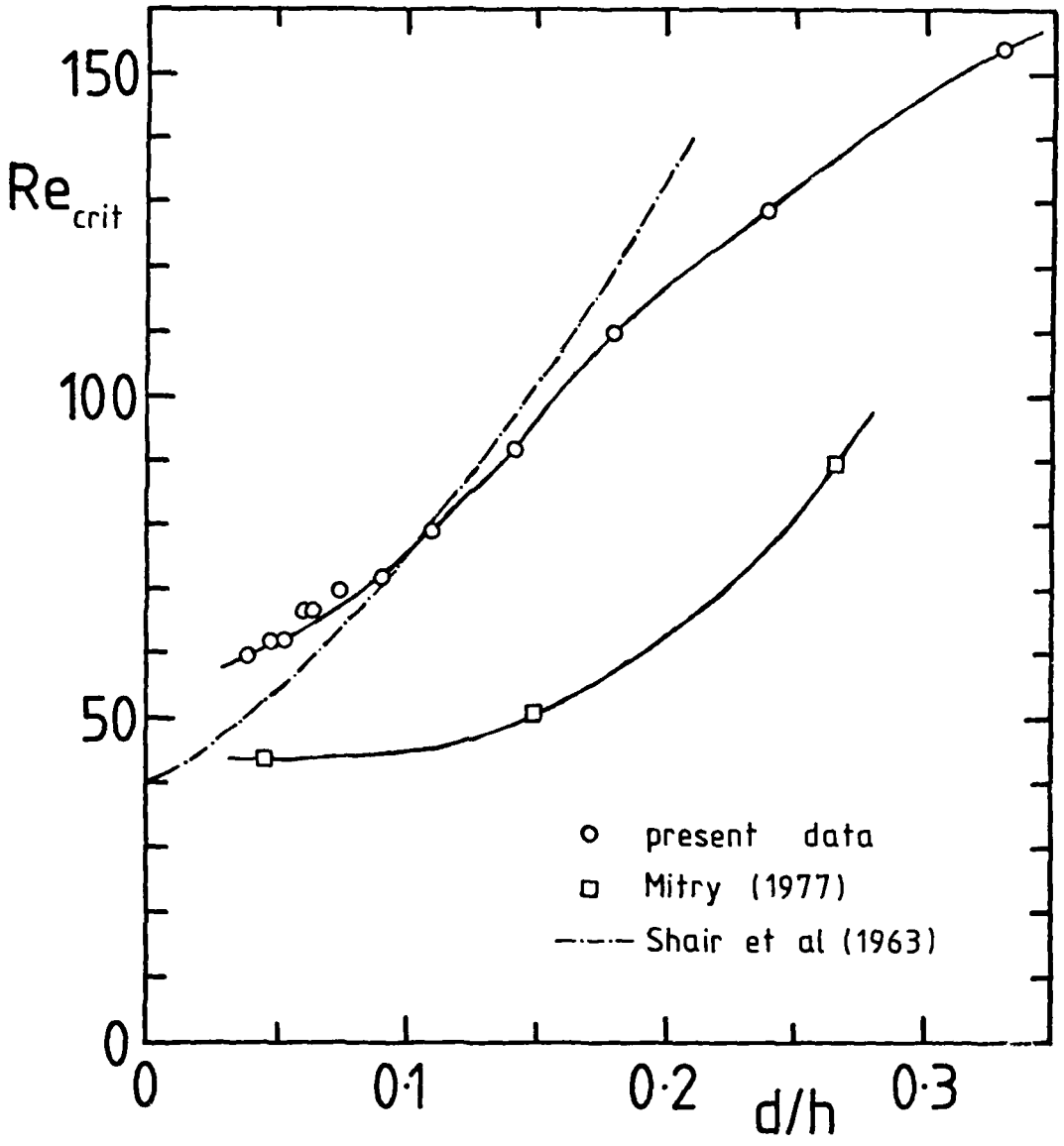

Figure 3·2. Effect of Blockage on Critical Reynolds Number.

VORTEX SHEDDING FREQUENCIES FOR A CYLINDER IN CONFINED FLOW

3.1 Introduction

The shedding frequency of vortices from a circular cylinder, corresponding to the frequency of the fluctuating components of the lift and half that of the drag, is of obvious interest in engineering. As windtunnel tests and engineering problems may involve significant blockage of the flow, the effect of blockage on shedding frequencies is of some importance. While extensive studies have been made of vortex shedding in unconfined flow (see, for example, Schlichting 1979, Kovásznay 1949, Drescher 1956, Roshko 1954) and despite early interest in the effect of blockage (see, for example, Rosenhead & Schwabe 1930) there is still inadequate information on the effect of blockage on the shedding frequency. This chapter describes some measurements of vortex shedding frequencies and critical Reynolds numbers as a function of blockage, and also illustrates possible uses of the magnetometer in obtaining information on fluid flows without the necessity of introducing a probe into the flow.

This work was performed in collaboration with Mr. W.G. Rees.

3.2 Experimental

The standard windtunnel test configuration was used, as described in section 2.3, but with cylinders of 1.63 mm dia. (blockage ratio d/h = 0.33), 1.17 mm dia. (d/h = 0.24) and 0.89 mm dia. (d/h = 0.18).

The cylinders spanned the test section at a point 120 mm downstream of the contraction and 90 mm upstream of the exit of the tunnel. Measurements of vortex shedding frequencies for flow speeds below 30 m s^{-1} were made using a constant temperature hot wire anemometer with a 2.5 μm diameter wire operated at an overheat ratio of 1.50. The probe was adjusted to give optimum signals, generally with the wire between 2 and 5 cylinder diameters down stream of the cylinder and slightly above or below the centreline. Signals were analysed with a CRO or the spectrum analyser. For flow speeds above 50 m s^{-1} data were taken with the magnetometer and analysed with the spectrum analyser.

The maximum cylinder Reynolds number attainable was $\sim 2 \times 10^4$.

Measurements of the Reynolds number at which vortex shedding begins were made for a wider range of blockages (down to d/h = 0.04), although the thinner cylinders were not used at higher speeds due to doubts about their rigidity.

Flow speeds were determined from the stagnation pressure using a precision dial manometer or a 25° tilt paraffin manometer, or, at the lowest speeds, using the hot wire amenometer in the absence of the cylinder, a fixed flow rate having been established.

3.3 Results and Discussion

Plots of the dimensionless shedding frequency (Strouhal number) as a function of cylinder Reynolds number are given in figure 3.1, together with the trends of data from Drescher (1956), Mitry (1977), Modi & El-Sherbiny (1971), Richter & Naudascher (1976) and Suzuki & Hirano (1979).

The Strouhal number is given by

$$St = \frac{fd}{u_\infty} \tag{3.1}$$

where d is the diameter of the cylinder and u_∞, in unconfined uniform flow, is the flow velocity far from the cylinder. The latter concept is not applicable in a confined flow, and the mean channel velocity, u, is used instead. This has been calculated from the continuity equation by

$$u = u_g(1-d/h) \tag{3.2}$$

where u_g is the flow velocity through the gap between the cylinder and the wall, and is calculated from the stagnation pressure. This assumes the static pressure in the wake region is negligible, which will strictly only be true in the limit of high blockage. However, this will not affect the trends of the data.

It can be seen that the magnetometer data (Solid Symbols) are in complete agreement with the hot wire data in the intermediate range of Reynolds numbers. Although there is some scatter in the magnetometer data, the method should be capable of some refinement, for example the response could be increased by imposing an external magnetic field.

The results show a marked peak in the Strouhal number at intermediate Reynolds numbers, with blockage having a relatively small effect in the subcritical range. Okamoto and Takeuchi (1975) reported that the Strouhal number was almost independent of blockage, at St = 0.19, for d/h in the range 0.09 - 0.34 and

$Re = 3.22 \times 10^4$. However, the data shown in figure 3.1 indicate that the effect is still significant.

At low Reynolds numbers the Strouhal number decreases with increasing blockage. This is in agreement with the trend of the critical Reynolds number for vortex shedding. This is shown in figure 3.2, together with data from Mitry (1977) and Shair et al (1963). The critical Reynolds number rises with increasing blockage, presumably as a result of the reduced wake width.

There is as yet very little information on the Strouhal number as a function of blockage for intermediate Reynolds numbers. The data of Mitry (1977) for $Re \sim 10^2$-10^3, shown in figure 3.1, exhibit the same trends as the present work, but with an even more dramatic rise in the Strouhal number, a blockage of 0.25 giving a maximum Strouhal number of $\sim$0.39

It is well known that the Strouhal number is influenced by turbulence intensity and cylinder vibration. The effect of such parameters is not well defined, but there was no evidence of the shedding locking onto the natural frequency of vibration of any of the cylinders.

Of some interest are the effect of boundary layers (including the sidewall boundary layer) and aspect ratio (including the effect of the horseshoe vortices from the ends of the cylinder). In this work and that of Mitry (1977) the boundary layers were thick, although this would be expected to become less significant with increasing blockage.

It is hoped that a study of these effects will be made at a later date.

3.4 Conclusions

Measurements of vortex shedding frequencies for a circular cylinder in a heavily confined flow have been obtained for blockage ratios up to 0.33 and Reynolds numbers up to 2×10^4. As the blockage ratio is increased, systematic deviations are observed from the Strouhal number for unconfined flow. The Strouhal number reaches a maximum in the Reynolds number range 10^3-10^4 for all blockage ratios. The Reynolds number at which vortex shedding just begins increases with blockage, showing that the confining walls increase the stability of the flow.

Measurements made with the magnetometer show that it is possible to determine shedding frequencies using a probe which is not introduced into or in contact with the fluid, illustrating the potential of such devices for vibration studies.

SKIN FRICTION DRAG MEASUREMENTS

4.1 Introduction

In order to identify possible applications of the effect reported by Clark, Kestin and Shah (Clark et al 1977, Kestin and Shah 1968) it was decided to investigate the effect of irradiation on air under conditions characteristic of flight. This necessitated a study of skin friction drag forces with air flows having speeds of up to a few hundred metres per second and static pressures near to atmospheric. The requirement of a high flow speed meant that it would be prohibitively expensive to work with large flow cross-sections and a miniature windtunnel run from a compressed air supply appeared to be the simplest way of meeting the requirements. The scale and speed of the flow place restrictions on the methods which can be used to measure skin friction drag forces, as discussed in the next section, and the final decision was to use a skin friction drag balance to measure the shear stress at the wall of a miniature windtunnel, with and without radioactive irradiation of the air flow.

4.2 Techniques for Measuring Skin Friction

In order to study methods of drag reduction one must, of course, be able to measure the skin friction drag accurately. As discussed in chapter 1, the skin friction shear stress at the wall is given by the Newtonian friction law

$$\tau_o = \mu \frac{\partial u}{\partial y}\bigg|_{y=o}$$

and provided that the mean free path is small compared with the physical dimensions of the system, the expression is valid for laminar and, due to the presence of the sublayer, turbulent gas flows. It follows that we can determine the shear stress by a direct measurement of τ_o, or infer the shear stress from measurements of μ and the velocity profile. If we know the viscosity and the density for example, the shear can be determined from measurements of the velocity profile using a pitotstatic tube or a hot wire anemometer. However, due to the size of the probes it is difficult, particularly if we have to look at a laminar sublayer or a thin boundary layer, to make accurate measurements of u near the wall, and errors in $\left.\frac{\partial u}{\partial y}\right|_{y=o}$ can be considerable.

This problem can be alleviated to some extent by using an integral method, in which the shear at the wall appears as a momentum deficit in the rest of the boundary layer. If we look at the boundary layer equations (1.4) for steady flow and integrate to a point y = h outside the boundary layer then

$$\int_{y=o}^{h} \left(u \frac{\partial u}{\partial x} + v \frac{\partial u}{\partial y} - U \frac{dU}{dx}\right) dy = - \frac{\tau_o}{\rho}$$

where the pressure gradient has been expressed in terms of the potential flow solution,

i.e. $$- \frac{1}{\rho} \frac{dp}{dx} = U \frac{dU}{dx}$$

From the continuity equation

$$v = -\int_o^y \frac{\partial u}{\partial x}\, dy' \qquad \text{and so}$$

$$y = \int_o^h \left\{ u \frac{\partial u}{\partial x} - \frac{\partial u}{\partial y} \int_o^y \frac{\partial u}{\partial x}\, dy' - \frac{UdU}{dx} \right\} dy = -\frac{\tau_o}{\rho}$$

With $\displaystyle\int_o^h \left\{ \frac{\partial u}{\partial y} \int_o^y \frac{\partial u}{\partial x}\, dy' \right\} dy = \left[u \int_o^y \frac{\partial u}{\partial x}\, dy' \right]_o^h - \int_o^h u \frac{\partial u}{\partial x}\, dy$

$$= U \int_o^h \frac{\partial u}{\partial x}\, dy - \int_o^h u \frac{\partial u}{\partial x}\, dy$$

We can see that

$$\int_o^h \left\{ 2u \frac{\partial u}{\partial x} - U \frac{\partial u}{\partial x} - U \frac{dU}{dx} \right\} dy = -\frac{\tau_o}{\rho}$$

and

$$\int_o^\infty \frac{\partial}{\partial x} \left\{ u\,(U - u) \right\} dy + \frac{dU}{dx} \int_o^\infty (U - u)\, dy = \frac{\tau_o}{\rho}$$

where we can let $h \to \infty$ since $U - u = o$ for $y > h$.

Defining the displacement thickness δ_1 and the momentum thickness δ_2 by

$$\delta_1 U = \int_o^\infty (U - u)\, dy \qquad 4.1$$

$$\delta_2 U^2 = \int_0^\infty u(U - u)\, dy \qquad 4.2$$

this becomes

$$\frac{\tau_o}{\rho} = \frac{d}{dx}\,(U^2\delta_2) + \delta_1\, U\,\frac{dU}{dx} \quad \text{(von Kármán's momentum integral)} \qquad 4.3$$

Although measurements at different x positions are now needed to determine τ_o, the method is not as sensitive to errors in velocity close to the wall. It is particularly practical if the pressure gradient is zero, when

$$\frac{\tau_o}{\rho U^2} = \frac{d\delta_2}{dx} \qquad 4.4$$

(see Schlichting 1979 for example)

Other methods rely on the similarity of the turbulent velocity profile. Writing the mean velocity as u and the free stream velocity as U, the equation for the logarithmic velocity profile (1.8) can be written as

$$\frac{u}{U}\cdot\frac{U}{u_\tau} = \frac{1}{K}\left[\ell n\,\left(\frac{yU}{\nu}\cdot\frac{u_\tau}{U}\right) + A\right]$$

Since $u_\tau = \sqrt{\frac{\tau_o}{\rho}}$ and $C_f = \frac{\tau_o}{\frac{1}{2}\rho U^2}$ we can write

$$\frac{u}{U} = \sqrt{\frac{C_f}{2}}\left[\frac{1}{K}\left(\ell n\left(\frac{yU}{\nu}\right) + \ell n\left(\sqrt{\frac{C_f}{2}}\right)\right) + A\right]$$

It follows that a velocity profile with $\frac{u}{U}$ plotted as a function of $\frac{yU}{\nu}$ belongs to a family of curves which has the local coefficient of skin friction as a parameter. Matching an experimental velocity profile to a "Clauser Chart" of such curves (see Clauser 1954) gives a value for the skin friction coefficient.

Another method relies on a measurement of only one velocity close to the wall. From considerations of wall similarity, the reading of a pitot tube with the local undisturbed static pressure subtracted, ΔP, is expected to be given by

$$\frac{\Delta P \; d^2}{\rho \quad \nu^2} = f\left(\frac{u_\tau y}{\nu}\right)$$

where d is the pitot tube diameter and f is some universal function. The method was first used by Preston (1954) for pipe flows. A revised calibration and limitations on the use of the "Preston tube" in pressure gradients were obtained by Patel (1965).

Surface pitot tubes with width much greater than height (Stanton tubes) have been widely used for measuring skin friction. A simple arrangement consists of the edge of a razor blade placed over a static hole.

The Reynolds analogy between heat transfer and momentum transfer has also been widely exploited. If q_o is the heat flux from the wall and k the thermal conductivity then

$$q_o = k \left.\frac{\partial T}{\partial y}\right|_{y=o}$$

The resemblance to the formula for the wall shear stress is apparent, and if the relationship between the velocity and temperature fields is known then the shear stress can be found from measurements of the heat transfer. Early measurements with heated shear gauges by Ludwieg (1950) showed that for a heated film of length ℓ

$$\frac{q_o \ell}{k(T_o - T_\infty)} = 0.807 \left(\frac{\ell^2 \rho \tau_o}{\mu^2} \cdot Pr \right)^{\frac{1}{3}}$$

provided that the thickness of the thermal layer is less than the boundary layer thickness. The Prandtl number, Pr, is constant for a given fluid and is given by

$$Pr = \frac{\mu C_p}{k}$$

where C_p is the specific heat capacity at constant pressure. (More generally, dimensional analysis predicts $Nu = f(Pr, R_\tau)$ where the Nusselt number $Nu = \frac{q_o}{k(T_o - T_\infty)}$, f is some universal function and $R_\tau = \frac{\ell u_\tau}{\nu}$ is a friction Reynolds number).

While the $\tau_o^{\frac{1}{3}}$ dependence may be observed, hot film shear gauges generally require extensive calibrations against known shear stresses. However, they have the advantage that it is relatively easy to measure fluctuating skin friction (see Bellhouse & Schultz 1968 for instance).

The thinning of a surface oil film of viscosity η under the influence of the surface shear stress was studied by Tanner (1977) using an interferometer. The thickness of the film, h,

as a function of time varies like

$$h = \frac{\eta x}{\tau_o t}$$

and so τ_o can be calculated from values of h measured with the interferometer. Obviously the method has limited applications, but could be useful in some circumstances.

One rather esoteric method of skin friction measurement utilises a film of liquid crystal material on the surface, the wavelength of maximum light scattering from the liquid crystal being shear dependent (Klein & Margozzi 1970). However, the accuracy is rather poor at present, partly because the wavelength of the scattered light fluctuates rapidly. Relatively thick liquid films are also needed, and these could perturb the flow. It seems unlikely that the method will be of widespread use.

This brings us to a consideration of direct methods of measurement. In principle the simplest method, the shear force acting on a moveable surface is measured directly by some kind of force balance system. The method is particularly attractive since it does not rely on any assumptions about the nature of the flow or of the velocity profile. Possibly the first systematic measurements of this nature were made by Froude (1872) who measured the drag on a series of planks towed along a water tank at various speeds. The apparatus used is illustrated in Figure 4.1. Usually the moveable surface or drag element forms part of a larger plate or test object, or of the wall of a

windtunnel. Difficulties arise, however, due to the relatively small magnitude of the shear forces, as compared with the inertial forces. It follows, for example, that the alignment of the drag element with the surface is critical. The gap around the moveable element is also important since it can perturb the flow and, in a pressure gradient, give rise to a pressure force on the drag element.

With regard to the way in which the force is balanced, it is possible either to measure the deflection of the drag plate against some resilient system (spring flexures or torsion wires for example *) or to maintain the plate at a null position by the application of a measured force (for example magnet and coil). The null position method has the advantage that the gap geometry is unaltered and that slow changes in the elastic properties of supporting or resilient members are not as important. With both deflection and null position systems it is necessary to resolve small deflections of the drag element, and a popular choice of transducer is the linear variable differential transformer (LVDT) which is capable of extremely high precision. This consists of a primary coil driven by an AC current, two secondaries connected in opposition and a moveable ferrous core whose position determines the output from the secondaries.

The suspension system for the plate can either be a parallel linkage system or a pivoted system (Kistler balance).

---

* or, indeed, the weight of the drag element in the case of a free hanging suspension. This method has been used very successfully to measure the drag coefficient of a mediaeval arrow. (Rees & Wilby 1982).

Other factors which must be considered are the effects of temperature, external vibration and flow fluctuations on the calibration and response of the balance.

We can now go on to consider the most appropriate method for the present work. With small scale, high speed flows, and with relatively small changes in drag expected, the velocity profile or momentum integral methods would not be practical since they are not sensitive to viscosity changes or are inaccurate in thin boundary layers. Hot film or similar shear gauges would in any case have to be calibrated against known shears and could conceivably be affected by irradiation.

The idea of a direct measurement seemed to be the most attractive, since, apart from the advantage previously mentioned, the various significant errors to be expected should be systematic and reproducible, and if no more than say, 10% in total, would only result in a slight change in the sensitivity with which small drag changes could be measured.

For these reasons the decision was made to use a skin friction drag balance in these experiments on the effect of boundary layer irradiation, with the drag element forming part of the windtunnel wall. The windtunnel and drag balance are described in the following sections. Since the form of the various error sources depends somewhat on the precise configuration of the balance, a more detailed discussion will be deferred to section 4.11, where an account of an experimental study of the error sources in the balance used will also be given.

Other discussions of the methods which can be used to measure skin friction, with particular emphasis on direct measurements, can be found in Dhawan (1953) and Brown and Joubert (1969). An excellent review of the techniques available for the measurement of skin friction has been given by Winter (1977).

4.3 Windtunnel Design

To meet the aforementioned requirements, a miniature blow-down windtunnel was designed by Clark. High pressure air from a compressed air cylinder, containing the equivalent of 6.38 m^3 at s.t.p. compressed to 2000 p.s.i. (1.4 MPa) is fed via pressure regulators into a "turbulence suppressor tank" containing a "honeycomb" assembly of over 1400 thin walled glass tubes (of 7 mm o.d. and 0.46 m lenth) with 100 mesh stainless steel cloth screens at either end. A fairing inside the tank then guides the air into a rectangular stagnation section measuring 51 mm x 126 mm. Different test sections, typically with cross sectional areas (determined by the volume flow available) of a few cm^2, can be connected to the stagnation section by two stage transition sections which reduce the height and then the width of the flow. The wall shape of each stage is formed by two circular arcs of opposite curvature, and the length of the transition section is typically 0.3 m. The test sections and transition sections were constructed from "perspex" (PMMA).

In later experiments (from section 4.8 inclusive) the air supply was obtained from an Ingersoll-Rand 100 p.s.i. compressor,

capable of delivering flow rates of up to 68 cu. ft./min. (2.5 m^3/min).

For experiments with flow over the exposed surface of a radioactive source, a flexible stainless steel duct of diameter 0.15 m could be attached to the end of the windtunnel. This exhausted to the outside of the building and would prevent any hazard arising in the (unlikely) event of leakage from the radioactive sources. It should be noted that if the duct was used for radioactive measurements it had also to be used for the null measurements, since its presence alters the flow parameters sufficiently for there to be a small apparent change in the drag. The windtunnel system and prototype drag balance are shown in figure 4.2.

4.4 Skin Friction Drag in Channel Flow

Let us now consider the form of the flow, and the magnitude of the skin friction shear stress to be expected with such a windtunnel system.

In general, for flow through a pipe or channel, we would expect that initially, near the entrance, there will be a "top - hat" velocity profile, and that as the fluid moves downstream, the fluid near the wall will be slowed by the action of viscosity. From the equation of continuity, there must also be a corresponding increase in the centreline velocity. It is reasonable to assume that in this region the velocity profile near the wall will develop in a similar way to that on a flat plate in a uniform flow, and that further downstream the boundary layers will grow

until their thickness is comparable with the channel half thickness. Ultimately, the velocity profile characteristic of the fully developed channel flow will be attained, for example, with laminar flow, the well known parabolic profile of Poiseuille flow.

The length of channel taken for the flow to develop fully depends, not surprisingly, on the Reynolds number and on the channel height, h. As a rule of thumb for intermediate Reynolds numbers ($Rc \sim 10^3$ say) it seems to take ~ 100 h for the flow to be within $\sim 5\%$ of the ultimate profile. It follows that to be sure of having fully developed flow we might need to have a test section with an entry length of a few metres. Conversly, for the flat plate approximation to be realistic, the boundary layer thickness should be less than a few mm for a channel height of ~ 5 mm. If we consider a low flow speed, say ~ 10 m s^{-1}, then the boundary layer thickness is ~ 2 mm at a downstream distance of only 10 cm.

Bearing in mind the possible effect of the entry length on the initial velocity profile, it is apparent that neither of these two viewpoints will be exactly correct, over the range of flow velocities likely to be encountered with a reasonably sized test section (although in the case of an initially turbulent flow, the final turbulent profile might be attained rather more quickly). This is not of course, of any great consequence in the context of the present investigation, since the velocity profiles and behaviour of the fluid are similar in both cases (an assumption underlying the connection we shall shortly establish

between the turbulent skin friction in a pipe and on a plate) but it makes it difficult to predict with a high accuracy the skin friction drag forces to be expected.

There is, naturally, information available on developing pipe flows, and, to a lesser extent, channel flows (see Schlichting 1979, Smith 1960, Mohanty & Asthaa 1978 for example) but the results usually assume a "top-hat" profile initially. Since the skin friction coefficient varies strongly with downstream distance in the inlet region, it follows that such analyses will be unhelpful if, as seems likely, the velocity profile at the end of the transition section deviates significantly from the "top-hat" profile. However, since we expect the developing flow to generate larger shear stresses at the wall, it seems logical that the flat plate approximation will give us an upper bound on the skin friction, while the lower bound will be provided by the results for channel flows. Provided that the difference is not too great, we should then have sufficient information to set out design criteria for the drag balance and to assess its performance.

To derive the formulae we need, let us start with the simplest case, that of fully developed laminar channel flow (Poiseuille flow). Considering a small element of the fluid of unit width, length dx and height dy, the pressure and viscous forces will be in equilibrium (i.e. the flow velocity at that height will remain constant) if

$$\frac{dp}{dx}\ dx\ dy = \mu \frac{\partial u^2}{\partial y^2}\ dy\ dx.$$

Since the pressure gradient will be constant in fully developed flow,

$$\frac{\partial^2 u}{\partial y^2} = \text{const}$$

and the velocity profile must be parabolic.

Writing u_∞ rather than u_o for the centre line velocity (to facilitate comparison with flat plate results and to avoid any confusion with the subscript o for wall conditions) and using symmetry and the no slip condition, we get

$$u(y) = u_\infty \left(1 - \left(\frac{y}{h/2} - 1\right)^2\right)$$

and hence

$$C_f = \frac{\tau_o}{\frac{1}{2}\rho u_\infty^2} = \frac{8}{R_c} \qquad 4.5$$

$$\text{where } R_c = \frac{\rho u_\infty h}{\mu} \qquad 4.6$$

If we use - to denote parameters scaled on the average flow velocity, then

$$\bar{C}_f = \frac{12}{R_c} \qquad 4.7$$

$$\text{since } \frac{\bar{u}}{u_\infty} = \frac{2}{3} \qquad 4.8$$

This result is in excellent agreement with experiment (Patel and Head 1969 for example).

For a flat plate we can use the Blasius equation for the local skin friction (equation 1.6). Since the drag will, in fact, be measured over a finite length of wall, ℓ say, we must integrate the shear stress to get

$$C_f = \frac{1.328}{\sqrt{R_\ell}} = \frac{0.344}{\sqrt{R_c}} \qquad 4.9$$

We can allow for the development of the boundary layer upstream of the drag measuring station by using the formula

$$C_f = \frac{0.344}{\sqrt{R_c}} \left(\sqrt{1 + \frac{X}{\ell}} - \sqrt{\frac{X}{\ell}} \right) \qquad 4.10$$

where X is the distance from the front of the drag element to the virtual origin of the boundary layer, although X would have to be determined experimentally.

With turbulent flows the problem is rather more complicated, but adequate formulae for channel and plate skin friction coefficients can be derived from experimental measurements in turbulent pipe flows (see Schlichting 1979 and references therein for a more detailed analysis).

Blasius established the following empirical equation for the skin friction in circular pipes, valid for $Re \lesssim 10^5$:

$$\lambda = 0.3164 \left(\frac{\bar{u}d}{\nu}\right)^{-\frac{1}{4}} \qquad 4.11$$

where d is the pipe diameter and λ a dimensionless friction

factor defined by

$$-\frac{dp}{dx} = \frac{\lambda}{d} \tfrac{1}{2} \bar{u}^2 \qquad 4.12$$

Since $\tau_o = -\frac{dp}{dx} \frac{d}{4}$ for a circular pipe we get

$$\tau_o = 0.03955\ \rho(\bar{u})^{7/4} \nu^{1/4} d^{-1/4} \qquad 4.13$$

Introducing the friction velocity we can see that

$$\rho u_\tau^2 \propto \rho(\bar{u})^{7/4} \nu^{1/4} d^{-1/4} \propto \rho u_\infty^{7/4} \nu^{1/4} r^{-1/4}$$

and hence

$$\left(\frac{u_\infty}{u_\tau}\right)^{7/4} \propto \left(\frac{u_\tau r}{\nu}\right)^{1/4}$$

so

$$\frac{u_\infty}{u_\tau} \propto \left(\frac{u_\tau r}{\nu}\right)^{1/7} \qquad 4.14$$

This suggests that the velocity profile varies like

$$\frac{u}{u_\tau} \propto \left(\frac{u_\tau y}{\nu}\right)^{1/7} \qquad 4.15$$

This is in agreement with the experiments of Nikuradse, who showed that the velocity profile could be described by

$$\frac{u}{u_\infty} = \left(\frac{y}{r}\right)^{1/n} \qquad 4.16$$

where the exponent varies slightly with Reynolds number, n being 7.0 at Re $\sim 10^5$. (Some doubt has, however, been cast on the relation between the Blasius friction law and the 1/7 power law by Patel and Head (1969), who observed deviations from the 1/7 power law at lower Reynolds numbers, $\sim 10^4$, although the friction law was obeyed).

With the hypothesis of similarity in the velocity profiles we can attempt to derive expressions for the shear stress in channel and plate flows. For a channel flow we can take the shear stress over directly if we first express equation 4.13 in terms of the centre line flow velocity:

$$\tau_o = 0.03955 \left(\frac{\bar{u}}{u_\infty}\right)^{7/4} \rho u_\infty^{7/4} \nu^{1/4} d^{-1/4} \qquad 4.17$$

$$= 0.0278\, \rho u_\infty^{7/4} \nu^{1/4} d^{-1/4} \qquad 4.18$$

with $\frac{\bar{u}}{u_\infty} = 0.817$ for a 1/7 power law pipe velocity profile.

It follows that

$$C_f = 0.056\, R_c^{-1/4} \qquad 4.19$$

for a channel flow.

This power law dependence has been observed in channels with low aspect ratios. In general, good agreement between friction laws for pipes with different cross sections can be attained by scaling the friction factor on the "hydraulic diameter" d_h. This is given by

$d_h = \frac{4A}{c}$ where A is the cross section area and c the circumference. For a circular pipe, of course, this reduces to the diameter of the pipe.

In channels of large aspect ratio these laws appear to break down and the power law dependence of the skin friction is rather different. Patel and Head (1969) found $\bar{C}_f = 0.0376\ \bar{R}_c^{-1/6}$ experimentally with a channel having an aspect ratio of 48. The high Reynolds number velocity distribution was close to the 1/7 power law profile, so $\frac{u}{u_\infty} = \frac{7}{8}$ and we can write

$$C_f = 0.0294\ R_c^{-1/6} \qquad 4.20$$

scaling on the centre line velocity.

For a flat plate we can adapt equation 4.18, replacing d by 2δ to get

$$\tau_o = 0.0234\ \rho u_\infty^2 \left(\frac{\nu}{u_\infty \delta}\right)^{\frac{1}{4}} \qquad 4.21$$

To remove δ from this equation we can use the momentum integral (4.3), assuming zero pressure gradient,

$$\frac{\tau_o}{\rho} = u_\infty^2 \frac{d\delta_2}{dx} \qquad 4.22$$

Since $\frac{u}{u_\infty} \approx \left(\frac{y}{\delta}\right)^{1/7}$ we can write

$$\delta_2 = \frac{1}{u_\infty^2} \int_0^\delta u(u_\infty - u)dy = \frac{7}{72}\ \delta \qquad 4.23$$

Combining equations 4.21-23 we can see that

$$\frac{d\delta}{dx} = \frac{72}{7 \times 0.0234} \left(\frac{\nu}{u_\infty \delta}\right)^{\frac{1}{4}}$$

and integration gives

$$\delta = 0.383 \left(\frac{\nu}{u_\infty x}\right)^{1/5} x$$

Substituting in 4.21 gives

$$\tau_o = \frac{0.0234}{(0.383)^{\frac{1}{4}}} \rho u_\infty^2 \left(\frac{u_\infty x}{\nu}\right)^{-1/5}$$

and the drag coefficient for a plate of length ℓ is then

$$C_f = 0.074 R_\ell^{-1/5} = 0.043 R_c^{-1/5} \qquad 4.24$$

in agreement with experiments where the flow is turbulent from the leading edge of the plate, and provided that the range of validity of the Blasius skin friction law is not exceeded. (For high Reynolds numbers, friction laws based on the logarithmic velocity profile can be obtained. In common use is the semi-empirical Schultz-Grunow formula,

$$C_f = 0.37 [\log(R_x)]^{-2.584}$$

However, this does not differ significantly from equation 4.24 in the Reynolds number range of interest).

If an allowance is made for the entry length then equation 4.24 becomes

$$C_f = 0.043 R_c^{-1/5} \left[\left(1 + \frac{X}{\ell}\right)^{4/5} - \left(\frac{X}{\ell}\right)^{4/5}\right] \qquad 4.25$$

We now have the required expressions for the skin friction in laminar or turbulent channel and flat plate flows, and it is appropriate to look briefly at the question of when transition

from laminar to turbulent flow is expected. Linear stability theory, in fact, predicts that the parabolic profile is stable with respect to infinitesimally small disturbances up to arbitrarly high Reynolds numbers. In practice, transition is observed at Reynolds numbers down to $\sim 10^3$. The inlet region will obviously play a part, since the developing inlet boundary layers can be unstable, causing transition in the inlet region or possibly further downstream as a result of a finite perturbation of the parabolic profile. Experimentally, transition is observed at $R_c \sim 2000$ when the fluid in the inlet region is disturbed. Patel and Head (1969) found that $\bar{R}_c = 1350$ corresponded to the first appearance of intermittency in the flow, which became continually turbulent at $\bar{R}_c \sim 1800$. The 1/6 power law for the skin friction was not, however, established until $\bar{R}_c \sim 2800$. Scaling on the centre line velocity again this corresponds to the onset of transition at $R_c \simeq 2000$ with transition being "complete" by $R_c \simeq 4200$.

With a low level of initial disturbance it is, of course, possible to maintain laminar flow to rather higher Reynolds numbers, up to a maximum of about 10^5.

To conclude this section, we can calculate approximate values for the skin friction drag to be expected in tests using the windtunnel. If we take $u_\infty \sim 100\ ms^{-1}$, $h \sim 5$ mm and $\ell \sim 100$ mm as likely values, then for a drag element with a surface area of 10 cm , equation 4.5 and 4.9 would predict laminar drag forces of $\sim 0.1 - 1$ gf and equations 4.19 and 4.24 would predict turbulent drag forces of ~ 2 gf. At 200 m s^{-1} (M = 0.6) we would

expect turbulent drags of several gf. Although small, these forces are quite resolvable, and this illustrates the feasibility of making direct measurements of the skin friction drag under the conditions envisaged.

4.5 Prototype Skin Friction Drag Balance

This section describes the construction of a prototype skin friction drag balance. The essential elements of the balance were designed by Clark.

The windtunnel test section had dimensions of 25 mm x 5 mm, and the drag element was a steel plate of dimensions 73.0 mm x 19.1 mm x 6.9 mm thick. This was of a comparable size with various commerical extended radiation sources which were being considered for use in the experiments, and should give drag forces of an appropriate size.

The drag plate was fixed to a supporting steel plate which had been drilled out (for lightness) and which was suspended from a framework of Invar steel by flat steel springs. The Invar base of the balance was fixed to the top of the "perspex" (PMMA) windtunnel test section and surrounded the support plate. The clearance between the windtunnel wall and the drag element was $\sim$ 0.5 mm at the ends and $\sim$ 0.25 mm at the sides. The motion of the plate was damped by an aluminium vane attached to the drag plate support and with two sections immersed in small oil dashpots.

The drag plate was aligned with the windtunnel wall by adjusting three screws on the support frame, when the balance

and upper perspex section had been removed from the windtunnel test section. The alignment could then be checked with dial gauges. The balance was covered by a "perspex" housing, sealed onto the base by a rubber gasket to ensure airtightness.

The balance was designed to operate in a null position mode, the streamwise position of the drag element being determined using a Schaevitz LVDT with a range of 0.010" (0.25 mm) and a Schaevitz CAS-025 signal conditioner, connected to a voltmeter. The output was approximately calibrated at 15 mV/μm by using feeler gauges. The forces on the plate were balanced by an 800 turn coil of 38SWG polyurethane coated copper wire, with a resistance of 23Ω, acting on a ¼" (6.35 mm) diameter Alnico-6 permanent magnet attached to the drag plate. The current through the coil was adjusted to keep the LVDT voltage as near to zero as possible (typically within 100 mV). The coil current was limited to ∿ 200 mA which gave a coil surface temperature of ∿ 60°C. Drag forces of up to ∿ 10 gf could be balanced. Both the coil and housing temperature were monitored by thermocouples using a Comark series 5000 ten channel digital thermometer with a precision of 0.1°C.

The average flow velocity at the balance was calculated from the static pressure at the stagnation section, either using the usual expression for an isentropic contraction.

$$\left(\frac{P+P_{at}}{P_{at}}\right) = \left(1 + \frac{\gamma-1}{2} M^2\right)^{\frac{\gamma}{\gamma-1}} \qquad 4.26$$

(M, the Mach number, is $\bar{u}/a$ where a is the speed of sound, and γ is the usual ratio of specific heats $\gamma = Cp/Cv$) or, adequate in most cases,

$$P - P_{at} = \tfrac{1}{2}\rho\bar{u}^2$$

The stagnation pressure was read on a Pennwalt, Wallace & Tiernan precision dial manometer, typically to an accuracy of $\sim$ 0.2%.

A schematic diagram and photograph of the balance are given in figures 4.3 & 4.4.

4.6 Calibration and Tests of Prototype Balance

Clark considered that a strain gauge calibration method would be superior to more obvious alternatives using the direct action of known weights, due to the absence of any sliding or rolling friction. Four strain gauges (M-line MA-06-125AC-350 steel compensated 350Ω gauges, obtained from Welwyn Strain Measurement) were cemented to a 0.004" (0.1 mm) flat, constant strength cantilever spring. These were connected to give a resistance bridge with four active arms and the strain read using a Philips PR9307 Carrier Wave Measuring Bridge. The spring itself was calibrated by being clamped horizontally and different known weights (analytical balance weights) hung from it. Calibration of the balance was then achieved by moving the spring (attached to the drag plate by a nylon thread) along a microscope type slide.

Sample calibrations are given below; and examples of

calibration curves shown in figures 4.5-4.7. (Note that the effective tare weight, of the pan for the weights plus the effective weight of the spring when horizontal, had to be corrected for, as the calibrations were non linear; this tare weight was estimated by a best fit power curve routine.)

If R denotes the strain gauge bridge reading and L the load, then the calibration curves can be fitted by a power curve of the form

$$R/mV = a_s (L/gf)^{b_s}$$

Typical results (from seven individual calibrations) were

$a_s = 0.533 \pm 0.002$

$b_s = 0.966 \pm 0.003$

The balance calibration took the form

$$R/mV = a_c (I/mA)^{b_c}$$

where I is the coil current. Typical results for ten measurements were

$a_c = 0.044 \pm 0.002$

$b_c = 0.93 \pm 0.02$

The final calibration of load as a function of coil current was of the form

$$L/gf = \alpha(I/mA)^{\beta}$$

where

$$\alpha = \left(\frac{a_c}{a_s}\right)^{1/b_s}$$

$$\beta = b_c/b_s$$

Error calculations are complicated by the dependence of the second calibration on the first and by a correlation between a_c and b_c ($a_c \approx 0.31 - 0.28\ b_c$)
but results with estimated errors are

$\alpha = 0.076 \pm 0.009$

$\beta = 0.96 \pm 0.02$

Although the calibrations were adequate, the non-linearity of the calibration, the laborious double calibration procedure and the observed calibration drift, considerably outweighed the potential advantages and this method was not subsequently used.

Sets of drag measurements were then taken over the range of (plate) Reynolds numbers of 10^5-10^6. The drag coefficient vs Reynolds number curve is shown in figure 4.8. More extensive measurements around Re = 10^6 are shown in figure 4.9. It can be seen that the accuracy of the measurements is quite good. The curve was initially misinterpreted, because Clark had supposed that laminar flow in this type of test section would be maintained up to 0.8 Mach number, $R_c \sim 10^5$ (Clark 1980a), and because the slope of the high Reynolds number curve was almost exactly $-\frac{1}{2}$. This was in good agreement with the Blasius formula (4.9), although the low Reynolds number behaviour was then difficult to account for. Of course, the drag curve was actually reflecting a laminar-turbulent transiton at $R_\ell \sim 3 \times 10^5$.

Tests of the reproducibility of measurements on changing drag plates suggested that it was not possible to align the drag plate to better than $\sim 50\ \mu m$ partly due to problems using

the dial gauges and also because of distortions when re-mounting the balance. This was totally inadequate for comparisons between different plates at the resolution required, and also hinted at future problems when mounting radioactive foils in drag elements.

Other problems with the prototype balance were the difficulty of measuring the drag and holding a constant flow velocity at the same time; the drag element tended to stick magnetically to the Invar base; it was difficult to adjust the plate to hang squarely in the gap in the windtunnel wall and without friction between the coil and magnet or the LVDT and core; there were concerns about possible lifting and twisting of the drag plate due to the fluctuating static pressure and, of course, there were the anomalously steep turbulent drag curves. In the light of later work, this latter problem was probably due to pressure gradient effects, which were not considered in detail at that stage.

To sum up, the prototype balance showed that it was possible to measure the skin friction drag in this way, but that to achieve a resolution better than several percent it was necessary to improve and simplify the methods of plate adjustment and balance calibration and control.

These problems were overcome by developing a new drag balance and an automatic control circuit, as described in the next sections, and it was thought that a resolution approaching 0.5 % might be attained ultimately. Any change less than this, of course, would be of no great practical significance.

4.7 Skin Friction Drag Balance

The principle of the drag balance is similar to that of the prototype. The perspex windtunnel test section has nominal dimensions 5 mm x 30 mm (a slight increase in aspect ratio was felt to be desirable, in order to reduce the influence of side wall boundary layers). The drag plate (brass, 74.4 mm x 19.35 mm x 6.85 mm thick) is attached to the crossbar of an H shaped bakelite holder (175 mm x 40 mm), supported from a rigid duralumin housing (220 mm x 220 mm in cross section by 200 mm long, with 10 mm thick walls). This avoids any possibility of magnetic sticking. The housing has portholes and bottom for access, sealed by perspex window and "O" rings, and two perspex panels at the front, sealed by gaskets, for electrical and pressure lead throughs. The suspension comprises twelve wires (steel piano wire, 0.010" (0.25 mm) in diameter and $\sim$ 100 mm long) attached up and down at the end of each prong of the holder, and side to side from the centre of each arm. This constrains the drag plate to motion parallel to the flow. The supporting wires are raked slightly fore and aft ($\sim 1^{\circ}$) and are fixed to tensioning screw adjusters at the wall of the housing. This obviously provides a degree of redundancy in adjusting the position of the plate, but if the tensions are kept roughly equal (this can be done by tuning the wires!) then this is not a problem, and extremely accurate levelling and location of the drag plate in the gap in the windtunnel wall is possible. The clearance around the plate is $\sim$ 0.5 mm at the ends and $\sim$ 0.25 mm at the sides. The resilient suspension also allows for deflection drag measurements. The

resonant frequency of the balance is typically ∿ 30 Hz.

A section of the lower windtunnel wall can be removed to permit drag plates to be changed easily and to allow the alignment to be checked. This is done using an electrical levelling plate. This has four steel contacts, set in a perspex block with two raised ridges on its surface which locate on the upper windtunnel wall, to the sides of the drag plate. A 9V potential is applied between the drag plate and the contacts, electrical contact being indicated by four light emitting diodes (LED's). The tension in the wires is adjusted until all four LED's flicker as the drag plate swings. The accuracy in the plate position is estimated to be ∿ 1μm, a considerable improvement over the prototype. (When the contacts are set up to be coplanar with the ridges, the maker's name etched onto the surface plate used can be detected by tracking the block over the surface).

The LVDT used has a range of ±0.025" (0.65 mm) and the bridge output is calibrated at ∿ 20 mV/μm.

The drag force is balanced by two solenoidal coils (of 1350 turns of 38 SWG polyurethane coated wire wound on 12 mm o/d, 1 mm thick aluminium formers, 25 mm long) acting on 10 mm diameter Alnico-6 magnets. The coils are connected in parallel (to give equal forces) and have resistances of 56Ω and 57Ω . The coils are enclosed in aluminium housings filled with a heat sink compound and fixed to the duralumin wall of the housing. This allows higher drags to be balanced and prevents any appreciable temperature rise in the balance housing.

Adjustment of the clearance between the core and casing of the LVDT, and also of the magnets and coils, is achieved by pivoting them about axes which are nominally aligned; if the alignment is not sufficiently accurate, clearance is obtained merely by altering the angles at which the components are clamped.

Damping is by the same method as before but with a larger vane area.

The centre line flow velocity at the balance section is determined from a pitot tube and static orifice, 15 mm downstream from the drag plate (it is assumed that there is no transverse pressure gradient). The pitot tube has a slightly smoothed flat end and has an o/d of 1.25 mm, an i/d of 0.65 mm and a length of 25 mm before the stem. The static orifice has the same diameter as the pitot tube. The centre line velocity is calculated from $p = \frac{1}{2}\rho u_\infty^2$ and no corrections for compressibility or turbulence were made. The static pressure at the plate, and the difference between this and the housing pressure, are also monitored. The latter gives a sensitive check for leaks from the housing. The flow static temperature and balance housing temperature are monitored using thermocouples.

During null position operation the position of the drag plate is controlled automatically using the circuit described in the following section.

A schematic diagram and photographs of the drag balance are shown in figures 4.10-4.12.

4.8 Automatic Control System

To overcome the problem of controlling the balance, a circuit was designed to interface between the LVDT signal conditioner and the coil power supply. The power supply has a high impedence input socket accepting voltages of $\sim -1V$ to $+1V$, giving stable proportional output currents from a power transistor of ~ -250 mA to $+250$ mA into a nominal 20Ω load.

The requirement was for a circuit which would adjust this input voltage so as to maintain a null output from the LVDT. With the LVDT voltage going positive for a downstream displacement, the control circuit must increase its output when the LVDT voltage is +ve, decrease it if -ve and hold a constant voltage for a null LVDT output.

After some initial development work a simple hybrid analogue/digital circuit was constructed which gives a constant rate of response for non zero inputs, with a narrow deadband. The LVDT voltage is fed (via a low pass RC filter which removes the 2.5 kHz ripple on the LVDT output) into an amplifer stage with a gain of $\sim 10^3$. Amplified signals of different polarity then trigger Schmitt Nand Gates, whose outputs gate clock pulses from an astable multivibrator. The pulses add or subtract voltage steps from low leakage polycarbonate capacitors storing the output voltage.

If the circuit is driven on, then, by an input outside the deadband between the +ve and -ve trigger levels, a fine staircase voltage is built up, approximating to a ramp function, until the input is within the deadband.

Schematic diagrams of the control system and a circuit diagram are given in figures 4.13-4.15.

The voltage decay rate from the capacitors was found to be negligible, at $\sim 0.05\%\ s^{-1}$ (see figure 4.16).

The trigger levels are adjustable using the 10k and 500k potentiometers (zero offset and gain adjust) from a few mV to a few V. They are set at $\sim$ 3.5mV with the drag balance. The clock frequency and mark/space ratio may be adjusted using the 2MΩ potentiometers. The frequency is set to $\sim$ 70Hz with a pulse width (-ve at the clock output) of 2.7 ms with an interval of 11.5 ms.

Figure 4.17 shows records of the drag plate position during drag balance tests at various flow speeds. It can be seen that the mean position of the drag plate is held to rather better than 1μm at all flow speeds. In fact, the control circuit exhibits excellent response and stability characteristics over the normal working range of Reynolds numbers, and allows drag measurements to be made accurately and with great ease. (For very low drag forces and flow speeds, better resolution can be obtained using the deflection method, although this was not necessary during any of the radioactive measurements).

4.9 Radiation Sources

There are various ways in which the air flow over the drag plate could be irradiated. The most important constraints on the radiation sources were considered to be the following:

1. they should be safe to handle and not present a signficant radiation hazard during use (this contrasts with the

97.5 Ci ^{137}Cs γ source and the ^{210}Po used by Kestin and Shah (1968). The latter contaminated their viscometer, which later had to be disposed of as radioactive waste).

2. the resultant ionisation level should be comparable to that attained by Kestin and Shah.
3. the sources should be extended, if possible, so as to give maximum irradiation over a length of windtunnel comparable to the length of the drag plate.

The nature of the radiation is also important, since the specific ionisation (ion pairs per unit length of track per particle) is very high for α particles, lower for β and very low for γ ray photons (figure 4.18). In terms of radiation hazard, γ sources are difficult to shield but generally have only moderate radiotoxicity, while α sources are extremely easy to shield but have extremely high radiotoxicity. The maximum permissible level of ^{210}Po in the body is $\sim$ 0.005 μCi for example (Whitehouse & Putman 1953).

Radioactive foils of appropriate sizes and quite high activities are commerically available, and it was thought that it might be possible to incorporate them into the surface of a drag plate.

The neutron irradiation of standard drag plates made from an appropriate metal was also considered, but there are few elements which would give appropriate results. Generally, one either gets high activity, short half life, γ sources or low acitivity β sources. One possibility could have been thalluim, but this has a physical nature similar to lead and is extremely toxic through ingestion or skin absorbtion. Irradiation of cobalt gives about the right characteristics with regard to β activity

and half life, but with a hard γ ray component.

In practice, attention was concentrated on three commercially available α,β and γ (or $\beta^{+}\rightarrow\gamma$) sources, and details of the sources used for initial experiments are given in table 4.1.

The ^{58}Co source consists of Co infused directly into a copper strip. The ^{147}Pm and ^{210}Po isotopes are sealed onto a substrate by a thin ($\sim$ 3μm) protective coating of silver. Note that the coating on the ^{210}Po foil is only effective over a limited period of time. The recoil due to the emission of the high energy α particles can cause radioactive material to penetrate the covering, making the foils unsafe after a year or so.

The α source is of a comparable specific activity to the 1mCi cm^{-2} of the previous work (Clark 1980b),and would be expected to give comparable ionisation levels.

We can estimate the degree of ionisation in a region of gas over such a source as follows (note that since we are interested in only $\sim$ 5 mm of path we can neglect the energy loss of the particles over this distance); for a 5 MeV particle in air at atmospheric pressure we expect $\sim$ 30,000 ion pairs / cm track (figure 4.18) where we can assume that electrons liberated during ionisation are rapidly captured to give negative ions.

If half of the emitted α particles enter this gas volume, neglecting losses through the protective surface, back scattering or secondary electron emission from the surface (or from anything stopping the particles at the other side), then the rate of

creation of ion pairs in 1 cm^3 is

$$q_\alpha = 30{,}000 . \tfrac{1}{2} . 3.7 \times 10^7 \text{ ip cm}^{-3} \text{ s}^{-1} = 5 \times 10^{11} \text{ ip cm}^{-3} \text{ s}^{-1}$$

If n_α denotes the concentration of ion pairs due to α irradiation, and r is the volume recombination rate, then

$$\frac{dn_\alpha}{dt} = q_\alpha - rn_\alpha^2 \qquad 4.28$$

With $r = 1.7 \times 10^{-6}$ cm^3 ip^{-1} s^{-1} at atmospheric pressure (Kestin and Shah 1968) the steady state concentration will be

$$n_\alpha = \sqrt{\frac{q_\alpha}{r}} \sim 5 \times 10^8 \text{ ip cm}^{-3} \qquad 4.29$$

For the ^{147}Pm foil the activity is $\sim$ 10 m Ci cm^{-2}. With 90 ip cm^{-1} for an 0.22 MeV β particle track (figure 4.18) we have

$$q_\beta \sim 10^{10} \text{ ip cm}^{-3} \text{ s}^{-1} \qquad 4.30$$

and

$$n_\beta = \sqrt{\frac{q_\beta}{r}} \sim 10^8 \text{ ip cm}^{-3} \qquad 4.31$$

The fractional degree of ionisation is therefore $\sim 5 \times 10^{-12}$, slightly less than the corrected value for Kestin & Shah's α experiments, and rather greater than their 97.5 Ci γ experiments.

The γ source had rather a high activity initially and it was difficult to provide adequate shielding to allow it to be handled over any extended period of time. Accordingly, at this time, only the α and β foils were mounted into milled out brass

drag plates. Experiments with dummy sources showed that it was difficult to keep the foil flat and accurately lined up with the edge of the drag plate. The most successful method which was developed gave surfaces which deviated by up to $\sim$ 0.2 mm from the correct level at certain parts of the surface, which suggested that there might be problems in using the plates in the drag balance. The method used is illustrated in figure 4.19. A milled-out drag plate, drilled completely through over part of its length, is placed over the radioactive foil (fitted to a brass backing strip to ensure that it is flat) and both are clamped down onto a surface impregnated with a thin oil. The assembly is then carefully warmed with a blowtorch and molten beeswax run into the space between the foil and the plate. (This is a surprisingly strong and versatile adhesive; it has the advantages that when molten ($\sim$ 70°C) it flows readily and is transparent (allowing a check on the position of the foil) and when set, it is extremely hard and rigid, although somewhat brittle. It can also, of course, be remelted if the foil has to be removed). The oily surface allows for easy separation from the flat plate when the wax has set hard (after $\sim$ 3/4 hour). The maximum temperature reached by the foil during this procedure should not have exceeded 100°C, but in all probability was considerably less. No release of radioactive material was observed, and radiation shielding was given by a screen of 2" thick interlocking lead bricks and a lead glass window. The foils were handled using tongs and disposible gloves and a radiation dosimetry badge were worn at all times. (During the

course of the thesis the maximum dosage recorded in a one month period was ∿ 40 mrem). Several "dummy" plates, with inactive silver foils, were also constructed for use in control experiments, and figure 4.20 shows such a plate.

4.10 Calibration and Initial Tests

The drag balance was calibrated and some preliminary tests run with the radioactive sources.

Calibrations were performed by hanging weights from a thread attached to the damping vane, passing through a hole in the wall of the balance (sealed during normal use) and over a pulley. The lightweight aluminium pulley is mounted using miniature precision bearings. The weights used are accurately weighed (0.6970 ± 0.0003 gf) steel spheres (ball bearings) and are handled using a lightly magnetised rod to prevent contamination. They were used instead of analytical balance weights to minimise the disturbance to the balance during loading and unloading. This is an extremely quick and accurate method of calibration. A sample calibration is shown in figure 4.21. The calibration deduced from six such measurements was

0.2466 ± 0.0004 gf/mA.

Before making extensive drag measurements, the effectiveness of the dashpot damping was checked by determining the resonant curve of the balance. Defining a damping factor k/ω_o through the equation of motion (the forcing function can have unit amplitude w.l.o.g.)

$$\ddot{x} + 2k\dot{x} + \omega_o^2 x = 1\, e^{iwt} \qquad 4.32$$

The amplitude response is given by

$$A = \frac{1}{\sqrt{1 - \frac{\omega^2}{\omega_o^2} + \frac{4k^2\omega^2}{\omega_o^2}}} \qquad 4.33$$

and the peak amplitude, given by $\left.\frac{\partial A}{\partial \omega}\right|_{\omega p} = 0$, is observed at

$$\omega_p = \omega_o \sqrt{1 - 2k^2/\omega_o^2} \qquad 4.34$$

and has a magnitude

$$A_p = \frac{1}{\frac{2k}{\omega_o}\sqrt{1 - \frac{k^2}{\omega_o^2}}} \qquad 4.35$$

Measuring A_p and ω_p therefore gives values for ω_p/ω_o and k/ω_o :-

$$\frac{\omega_p^2}{\omega_o^2} = \sqrt{1 - \frac{1}{A_p^2}} \qquad 4.36$$

$$\frac{k^2}{\omega_o^2} = \tfrac{1}{2}\left(1 - \frac{\omega_p^2}{\omega_o^2}\right) \qquad 4.37$$

The observed values gave

$\omega_o = 2\pi f_o = 2\pi(29\text{Hz})$

and $k/\omega_o \simeq 0.14$,

this latter value corresponding to a Q of ~ 3.6.

Figure 4.22 shows the observed resonance curve and the curve calculated using equation 4.33 with the above values.

The balance is slightly underdamped, but in subsequent tests, with or without the control system, this did not cause any problems.

A drag curve obtained using the control system is shown in figure 4.23. The behaviour is similar to before, with the slope in the turbulent region again being rather steep. To check the reproducibility of the measurements, tests were made at various flow speeds with two different drag plates, the balance being levelled and calibrated separately for each plate. The results (tables 4.2 and 4.3) showed that the reproducibility at all except the lowest flow speeds was of the order of 0.5% as intended, a considerable improvement over the prototype.

This suggested that the major problem in the work would indeed be the accuracy with which the radioactive drag plate surface could be constructed, and this was rapidly confirmed by a few tests.

The drag should, however, be less sensitive to imperfections on the opposite windtunnel wall, and so some preliminary experiments were performed with the radioactive drag plates mounted in the wall of the windtunnel opposite to the drag element. The results showed that the surface roughness still had an appreciable effect on the apparent drag. With the promethium foil an apparent drag reduction of $\sim$ 5% was observed, although at a low level of confidence (see table 4.4). Experiments with the polonium foil gave an increase in drag of $\sim$ 2% with similar uncertainties. The level of confidence was not considered high enough to conclude that any changes in drag had occured.

4.11 Analysis of Error Sources

In view of the problems encountered with the radioactive drag plates, a more effective approach seemed to be to fix a thin, permanent, shield in the windtunnel, flush with the lower surface, and to place the radiation sources behind it. While this rules out the use of the $^{210}P_o$ source, due to the very short range of α particles, it is still possible to get high radiation levels with β or γ rays. Since the drag plate does not need to be removed, the maximum resolution of the balance can be achieved, and it is appropriate, therefore, to look in more detail at the other possible error sources.

The effect of the pressure gradient was of primary concern, since it is well known that pressure forces can contribute very significantly to the apparent drag in floating element balances. In this case a simple analysis illustrates the point:

the pressure gradient is approximately $\frac{P}{L}$ where P is the pitotstatic pressure and L the channel length. If the balance housing takes up some intermediate pressure and we treat the gaps at the ends of the plate as small channels (i.e. assume a linear variation or pressure over the ends of the plate), then the average pressure force on the ends of a plate of width w, thickness z and length ℓ is

$$f_p = \frac{P\ell wz}{2L} \qquad 4.38$$

and so the total force is

$$f_{tot} = \tau_o \ell w + \frac{P\ell wz}{2L}$$

The total drag coefficient is then

$$c_{tot} = c_f + \frac{z}{2L} \qquad 4.39$$

Taking $L \sim 350$ mm and $z \sim 7$ mm gives

$$c_{tot} \sim c_f + 10^{-2}$$

Since we expect a skin friction coefficient of the order of 10^{-2} or less this is a potentially serious contribution (although this must be an upper limit as the observed drag curves would be almost flat otherwise).

One would also expect there to be a flow through the gaps due to the pressure difference between opposite sides of the plate. A wider gap would, presumably, reduce the pressure forces by reducing the resistance to flow through the gap, but the increased flow would then be expected to cause a greater perturbation of the flow over the plate. As an illustration, in experiments with a skin friction drag balance in an adverse pressure gradient, Brown & Joubert (1969) observed maximum secondary forces of $\sim$ 15%, although only 3% of the error was attributed to direct pressure gradient effects, the remainder being due to the indirect effects of the pressure gradient, and of the gap, on the flow over the surface.

Systematic studies of the effects of misalignment and gap size have been made by Allen (1977) with a pivoted balance in a zero pressure gradient flow. (note that with a pivoted design there is the possibility of errors from normal forces on the plate surface, as well as from lip forces). Some of Allen's

results for the effect of misalignment (Δz) and gap size (g) are shown in figure 4.24, with the approximation $\delta \sim h/z$. With $\frac{\Delta z}{h} \sim 0.0002$ and $\frac{g}{\ell} \sim 0.007$ we can see that these effects should be less severe than those due to the pressure gradient. Allen's work also shows that a larger gap size reduces the sensitivity to misalignment and that, contrary to what one might intuitively expect, there is no evidence that a recessed element is preferable to a protruding one, for small misalignments. This is in agreement with the work of O'Donnell & Westkaemper (1965) who found $\sim$ 4% errors for 20μm misalignments in either direction, although as the misalignment was increased the errors for a protruding element became progressively worse (figure 4.25).

The gap size should not, of course, be increased too much, since the gap must cause some kind of perturbation of the flow. Winter (1977) suggests that the gap Reynolds number, $R_g = \frac{u_\tau g}{\nu}$, should be less than $\sim$ 100 if high accuracy is desired. This corresponds to pitotstatic pressures of $\sim$ 10 mmHg in this work, and so the gap size should not be too great a concern for relative measurements except insofar as a gap Reynolds number of $\sim$ 100 corresponds approximately to the critical Reynolds number for such a roughness element. It is likely, therefore, that the observed transition at P $\sim$ 10 mmHg is initiated at the upstream gap.

The effects of misalignment and gap size may well, of course, be exacerbated by the pressure gradient, and it is impossible to predict the exact form of the errors with a particular balance. The only conclusion that can really be drawn at this stage is

that a parallel linkage balance is likely to be better than a pivoted balance owing to the elimination of the effect of normal forces.

In order to assess these error sources experimentally, a special drag plate was constructed with small (∿ 0.65 mm diameter) static holes at the ends of the plate. The pressure difference between corresponding holes was measured with tilt, capillary, paraffin manometers, sensitive to ∿ 0.025 mmHg. The manometers were fixed to the drag plate support and floated freely with the drag plate. They could be read through the perspex window on the upper surface of the balance housing. Measurements of the pressure differences (ΔP) and the total drag forces were made with the plate aligned and also with it vertically misaligned. Figure 4.26 shows the results for static taps at two different distances from the surface of the plate, 1.75 mm and 3.5 mm. The most striking feature of the curves is the fact that the pressure force can act upstream, contrary to what one would expect from the pressure gradient. The points at which the pressure forces are effectively zero allow the drag curve to be "pinned" at three flow speeds where the secondary forces are known to be small, showing that the basic character of the drag curve is correct.

The effects on the pressure forces, and on the total drag, of misalignments of ∿ 60μm in either direction are shown in figures 4.27 (for the hole at 1.75 mm) and 4.28. With these relatively large displacements, it can be seen that a protrusion causes a much greater change in the total drag coefficient.

Taking the measurements with the static tap located at 3.5 mm from the surface as characteristic of the average pressure on the

plate, we can estimate the contribution of the pressure forces to the total drag, and this is shown in figure 4.29. At low speeds the contribution is dramatic and could well account for the rather high laminar drag coefficients. Note also the large negative error during transition. Measurements with low speed turbulent flows were not made, but extrapolating the high speed data (admittedly over a rather large range of Reynolds number) would predict errors rising to $\sim$ 40% at the lowest speeds of interest. The behaviour at high speeds correlates well with the excessively large exponent in the Reynolds number dependence of the drag coefficient, and the application of corrections derived from figure 4.29 brings the data into much better agreement with the analysis of section 4.4

Since the pressure forces appeared large enough to significantly reduce the sensitivity of the drag reduction experiments at low speeds (although if irradiation were to have an effect on the skin friction drag, one might also conjecture that it could have an effect on the secondary forces) it seemed worthwhile to try to reduce the pressure forces as much as possible.

This can be done in various ways. Frei & Thomann (1980) sealed the gaps around the floating element of their drag balance with a liquid (glycerine) to eliminate the pressure forces. Unfortunately, the analysis of the surface tension forces then becomes rather involved and, one would suspect, vulnerable to errors.

The most obvious approach, adopted in this work and by Morsy

(1974), Allen (1980) and others, is simply to reduce the lip area. This was done (with non-radioactive drag plates) by machining the ends of the plate at 45° to a sharp edge, as shown in figure 4.10. This could possibly cause a slight increase in the sensitivity to misalignment, and such an effect was observed by Allen (1980), although the additional change in balance design and consequent removal of normal forces may have been responsible. It is also worth noting that while the approximation involved in equation 4.38 is satisfactory for a large edge thickness, it progressively underestimates the pressure force for smaller values of z/ℓ (Everett 1958).

However, with the precision of alignment possible, the considerable reduction in the pressure force expected should lead to significant reduction in the sizes of the secondary forces measured by the balance.

4.12 Final Tests

A comprehensive set of drag measurements was taken with the new drag plates, the drag plates being relevelled and the balance calibrated whenever the drag plate was changed. Measurements with turbulent flow were extended by placing a boundary layer trip (a 0.91 mm dia., 20SWG, copper wire) against the upper windtunnel surface, at a point 110 mm upstream of the leading edge of the drag plate (as shown in figure 4.10).

Some low speed measurements were taken using the deflection mode, while null position measurements were facilitated by recording the drag values over a short period of time on the

x-y plotter. This was done by tapping the voltage off a 2.7 Ω resistor in series with the coils, and feeding the voltage into the plotter (and a DVM for quicker measurements with less precision). Typically, traces were taken over about 5 seconds, once the correct flow speed had been established. The plotter was controlled through its remote control contact closure connections using the circuit shown in figure 4.30. The advantage of this system is that it is possible to concentrate on holding the correct flow speed and later to analyse the traces, using an optical integrating system to eliminate the effects of vibration. Figure 4.31 shows the balance and windtunnel system in their final configuration.

Sample calibrations for both modes of measurement are shown in figures 4.32 and 4.33. A plot of the drag coefficient as a function of the channel Reynolds number is shown in figure 4.34, together with the theoretical limiting curves from section 4.4.

The slope of the turbulent curve is now between $-1/4$ and $-1/5$, as expected, and the magnitude of the drag coefficient is also in good agreement with the analysis of section 4.4. The magnitude is in closest agreement with equations 4.20 and 4.24 (from large aspect ratio channel flows and flat plate flows), while the slope is in slightly better agreement with equation 4.19 (for flows in pipes or low aspect ratio channels).

It is noticeable that the turbulent drag curve is slightly higher for the tripped flow, presumably because the transition is initiated further upstream, rather than at the front of the plate.

In the laminar regime, both the magnitude of the drag coefficient and the slope of the curve are between the Blasius solution for a flat plate (equation 4.9) and that for Poiseuille flow (equation 4.5). Use of the Blasius formula with an allowance for the entry length (equation 4.10) gives a value for the entry length of $X \sim 13$ mm. However, the fit is not particularly good, and while this value is of the correct order of magnitude, it does not bear any obvious relation to the dimensions of the channel. This does not seem, therefore, to be a particularly useful correction.

The two transition regimes shown in figure 4.34 reflect a transition at the critical channel Reynolds number, if the inlet flow is disturbed by a boundary layer trip, or a transition at a Reynolds number corresponding to the critical roughness Reynolds number for the gap at the end of the drag plate.

Considered together with the analysis of Section 4.11, the inference from these results is that the systematic errors due to secondary forces are now at a negligible level.

The first sets of measurements with irradiation in this configuration were taken using ^{147}Pm sources, one (labelled A1) as described in table 4.1 and another (A2) with identical specifications expect for a later date of manufacture. The activities were $\sim$ 50 and 100 mCi respectively at the date of the experiments. A thin (1/16" or 1.6 mm), rigid, perspex shield was used, fixed into the lower windtunnel wall and very slightly recessed below the surface. The activity measured by a Geiger Counter (Mini Monitor Model E) at a distance of 5 mm

from the perspex was $\sim 5 \times 10^3$ counts s^{-1} (with a background of $\simeq 1$ count s^{-1}), and checks with additional shields showed that the major part of the count rate was due to bremβtrahlung. Using the quoted calibration data for $^{60}Co\ \gamma$ radiation as a guide, this would predict an ion pair creation rate of

$$q \sim 7 \times 10^4 \text{ ip cm}^{-3} \text{ s}^{-1} \tag{4.40}$$

and hence

$$n \sim 2 \times 10^5 \text{ ip cm}^{-3} \tag{4.41}$$

This corresponds to a fractional ionisation of $\sim 10^{-14}$, slightly higher than the pilot tests of Kestin & Shah (1968).

Control experiments were made with several of the blank plates. In principle, of course, with a rigid shield it should not be necessary to do this, but as rough handling of the balance can result in a slight shift in calibration and any movement of the shield would cause an apparent change in drag, blank plates were used to simulate the effect of insertion and removal of the radioactive plates from the balance.

The results obtained are shown in tables 4.5 & 4.6 (* denotes a measurement which has been estimated for computational purposes as the original was either missing or more than three standard deviations from the mean).

The measurements have been corrected to 20°C by using a least squares regression on the balance housing temperature. This includes the temperature dependence of the calibrations, which otherwise showed no significant systematic errors. Tables

4.7 and 4.8 show the regression parameters and the means and standard errors of the various sets of data. "N" and "A" denote combined drag values for the null or dummy plates and the radioactive plates respectively.

Tables 4.9 and 4.10 show the % drag changes observed. The errors have been calculated from the standard errors combined in quadrature and expressed as a percentage of the null measurement. Figure 4.35 shows the null measurements in the form D/P vs $\sqrt{P}$ (i.e. C_f vs Re) illustrating the state of the flow at each of the test points.

The results show that all changes in drag are less than two standard deviations from no change, and there is therefore no firm evidence for any drag changes with this level of radiation.

The accuracy of the high speed measurements is of the order of 0.2%. and this shows that very high precision can be achieved with the drag balance in an extended series of measurements.

4.13 The Effect of Irradiation on Skin Friction Drag

It was obviously desirable to make measurements with as high a degree of ionisation as possible. Reference to range and half thickness data (see figure 4.36) showed that it would be almost impossible to use the ^{210}Po sources, since the shield would have to be too fragile, but that it should be possible to use very thin shields with ^{147}Pm β particles, without the excessive loss of activity observed with the perspex shield. The best material for the shield seemed to be aluminium foil, despite its lack of rigidity, since Aℓ has low atomic weight and thin sheets

of the material are readily available.

Trials were made with a foil of thickness 4.1 mg cm^{-2}, covering a rectangular perspex frame which fitted into the windtunnel. It was not possible to prevent the foil becoming recessed (even by tensioning it while it was glued to the frame) without obstructing a significant portion of the radiation source with stiffening members. However, a recessed lower windtunnel surface (causing slightly lower drag values than before) could be tolerated in the interests of a maximum radiation level. The source used was the strongest ^{147}Pm plate, and it was held approximately 1mm below the foil.

The ionisation level was measured directly, with and without the shield, by determining the electrical resistance of the air between the radioactive plate (or Aℓ shield) and a standard brass drag plate 5 mm away (it was not possible to measure the radiation level directly with a standard Geiger counter, as the radiation level was far too high). Without the shield, the resistance was measured to be 3GΩ using a Marconi Instruments TF2650 FET multimeter.

If σ is the conductivity of the irradiated air, A is the plate area and h the thickness of the layer of air, then

$$R = \frac{1}{\sigma}\frac{h}{A} \tag{4.42}$$

so

$$\sigma \simeq 10^{-9}\ \Omega^{-1}m^{-1}. \tag{4.43}$$

If w_+ and w_- are the mobilities (drift velocity per unit field) of the positive and negative ions, and n is the number density of ion pairs, then

$$\sigma = ne\,(w_+ + w_-) \tag{4.44}$$

With mobilities of $\sim 2 \times 10^{-4}$ $(m\ s^{-1})/(Vm^{-1})$ for small ions (for example, 1.8×10^{-4} $(m\ s^{-1})/(Vm^{-1})$ for O_2^+ in O_2, Morgan & Turner 1967), and assuming that only singly charged ions are produced and that free electrons are rapidly captured to form negative ions of similar mobility, we get

$$n \simeq 2 \times 10^{13}\ ip\ m^{-3} \tag{4.45}$$

a fractional degree of ionisation of $\sim 10^{-12}$. Allowing for the slight differer in specific activity compared with the values used in equation 4.31, this is in very good agreement with the predicted ionisation level (although this may, of course, be altered slightly in windtunnel experiments with a flowing gas).

With the Aℓ foil in place, the observed resistance was 4GΩ . Since a thickness of 4.1 mg cm^{-2} corresponds almost exactly to one half thickness for 0.22 MeV β particles (figure 4.36) we would expect the resistance to have increased by a factor of $\sqrt{2}$ (see equation 4.31), in complete agreement with the observed change.

The effect on the drag of this high level of ionisation was investigated in a similar fashion to the tests with a perspex shield, as described in section 4.12. It is worth noting that the flexibility of the Aℓ foil caused a spurious reduction in

drag (of $\sim 0.5\%$) in an initial set of measurements. This arose because on each occasion the active plate was fixed into the windtunnel wall rather move firmly than the blank plate (due to greater concern about possible damage if it became detached). This caused a slight deformation of the perspex frame and consequent distortion of the Aℓ foil. An alternative method of holding the plates, which required forces of a much lower order, was designed using rubber bands, and an extensive series of drag measurements was then made.

The results are presented in tables 4.11 (fully turbulent flow) and 4.12 (laminar/transitional flow). Note that the test flow speeds for the latter measurements have been altered in response to the slight shift in transition caused by the recessed Aℓ shield (see figure 4.37 for the corresponding drag curve). Data from calibrations performed during the series of tests have been omitted from the tables since, as before, they showed no significant drift. The calibration for both sets of measurements can be taken as 0.08582 ± 0.00008 gf mV^{-1}.

The results of least squares regressions on the balance housing temperature are given in tables 4.13 and 4.14. The low correlation coefficients for the turbulent data did not warrant the application of a temperature correction, and the mean, standard deviation and standard error of the uncorrected drag values are given in table 4.15. The average housing temperature was $21^{\circ}C$ during this series of tests.

In the case of the laminar/transitional flow, both corrected and uncorrected values are given (table 4.16).

AD-A137 740 STUDIES OF AERODYNAMIC DRAG(U) CAMBRIDGE UNIV (ENGLAND) CAVENDISH LAB W A WILBY ET AL. DEC 82 AFOSR-TR-84-0071 AFOSR-79-0057 2/3

UNCLASSIFIED F/G 20/4 NL

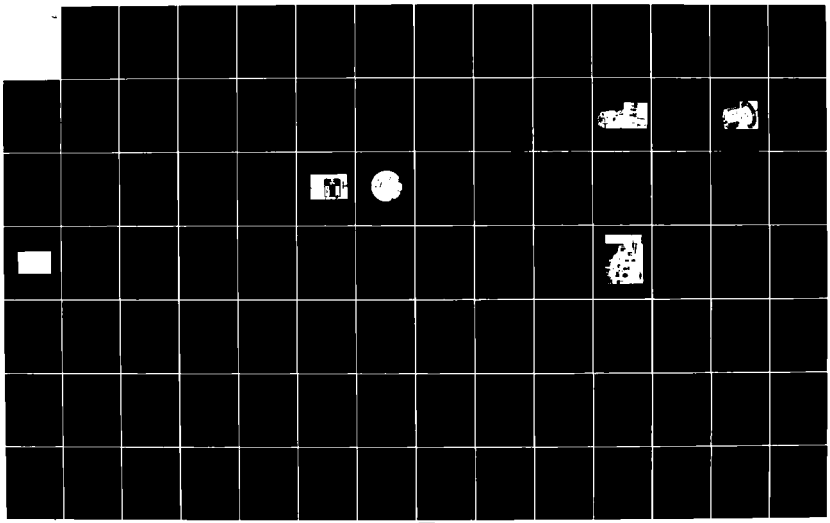

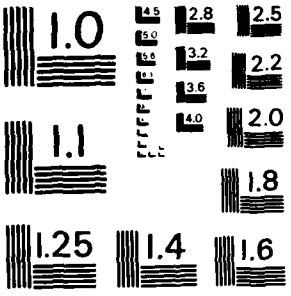

MICROCOPY RESOLUTION TEST CHART
NATIONAL BUREAU OF STANDARDS-1963-A

Calculations of the percentage drag changes are given in tables 4.17 and 4.18. The errors have again been calculated by combining standard errors in quadrature, and expressing then as a percentage of the null measurements. (Note that due to the discrete nature of the measured drag values, there was a possibility that the errors calculated from the standard deviations could underestimate the true uncertainty. However, as in all cases there was sufficient variation to span three or more "bins", the statistical errors should give a realistic measure of the uncertainty).

Tables 4.17 and 4.18 show clearly that no significant changes in drag were observed for fully turbulent or transitional flow. The most accurate measurements are within 0.1 - 0.2 % (one standard deviation) of zero change in drag.

4.14 Discussion

It has been shown that the drag balance is capable of accurate and reproducible measurements of the skin friction drag, and that the secondary forces are of a sufficiently low level not to affect measurements of small changes in drag.

Boundary layer irradiation is seen to have no significant effect on skin friction drag in turbulent or laminar flow. Although the errors with transitional flow are worse than for fully turbulent flow, even a small shift in the transition Reynolds number would cause a dramatic change in the drag in this region. It follows, therefore, that any change in transition can be ruled out.

The range of flow speeds covered in this investigation was $\sim 15\ m\ s^{-1} - 100\ m\ s^{-1}$ ($\sim 0.04 - 0.30$ Mach number).

The maximum ionisation level used, measured with static air in a configuration identical to that of the balance, was $\sim 2 \times 10^{13}$ ip m^{-3}, a fractional ionisation of $\sim 10^{-12}$ and a factor of 10^4 greater than the normal level due to background radiation. This was achieved using a 0.22 MeV β particle source, with a specific activity of ~ 100 Ci m^{-2}. In practical applications, a β source would seem to be the most appropriate, since it gives a fairly high ionisation level, but has moderate radiotoxicity, can be protected from the flow, and gives fairly short range radiation. The use of α sources would not be practical since the surface could not be adequately protected, giving an acute radiotoxic hazard.

Since the ionisation level varies as the square root of the source activity, the prospects of increasing the ionisation level without using excessively strong sources are poor. It would be possible to obtain ionisation by other methods such as an electric discharge. However, even if a slight drag reduction could be obtained, the power used to sustain a high voltage discharge with a high speed air flow would almost certainly negate the energy saving due to any drag reduction. There would also be other drawbacks such as radio and electrical interference and the fire or explosion hazard caused by the spark discharge.

4.15 Conclusions

Skin friction drag balance experiments have been performed on air flows at atmospheric pressure with speeds of up to 0.3

Mach number. It was observed that boundary layer irradiation from a β particle source, having a specific activity of 100 Ci m^{-2}, did not result in any signficant changes in skin friction drag with either laminar or turbulent flow, and there was no significant effect on transition.

With errors of 0.1 - 0.2% for the high speed turbulent flow, and ∿ 1% in the transition regime, this conclusion has a very high level of confidence.

Boundary layer irradiation or ionisation does not appear to offer any prospects for achieving significant, measureable drag reductions with aircraft.

TABLE 4.1

SPECIFICATIONS OF RADIOACTIVE FOILS

Isotope	Radiation	Activity/mCi	Max. Energy of Particles /MeV	Half-Life	Overall Size/mm^2	Active Area/mm^2
^{210}Po	α	5.5(Feb.'80)	5.30	138d	70 × 20	60 × 11
^{147}Pm	β	120(Apr.'80)	0.22	2.6a	70 × 17	60 × 10
^{58}Co	β^+ (γ)	10(Apr.'80)	0.47	71d	70 × 17	60 × 10

TABLE 4.2

DRAG VALUES - FIRST SET

P/mmHg	D/gf
5	0.22 ± 0.01
10	0.52 ± 0.01
25	2.42 ± 0.01
50	4.87 ± 0.02
100	9.01 ± 0.03
150	12.37 ± 0.03
200	15.18 ± 0.04

TABLE 4.3

DRAG VALUES - SECOND SET

P/mmHg	D/gf
5	0.22 ± 0.01
10	0.51 ± 0.01
25	2.41 ± 0.02
50	4.85 ± 0.03
100	N/A
150	11.9 ± 0.1
200	15.2 ± 0.1

TABLE 4.4

PRELIMINARY TESTS - ^{147}Pm PLATE - NO SHIELD

P/mmHg	Ag Plate	^{147}Pm Plate	% Decrease in Drag
5	0.55 ± 0.05	0.35 ± 0.05	36 ± 13
10	1.6 ± 0.1	1.4 ± 0.1	13 ± 9
25	9.6 ± 0.2	8.9 ± 0.2	7 ± 3
50	19.2 ± 0.2	18.3 ± 0.2	5 ± 2
100	33.5 ± 0.5	31.7 ± 0.5	5 ± 2
150	45.2 ± 0.6	42.8 ± 0.6	5 ± 2
200	55.3 ± 0.3	52.9 ± 0.3	4 ± 1

TABLE 4.5

DRAG MEASUREMENTS IN FULLY TURBULENT FLOW (PERSPEX SHIELD)

Expt.	Plate	T /°C	Calib./(gf/mV)	r^2	Drag/mV P = 2	5	10	15	30	50 mmHg
C401										
D402	N2	18.2			3.6	8.3	15.3	22.6	42.6	67.6
C403										
D404	N4	18.8			3.7	8.2	15.1	22.5	42.3	67.6
C405		19.1	0.08842	0.99999						
C406		19.4	0.08929	0.99999						
D407	N5	19.4			3.5	8.1	15.2	22.6	42.8	67.8
C408		19.8	0.08912	0.99999						
D409	N3	19.8			3.6	8.0	15.1	22.7	42.8	67.8
C410		19.6	0.08845	0.99999						
C411		20.0	0.08838	0.99999						
D412	N1	20.1			3.5	8.0	15.1*	22.4	42.6	67.7
C413		20.1	0.08871	0.99998						
D414	N2	20.0			3.4	8.0	15.1	22.5	42.6	67.8
C415		20.1	0.08952	0.99999						
C416		20.7	0.08914	0.99999						
D417	N3	20.7			3.6	8.3	15.3	22.7	42.8	68.0
C418		20.6	0.08940	0.99998						
D419	N4	20.4			3.8	8.1	15.0	22.7	42.9	68.2
C420		20.4	0.08883	1.00000						
C421		20.9	0.08897	0.99998						
D422	N5	20.9			3.5	8.0	15.2	22.6	43.1	67.9
C423		20.6	0.08870	1.00000						
D424	N1	21.1			3.6	8.0	15.1	22.7	42.7	67.9
C427		21.2	0.08920	0.99999						
D428	A1	21.0			3.5	8.0	15.3	22.4	42.7	68.1
C429		20.9	0.08942	0.99998						
D430	N2	21.2			3.5	8.0	15.1	22.5	42.6	68.1
C431		21.2	0.08897	0.99999						

TABLE 4.5 (continued)

C432		21.5	0.08854	0.99999						
D433	N3	21.2			3.5	8.1	15.2	22.4	42.7	68.0
C434		21.7	0.08942	0.99999						
D435	N4	21.4			3.6	8.0	15.1	22.3	42.8	68.3
C436		21.8	0.08925	0.99999						
D437	A2	21.5			3.4	8.0	15.3	22.5	42.7	68.4
C438		21.5	0.08849	0.99997						
D439	N5	21.7			3.6	8.1	15.1	22.4	42.6	68.2
C440		21.7	0.08843	0.99997						
C501		19.0	0.08959	0.99999						
C502		19.0	0.08886	0.99999						
D503	N3	18.8			3.6	8.1	15.1	22.4	42.3	67.2
C504		19.1	0.08944	0.99998						
D505	N4	19.1			3.6	8.1	15.0	22.6	42.3	67.5
C506		20.2	0.08886	0.99994						
D507	A2	19.8			3.6	8.2	15.1	22.5	42.4	67.8
C508		19.8	0.08918	0.99999						
D509	N5	20.0			3.6	8.1	15.1	22.6	42.5	67.2
C510		20.0	0.08827	0.99999						
C511		20.9	0.08918	0.99999						
D512	N1	20.5			3.3	8.1	15.2	22.4	42.4	67.4
C513		21.0	0.08916	0.99998						
D514	A1	20.7			3.6	7.9	15.1	22.6	42.3	67.6
C515		20.7	0.08902	0.99999						
C516		21.3	0.08936	0.99998						
D517	N2	21.0			3.6	8.0	15.1	22.4	42.7	67.9
C518		21.0	0.08865	0.99998						
D519	N3	21.3			3.7	8.3	15.0	22.5	42.6	68.0
C520		21.8	0.08881	0.99999						
D521	N4	21.5			3.6	8.0	15.1	22.4	42.6	67.4
C522		22.0	0.08895	1.00000						
D523	A2	21.7			3.5	8.0	15.1	22.5	42.7	67.6
C524		21.7	0.08865	0.99999						

TABLE 4.5 (continued)

C525		22.2	0.08901	1.00000						
D526	N5	21.9			3.7	8.0	15.2	22.6	42.6	68.1
C527		22.0	0.08959	0.99999						
D528	N1	22.1			3.6	8.0	15.0	22.4	42.7	67.8
C529		22.6	0.08891	0.99999						
D530	A1	22.3			3.4	7.9	15.0	22.5	42.7	67.9
C531		22.4	0.08840	1.00000						
D532	N2	22.4			3.5	8.0	15.1	22.5	42.6	68.0
C533		22.4	0.08906	1.00000						
C534		22.7	0.08870	1.00000						
D535	N4	22.5			3.5	7.9	15.0	22.2	42.7	67.9
C536		22.9	0.08939	0.99998						
D537	A2	22.6			3.5	7.9	15.2	22.4	42.6	67.7
C539		22.3	0.08887	0.99998						
D540	N5	22.7			3.5	7.9	15.1	22.5	42.9	68.1
C541		22.9	0.08943	0.99999						
D542	N1	22.8			3.6	7.8	14.9	22.4	42.5	67.9
C543		23.1	0.08871	0.99999						
D544	A1	23.1			3.5	7.9	15.2	22.5	42.6	68.3
C545		22.9	0.08878	0.99999						
D546	N2	23.0			3.6	7.8	15.0	22.6	42.7	67.8
C547		23.0	0.08904	0.99999						
C548		23.1	0.09132	0.99901						
D549	N3	22.9			3.6	7.9	15.2	22.7	42.8	67.9*
C550		23.1	0.08943	0.99999						
D551	N4	22.9			3.3	7.9	15.1	22.4	42.7	67.9

TABLE 4.6

DRAG MEASUREMENTS IN LAMINAR AND TRANSITIONAL FLOW (PERSPEX SHIELD)

Expt.	Plate	T_h/ °C	Calib./(gf/mV)	r^2	Drag/mV P = 2	5	10	15	30	50 mmHg
C601		16.1	0.08951	0.99999						
C602		16.1	0.09014	0.99997						
C603		16.0	0.08875	0.99999						
C604		16.0	0.08898	0.99997						
D605	N1	16.1			1.3	2.4	6.7	13.3	32.7	53.0
D606	A1	16.9			1.3	2.3	6.7	13.1	32.8	53.1
D607	N2	17.1			1.3	2.5	6.8	13.2	32.7	53.4
D608	N3	17.4			1.3	2.5	6.6	12.9	32.8	53.4
D609	A2	17.8			1.4	2.6	6.7	12.9	32.7	53.3
D610	N4	17.9			1.4	2.5	6.5	12.9	32.6	53.5
C611		17.9	0.08894	0.99999						
C612		17.8	0.08840	0.99997						
C613		17.8	0.08909	0.99999						
C614		17.8	0.08893	0.99998						
D615	N1	18.1			1.5	2.5	6.7	12.9	32.6	53.3
D616	A1	18.1			1.5	2.6	6.7	13.0	32.5	53.3
D617	N2	18.3			1.5	2.5	6.5	13.1	32.5	53.4
D618	N3	18.5			1.4	2.4	6.7	13.0	32.3	53.3
D619	A2	18.6			1.3	2.6	6.6	12.8	32.4	53.4
D620	N4	18.7			1.5	2.5	6.5	13.0	32.3	53.3
C621		18.7	0.08875	0.99994						
C622		18.7	0.08847	0.99999						
C623		18.7	0.08897	0.99999						
C624		18.7	0.08845	0.99999						
D625	N1	18.8			1.3	2.5	6.7	12.7	32.5	53.5
D626	A1	19.0			1.4	2.6	6.4	12.3	32.6	53.5
D627	N2	19.1			1.4*	2.5	6.6	12.5	32.6	53.7
D628	N3	19.2			1.4	2.5	6.8	12.2	32.6	53.4
D629	A2	19.2			1.4	2.6	6.7	12.2	32.5	53.3
D630	N3	19.3			1.5	2.6	6.5	12.1	32.5	53.5

TABLE 4.6 (continued)

C631		19.3	0.08898	0.99998						
C632		19.2	0.08879	0.99999						
C633		19.2	0.08988	0.99998						
C634		19.2	0.08966	0.99999						
D635	N1	19.2			1.4	2.6	6.3	12.3	32.8	53.7
D636	A1	19.1			1.3	2.7	6.2	12.2	32.7	53.7
D637	N2	19.1			1.4	2.4	6.3	12.4	32.7	53.6
D638	N3	19.1			1.3	2.4	6.3	12.2	32.4	53.7
D639	A2	19.2			1.3	2.6	6.5	12.4	32.4	53.4
D640	N4	19.3			1.5	2.4	6.4	12.5	32.5	53.5
C641		19.3	0.08928	0.99998						
C642		19.3	0.08970	0.99997						
C701		16.0	0.08920	0.99998						
C702		16.0	0.08933	0.99998						
D703	N2	15.9			1.4	2.4	6.7	13.2	32.4	53.1
D704	A1	16.3			1.4	2.4	6.8	13.4	32.2	53.2
D705	N2	16.6			1.5	2.4	6.6	13.4	32.5	53.1
D706	N3	16.8			1.4	2.4	6.7	13.1	32.6	52.9
D707	A2	17.0			1.4	2.4	6.6	12.9	32.6	52.9
D708	N4	17.3			1.4	2.4	6.8	13.1	32.9	53.2
C709		17.3	0.08863	0.99998						
C710		17.4	0.08871	0.99999						
C711		17.4	0.08878	0.99999						
C712		17.4	0.08929	0.99999						
D713	N2	18.0			1.4	2.6	6.8	12.9	32.6	53.3
D714	A1	18.1			1.5	2.5	6.7	12.7	32.8	53.4
D715	N2	18.4			1.5	2.6	6.7	12.7	32.9	53.3
D716	N3	18.5			1.5	2.6	6.7	12.6	32.7	53.1
D717	A2	18.9			1.4	2.5	6.7	12.8	32.8	53.3
D718	N4	18.8			1.3	2.5	6.5	12.6	32.3	52.9
C719		18.8	0.08855	0.99999						
C720		18.8	0.08879	0.99998						
C721		18.7	0.08912	0.99999						
C722		18.7	0.08849	0.99972						

TABLE 4.7

DRAG VALUES FOR FULLY TURBULENT FLOW(PERSPEX SHIELD)

Mean and Standard Error (in mV) quoted. Calibration = 0.0890 ± 0.0002 gf/mV .
Corrected to 20°C.

P/mmHg	N		A1		A2		A		Regression Parameters Slope/(mV/°C)	r^2
2	3.583	0.019	3.534	0.036	3.527	0.036	3.530	0.023	-0.019	0.059
5	8.104	0.017	8.044	0.035	8.119	0.025	8.081	0.024	-0.067	0.493
10	15.120	0.017	15.173	0.064	15.193	0.052	15.183	0.038	-0.013	0.030
15	22.529	0.025	22.539	0.043	22.506	0.020	22.522	0.022	-0.022	0.052
30	42.598	0.034	42.484	0.083	42.529	0.053	42.507	0.048	+0.051	0.122
50	67.72	0.045	67.78	0.12	67.72	0.20	67.75	0.11	+0.108	0.249

TABLE 4.8

DRAG VALUES FOR LAMINAR/TRANSITIONAL FLOW (PERSPEX SHIELD)

Values in mV, corrected to 20°C. Calibration = 0.08905 ± 0.00009 gf/mV .

P/mmHg	N		A1		A2		A		Regression Parameters Slope/(mV/°C)	r^2
2	1.420	0.016	1.414	0.037	1.377	0.022	1.395	0.021	+0.007	0.008
5	2.575	0.015	2.619	0.042	2.626	0.026	2.623	0.023	+0.049	0.291
10	6.449	0.029	6.413	0.067	6.507	0.043	6.460	0.041	-0.082	0.265
15	12.203	0.040	12.131	0.072	12.181	0.084	12.156	0.053	-0.313	0.729
30	32.570	0.038	32.585	0.094	32.555	0.065	32.570	0.057	-0.007	0.002
50	53.613	0.040	53.676	0.040	53.497	0.053	53.586	0.049	+0.149	0.465

TABLE 4.9

% DRAG CHANGES ON IRRADIATION (FULLY TURBULENT FLOW - PERSPEX SHIELD)

(maximum accuracy quoted :- nearest 0.05)

P/mmHg	A1	A2	A
2	-1.4 ± 1.1	-1.6 ± 1.1	-1.5 ± 0.8
5	-0.75± 0.5	+0.2 ± 0.35	-0.3 ± 0.35
10	+0.35± 0.45	+0.5 ± 0.35	+0.4 ± 0.3
15	+0.05± 0.2	-0.1 ± 0.15	-0.05± 0.15
30	-0.25± 0.2	-0.15± 0.15	-0.2 ± 0.15
50	+0.1 ± 0.2	0.0 ± 0.3	+0.05± 0.2

TABLE 4.10

% DRAG CHANGES ON IRRADIATION (LAMINAR/TRANSITIONAL FLOW - PERSPEX SHIELD)

(maximum accuracy quoted :- nearest 0.05)

P/mmHg	A1	A2	A
2	-0.4 ± 2.8	-3.0 ± 1.9	-1.8 ± 1.9
5	+1.7 ± 1.7	+2.0 ± 1.2	+1.9 ± 1.1
10	-0.6 ± 1.1	+0.9 ± 0.8	+0.15± 0.8
15	-0.6 ± 0.65	-0.2 ± 0.75	-0.4 ± 0.55
30	+0.05± 0.3	-0.05± 0.25	0.0 ± 0.2
50	+0.1 ± 0.1	-0.2 ± 0.1	-0.05± 0.1

TABLE 4.11

FULLY TURBULENT FLOW - ALUMINIUM SHIELD

Expt. Code	T/ °C	P =	Drag/mV 2	5	10	15	30	50 mmHg
N25603	20.5		2.9	6.5	12.0	17.7	33.0	51.3
N25604	20.5		2.8	6.3	11.9	17.6	32.9	50.9
N25605	20.5		2.9	6.4	11.9	17.6	32.9	51.0
N25606	20.5		2.9	6.4	11.8	17.7	32.8	51.0
A25609	20.9		3.0	6.4	12.0	17.7	33.0	51.3
A25610	20.8		2.9	6.3	12.0	17.7	33.0	51.3
A25611	20.7		3.0	6.3	12.1	17.7	33.1	51.2
A25612	20.7		2.9	6.4	11.9	17.6	33.1	51.0
N25615	21.0		2.9	6.5	12.0	17.5	32.9	51.2
N25616	21.0		2.8	6.3	12.0	17.6	32.9	51.2
N25617	20.9		2.8	6.4	11.9	17.5	32.8	51.1
N25618	20.9		2.8	6.3	11.9	17.4	32.7	50.9
A25621	21.2		2.9	6.4	11.9	17.5	32.9	51.2
A25622	21.2		2.9	6.3	12.0	17.6	33.0	51.1
A25623	21.1		2.9	6.2	11.9	17.5	32.8	51.0
A25624	21.1		2.7	6.2	11.9	17.4	32.8	50.8
N25627	21.3		2.9	6.3	11.9	17.5	32.9	51.0
N25628	21.3		2.9	6.3	11.9	17.5	32.7	50.7
N25629	21.2		2.8	6.3	11.8	17.6	32.8	50.9
N25630	21.2		2.8	6.2	11.8	17.5	32.8	50.9
A25633	20.6		2.8	6.3	11.8	17.7	32.9	51.3
A25634	20.6		2.9	6.3	11.9	17.5	33.0	51.1
A25635	20.6		2.9	6.4	11.9	17.6	33.1	51.0
A25636	20.6		2.8	6.3	11.9	17.6	32.9	50.9
N25639	20.8		2.9	6.3	12.1	17.5	33.1	51.2
N25640	20.8		2.9	6.2	11.9	17.7	32.9	51.1
N25641	20.8		2.9	6.2	11.9	17.6	32.8	50.8
N25642	20.8		2.8	6.3	11.9	17.5	32.7	51.0
A25645	21.0		2.8	6.3	11.9	17.4	33.0	51.0
A25646	20.9		2.8	6.2	11.8	17.6	32.7	50.9
A25647	20.9		2.9	6.4	11.8	17.6	32.8	50.9
A25648	20.9		2.7	6.3	11.7	17.5	33.0	50.9
N25651	21.2		2.8	6.3	11.9	17.7	33.0	51.1
N25652	21.2		2.8	6.2	12.0	17.7	32.7	51.1
N25653	21.1		2.8	6.3	11.9	17.6	32.8	50.7
N25654	21.0		2.8	6.3	11.7	17.4	32.8	50.8
A25657	21.2		2.9	6.2	11.9	17.5	32.7	51.0
A25658	21.1		2.7	6.4	11.8	17.3	32.8	51.0
A25659	21.1		2.8	6.4	11.8	17.5	32.9	50.8
A25660	21.1		2.7	6.3	11.8	17.4	32.7	50.7
N26603	20.8		2.9	6.4	11.9	17.4	32.8	51.2
N26604	20.8		2.8	6.3	11.8	17.4	32.7	50.8
N26605	20.8		2.9	6.3	11.8	17.5	32.8	51.0
N26606	20.8		2.8	6.3	11.9	17.5	32.8	50.8
A26609	21.0		2.9	6.3	11.8	17.4	32.7	51.1
A26610	21.0		2.8	6.3	11.9	17.4	32.9	50.9
A26611	20.9		2.8	6.3	11.8	17.3	32.8	51.0
A26612	20.9		2.8	6.3	11.8	17.5	32.7	51.0

TABLE 4.11 (continued)

N26615	21.0	2.8	6.3	12.0	17.6	32.9	50.9
N26616	20.9	2.9	6.3	11.7	17.3	32.9	50.9
N26617	20.9	2.9	6.2	11.8	17.5	32.9	50.8
N26618	20.9	2.8	6.2	11.9	17.4	32.9	51.0
A26621	20.8	2.9	6.3	11.8	17.6	32.9	50.8
A26622	20.8	2.9	6.4	11.9	17.5	32.9	51.0
A26623	20.8	2.8	6.2	11.9	17.5	32.9	51.0
A26624	20.8	2.8	6.1	11.8	17.6	32.9	50.7
N26627	20.9	2.8	6.3	12.0	17.5	32.8	50.9
N26628	20.8	2.8	6.2	11.9	17.5	32.8	50.6
N26629	20.8	2.9	6.3	11.9	17.4	32.9	50.9
N26630	20.8	2.7	6.4	11.8	17.5	32.7	50.6

TABLE 4.12

LAMINAR/TRANSITIONAL FLOW - ALUMINIUM SHIELD

Expt. Code	T/ °C	P =	2 x Drag/mV 1	2	5	10	15	30 mmHg
N28603	20.4		1.1	2.9	8.6	18.6	28.7	57.0
N28604	20.4		1.0	2.8	8.6	18.7	29.8	57.0
N28605	20.5		1.0	3.0	9.5	19.8	29.4	56.8
N28606	20.6		0.9	2.9	9.4	20.1	29.4	56.9
N28607	20.6		1.0	3.2	9.7	19.8	29.3	56.8
A28608	21.4		1.1	3.1	9.4	20.2	29.6	56.9
A28609	21.2		0.9	2.8	8.5	18.6	29.0	56.8
A28610	21.1		0.9	2.8	8.5	18.6	28.8	56.9
A28611	21.0		1.0	2.8	8.6	18.4	28.7	56.7
A28612	21.1		0.9	2.7	8.5	18.5	28.5	56.8
N28613	21.4		0.9	2.5	8.3	17.9	28.7	56.3
N28614	21.4		0.9	2.6	8.4	17.8	28.1	56.2
N28615	21.3		1.0	2.6	8.3	18.3	28.2	56.5
N28616	21.3		1.0	2.7	8.4	17.9	28.2	56.4
N28617	21.3		0.9	2.7	8.3	17.8	27.8	56.1
A28618	21.9		1.0	2.8	8.6	18.4	28.8	57.1
A28619	21.9		1.0	2.7	8.4	18.4	28.6	57.1
A28620	21.8		1.0	2.7	8.7	18.3	28.6	56.7
A28621	21.9		1.1	2.9	8.6	17.9	28.9	57.0
A28622	21.9		1.0	2.6	8.4	18.1	28.6	57.0
N28623	22.2		1.0	2.8	8.5	18.2	28.9	57.3
N28624	22.0		0.9	2.7	8.4	18.4	28.6	56.8
N28625	22.0		1.1	2.8	8.5	18.2	28.7	56.7
N28626	22.0		1.0	2.8	8.3	18.4	28.6	56.8
N28627	22.0		1.0	2.5	8.6	18.3	28.5	57.1
A28628	22.3		1.0	2.9	8.7	18.2	28.7	57.3
A28629	22.2		1.0	2.8	8.7	18.2	28.7	57.1
A28630	22.2		1.0	2.7	7.9	18.3	28.5	56.7
A28631	22.2		0.9	2.7	8.4	18.3	28.7	57.0
A28632	22.2		1.1	2.8	8.5	18.3	28.6	56.9
N28633	22.5		0.9	2.7	8.4	18.2	28.6	56.8
N28634	22.3		0.9	2.9	8.3	18.1	28.5	56.4
N28635	22.3		0.9	2.6	8.6	18.2	28.7	56.5
N28636	22.3		1.0	2.8	8.3	18.2	28.5	56.8
N28637	22.3		1.0	2.7	8.5	18.3	28.5	56.5

TABLE 4.13

TEMPERATURE REGRESSION PARAMETERS

FULLY TURBULENT FLOW - Al SHIELD

P/mmHg	Intercept/mV	Slope/(mV/°C)	r^2
2	4.07	-0.0589	0.0313
5	7.60	-0.0618	0.0242
10	11.69	+0.0093	0.0004
15	19.91	-0.1143	0.0440
30	34.18	-0.0629	0.0096
50	50.97	0.0000	0.0000

TABLE 4.14

TEMPERATURE REGRESSION PARAMETERS

LAMINAR/TRANSITIONAL FLOW - Al SHIELD

P/mmHg	2xIntercept/mV	2xSlope/(mV/°C)	r^2
1	1.07	-0.0042	0.0017
2	4.52	-0.0807	0.1181
5	15.05	-0.2988	0.2587
10	29.48	-0.5094	0.2896
15	34.45	-0.2650	0.1701
30	55.46	+0.0614	0.0188

TABLE 4.15

DRAG VALUES FOR FULLY TURBULENT FLOW - Al SHIELD

Mean μ , standard deviation σ and standard error $\sigma/\sqrt{n}$ are quoted in mV. Average balance housing temperature = 21°C.

	Null			Active		
P/mmHg	μ	σ	$\sigma/\sqrt{n}$	μ	σ	$\sigma/\sqrt{n}$
2	2.841	0.056	0.010	2.843	0.082	0.015
5	6.306	0.079	0.014	6.304	0.078	0.015
10	11.891	0.092	0.016	11.871	0.090	0.017
15	17.528	0.11	0.019	17.525	0.11	0.022
30	32.837	0.12	0.021	32.889	0.13	0.025
50	50.947	0.18	0.031	50.996	0.17	0.033

TABLE 4.16

DRAG VALUES FOR LAMINAR/TRANSITIONAL FLOW - Al SHIELD

Mean μ , standard deviation σ and standard error $\sigma/\sqrt{n}$ are quoted in mV/2.

Not corrected for temperature

P/mmHg	μ	σ	$\sigma/\sqrt{n}$	μ	σ	$\sigma/\sqrt{n}$
1	0.970	0.064	0.014	0.987	0.062	0.016
2	2.760	0.17	0.037	2.787	0.12	0.030
5	8.595	0.41	0.092	8.560	0.29	0.076
10	18.46	0.65	0.15	18.45	0.50	0.13
15	28.69	0.47	0.11	28.753	0.26	0.068
30	56.685	0.32	0.071	56.933	0.19	0.049

Corrected to 20°C

P/mmHg	μ	σ	$\sigma/\sqrt{n}$	μ	σ	$\sigma/\sqrt{n}$
1	0.977	0.063	0.016	0.994	0.062	0.016
2	2.885	0.15	0.033	2.928	0.12	0.030
5	9.060	0.33	0.074	9.084	0.29	0.075
10	19.25	0.52	0.12	19.34	0.46	0.12
15	29.097	0.42	0.093	29.218	0.26	0.067
30	56.589	0.33	0.073	56.826	0.18	0.048

TABLE 4.17

DRAG CHANGES ON IRRADIATION

FULLY TURBULENT FLOW - Al SHIELD

P/mmHg	% Drag Change
2	+0.07 ± 0.65
5	-0.03 ± 0.33
10	-0.17 ± 0.20
15	-0.02 ± 0.16
30	+0.16 ± 0.10
50	+0.10 ± 0.09

TABLE 4.18

DRAG CHANGES ON IRRADIATION

LAMINAR/TRANSITIONAL FLOW - Al SHIELD

Not corrected for temperature

P/mmHg	% Drag Change
1	+1.8 ± 2.2
2	+1.0 ± 1.7
5	-0.4 ± 1.4
10	-0.1 ± 1.1
15	+0.24 ± 0.44
30	+0.44 ± 0.15

Corrected to 20°C

P/mmHg	% Drag Change
1	+1.7 ± 2.2
2	+1.5 ± 1.6
5	+0.3 ± 1.2
10	+0.46 ± 0.86
15	+0.42 ± 0.39
30	+0.42 ± 0.15

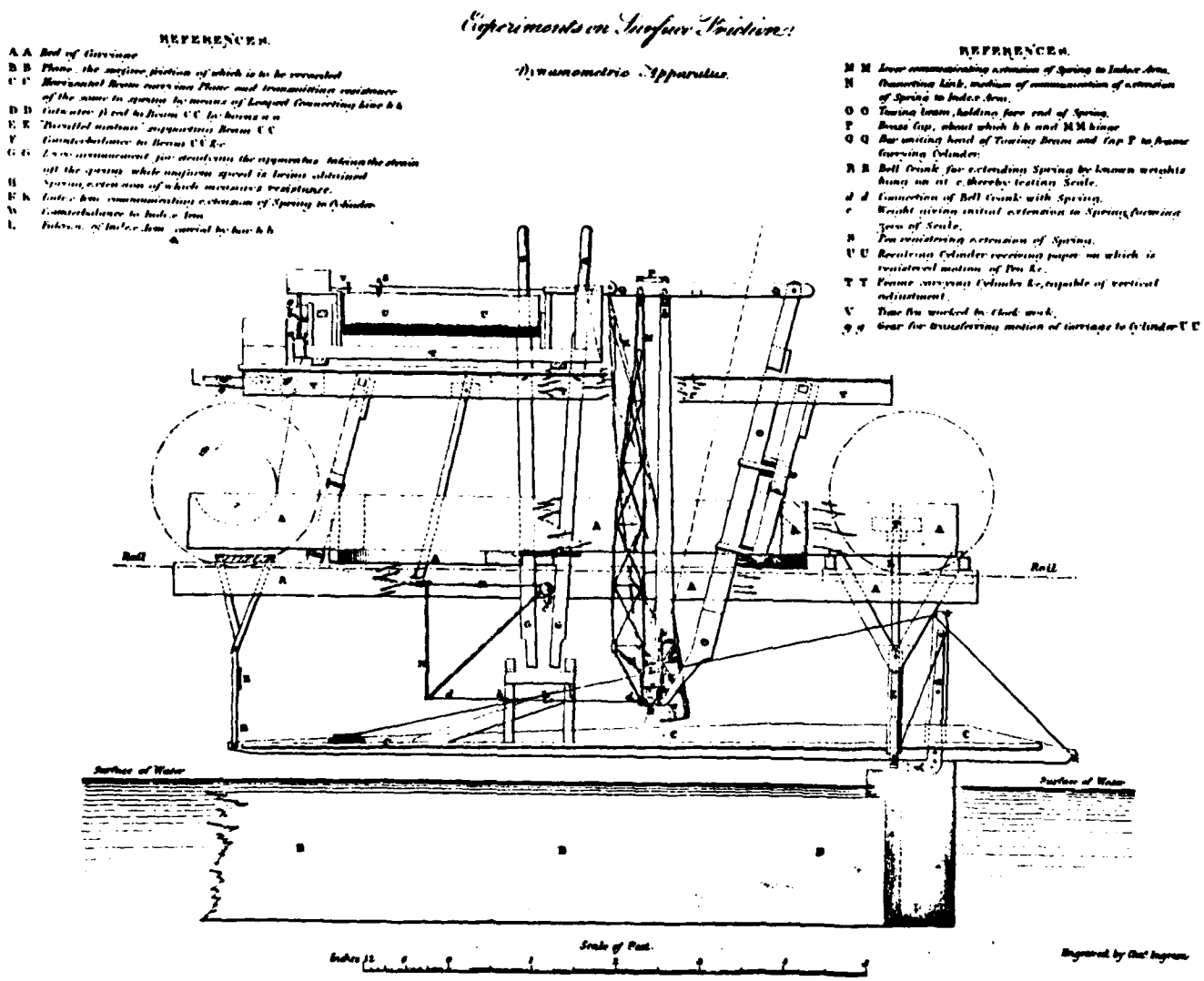

Figure 4·1. Drag Balance used by Froude (1872).

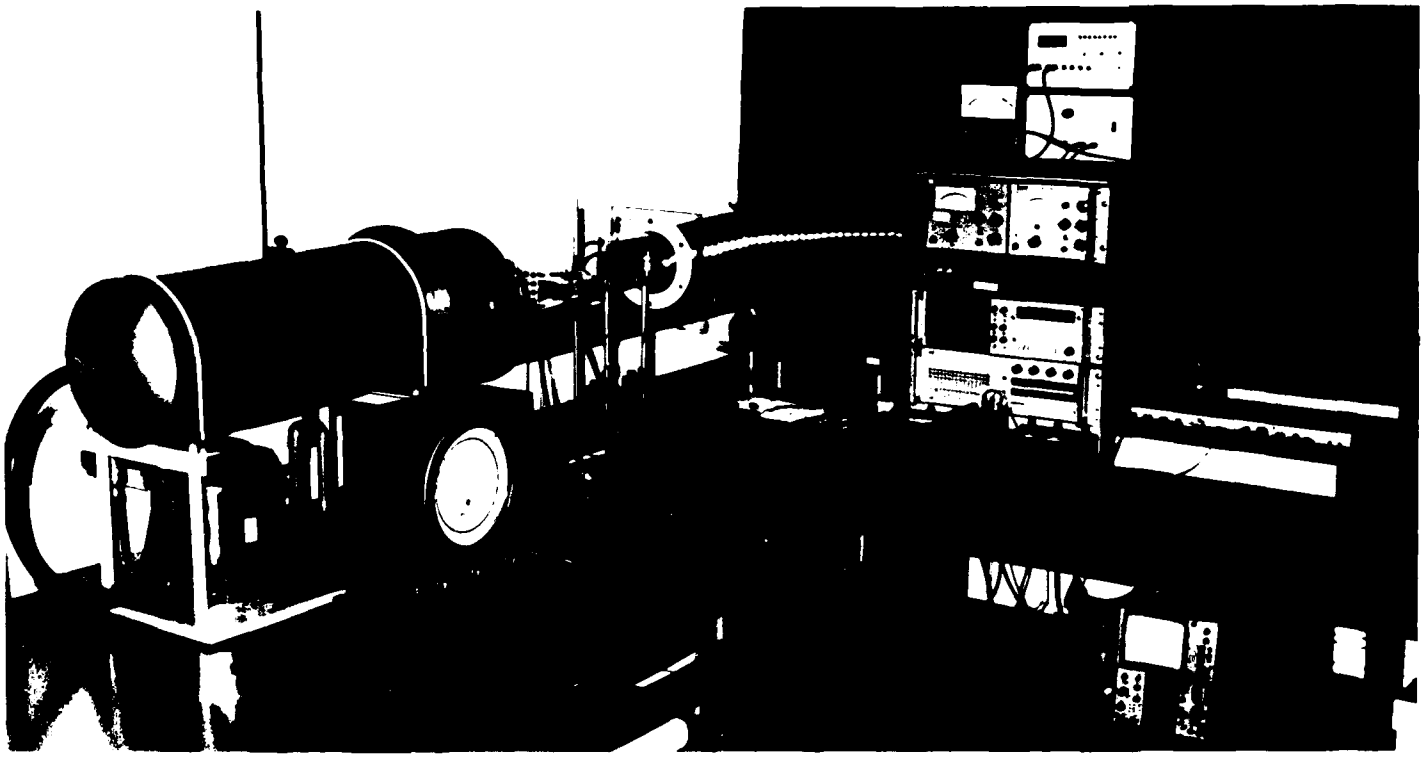

Figure 4.2 Windtunnel System: This photograph shows the essential elements of the wind-tunnel system. The turbulence suppressor tank and a dial manometer can be seen to the left hand side of the photograph, with the prototype balance and exhaust duct in the centre. The spectrum analyser used for the work described in chapters 2 & 3 can be seen in the equipment rack to the right hand side.

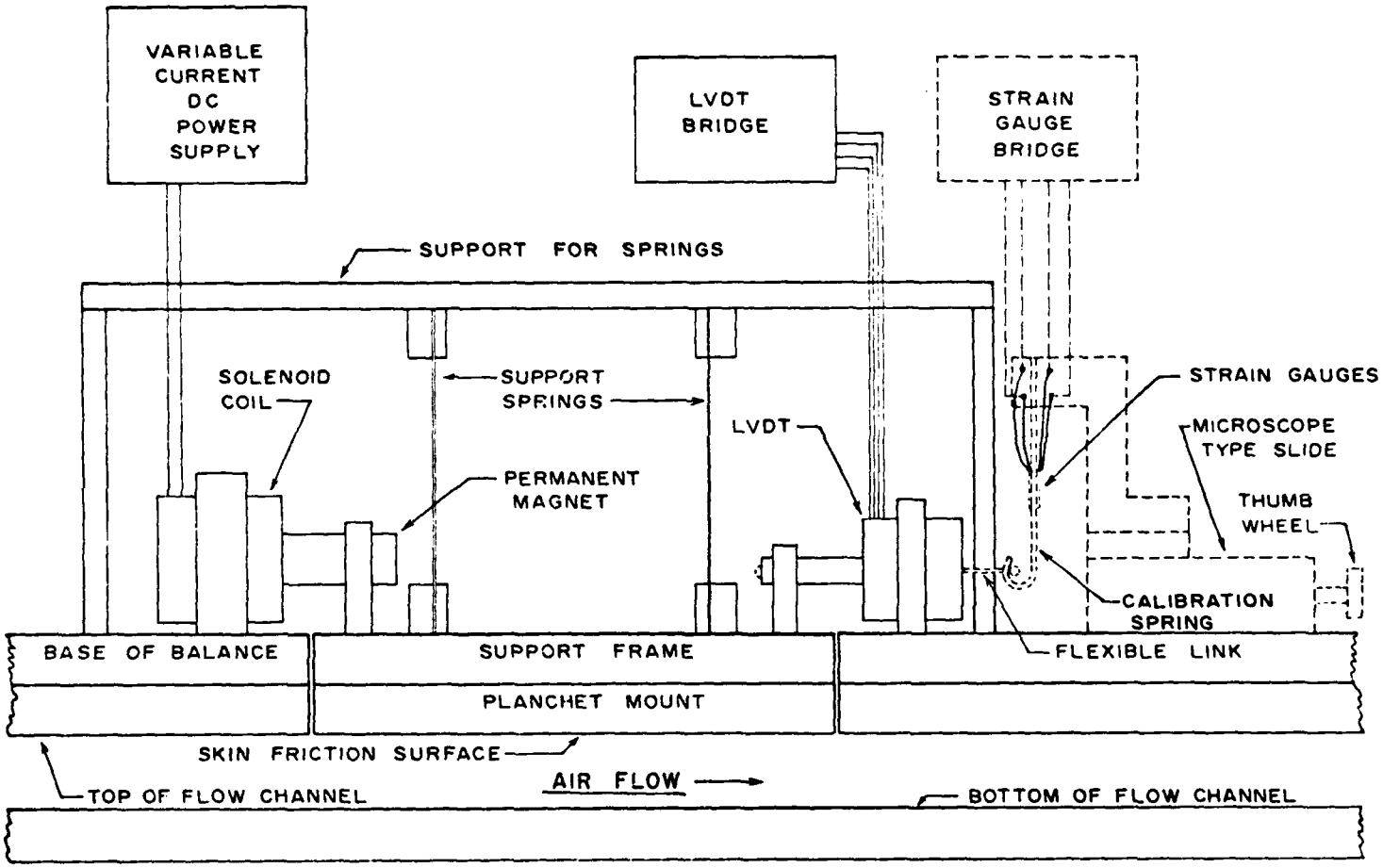

Clark '79

Figure 4-3. SCHEMATIC OF SKIN FRICTION BALANCE.

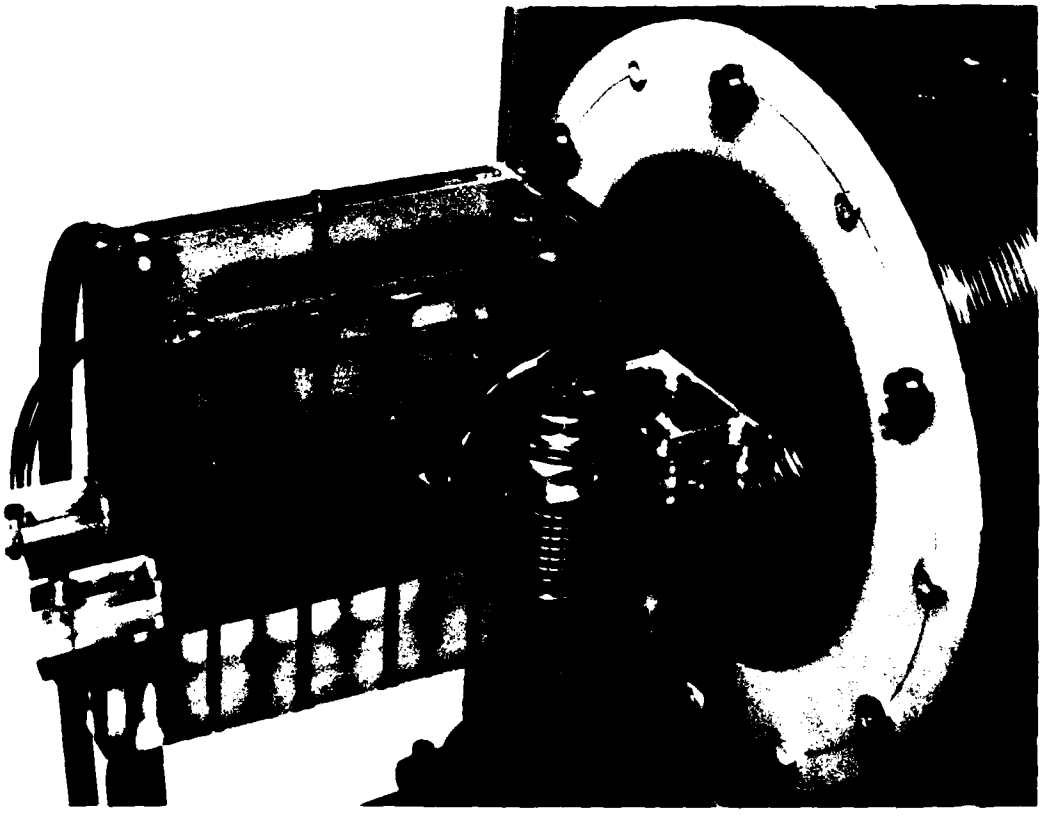

Figure 4.4 Prototype Drag Balance: This photograph shows the prototype drag balance and windtunnel test section. The Invar framework, oil dashpots and support springs can be seen through the perspex housing.

Figure 4·5. Calibration of Strain Gauge Spring.

BEST FIT POWER CURVE: (BRIDGE READING/mV) = 0.534 x (LOAD/g force)$^{0.971}$

$r^2 = 1.000$

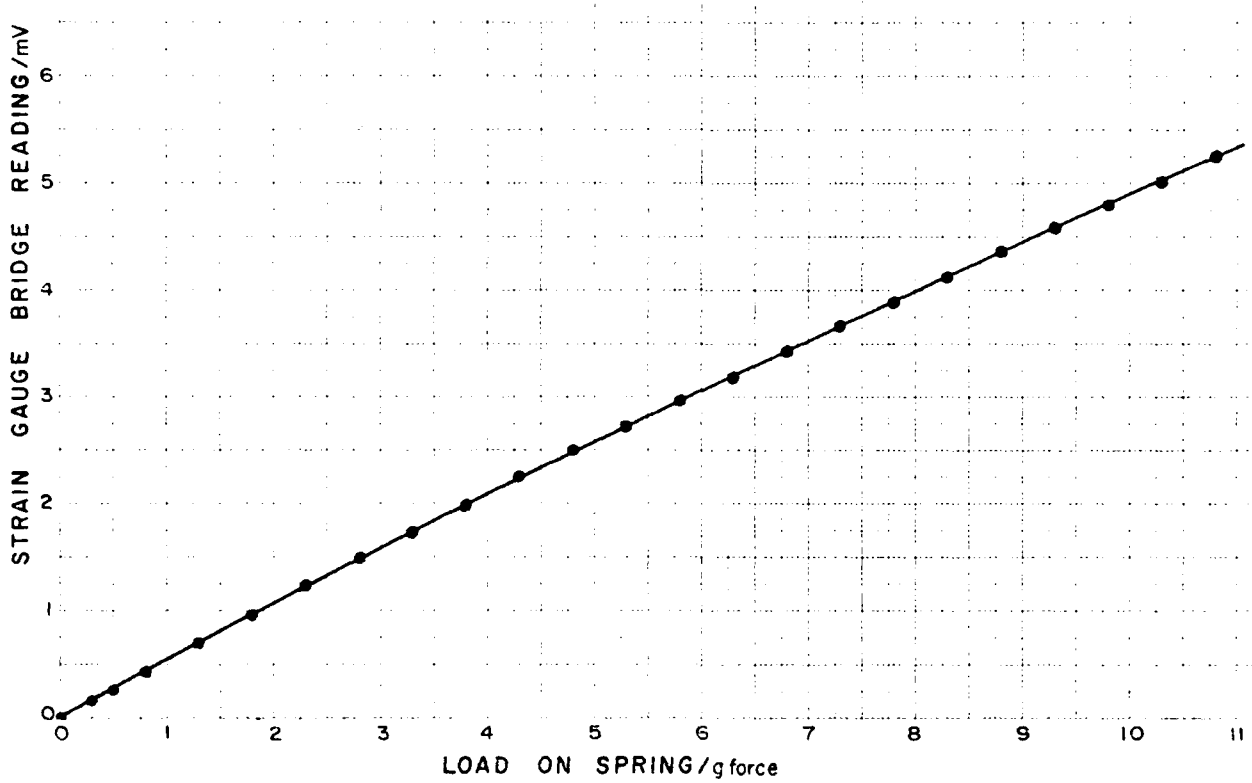

Figure 4·6. Calibration of Balance against Spring.

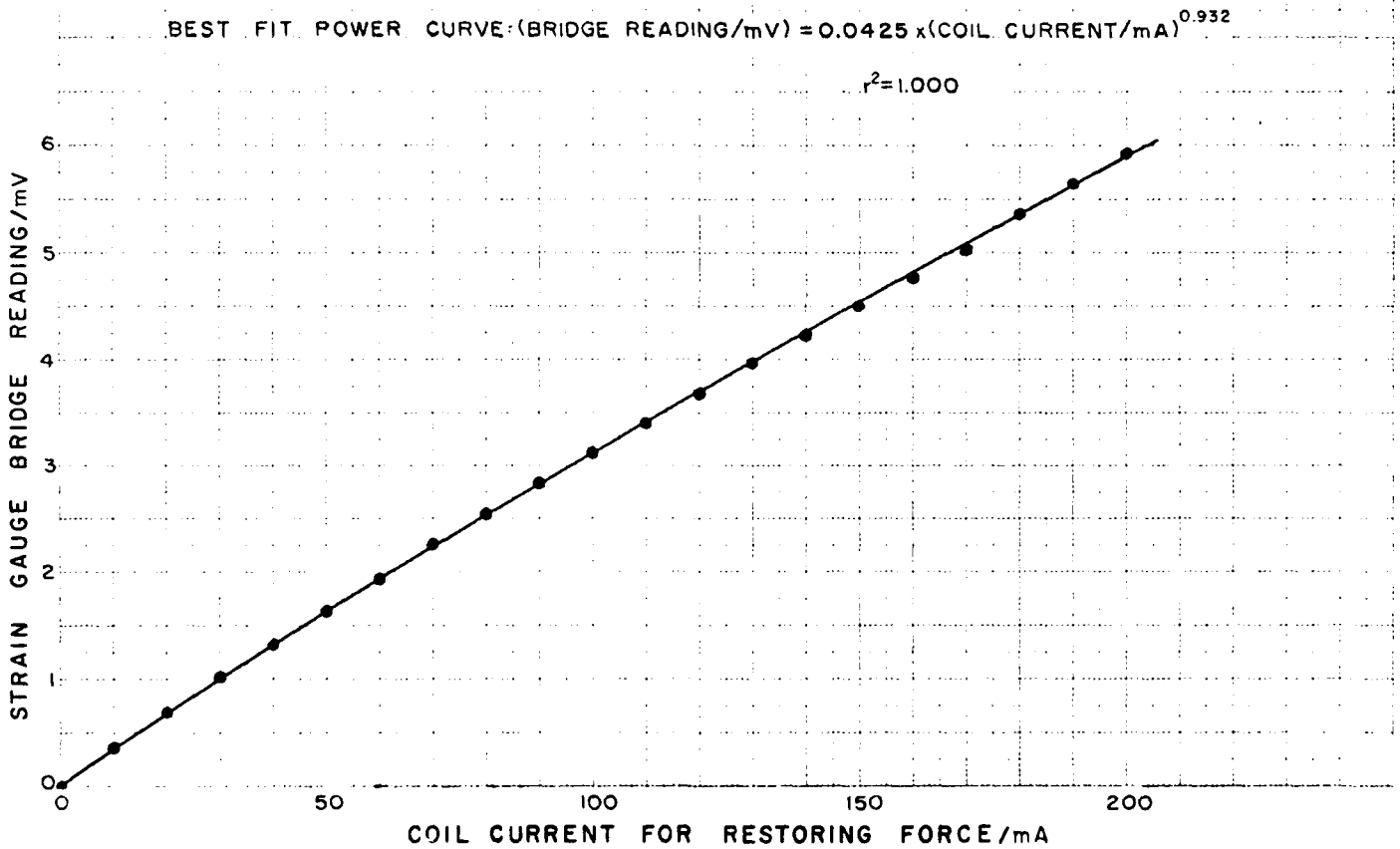

Figure 4·7. Final Calibration of Prototype Balance.

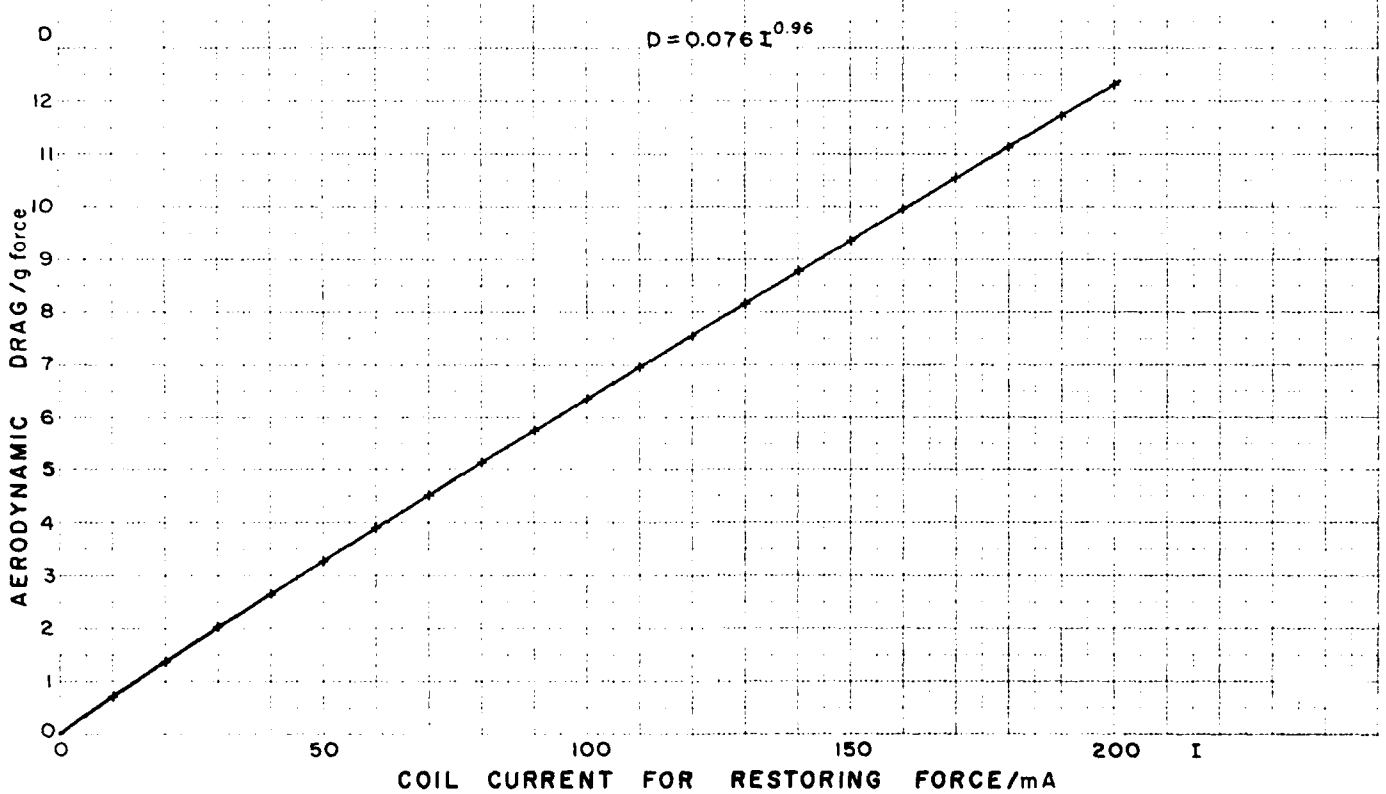

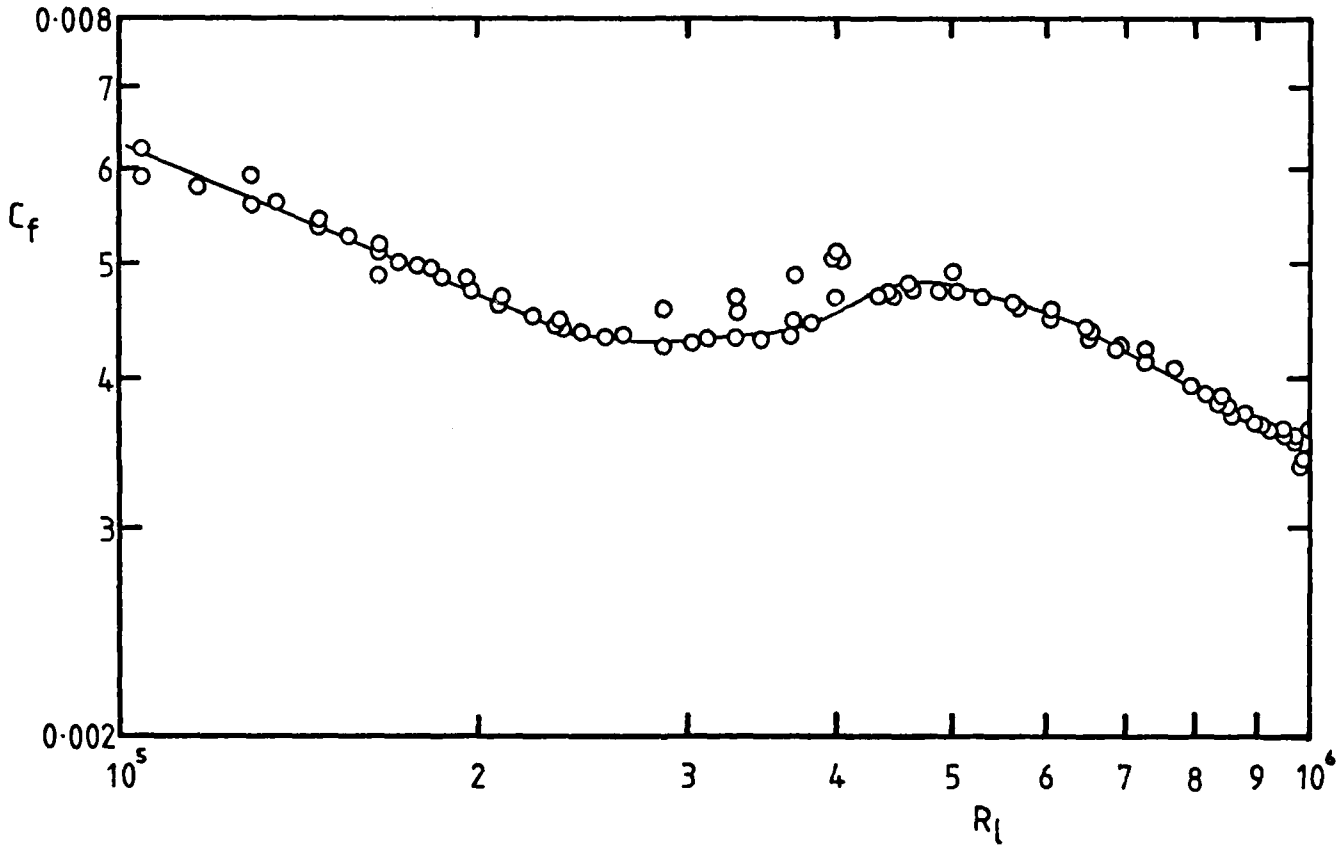

Figure 4·8. Drag Coefficient vs Reynolds Number - Prototype Balance.

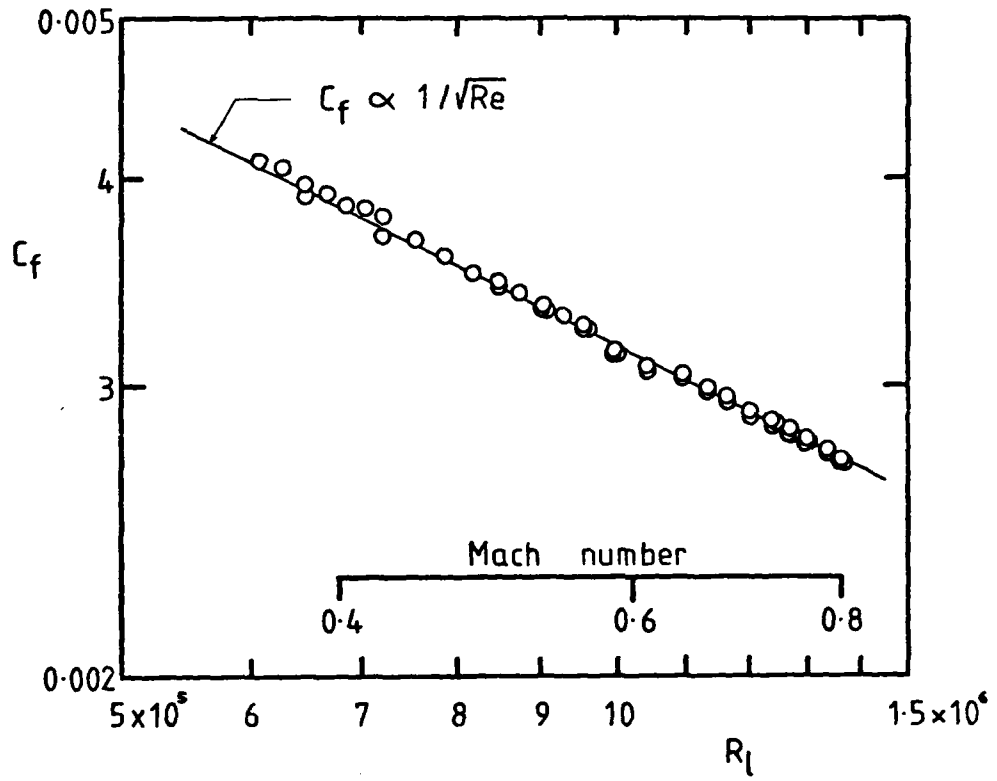

Figure 4·9. C_f vs R_l - Prototype Balance.

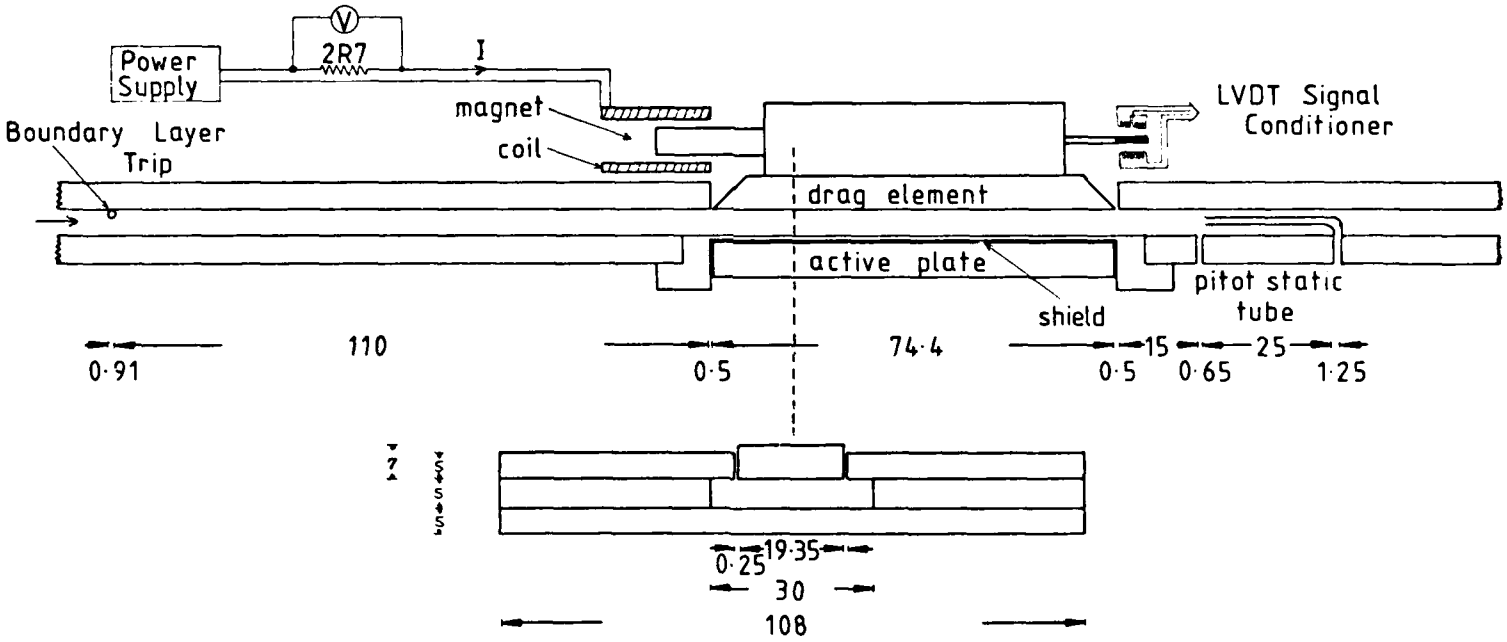

Figure 4·10. Diagram of Windtunnel Test Section.

Dimensions in mm. Details of Suspension and Housing Not Shown.

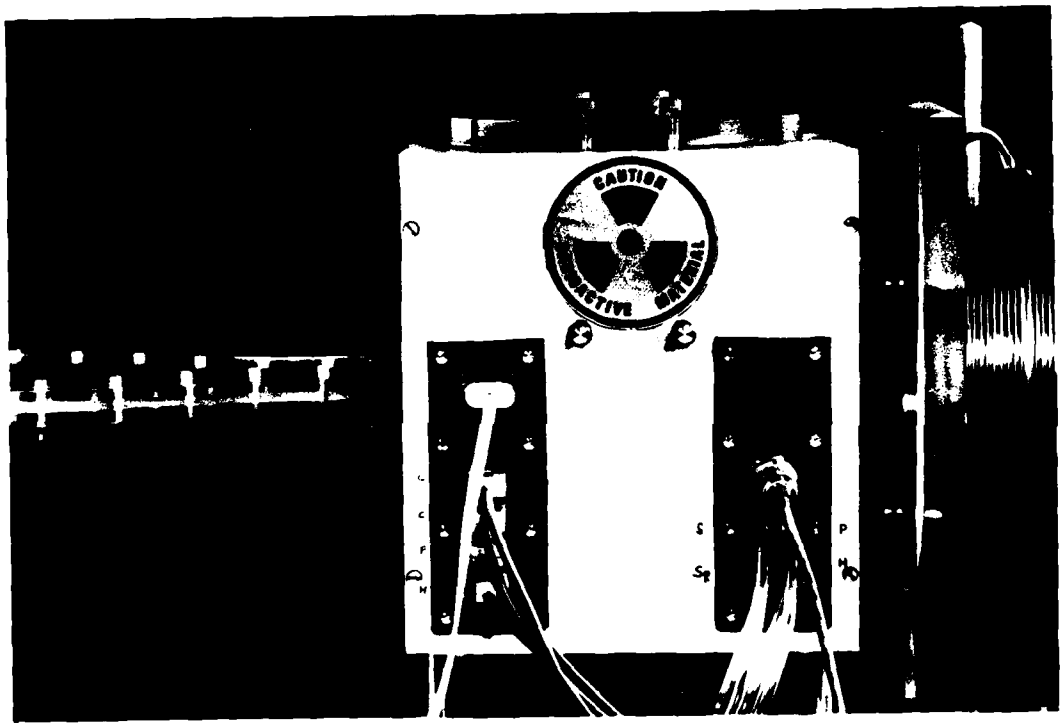

Figure 4.11 Skin Friction Drag Balance: This photograph shows the drag balance in its final form. The panels at the front contain gas tight leadthroughs for the LVDT, coils, pitot tube etc. as well as the LED's of the levelling system. Perspex windows cover portholes for access in both the upper and lower surfaces of the housing. The knurled adjusters visible are attached to the suspension wires and are used to align the drag plate.

Figure 4.12 View from Above of the Drag Balance: This view through the upper porthole shows the perspex test section, supported by dural ribs. The air flow is from the 10 o'clock position to 4 o'clock position. The "H" shaped holder and dashpots can be seen in the centre of the photograph, with the coils and magnets upstream and the LVDT downstream.

Figure 4·13. **DRAG BALANCE CONTROL SYSTEM**

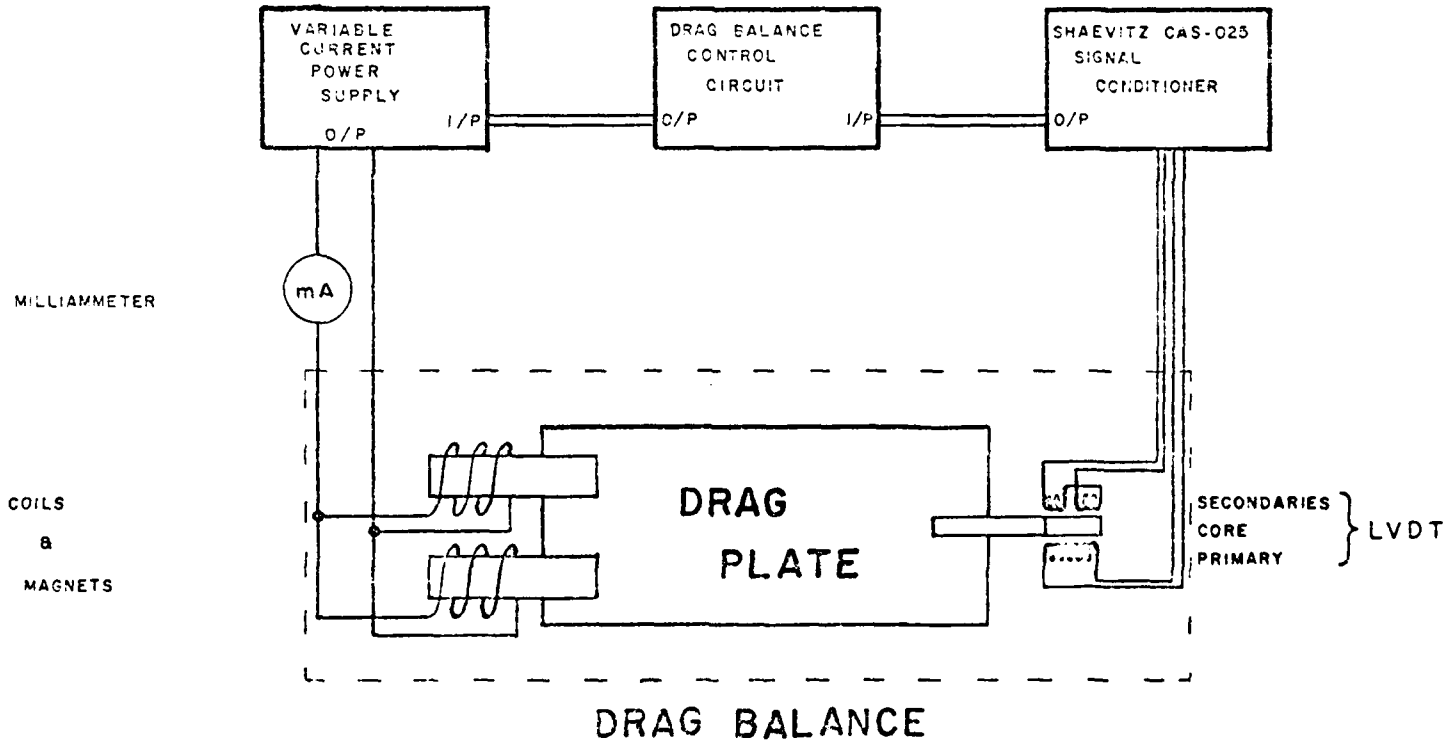

Figure 4-14. SCHEMATIC DIAGRAMS OF CONTROL CIRCUIT AND SIGNAL CONDITIONER

SHAEVITZ CAS-025 SIGNAL CONDITIONER

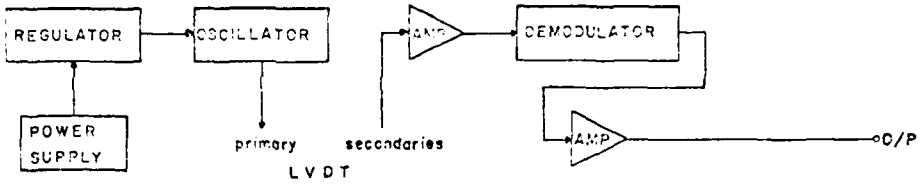

DRAG BALANCE CONTROL CIRCUIT

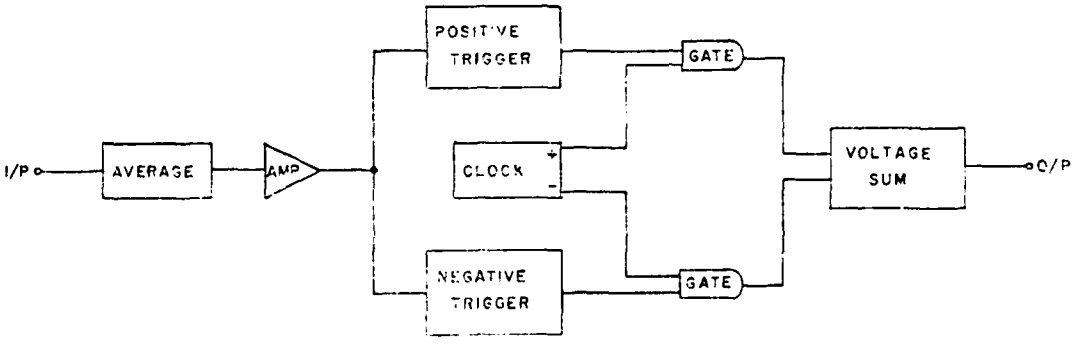

Figure 4·15. DRAG BALANCE CONTROL CIRCUIT

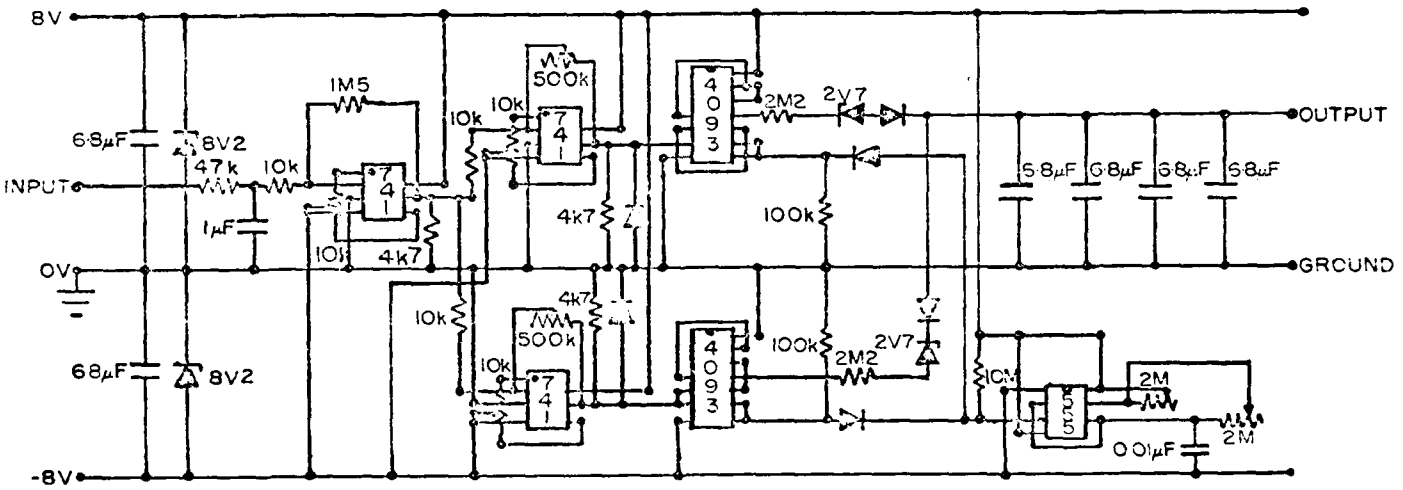

Diodes - IN4148 Capacitors - polycarbonate

Figure 4·16. CONTROL CIRCUIT OUTPUT vs TIME FOR A RANGE OF TRIGGER CONDITIONS

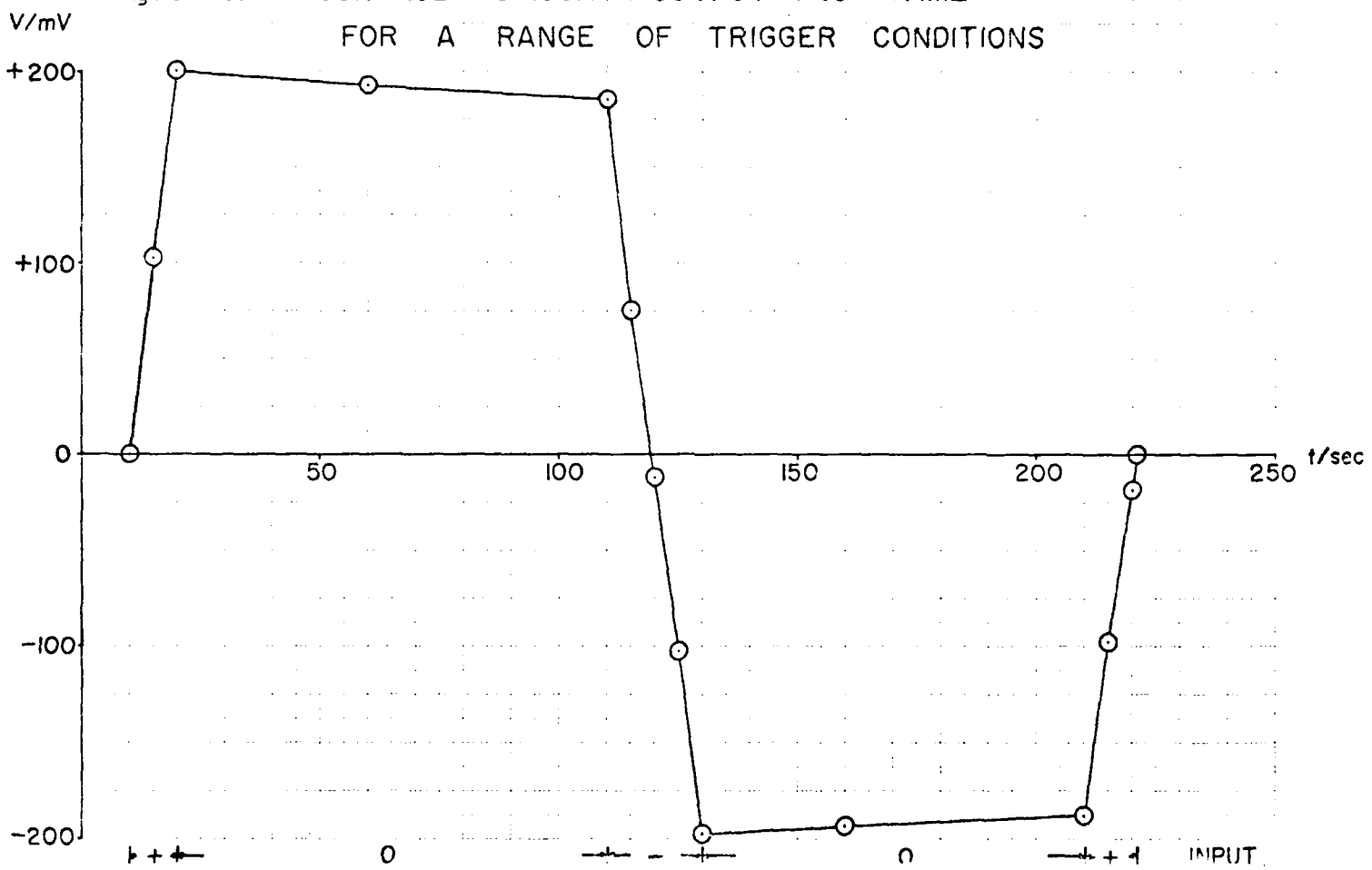

Figure 4·17 PERFORMANCE OF DRAG BALANCE CONTROL SYSTEM

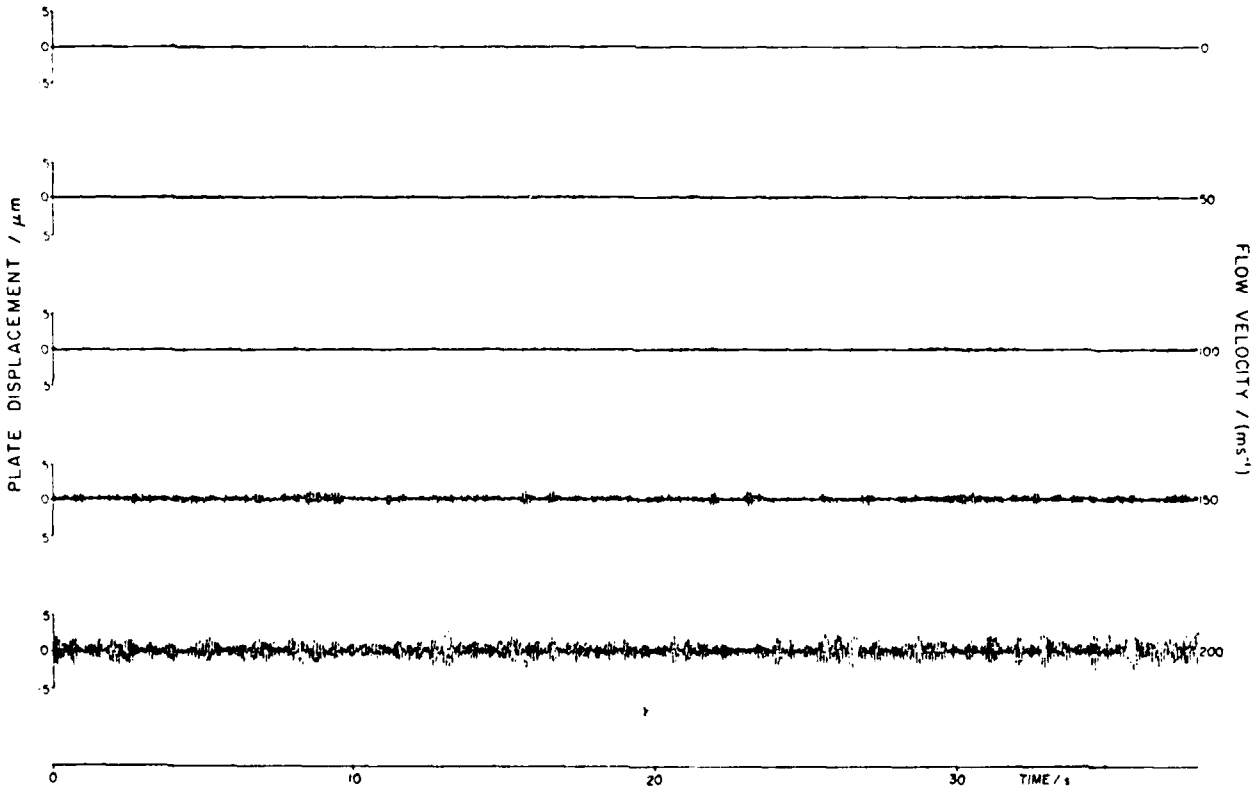

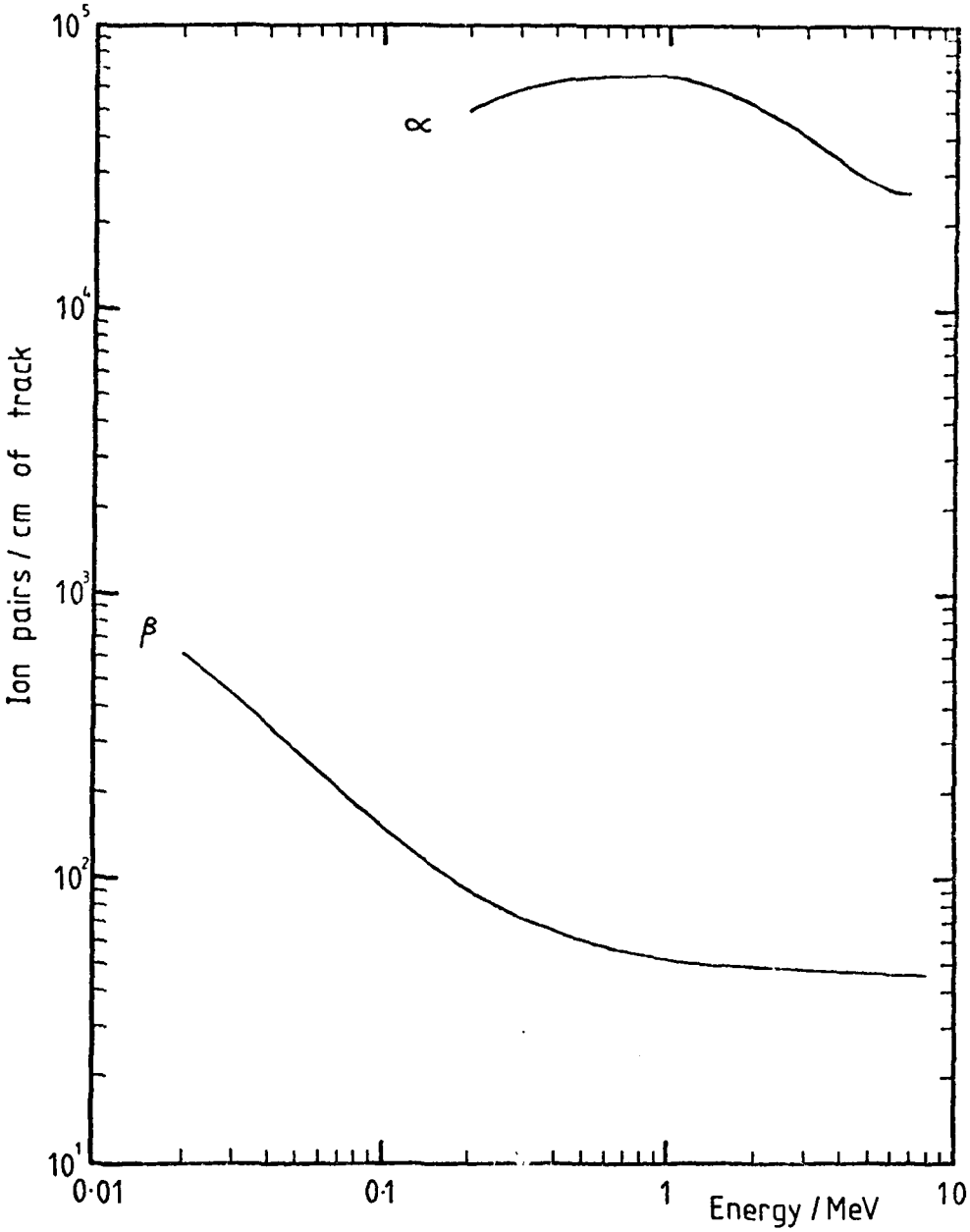

Figure 4·18 . Specific Ionisation of α and β Particles in Air (after Whitehouse & Putnam 1953) .

Figure 4-19 RADIOACTIVE DRAG PLATE CONSTRUCTION

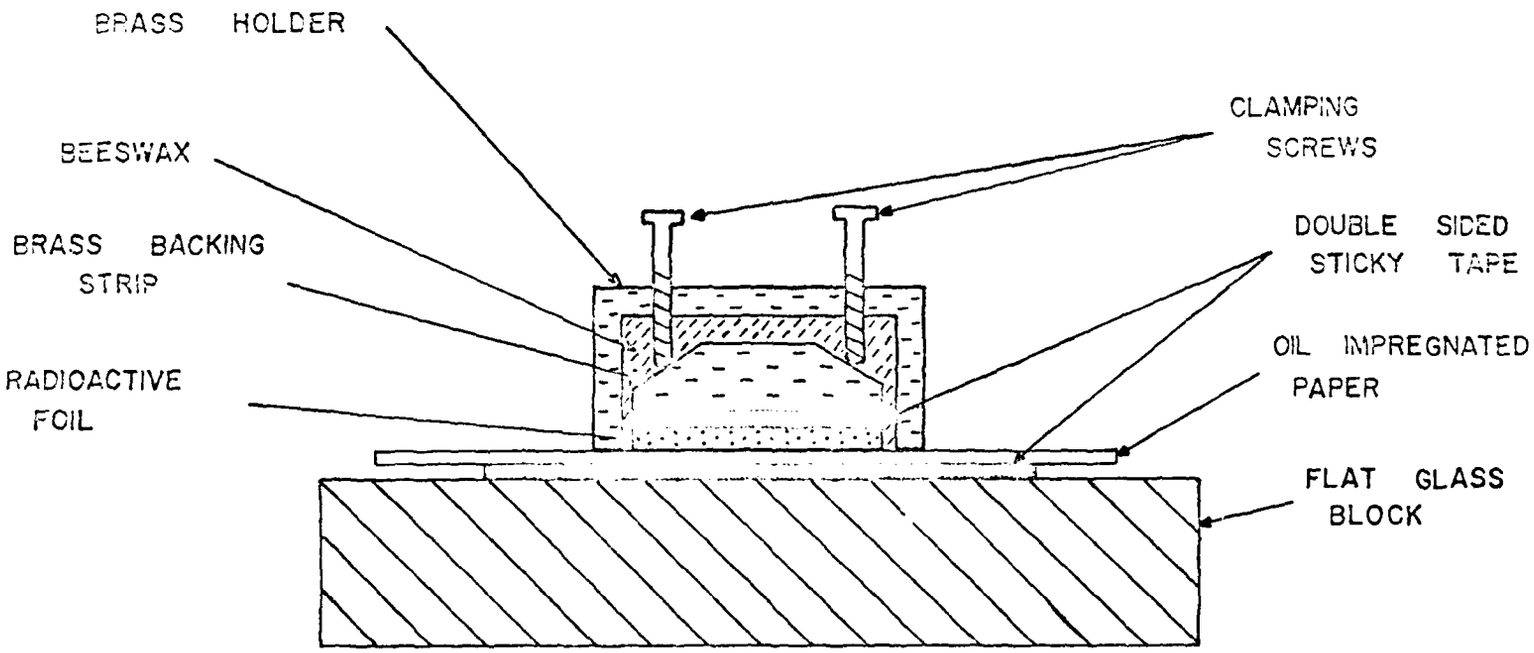

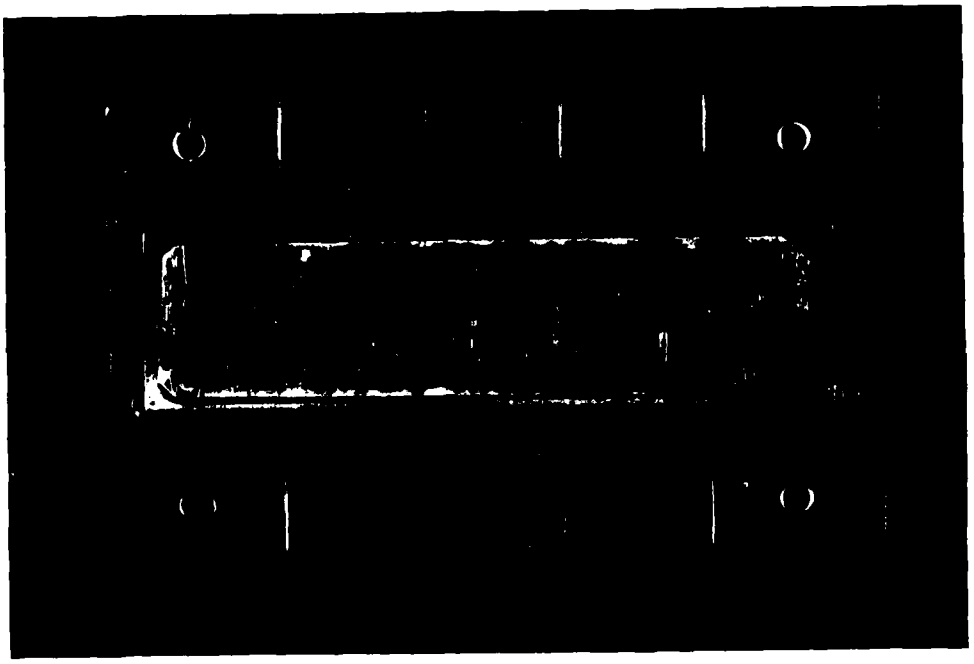

Figure 4.20 Radioactive Plate: This shows a (dummy) radioactive foil mounted into a brass holder. The larger perspex plate holds the radioactive plate in position in the windtunnel. (The surface scratches visible in the photograph are actually quite fine, but have been highlighted by the illumination used for the photograph).

Figure 4·21 DRAG BALANCE CALIBRATION CURVE

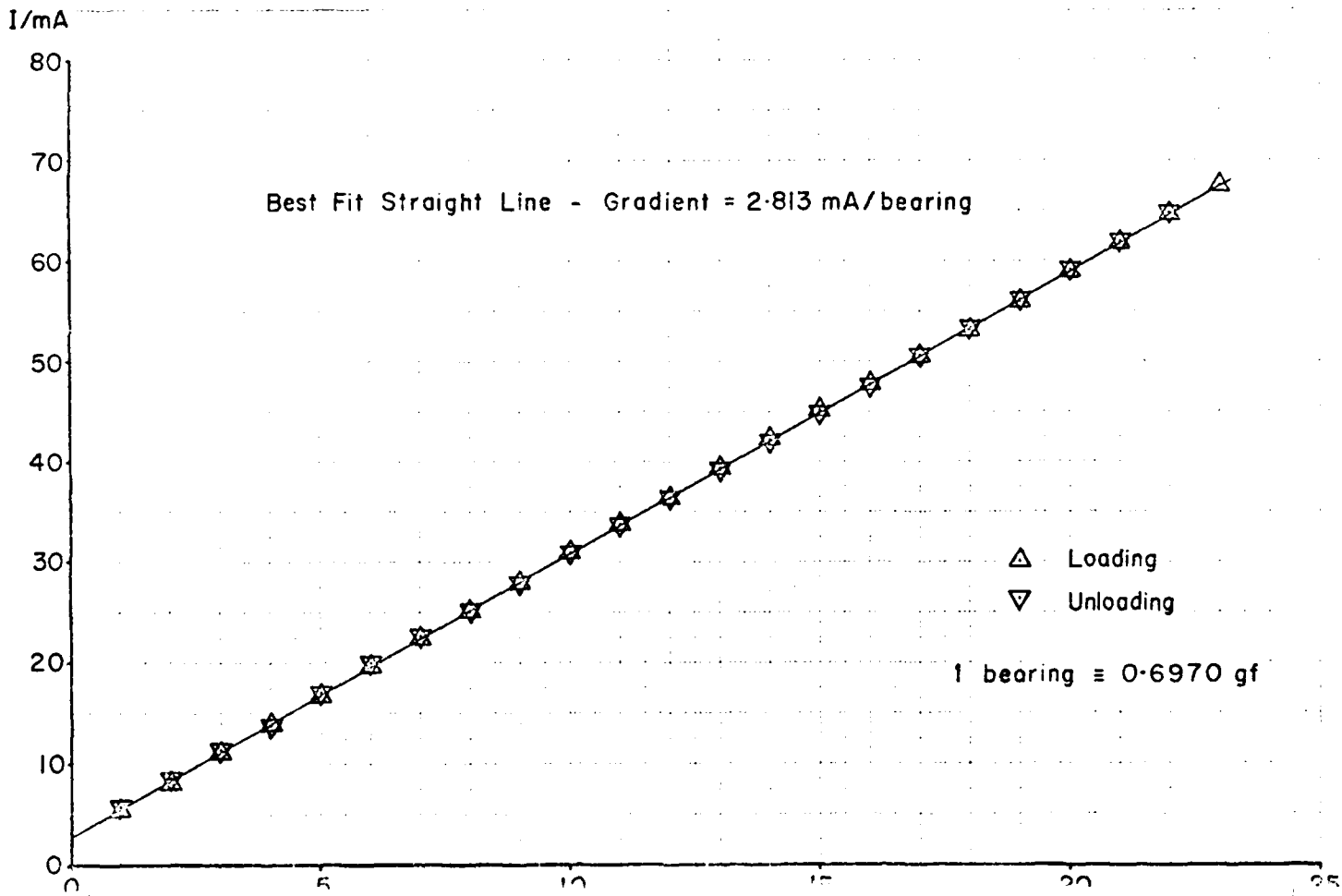

DRAG BALANCE FREQUENCY RESPONSE CURVE

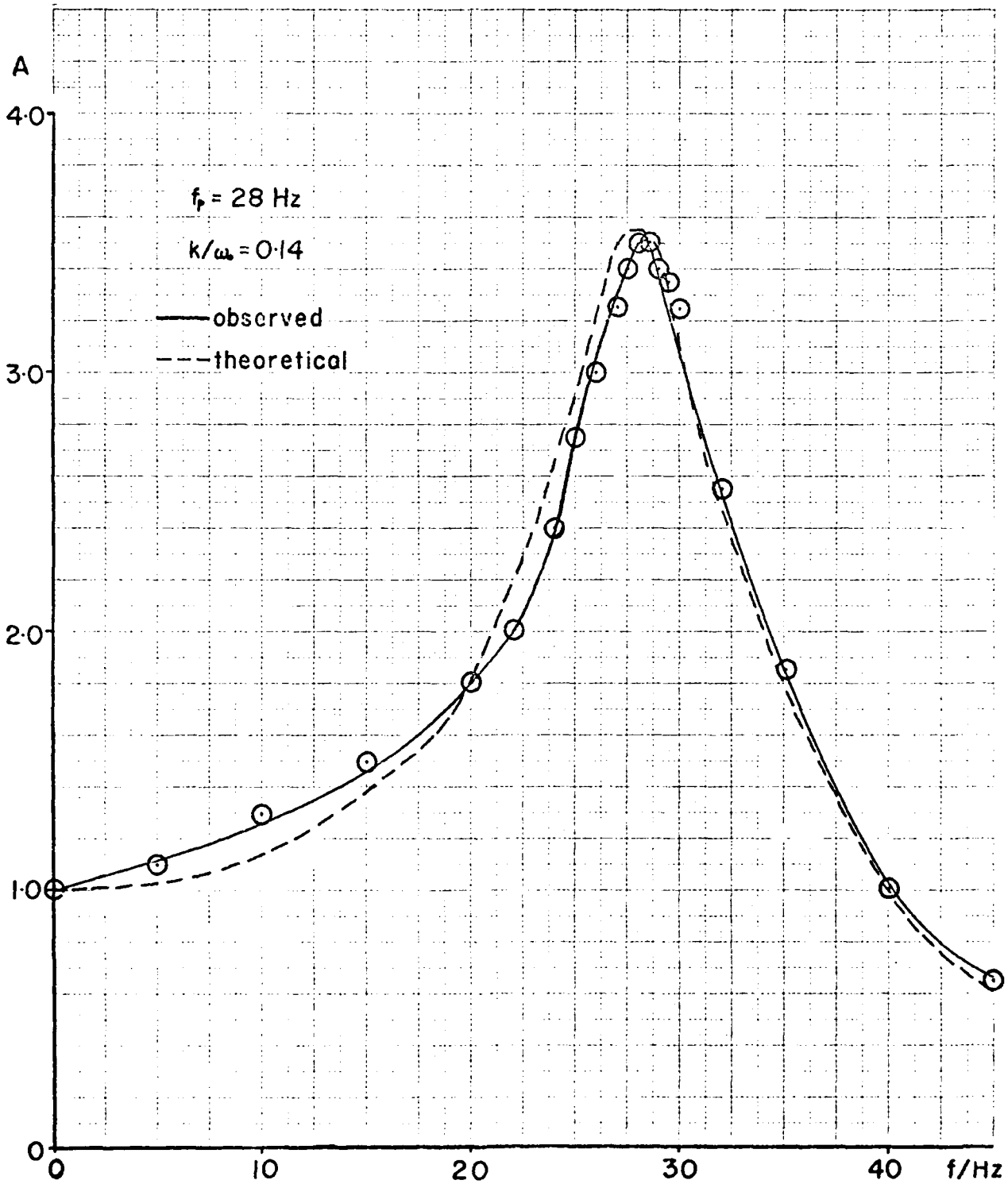

Figure 4·22

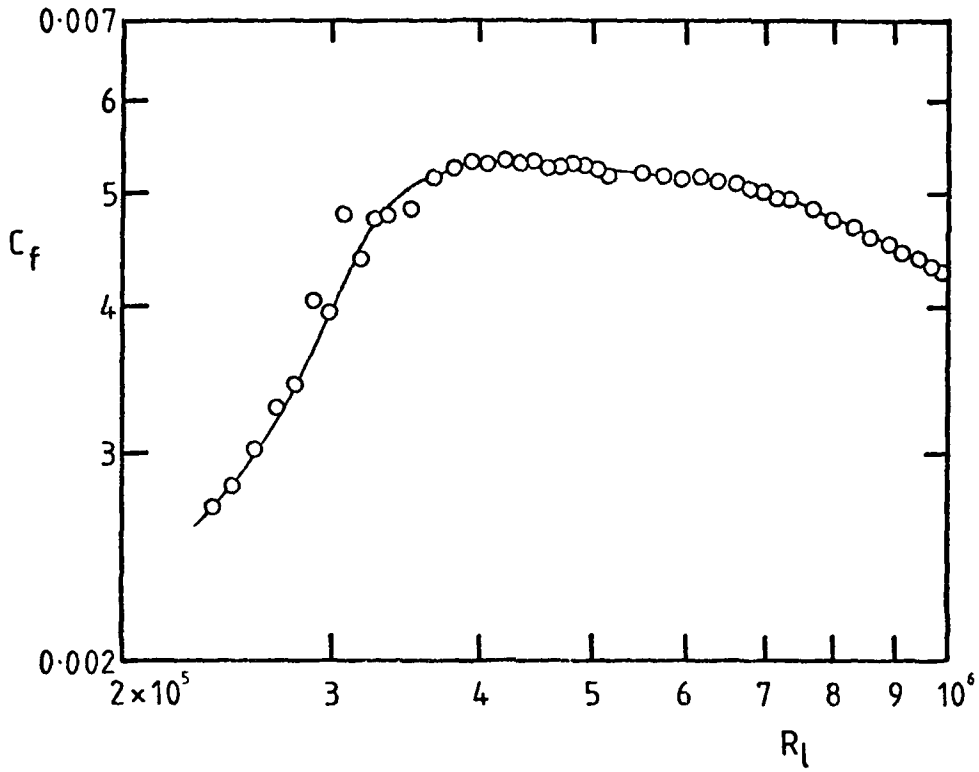

Figure 4·23 . C_f vs R_l - Initial Tests .

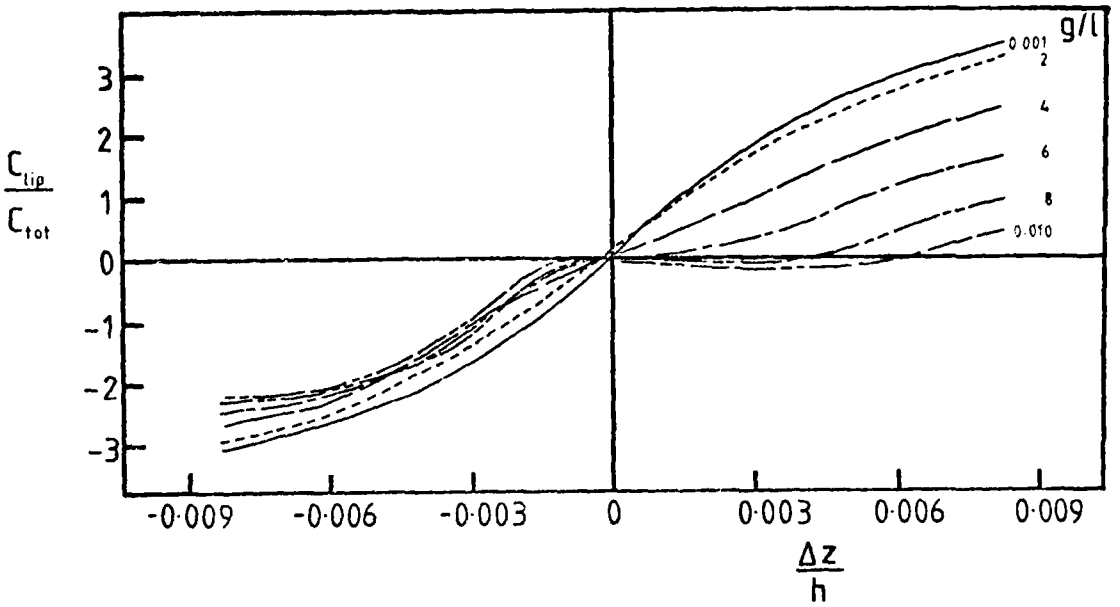

Figure 4·24. Effect of Protrusion and Gap Size on Lip Force (after Allen 1977).

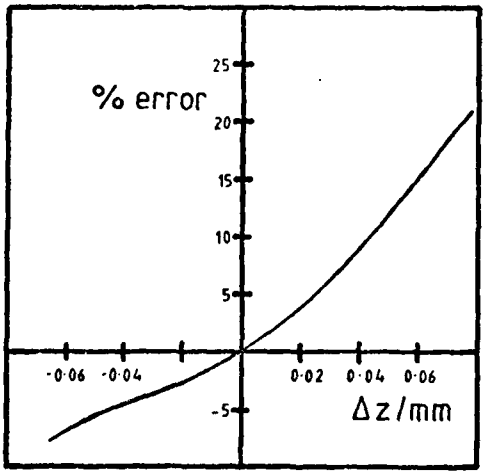

Figure 4·25. Error due to Misalignment (after O'Donnel & Westkaemper 1965)

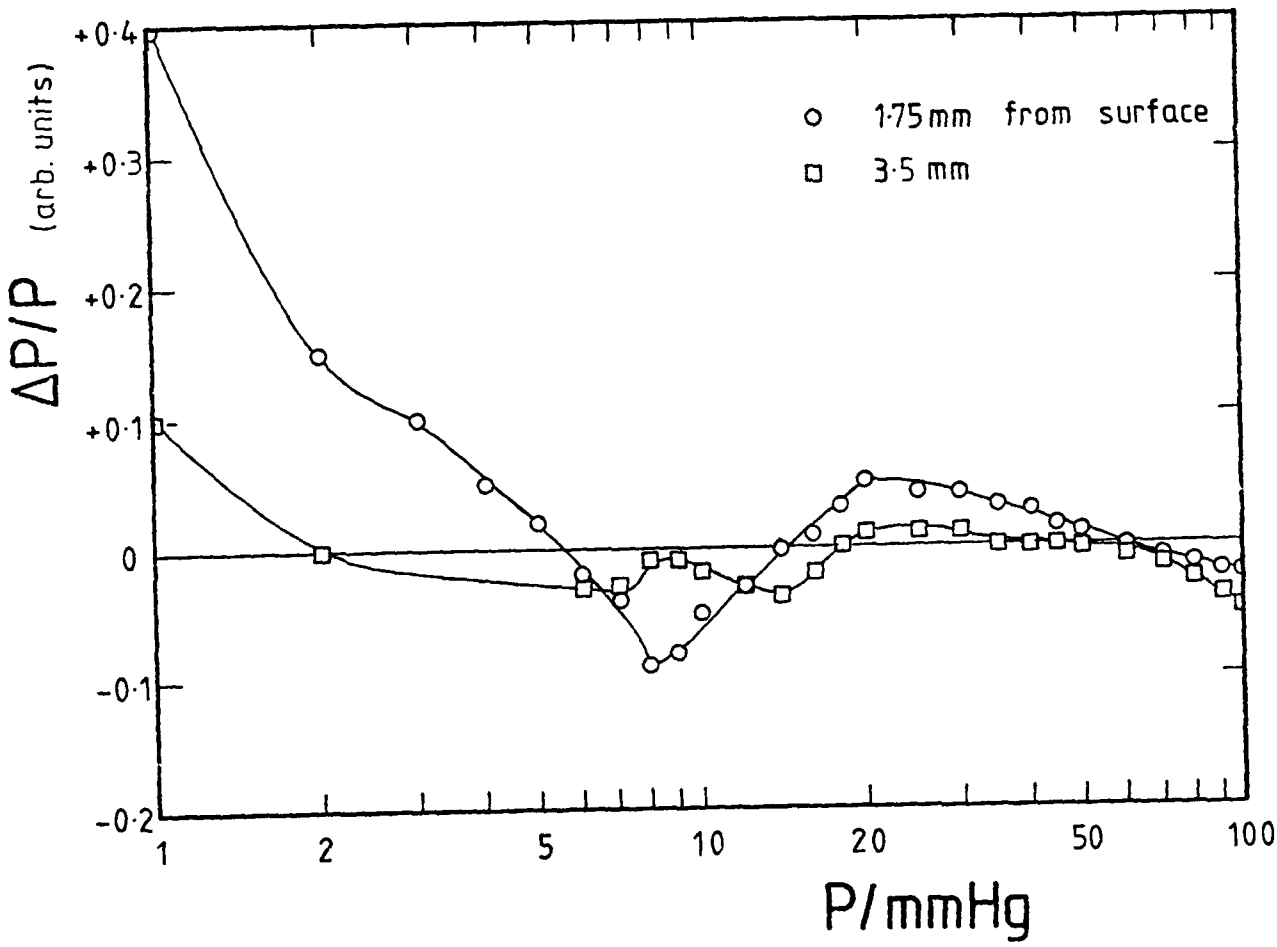

Figure 4·26. Reduced Pressure Difference on Drag Element.

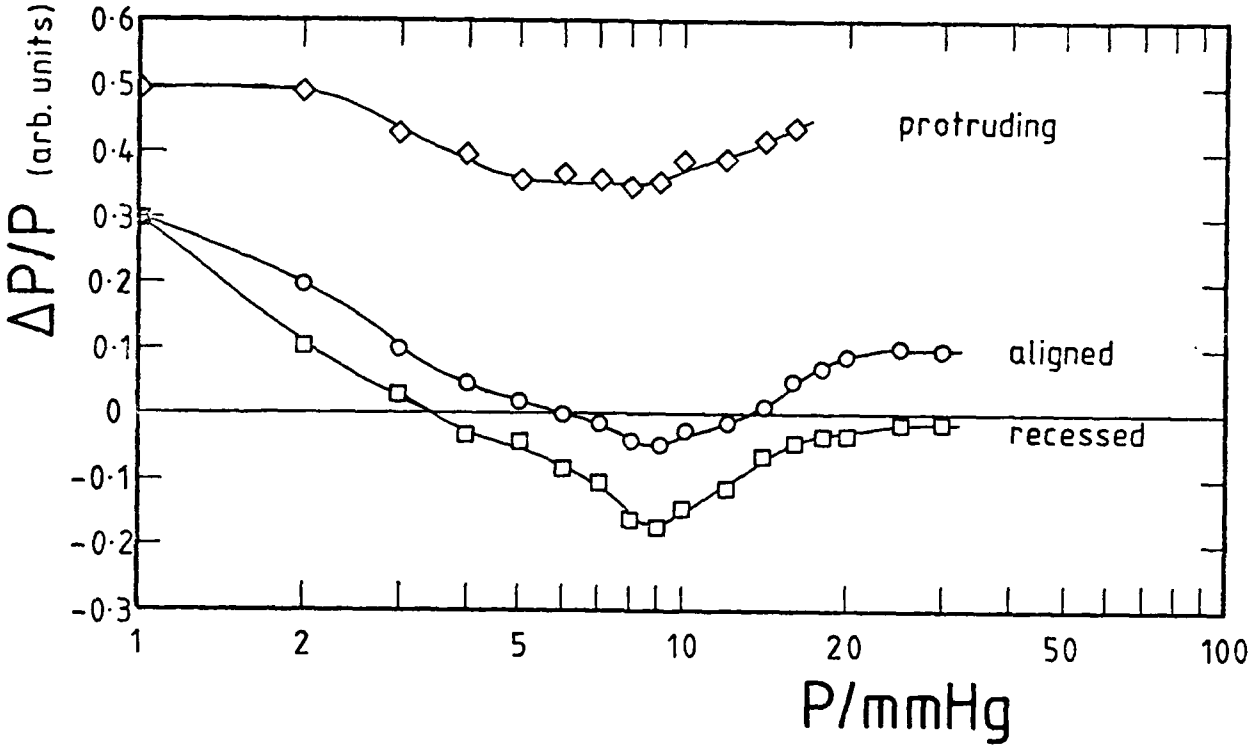

Figure 4·27. Effect of Plate Alignment on Pressure Difference.

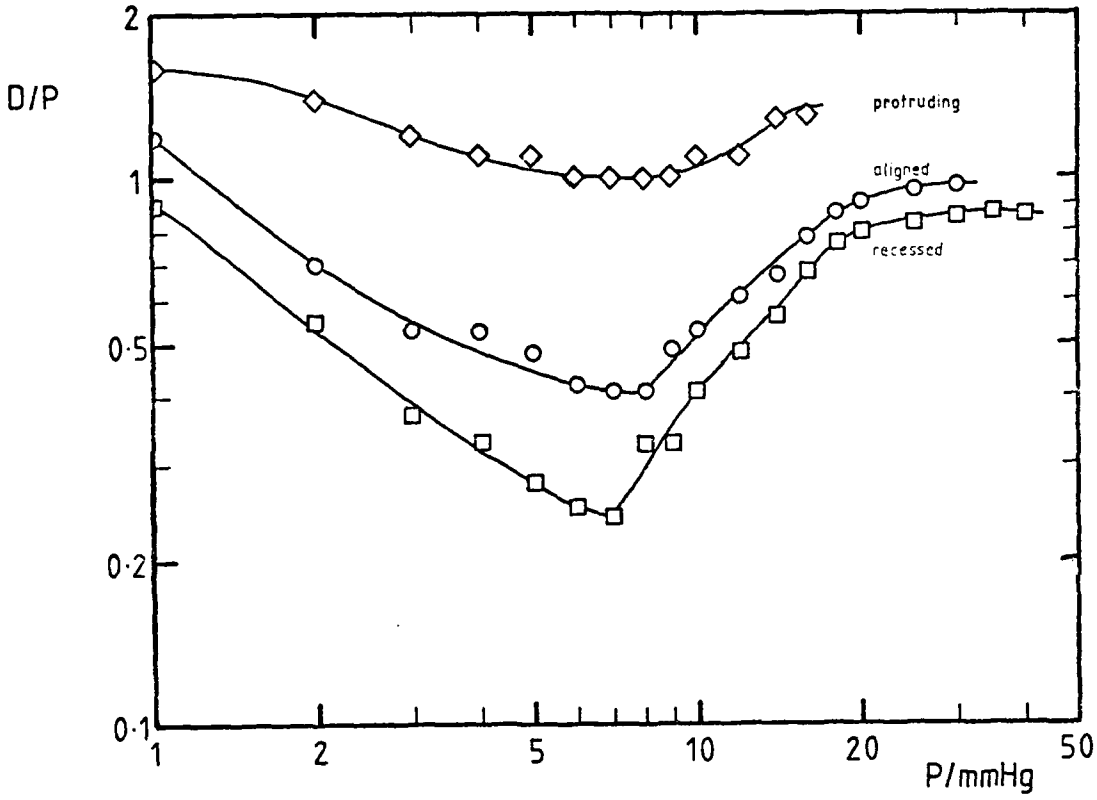

Figure 4·28. Effect of Misalignment on Drag.

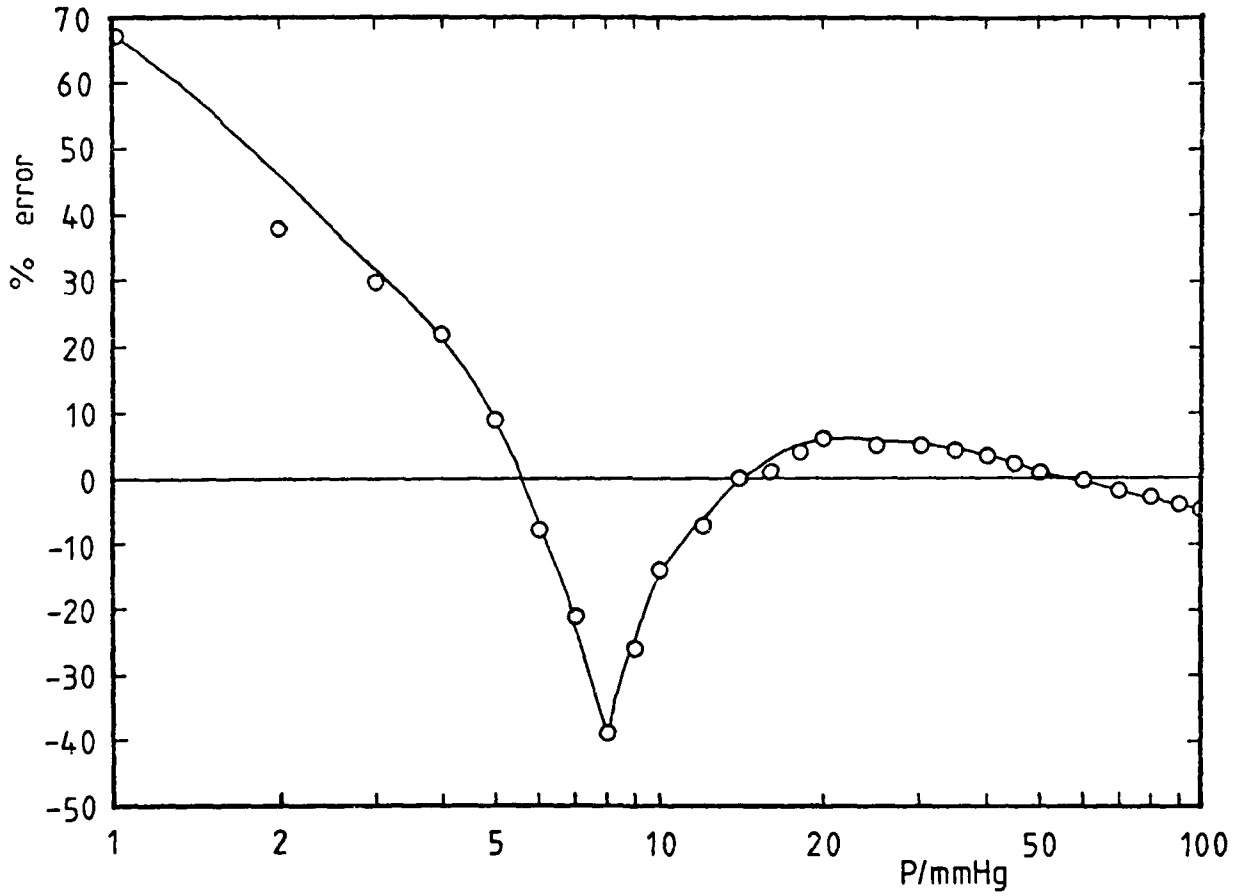

Figure 4·29. Contribution of Pressure Force.

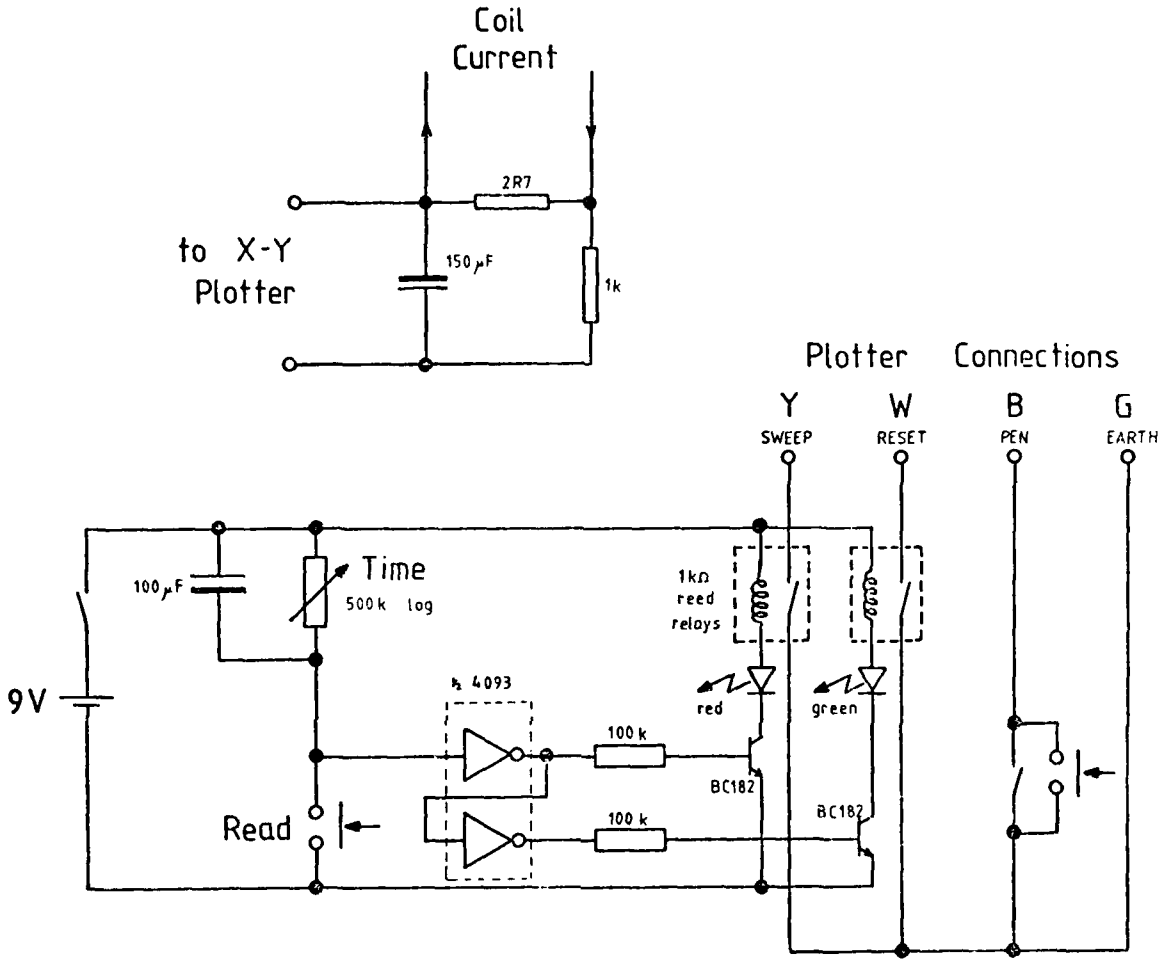

Figure 4·30. Plotter Control Circuit.

ure 4.31 Final Configuration of Windtunnel System: This photograph shows the windtunnel, g balance and instrumentation contained within a dexion framework.

To the left are the pressure gauges, coil power supply, control circuits and DVM. The T signal conditioner and mercury and paraffin manometers are to be found in the centre tion of the framework, with the X-Y plotter in the foreground. In the background, the lead elding of the radioactive working area can be seen.

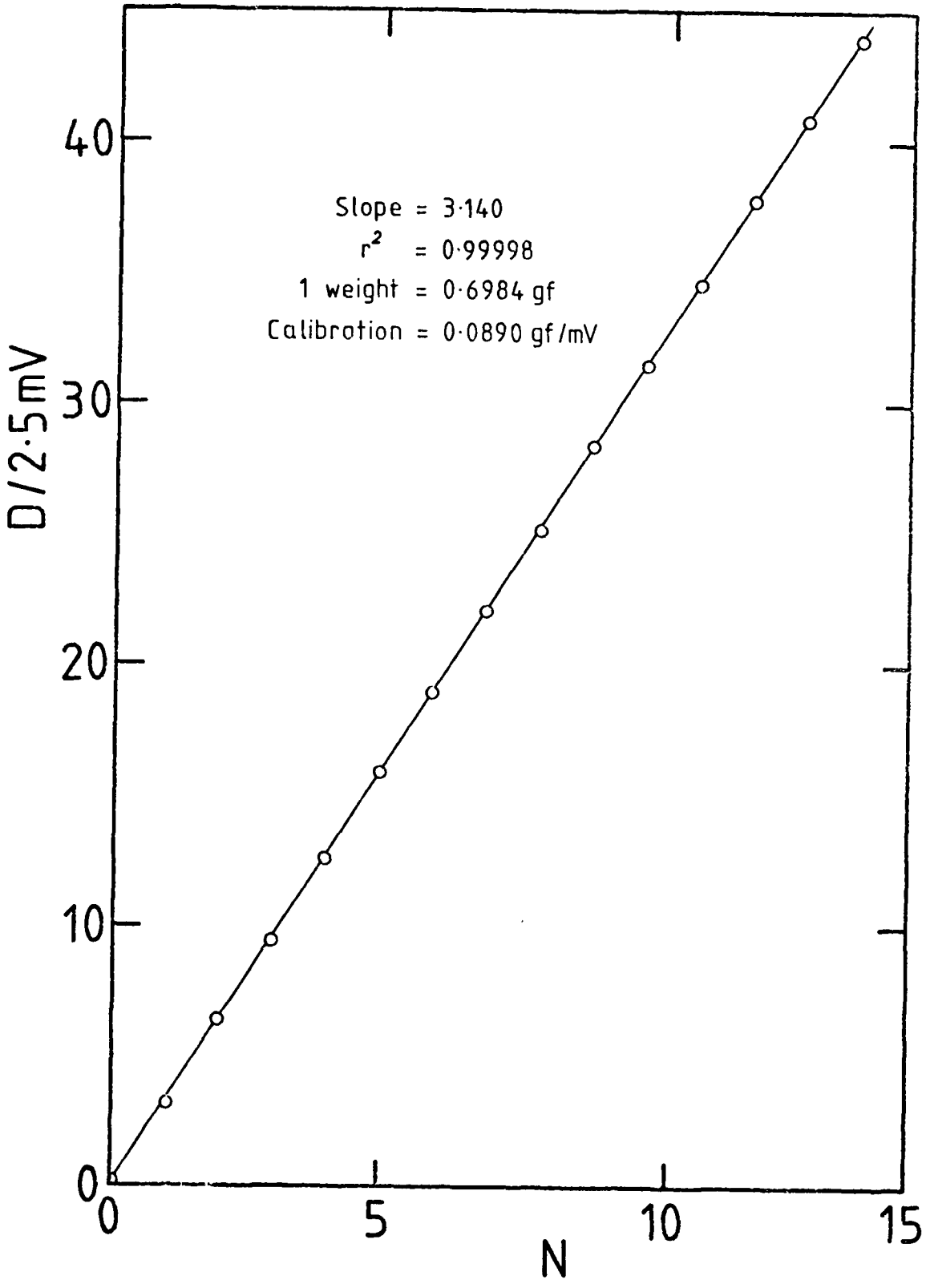

Figure 4·32. Typical Calibration Curve (null position mode).

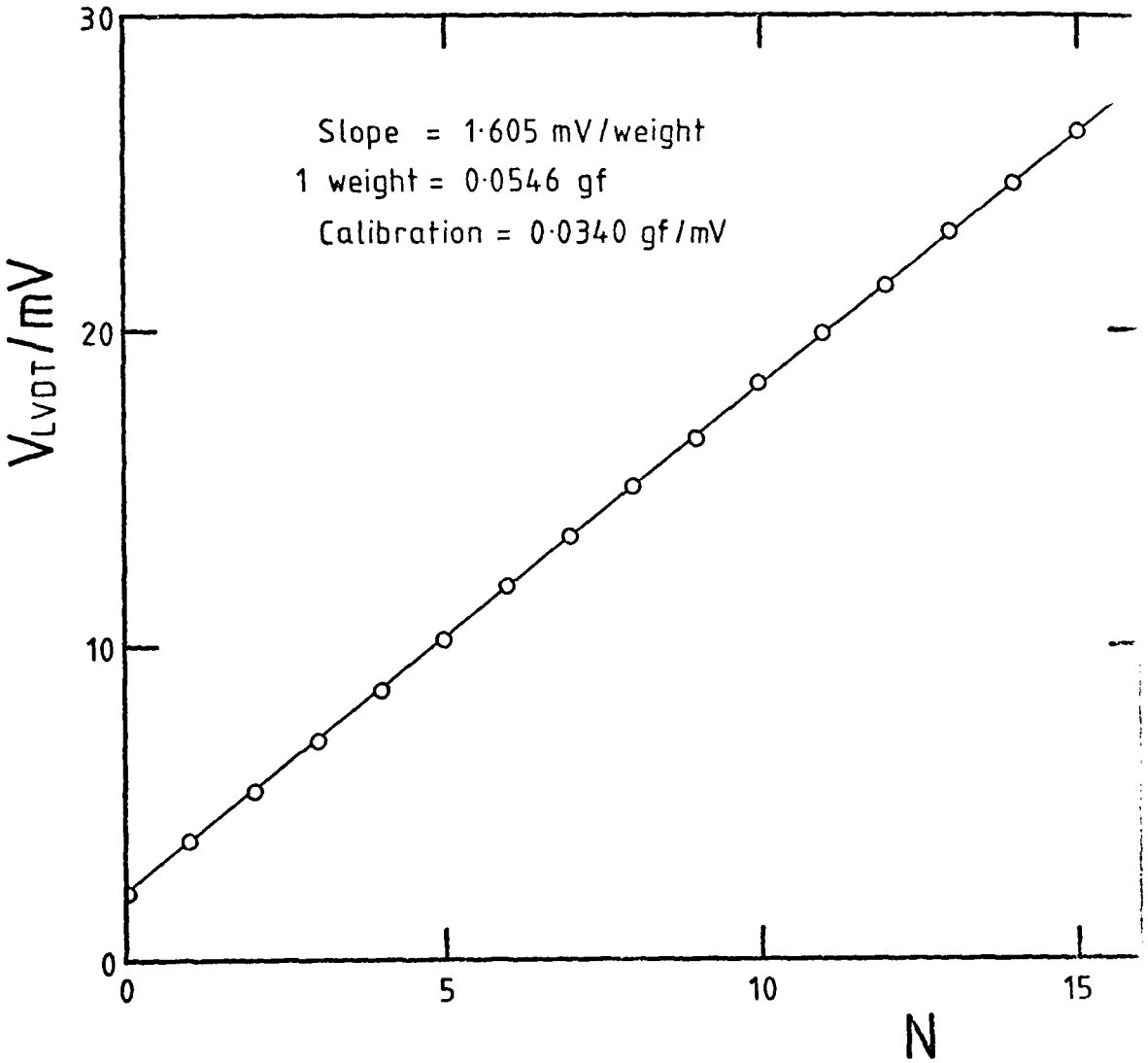

Figure 4·33. Typical Calibration Curve (deflection mode).

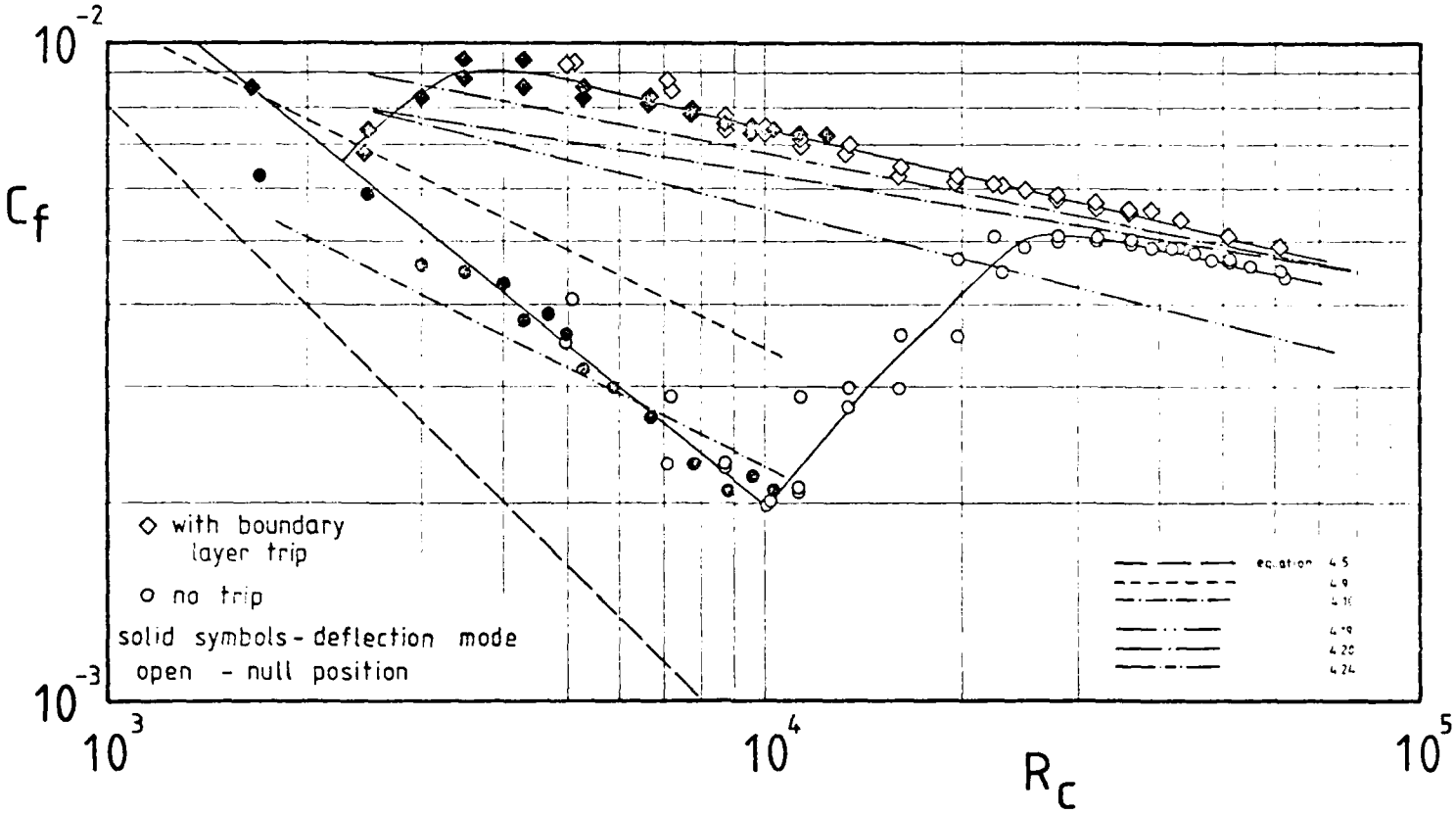

Figure 4·34. Drag Coefficient vs Reynolds Number.

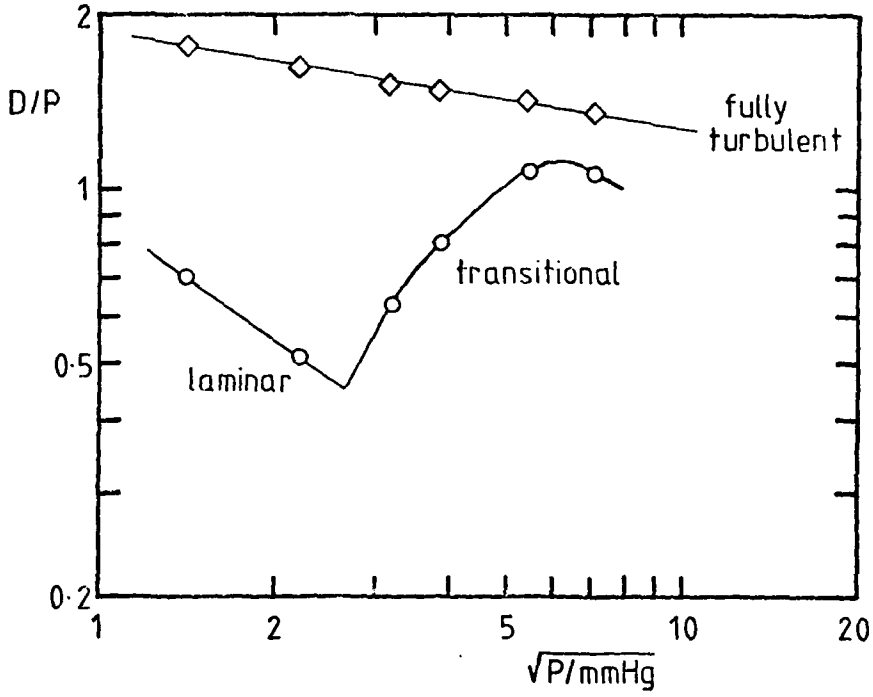

Figure 4·35 . Drag Curves for Irradiation Experiments (perspex shield).

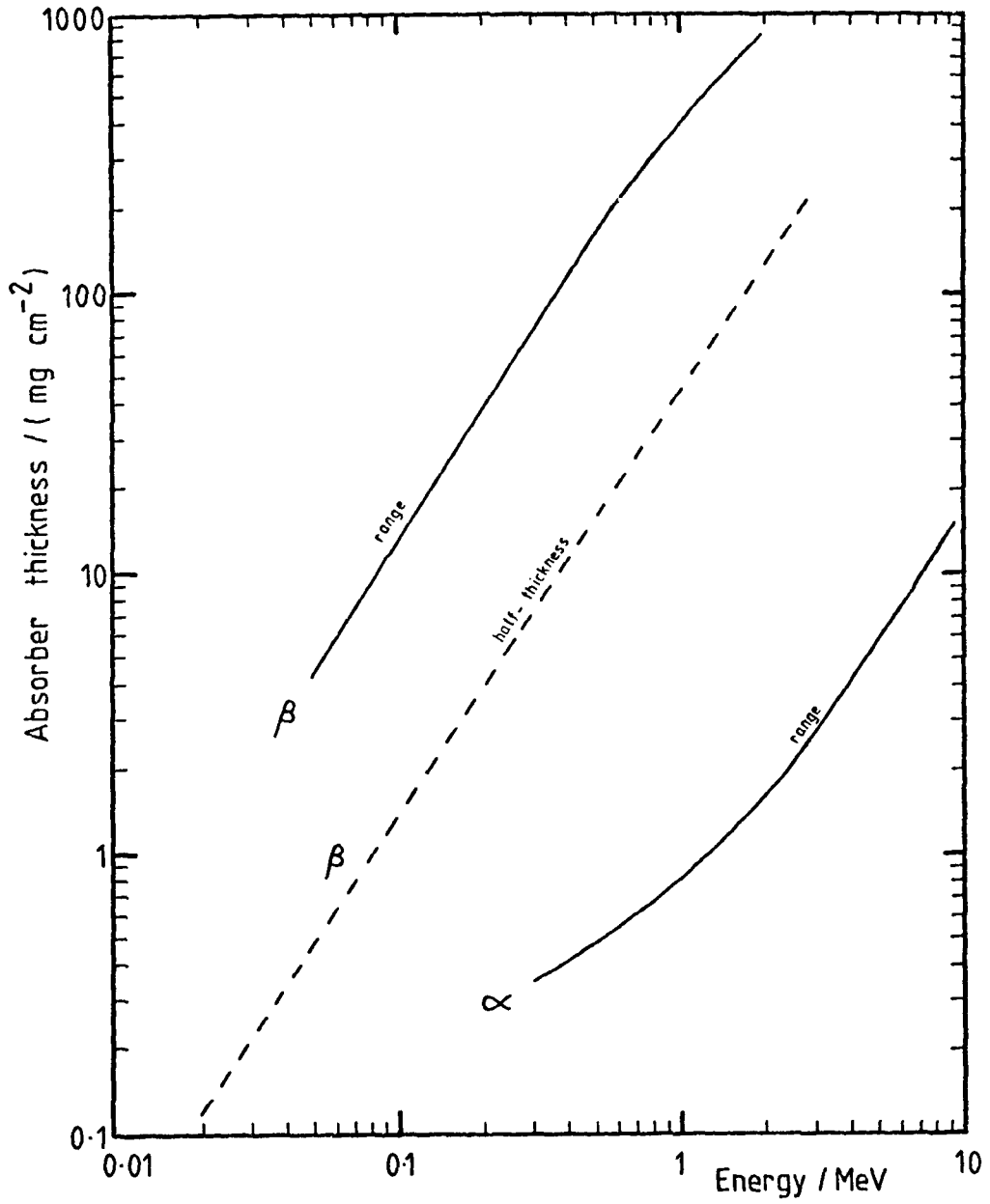

Figure 4·36. Approximate Range - Energy Curves for α and β Particles (derived from Whitehouse & Putman 1953).

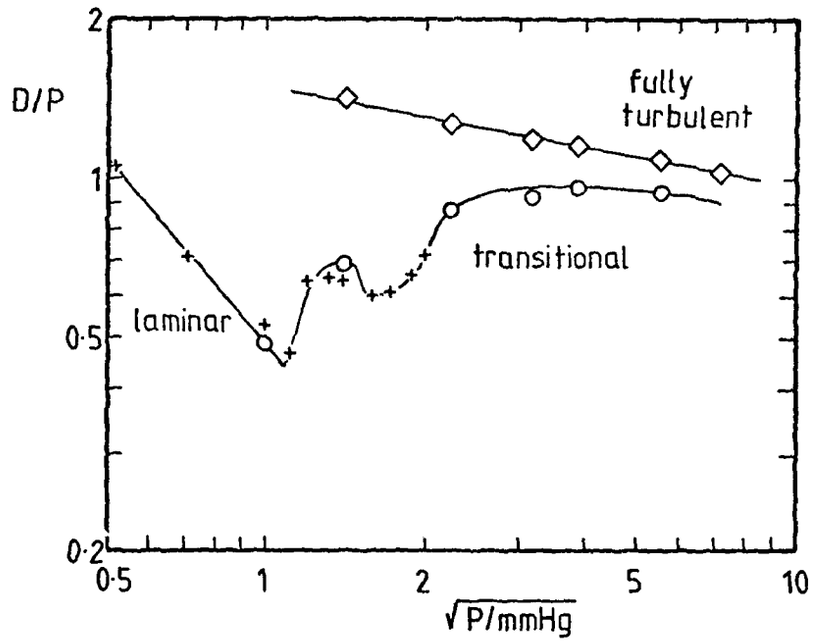

Figure 4·37 . Drag Curves for Irradiation Experiments (aluminium shield) .

TORSION DISC VISCOMETER MEASUREMENTS

5.1 Introduction

The work described in chapter 4 shows that, with the radiation levels used, irradiation has no effect on aerodynamic skin friction drag at atmospheric pressure. It was obviously desirable to try and investigate the effect of irradiation on viscosity (or, equivalently, low speed laminar skin friction drag) at atmospheric and reduced pressure in order to see if any significant changes could be induced, and to repeat those experiments of Kestin and Shah which gave large changes in viscosity. Their results for low pressure air were of particular interest, from the point of view of potential applications to high altitude flight.

The accurate measurements of viscosity has long been a prominent problem, often not so much because of an intrinsic interest in the viscosity, but because of its involvement in the determination of other important physical constants. A good example is Millikan's classic oil drop experiment, in which the largest error in the calculated value of the electronic charge derived from an incorrect value for the viscosity of air (see Millikan 1947).

Typically, measurements of gas viscosity are made either by transpiration measurements on gases flowing through fine capillaries, following the very early work of Graham (1846, 1849), or by measurements of the viscous torque on a driven or freely damped moving surface. Transpiration measurements can have drawbacks, since the pressure gradients may not be constant near the ends of the tube, and with very fine capillaries, or at reduced pressures, errors due to mean free path or Knundsen effects may arise.

Torsion pendula have a long, if not always distinguished, history with regard to the measurement of viscosity. It is easy to show that they are capable of very high apparent precision, but due to inadequate theoretical expressions for the motion of the gas, there can be extremely large systematic errors in the calculated viscosity.

Probably the first such accurate determination of the viscosity of air was made by Maxwell (1866), using the torsion pendulum illustrated in figure 5.1, to be found today in the museum at the Cavendish Laboratory. Three glass discs attached to a torsion wire were interleaved with other, stationary, discs. The narrow gaps allowed a relatively simple calculation of the fluid velocity and, hence, of the viscous damping. The damping due to the wire could be eliminated by taking measurements with the moving discs in contact with each other, reducing the number of surfaces exposed to the air, but leaving the damping due to the wire unchanged.

Early experiments with the mechanically simpler "free disc" (i.e. a single disc immersed in an effectively infinite body of fluid) were made by Meyer among others (see Meyer & Jahde 1861, Meyer 1965 the calculated viscosities were typically almost twice the magnitude of those calculated by Maxwell. This was due, as was clearly recognised by Maxwell, to the deficiencies of the correction for the edge of the disc

Of historical interest are Maxwell's measurements of the temperature dependence of the coefficient of viscosity. Using steam to raise the temperature of the apparatus, Maxwell found that the viscosity was almost exactly proportional to the absolute

temperature. It was well known that the "billiard ball" kinetic theory would predict a square root dependence, and so this result was in rather poor agreement, particularly when compared with the accuracy of other predictions from this simple model. Maxwell made the rather bold assumption that

"The simplicity of the other known laws relating to gases warrants us in concluding that the viscosity is really proportional to the temperature, measured from the absolute zero of the air thermometer"

and hence, fortuitously, obtained the result that the law of force between two molecules should vary inversly as the fifth power of the separation. The temperature dependence must, of course, reflect the form of the intermolecular potential, but in fact the intermolecular potential between many non-polar molecules can be better described by the Lennard-Jones 6-12 potential

$$\Phi(r) = 4\varepsilon \left[\left(\frac{\sigma}{r}\right)^{12} - \left(\frac{\sigma}{r}\right)^{6} \right] \tag{5.1}$$

or, in the case of polar molecules, by the Stockmayer potential which includes a correction term describing the angle dependent part of the dipole-dipole interaction (σ is the molecular cross section "radius" and ε the depth of the intermolecular potential well). The temperature dependence of the viscosity is often modelled by Sutherland's semi-empirical expression

$$\mu \propto \frac{T^{3/2}}{T+S} \tag{5.2}$$

where the constant S, Sutherland's constant, takes different values for different gases. This expression follows from a simple

model for the intermolecular potential, with a hard core of radius σ and a long range interaction described by

$$\Phi(r) = -\varepsilon \left(\frac{\sigma}{r}\right)^{\gamma} \tag{5.3}$$

where $\gamma \sim 6$ (cf. equation 5.1; see Hirschfelder et al (1954) and Monchick & Mason (1961) for more details).

With a Sutherland constant of 117K for air (Kaye & Laby 1966) we find that the viscosity is approximately proportional to the first power of the absolute temperature, for temperatures near to room temperature.

As already mentioned, for a disc rotating between parallel plates with a small separation, the theoretical calculations of the flow are good enough to permit very accurate absolute measurements of viscosity (see Kestin & Leidenfrost (1959) for example).

Other absolute measurements have been made using the rotating cylinder type of viscometer. This generally has two coaxial cylinders, of which one is rotated at a constant known speed and the other deflected against a torsion wire by an amount depending on the viscosity of the gas between the cylinders. A very accurate measurement using this type of apparatus was made by Bearden (1939) with a specific interest in the oil drop experiment. This configuration is probably the simplest from the point of view of the end corrections, but unless torsion damping measurements are made, there is the added complication of having to drive the rotating cylinder at a very precise speed.

With a free disc, there still does not seem to be a useable theory which would permit extremely accurate absolute measurements of viscosity. However, it is possible to make precise relative measurements with this very simple configuration, and this makes the free disc viscometer particularly suitable for the present investigation. It also has the advantages that measurements can be made under very similar conditions to those in Kestin & Shah's work, and that a greater insight can be gained into their experiments.

It was decided not to attempt to coat the torsion disc with radioactive material, the approach used by Kestin & Shah, but to instead use the same radiation sources as in the drag balance experiments and place them close to the disc. This was in order to avoid the loss of accuracy entailed by changing the disc, a major source of error in Kestin & Shah's work with ^{210}Po and one which would seem to be inevitable with such an approach.

As will be seen, there are also several other advantages with the present apparatus. In particular, the logarithmic decrement and viscosity can be determined in a very simple fashion, and there is no loss of precision at low gas pressures. This is of particular importance, since the largest changes in viscosity reported by Clark, Kestin & Shah were obtained with gases at low pressures.

A detailed summary of the results of Kestin & Shah's experiments is given in the next section, followed by an analysis of the theory of the torsion disc viscometer and a description of the present torsion disc viscometer and the results obtained with it.

5.2 Summary of Results Obtained by Kestin & Shah

Kestin & Shah performed four series of tests on various gases using a free disc torsion disc viscometer. The first series consisted of calibrations (the method of calibration used will be discussed in section 5.3), the second of measurements with a ^{137}Cs source irradiating the viscometer, the third with a disc which had been removed from the viscometer, coated wtih ^{210}Po and replaced, and a fourth set with the same disc but at reduced pressures.

In pilot tests with a 10 mCi ^{137}Cs source, an increase in the viscosity of argon of 0.08% was observed.

Figure 5.2, taken from Kestin & Shah (1968) shows the results obtained with a 97.5 Ci ^{137}Cs source. The precision was considered to be ± 0.05%. A reduction in the viscosity of air of 0.24% was observed, although it is noticeable that the change was not reproduced at elevated pressure. The results obtained with series 3 are shown in figure 5.3. Generally, slight increases in viscosity were observed, the largest change being +5.2% for argon. The precision was reputedly about 1%. At low pressure (∿ 1mmHg) the same conclusions were preserved on the whole, but with the significant exception of air for which a decrease of 7.6% was observed (figure 5.4) with a precision of 1.8%. Since this could be of practical significance it was essential to repeat these measurements and to improve the precision. It was also important to improve the control of pressure and temperature at low pressures so that it would not be necessary to correct for variations in these parameters.

5.3 Theory of the Torsion Disc Viscometer

Consider a circular disc of radius R and moment of inertia I, with a finite but small thickness h, suspended in a fluid of density ρ and viscosity μ by a thin torsion wire giving a restoring force $K\theta$ where θ is the angular position of the disc.

If the disc is set oscillating, the amplitude will be damped by the viscous action of the fluid (there will also be a contribution from the wire, and this will be considered later).

The equation of motion of the disc can be written

$$I\ddot{\theta} + L(\dot{\theta},\theta) + K\theta = 0 \qquad (5.4)$$

where the viscous damping, L, is some function of θ and $\dot{\theta}$ and the properties of the fluid. If the damping is small and roughly proportional to $\dot{\theta}$ (i.e. the fluid velocity is small) and any initial transients have died away, the motion approximates to a damped simple harmonic motion.

Writing

$$I\ddot{\theta} + L\dot{\theta} + K\theta = 0$$

the damped motion takes the form

$$\theta = \theta_o e^{-Lt/2I} e^{i\omega t}$$

where $\omega^2 = \left(\frac{2\pi}{T}\right)^2 \simeq \left(\frac{2\pi}{T_o}\right)^2 = \frac{K}{I}$

and can be characterised by the logarithmic decrement, Δ

$$\Delta = \ln\left(\frac{\theta n}{\theta_{n+1}}\right) = \frac{LT}{2I} \qquad (5.5)$$

where T, T_o are the periods with and without damping respectively, and θ_n is the amplitude of the nth oscillation.

An experimental determination of Δ will therefore give us information about μ provided that we can get an expression for L.

A simple analysis which illustrates the character of the solution will be given first, followed by a slightly more involved derivation of the equations used in the experiments.

Note that an expression for the natural period, T_o, can easily be found in terms of the properties of the suspension wire. According to Landau and Lifshitz (1959 b) the restoring couple for a rod of length ℓ and radius r_w twisted about its axis is

$$\frac{C\theta}{\ell}$$

where $C = \frac{1}{2}S\pi r_w^{\,4}$. The shear modulus, S, is related to the Young's Modulus, E, and Poisson's ratio, σ, by

$$S = \frac{E}{2(1+\sigma)}$$

and hence

$$T_o = 16\sqrt{\frac{\pi(1+\sigma)I\ell}{Ed_w^{\,4}}} \qquad (5.6)$$

where d_w is the diameter of the wire.

To find an expression for L, we need to solve the equation of motion for the fluid around the disc. Assuming cylindrical symmetry, no pressure gradient, and the coordinate system defined in figure 5.5, the Navier Stokes equation (1.3) becomes

$$\frac{\partial u_r}{\partial r} + \frac{u_r}{r} + \frac{\partial u_z}{\partial z} = 0 \quad \text{(Continuity)} \qquad (5.7a)$$

$$\rho\left[\frac{\partial u_r}{\partial t} + u_r\frac{\partial u_r}{\partial r} + u_z\frac{\partial u_r}{\partial z} - \frac{u_\phi^{\,2}}{r}\right] = \mu\left[\frac{\partial^2 u_r}{\partial r^2} + \frac{1}{r}\frac{\partial u_r}{\partial r} - \frac{u_r}{r^2} + \frac{\partial^2 u_r}{\partial r^2}\right] \quad (5.7\ b)$$

$$\rho\left[\frac{\partial u_\phi}{\partial t} + u_r\frac{\partial u_\phi}{\partial r} + \frac{u_r\,u_\phi}{r} + u_z\frac{\partial u_\phi}{\partial z}\right] = \mu\left[\frac{\partial^2 u}{\partial r^2} + \frac{1}{r}\frac{\partial u_\phi}{\partial r} - \frac{u_\phi}{r^2} + \frac{\partial^2 u_\phi}{\partial z^2}\right] \quad (5.7\ c)$$

$$\rho\left[\frac{\partial u_z}{\partial t} + u_r\frac{\partial u_z}{\partial r} + u_z\frac{\partial u_z}{\partial z}\right] = \mu\left[\frac{\partial^2 u_z}{\partial r^2} + \frac{1}{r}\frac{\partial u_z}{\partial r} + \frac{\partial^2 u_z}{\partial z^2}\right] \quad (5.7\ d)$$

The presence of the non-linear terms makes a full solution difficult, but we would expect u_r and u_z to be small compared with u_ϕ, provided that the motion is so slow that centrifugal forces are negligible*,

$$\rho\frac{\partial u_\phi}{\partial t} \simeq \mu\left[\frac{\partial^2 u_\phi}{\partial r^2} + \frac{1}{r}\frac{\partial u_\phi}{\partial r} - \frac{u_\phi}{r^2} + \frac{\partial^2 u_\phi}{\partial z^2}\right] \quad (5.8)$$

If we neglect the damping initially and write

$u_\phi\ (z = o,\ r < R) = r\omega\theta_o \cos \omega t = u_o \cos \omega t$

we can see that near the disc

$u_\phi \sim r\omega \cos \omega t$

and so

---

* A numerical solution for the problem of a constantly, rapidly, rotating disc has been obtained by Sparrow & Gregg (1960) and the solution for the flow is illustrated in Schlichting (1979).

$$\frac{\partial^2 u}{\partial r^2} + \frac{1}{r}\frac{\partial u_\phi}{\partial r} - \frac{u_\phi}{r^2} \sim 0$$

suggesting that in the neighbourhood of the disc a reasonable approximation to the equation of motion is

$$\rho\frac{\partial u_\phi}{\partial t} = \mu \frac{\partial^2 u_\phi}{\partial z^2}$$

or

$$\frac{\partial u_\phi}{\partial t} = \nu \frac{\partial^2 u_\phi}{\partial z^2} \tag{5.9}$$

This linear equation can be readily solved by the separation of variables, i.e. put

$$u_\phi \propto f(t)\, g(z)$$

to get

$$\frac{1}{f}\frac{df}{dt} = \nu \frac{1}{g}\frac{d^2 g}{dz^2} = \Omega$$

where Ω is some complex constant

Then

$$f(t) = e^{\Omega t}, \quad g(z) = \exp\left(\sqrt{\frac{\Omega}{\nu}}\, z\right)$$

neglecting the arbitrary multiplicative constants for the moment. To match the boundary conditions at the disc we put

$$\Omega = i\omega$$

and so

$$\sqrt{\frac{\Omega}{\nu}} = \pm \sqrt{\frac{\omega}{2\nu}}\,(1 + i)$$

If we assume that the boundaries of the fluid are far enough away not to influence the flow appreciably, then we need the -ve root and so

$$u_\phi \propto \exp(i\omega t)\exp\left(-\sqrt{\frac{\omega}{2\nu}}(1+i)z\right)$$

Taking the real part and matching with the velocity of the disc gives

$$u_\phi = r\omega\theta_o \cos(\omega t - z/\lambda)e^{-z/\lambda} \tag{5.10}$$

where $_o$ is the amplitude of the motion of the disc,

$$\lambda = \sqrt{\frac{2\nu}{\omega}} = \sqrt{\frac{\mu T}{\pi\rho}} \tag{5.11}$$

is the penetration depth, and we take z = o at the surface of the disc for convenience.

The fluid oscillates with time and with z, with a varying phase relationship to the disc, and the amplitude of the motion is damped exponentially in the z direction so that only fluid within a few λ of the disc is moving appreciably. Note that at atmospheric pressure λ will generally be small compared with the radius of the disc.

The surface shear stress is given by

$$\tau = \mu \left.\frac{\partial u_\phi}{\partial z}\right|_{z=o} = \frac{\theta_o r\,\omega}{\lambda}(\sin\omega t - \cos\omega t)$$

$$= \frac{\mu r}{\lambda}(\omega\theta - \dot{\theta}) \tag{5.12}$$

and the term in θ can be thought of as an effective increase in the moment of inertia of the disc due to the fluid carried round by it. For small damping we can neglect this term and our expression for the total damping is

$$L = 2\int_o^R \frac{\mu}{\lambda} 2\pi r^3 dr$$

and, if we assume a similar equation of motion in the radial direction near the edge, we get

$$L = \pi R^4 \sqrt{\frac{\mu\omega\rho}{2}} \left(1 + \frac{2h}{R}\right)$$

so the logarithmic decrement is then

$$\Delta = \frac{\pi R^4 \sqrt{\pi\mu\rho T}}{2I} \left(1 + \frac{2h}{R}\right) \tag{5.13}$$

The damping due to the wire (i.e. the logarithmic decrement which would be observed in a vacuum), Δ_o, can simply be added to this expression if Δ_o is small. For gases, Δ will generally be $\ll 1$.

This equation is correct to within a factor of 1.5 or so, underestimating the actual drag. The discrepancy can be attributed to the drag of the fluid near the edge of the disc.

To improve on this result we must allow for the drag of the fluid in this region by including the derivatives with respect to r in the Navier Stokes equation. Writing

$$u_\phi = r\dot{\psi}$$

where $\psi(r,z,t)$ is the angular position of the fluid (which we would expect to be essentially independent of r directly above the disc) the simplified Navier Stokes equations (5.8) become

$$\frac{\partial\dot{\psi}}{\partial t} = \nu \left(\frac{\partial^2\dot{\psi}}{\partial r^2} + \frac{3}{r}\frac{\partial\dot{\psi}}{\partial z} + \frac{\partial^2\dot{\psi}}{\partial z^2}\right)$$

or, equivalent but for a trivial integration

$$\frac{\partial\psi}{\partial t} = \nu \left(\frac{\partial^2\psi}{\partial r^2} + \frac{3}{r}\frac{\partial\psi}{\partial r} + \frac{\partial^2\psi}{\partial z^2}\right) \tag{5.14}$$

An approximate solution of this equation has been obtained

by Mariens & van Paemel (1956). (Note that in their paper, as well as many others, Δ is taken to be the logarithmic decrement divided by 2π). They assume that the time dependence is as for damped simple harmonic motion, i.e. we can write

$$\psi(r,z,t) = \psi(r,z)\ \theta(t) \tag{5.15}$$

where

$$\Omega = i\omega - \Delta/T = \frac{2\pi i - \Delta}{T} \tag{5.16}$$

and $\theta(t) = \theta_0 e^{\Omega t}$

We see that

$$\frac{1}{\nu}\frac{\partial\psi}{\partial t} = \frac{\Omega}{\nu}\psi = -p^2\psi \tag{5.17}$$

where

$$p = \frac{ai-b}{\lambda} \tag{5.18}$$

$$a = ((1 + (\Delta/2\pi)^2)^{\frac{1}{2}} - \Delta/2\pi)^{\frac{1}{2}} \tag{5.19a}$$

$$b = ((1 + \Delta/2\pi)^2)^{\frac{1}{2}} + \Delta/2\pi)^{\frac{1}{2}} \tag{5.19b}$$

and λ is the penetration depth already defined.

The solution for the damping is pieced together by considering adjacent regions of the fluid in turn. Near the edge (region 1 of figure 5.5) it can be assumed that there is no z dependence, and so

$$\frac{d^2\psi_1}{dr^2} + \frac{3}{r}\frac{d\psi_1}{dr} + p^2\psi_1 = 0 \tag{5.20}$$

Writing $\psi_1 = \frac{f(r)}{r}$ we see that

$$\frac{d^2f}{dr^2} + \frac{1}{r}\frac{df}{dr} + (p^2 - \frac{1}{r^2})\ f = 0$$

or, with $\xi = pr$

$$\frac{d^2f}{d\xi^2} + \frac{1}{\xi}\frac{df}{d\xi} + (1 - \frac{1}{\xi^2})f = 0 \tag{5.21}$$

which is Bessels equation of order 1.

The solution for ψ_1 can therefore be expressed as a linear combination of first order Hankel functions of the first and second kinds:

$$\psi_1 = \frac{C_1 H_1^{(1)}(\xi)}{\xi} + \frac{C_2 H_1^{(2)}(\xi)}{\xi}$$

To meet the boundary conditions at infinity and at the disc it can be seen that we need

$$\psi_1 = \frac{\theta(t) R\ H_1^{(1)}(pr)}{r H_1^{(1)}(pR)} \tag{5.22}$$

since arg (pr) $\sim \frac{3\pi}{4}$

Off the edge of the disc, Mariens and van Paemel assume that it is possible to separate variables in such a way that

$$\psi_2 = \psi_1(r)\ g(z)$$

where g(z) satisfies

$$\frac{d^2g}{dz^2} + p^2 g = 0$$

The solution which satisfies the boundary conditions

$g\ (z = 0) = 1$

$g\ (z = \infty) = 0$

is

$$g(z) = e^{ipz}$$

and so

$$\psi_2 = \frac{\theta(t)e^{ipz}RH_1^{(1)}(pr)}{rH_1^{(1)}(pR)} \tag{5.23}$$

Note that this does not satisfy the differential equation (5.14), but that at the edges of regions 1 and 3 it matches the solutions which would be obtained assuming no z and no r dependence respectively.

In region 3 it is assumed that there is no r dependence, and that the drag due to the fluid in region 2 can be accounted for by writing the differential equation for ψ_3 as

$$\frac{1}{\nu}\frac{\partial\psi_3}{\partial t} = \frac{\partial^2\psi_3}{\partial z^2} + \frac{4}{R}\left[\frac{\partial\psi_2}{\partial r}\right]_{r=R} \tag{5.22}$$

(an approximation first used by Meyer 1887)

Using the identity

$$\frac{dH_1^{(1)}(pr)}{dr} = -\frac{H_1(pr)}{r} + p\,H_o^{(1)}(pr)$$

we see that

$$\left[\frac{\partial\psi_2}{\partial r}\right]_{r=R} = \theta Re^{ipz}\left[-\frac{2}{R} + \frac{pH_o^{(1)}(pR)}{RH_1^{(1)}(pR)}\right]$$

and ψ_3 is therefore given by

$$\psi_3 = \theta(t)\left\{1 - (2iz/R)\left(\frac{2}{pR} - \frac{H_o^{(1)}(pR)}{H_1^{(1)}(pR)}\right)\right\}e^{ipz} \tag{5.24}$$

The total viscous damping couple (neglecting wire damping) is then

$$L = -2\pi R^3 h\mu\left[\frac{\partial\dot{\psi}_1}{\partial r}\right]_{r=R} - \pi R^4\mu\left[\frac{\partial\dot{\psi}_3}{\partial z}\right]_{z=o} \tag{5.25}$$

and so

$$L = -\pi R^4 \mu i p \left[1 - \frac{4h}{ipR^2} + \frac{4}{(ipR)^2} - 2i \left(\frac{h}{R} - \frac{1}{ipR}\right) \frac{H_o^{(1)}(pR)}{H_1^{(1)}(pR)} \right] \qquad (5.26)$$

Remembering that λ is usually small (i.e. pR is large) the last term can be expanded using Hankel's asymptotic series

$$\frac{H_o^{(1)}(pR)}{H_1^{(1)}(pR)} = i \left[1 + \frac{1}{2ipR} + \frac{3}{8} \frac{1}{(ipR)^2} + \frac{3}{8} \frac{1}{(ipR)^3} + \ldots \right]$$

and so, using $ip = -\frac{(a+ib)}{\lambda}$

$$L = \pi R^4 \left(\frac{\pi\mu\rho}{T}\right)^{\frac{1}{2}} \left[\left(1 + \frac{2h}{R}\right)(a+ib) + \left(2 + \frac{3h}{R}\right) \frac{\lambda}{R} \right.$$

$$\left. + \left(3 + \frac{3h}{4R}\right) \left(\frac{\lambda}{R}\right)^2 \frac{1}{(a+ib)} + 0 \left(\left(\frac{\lambda}{R}\right)^3\right) \right] \qquad (5.27)$$

To obtain an expression for Δ we must look again at the equation of motion

$$I\ddot{\Theta} + L\dot{\Theta} + K\Theta = 0$$

Using the assumed time dependence

$$I\Omega^2 + L\Omega + K = 0 \qquad (5.28)$$

Writing

$$K = I \frac{4\pi^2}{T_o^2}$$

and

$$\Omega = \frac{2\pi i - \Delta}{T}$$

we can separate the real

$$4\pi^2 I \left(\frac{1}{T^2} - \frac{1}{T_o^2}\right) + \frac{\Delta^2 I}{T^2} = \frac{Re(L)\Delta}{T} + \frac{2\pi}{T} Im(L)$$

and imaginary

$$2I\Delta + \frac{T}{2\pi} Im(L)\Delta = T\, Re(L)$$

parts of equation (5.28)

This gives us two expressions for Δ, although the first is not suitable for experimental purposes due to the difference of similar terms

$$\frac{1}{T^2} - \frac{1}{T_o^2}$$

Using the second equation, then, we get

$$\Delta = \frac{T Re(L)}{2I + \frac{T}{2\pi} Im(L)}$$

With L given by (5.27) this formula has been experimentally verified as accurate to within a few percent, for small λ/R, by Mariens & van Paemel (1956) and by Kestin & Wang (1957)

Noting that $a \sim b \sim 1$

and $\Delta << 1$

the expression obtained by Mariens and van Paemel can be simplified for the purposes of the present experimental work to the following:

$$\Delta = \Delta_o + \frac{\pi R^4 \sqrt{\pi\mu\rho T}}{2I} \left[1 + \frac{2h}{R} + \frac{\lambda}{R}\left(2 + \frac{3h}{R}\right) + \frac{3}{2}\left(\frac{\lambda}{R}\right)^2 \left(1 + \frac{h}{4R}\right) + O\left(\left(\frac{\lambda}{R}\right)^4\right)\right] \qquad (5.30)$$

To calculate μ one can either use charts of Δ vs μ, or use an iterative procedure. Since the correction terms are small, convergence is extremely rapid. This expression has been used for all experiments with gases at atmospheric pressure, i.e. when λ/R is small. Note that it reduces to the initial approximation (5.13) if $\lambda/R << 1$.

Of general interest, is the problem of a disc rotating in a housing, i.e. when B, D_1 and D_2 as shown in figure 5.5 are not $>>\lambda$. An extension of Mariens and van Paemel's approach which allows for this is given here.

Choosing to write

$$\frac{\partial\psi}{\partial t} = q^2\psi$$

where $q = -ip = \frac{(a+ib)}{\lambda}$

the differential equation for ψ_1 becomes

$$\frac{\partial^2\psi_1}{\partial\xi^2} + \frac{1}{\xi}\frac{\partial\psi_1}{\partial\xi} - (1 + \frac{1}{\xi^2})\psi_1 = 0 \qquad (5.31)$$

where ξ is now $\xi = qr$.

This is the modified Bessel equation of order 1 and the solution can therefore be written in terms of $I_1(\xi)$, the first order modified Bessel function of the first kind, and $K_1(\xi)$, MacDonalds function of the first order. The solution which matches the boundary conditions

$\psi_1(R) = \theta$

$\psi_1(B) = 0$

is

$$\psi_1\ (r,t) = \frac{\Theta(t)R}{r}\left(\frac{I_1(qr)K_1(qB)-I_1(qB)K_1(qr)}{I_1(qR)K_1(qB)-I_1(qB)K_1(qR)}\right) \tag{5.32}$$

In region 2 we try

$$\psi_2 = \psi_1\ g(z)$$

and solve

$$\frac{d^2g}{dz^2} - q^2g = 0$$

whence

$$g(z) = \frac{\sinh\ (q[D-z])}{\sinh\ (qD)}$$

and

$$\psi_2\ (r,z,t) = \frac{\Theta(t)R}{r}\left(\frac{I_1(qr)K_1(qB)-I_1(qB)K_1(qr)}{I_1(qR)K_1(qB)-I_1(qB)K_1(qR)}\right)\frac{\sinh(q[D-z])}{\sinh\ (qD)} \tag{5.33}$$

ψ_3 satisfies the equation

$$\frac{\partial\psi_3}{\partial z^2} - q^2\psi_3 + \frac{4}{R}\left[\frac{\partial\psi_2}{\partial r}\right]_{r=R} = 0$$

of the form

$$\frac{\partial^2\psi_3}{\partial^2} - q^2\psi_3 + k\ \sinh\ (q[D-z]) = 0$$

This has the particular integral

$$\psi_3 = \frac{kz}{2q}\ \cosh\ (q[D-z])$$

while the complementary function may be written

$$\psi_3 = c_1\cosh\ (q[D-z]) + c_2\ \sinh\ (q[D-z])$$

With the identities

$$\frac{d}{dr} I_1(qr) = -\frac{I_1(qr)}{r} + q\, I_o(qr) \tag{5.34a}$$

$$\frac{d}{dr} K_1(qr) = -\frac{K_1(qr)}{r} - q\, K_o(qr) \tag{5.34b}$$

we get

$$\left[\frac{\partial\psi_2}{\partial r}\right]_{r=R} = \frac{\Theta(t)R\sinh(q[D-z])}{\sinh(qD)} \left(-\frac{2}{R^2} + \frac{q}{R}\left(\frac{I_o(qR)K_1(qB) + I_1(qB)K_o(qR)}{I_1(qR)K_1(qB) - I_1(qB)K_1(qR)}\right)\right)$$

and using the boundary conditions

$$\psi_3(z = 0) = \theta(t)$$

$$\psi_3(z = D) = 0$$

we need

$$\psi_3 = \theta\left\{\frac{\sinh(q[D-z])}{\sinh(qD)}\left(1 + \frac{2D}{q}\left[-\frac{2}{R^2} + \frac{q}{R}\left(\frac{I_o(qR)K_1(qB) + I_1(qB)K_o(qR)}{I_1(qR)K_1(qB) - I_1(qB)K_1(qR)}\right)\right]\coth(qD)\right) + \frac{2(z-D)}{q}\left[-\frac{2}{R^2} + \frac{q}{R}\left(\frac{I_o(qR)K_1(qB) + I_1(qB)K_o(qR)}{I_1(qR)K_1(qB) - I_1(qB)K_1(qR)}\right)\right]\frac{\cosh(q[D-z])}{\sinh(qD)}\right\} \tag{5.35}$$

The viscous damping couple is then, using $q = \frac{(a+ib)}{\lambda}$,

$$L = \pi R^4 \mu \left(\frac{a+ib}{\lambda}\right) \Bigg\{ \coth(qD) \left(1 + \frac{4}{(qR)^2}\right) + \frac{4h}{qR^2} \left(1 + \frac{D}{h} (1 - \coth^2 (qD))\right) - 2\left(\frac{h}{R} + \frac{D}{R} (1 - \coth (qD)) + \frac{\coth(qD)}{qR}\right) \times \left(\frac{I_o(qR)K_1(qB) + I_1(qB)K_o(qR)}{I_1(qR)K_1(qB) - I_1(qB)K_1(qR)}\right)\Bigg\} \tag{5.36}$$

where it is understood that if $D_1 \neq D_2$, terms involving D are replaced by an appropriate average.

The logarithmic decrement, including the additive term due to the wire, can be written

$$\Delta = \frac{\Delta_1 Re\ (\Lambda)}{1 + \Delta_1 Im(\Lambda)/2\pi} + \Delta_o \tag{5.37}$$

where

$$\Delta_1 = \frac{\pi R^4 \sqrt{\pi \mu \rho T}}{2I}$$

and

$$\Lambda = (a+ib) \Bigg\{ \coth(qD)\left(1 + \frac{4}{(qR)^2}\right) + \frac{4h}{qR^2} \left(1 + \frac{D}{h} (1 - \coth^2(qD))\right) + 2\left(\frac{h}{R} + \frac{D}{R}(1 - \coth^2(qD) + \frac{\coth(qD)}{qR}\right) \left(\frac{I_1(qB)K_o(qB) + I_o(qR)K_1(qB)}{I_1(qB)K_1(qR) - I_1(qR)K_1(qB)}\right)\Bigg\} \tag{5.39}$$

The modified Bessel functions have the following asymptotic forms

$$I_\nu(\xi) \sim \frac{e^{\xi}}{\sqrt{2\pi\xi}} \qquad (|\arg(\xi)| < \tfrac{1}{2}\pi)$$

$$K_\nu(\xi) \sim \sqrt{\frac{\pi}{2\xi}}\, e^{-\xi} \qquad (|\arg(\xi)| < \frac{3\pi}{2})$$

and so the last term takes the simple form

$$2\,(\ldots\ldots)\coth(q[B-R]) \tag{5.40}$$

if λ is small.

With $\coth(qD) \sim 1$ for $qD \gg 1$ it can be seen that the equation for the logarithmic decrement tends to Marien and van Paemels solution if B and D are large. Note that both of these formulae become incorrect if $\lambda \gtrsim R$ and overestimate the drag. (This must obviously happen with our simplified formula (5.30) due to the form of the asymptotic series, but the problem is more fundamental than this). The reason for the divergence can be clearly seen when we look at the approximation involved in assuming that ψ_3 is independent of r. As λ increases, the influence of the fluid at the edge pervades further in and must reduce the velocity gradient in the r direction near the edge of the disc. However, if $\lambda \ll R$ the theory will hold for arbitrary B and D.

It should also be correct for arbitrary λ if $D \ll R$, since, to a good approximation, ψ will again be independent of r above the disc. A rough calculation does give agreement within several percent with values obtained by Kestin & Leidenfrost (1959) with this configuration, but it has not yet been possible to test the theory rigorously.

At low pressure, or with narrow gaps, we would expect the damping to become essentially independent of density and proportional to viscosity. However, the edge effects become very important and make an exact solution difficult.

For example, if we make a comparable approximation to that used in deriving equation (5.13), and assume linear velocity profiles, we get

$$\Delta = \frac{\pi R^4 \mu T}{2I} \left(\frac{1}{D_1} + \frac{1}{D_2} + \frac{4h}{(B-R)}\right) \tag{5.41}$$

which predicts a value for Δ which is about a factor of 10 too small. The discrepancy between theory and experiment can again be attributed to edge effects. We can illustrate the problem when $\lambda \sim R$ by looking at the drag on a cylinder of height 2λ, i.e. we assume that the disc carries a rigidly bound layer of fluid of height λ on each surface. Then, noting the form of the now dominant edge correction factor in (5.13)

$$\Delta \sim \frac{\pi R^4 \mu T}{2I\lambda} \quad \frac{4\lambda}{R}$$

$$\sim \frac{2\pi R^3 \mu T}{I} \tag{5.42}$$

which is, as will be seen, in good agreement with experiment.

A further semi-empirical approximation can be obtained by noting that for large λ, the term of order $(\lambda/R)^2$ will dominate in the expression for the viscous couple (5.26 or 5.36) and so

$$\Delta \sim \frac{\pi R^4 \mu T}{2I\lambda} \quad \frac{4\lambda^2}{R^2} \quad \frac{1}{2}$$

Bearing in mind that this term orginates with the edge correction,

so that the "physical" penetration depth is limited to B-R, we see that

$$\Delta \sim \frac{\pi R^2 (B-R)\ \mu T}{I} \tag{5.43}$$

again a fair approximation to the observed damping. In a low pressure regime, if Δ is observed to be independent of ρ, it follows that it should be sufficient to assume

$$\Delta \propto \mu \tag{5.44}$$

Newell (1959) has given a solution for the problem of a disc in a housing when λ is large compared with B and D and, also, D,h << R (cf equation 3.57, but with added restriction on B and D) and this was used by Kestin & Leidenfrost (1959) in some absolute determinations of gas viscosity.

The approach used was essentially to Laplace transform the equations of motion of the fluid and of the disc with respect to time, and to obtain a Bromwich integral for the fluid position of the form

$$\psi = \frac{1}{2\pi i} \int_{c-i\infty}^{c+i\infty} ds\ \frac{e^{st}}{s} \cdot \frac{1}{F(s)} \tag{5.45}$$

Since the integral is determined by the poles of the integrand it is necessary only to find the zeros of the characteristic equation, F(s), which depends on the geometry of the viscometer and the properties of the fluid. This approach underlies the semiempirical formulae derived by Kestin and Shah in their work with irradiation, as well as a series of papers on the general theory of oscillation

type viscometers, to be found in Z. angew. Math. Phys. (Kestin & Newell 1957, Beckwith & Newell 1957, Azpeitia & Newell 1958, 1959). In these latter references a rather more rigorous approach is taken initially, using various analytical techniques, for example Schwarz-Christoffel conformal transformations to "straighten" the corners of the disc. However, various approximations must be made in order to obtain a tractable solution, and the results offer no great incentive with regard to their use in the present work. As a general comment, one might also observe that since the time dependence is well known to be as for damped simple harmonic motion, to a very good approximation, the use of the Laplace transform with respect to time results is an unnecessary complication of an already difficult problem.

In Kestin & Shah's work, the exact solutions for the viscous couples on infinite discs and cylinders are used, and the assumption is made that the actual viscous torque, M, is "proportional" to that calculated on the assumption that the surfaces of the disc contribute the same amounts as if they were part of the respective infinite surfaces, M_∞

Thus

$M = CM_\infty$

where C is a correction factor which is a function of the geometry of the viscometer and of the boundary layer thickness, and which tends to 1 as $\lambda/R \to 0$. The formula used for high pressure (i.e. $\delta/R < 1$) was derived by Kestin & Wang (1957) and is

$$\frac{3\pi\rho R^4 h}{I} \; C\left(\frac{\delta}{R}\right)^2 + \frac{\sqrt{2}}{2}\left(1+\frac{2h}{R}\right)\frac{1}{\sqrt{\Theta}}\left(1-\frac{3}{2}\Delta-\frac{3}{8}\Delta^2\right)\frac{\pi\rho R^5}{I}\; C\left(\frac{\delta}{R}\right)-2\left(\frac{\Delta}{\Theta}-\Delta_o\right)=0 \tag{5.47}$$

where $\Theta = T/T_o$, the boundary layer thickness, δ , is $\frac{\lambda}{\sqrt{2\Theta}}$, and Δ is now the logarithmic decrement divided by 2π. The viscosity must again be calculated by iteration.

The correction factor is then empirically determined by calibration with a series of gases of known viscosity, and represented by a polynomial in δ/R (figure 5.6)

This approach warrants some criticism. We can see that since Kestin and Wang (1957) are making a worse initial approximation than Mariens and van Paemel (1956), who then make no further approximations other than to truncate an asymptotic expansion, we must not expect Kestin and Wang's uncorrected equation to be a better approximation to the true solution. It therefore follows that, despite the impressive appearance of equation 5.47, the terms of order Δ compared with 1 are entirely superfluous. Neglecting such terms, we can rearrange (5.47), replacing δ by $\lambda/\sqrt{2\Theta}$ and neglecting Δ_o to get

$$\Delta = \frac{\pi\rho R^4\lambda}{4I} \left(1 + \frac{2h}{R} + \frac{3h}{R} \frac{\lambda}{R}\right) C \qquad (5.48)$$

The corresponding simplified expression using Mariens and van Paemels theory (5.30) is

$$\Delta = \frac{\pi\rho R^4\lambda}{4I} \left(1 + \frac{2h}{R} + \left(2 + \frac{3h}{R}\right) \frac{\lambda}{R} + \frac{3}{2} \left(1 + \frac{h}{4R}\right) \left(\frac{\lambda}{R}\right)^2\right) \qquad (5.49)$$

where Δ is now taken to be the logarithmic decrement divided by 2π. It can be seen that the "new" approach of Kestin and Wang is tantamount to applying an empirical correction to a formula which is slightly worse that that of Mariens and van Paemel, but is of the same general form. (Considering the form of equation 5.47,

this is somewhat ironic, in view of the fact that Kestin & Wang (1957) describe calculations using Marien & van Paemel's equation as "tedious").

It is instructive to look at the effect of the correction factor determined by Kestin and Shah (1968) on this expression. Taking the data for series 1 we have

$h = 0.115$ cm

$R = 3.25$ cm

and the correction factor, replacing δ by $\lambda/\sqrt{2}$, is

$$C = 1.000 + 1.904 \frac{\lambda}{R} + 0.8237 \left(\frac{\lambda}{R}\right)^2 \qquad (5.50)$$

The simplified Mariens and van Paemel equation (5.49) becomes (to order $(\lambda/R)^2$)

$$\Delta = \frac{\pi\rho R^4\lambda}{4I} \left(1 + \frac{2h}{R} + 2.11 \frac{\lambda}{R} + 1.5 \left(\frac{\lambda}{R}\right)^2\right) \qquad (5.51)$$

while Kestin and Shah's corrected formula is now

$$\Delta = \frac{\pi\rho R^4\lambda}{4I} \left(1 + \frac{2h}{R} + 2.14 \frac{\lambda}{R} + 1.1 \left(\frac{\lambda}{R}\right)^2\right) \qquad (5.52)$$

which differs significantly only in the smallest correction term, the agreement in Δ being within a few percent. Figure 5.7 shows the calibration for series 3, together with the calibration which would be predicted by formula 5.49, to order $(\delta/R)^2$, (dashed line), again illustrating the minimal additional correction necessary.

Equation 5.47 is therefore a complicated alternative to either applying a small correction to equation 5.49 or using an expression of the form

$$\Delta = \frac{\pi\rho R^4\lambda}{4I} \; f\left(\frac{\lambda}{R}, \frac{h}{R}\right) \qquad (5.53)$$

where, for a given viscometer, f becomes an experimentally determined polynomial of λ/R. This form is strongly suggested by equations 5.49 and 5.39, and, indeed, by dimensional analysis, since we would anticipate that Δ could be represented by an expression of the form

$$\Delta = f_1\left(\frac{\rho R^4 \lambda}{I}\right) f_2\left(\frac{\lambda}{R}\right) f_3\left(\frac{h}{R}\right)$$

and we know that $\Delta = \frac{\pi\rho R^4 \lambda}{4I}$ when $\lambda/R \ll 1$, $h/R \ll 1$.

At low pressure, if anything, the approach used by Kestin and Shah is even worse. A correction factor was applied to the solution of Azpeitia & Newell (1958), which is valid for $h \ll \delta \ll R$. This was then used for $0.5 < \frac{\delta}{R} < 3.0$ and $\frac{\delta}{R} > 3.0$ with two different calibration curves (figure 5.8), the equation determining the correction factor being (Shah 1970)

$$C_L \left\{ \frac{m}{\sqrt{2}\,\Theta^{3/2}} \left(1 - \frac{3}{2}\Delta - \frac{3}{8}\Delta^2\right) \left[1 + \frac{4\eta_o}{\pi\xi_o}\left(2.14 - \tfrac{1}{2}\ln\left(\frac{\eta_o^2\sqrt{1+\Delta^2}}{\Theta}\right)\right)\right] \right.$$

$$+ \frac{4m\eta_o}{2\pi\xi_o\sqrt{2}\Theta^{3/2}} \left(\frac{\pi}{2} + \phi\right)\left(1 + \frac{3}{2}\Delta - \frac{3}{8}\Delta^2\right) + \frac{2m}{\xi_o\Theta}$$

$$+ \frac{6m\eta_o}{\pi\xi_o^2\Theta} \left(2.0 - \tfrac{1}{2}\ln\left(\frac{\eta_o^2\sqrt{1+\Delta^2}}{\Theta}\right)\right)$$

$$\left. + \frac{\Delta}{2\Theta}\,\frac{6m\eta_o}{\pi\xi_o^2}\left(\frac{\pi}{2} + \phi\right)\right\}$$

$$- \frac{2}{\Theta}\left(\frac{\Delta}{\Theta} - \Delta_o\right) = 0 \qquad (5.54)$$

where $m = \frac{\pi\rho\delta R^4}{I}$, $\eta_o = \frac{d}{2\delta}$, $\xi_o = \frac{R}{\delta}$ and $\phi = \tan^{-1}(\Delta)$

The use of two quite different polynomials to cover the supposed range of validity of equation 5.54, with a maximum correction factor ~ 2, illustrates the inherent weakness of the approach.

Neglecting small terms again, the equation becomes

$$\Delta = \frac{\pi\rho\lambda R^4}{4I}\left\{1 + \frac{2h}{R}\ [2.64 - \ln\eta_o] + [2 + \frac{6}{2\pi}\ (2.0 - \ln\eta_o)\frac{h}{R}]\ \frac{\lambda}{R}\right\} C_L$$

At low pressure, in the density independent regime, η_o is small, and $\ln\eta_o$ might be ~ -5 typically. With h/R small it follows that

$$\Delta \sim \frac{\pi\rho\lambda R^4}{4I}\ \frac{2\lambda}{R}\ C_L$$

and so

$$\Delta \sim \frac{\mu T R^3}{I}\ \frac{C_L}{2} \tag{5.55}$$

With $C_L \simeq 2.0$ for low pressure, this reduces to equation (5.42), remembering that Δ here is still the logarithmic decrement divided by 2π. In fact, for $\delta/R > 3$, the relation C_L = const. fits the calibration data at least as well as the quadratic in δ/R used. There is thus very little merit in the use of equation 5.54, and for relative measurements it is sufficient to use (5.30) and (5.44) or to observe that, over the whole range of boundary layer thickness, we expect Δ to be of the form

$$\Delta = \frac{\pi\rho R^4\lambda}{4I}\ f(\frac{\lambda}{R})$$

Equivalently, if we prefer ρ not to appear explicitly, this becomes

$$\frac{\Delta}{\mu} = \frac{R^4 T}{I\lambda} \; g\left(\frac{\lambda}{R}\right) \tag{5.56}$$

where, for a given viscometer, g can be represented as a fixed polynomial in λ/R.

In conclusion, it is perhaps worth mentioning briefly a few other possible approaches to the problem of an oscillating disc with $\lambda \gtrsim R$. It is possible to obtain integral representations for ψ by applying either a Laplace transform with respect to z, or a first order Hankel transform with respect to r, to the simplified Navier-Stokes equation, and solving the resultant differential equation. With the former, the velocity gradient (and hence torque) appears explicitly in the transformed equation of motion for $r < R$, while for $r > R$ we are justified in writing $\left.\frac{\partial\psi}{\partial z}\right|_{z=0} = 0$. Also writing $\psi(z=0, r>R) = \psi_1$, where ψ_1 is given by 5.32, allows for the effect of a cylindrical housing.

The inversion of the transforms are by no means trivial, but they might offer a worthwhile approach. Finally, an attempt to solve the general problem numerically would be well worthwhile. Since the results are not of central importance to the present work, these themes have as yet not been developed to any great extent; but in view of the fact that the semi-empirical formulae in use have apparently not advanced in the past twenty years (see Clifford et al 1981, Kestin & Shankland 1981) the problem is of some interest.

(General references used:- Abramowitz & Stegun 1970, Mathews & Walker 1970, Lebedev 1965, Davies 1978).

5.4 Design of the Torsion Disc Viscometer

In designing the viscometer, it was necessary to choose a wire and a disc which would give a reasonable logarithmic decrement and period. Early studies with various discs and wires led to discs of several cms in diameter and a few mm thick, and wires of about 20 cm in length with diameters of a few tenths of a mm. The length of the wire was chosen to be long enough so as not to subject the wire to excessive twists, yet short enough to ensure that the simple pendulum mode of oscillation was not too obtrusive. The wires finally used were 38 SWG copper-beryllium, although some attention was paid to steel piano wire. Both have good elastic properties, giving accurately linear restoring forces, and show no marked change in strength over an extended period of time. The piano wire does, however, have a tendency to rust. Mr. W.G. Rees made some experiments with drawn quartz fibres, but concluded that their brittleness made them unsuitable for the prolonged investigation anticipated. It is also possible that their long term strength could be affected by water vapour.

With a copper-beryllium wire of $\sim$ 16 cm length and a brass disc of 85 mm diameter and 1 mm thickness, logarithmic decrements of $\sim$ 0.005 were obtained with air at atmospheric pressure, with a period of about 11 s.

The wire was attached to the disc and to its support by means of pinchucks, the lower pinchuck having a section ground flat to take a 5 mm diameter galvanometer mirror, so that the motion can be imaged by an optical lever.

The disc was enclosed in a cylindrical glass housing, free from significant optical flaws, and fitted with ground glass flanges at either end. The glass is 6 mm thick and the internal diameter of the viscometer is 18.3 cm with a height of 32 cm. The ends are covered by 1 cm thick dural plates, sealing by "O" rings. The lower plate is held by spring clips, so that it can be easily removed to insert radioactive sources into the viscometer. The upper plate holds a glass probe containing a thermocouple, and is connected to a Schaevitz PTD-310-W pressure transducer, an Edwards Model 17 analogue pirani gauge and the gas vacuum lines. (Under vacuum the viscometer leaks at a rate of 0.02 mbar/hour at best, ocassionally rising to $\sim$ 0.2 mbar/hour at worst. This was probably a result of the use of rubber tubing to connect the viscometer to the vacuum pump, but this was necessary in order to isolate the viscometer from the vibration of the pump).

It is essential to know the pressure and temperature accurately, since, for example, at atmospheric pressure a 2 mbar change in pressure and a 0.3^{o}C change in temperature both correspond to errors of $\sim$ 0.1% in the measurement of the viscosity. Maximum accuracy can be achieved at atmospheric pressure by allowing the viscometer to equalise to ambient atmospheric pressure through a liquid paraffin bubbler, the pressure being read to the nearest mbar on an aneroid barometer which has been calibrated against a standard Fortin barometer. At reduced pressure, both the pirani gauge and pressure transducer are necessary. The pirani gauge is useful at pressures below about 100 mbar, but can be

inaccurate at higher pressures, particularly with gases other than air. For example, argon at atmospheric pressure gives a reading of 30 mbar while helium at 10 mbar reads atmospheric pressure. The pressure transducer, however, is extremely accurate in the range 100–1000 mbar and is not dependent on the particular gas in use.

It was considered desirable to maintain the viscometer and its enclosure at a constant temperature. This was done by surrounding the viscometer with an insulating housing, comprising a dexion framework with thick polystyrene walls and a 6 mm thick perspex front. The viscometer is suspended from the dexion frame, which stands on a heavy steel base resting on plastic foam. This provides a certain degree of vibrational isolation. The temperature in the viscometer is controlled to ± 0.05°C using low powered light bulbs which heat the housing, switched by a Comark series 5000 digital trip unit connected to the Comark series 5000 10 channel digital thermometer. The system is arranged so that the viscometer itself is subjected only to small temperature gradients, but with, if anything, an increasing temperature towards the top. This ensures that there is no possibility of the gas in the viscometer being disturbed by convection currents.

The system was originally intended to run at 20°C during winter and 25°C during summer. However, as the room temperature repeatedly exceeded this mark, water cooling was also installed.

In order to start the motion of the disc, the upper pin chuck was attached to the spindle of a small d.c. electric motor,

fixed in a housing on the upper dural plate. A vane attached to the pinchuck acts against a spring, which normally holds the vane against a rigid stop. A circuit feeds a preset number of pulses into the motor at the resonant frequency of the viscometer, so that the required starting amplitude can be built up. Figure 5.9 shows the layout of the viscometer, and figure 5.10 shows the starter circuit.

A general view of the viscometer and a close up of the disc in the glass housing are shown in figures 5.11 and 5.12. The equipment used for determining the logarithmic decrement can also be seen, and will be described in the next section.

5.5 Data Logging Circuit

We now come to the problem of determining the logarithmic decrement. The conventional approach is that suggested by the definition (5.5), namely the measurement of sucessive amplitudes, or, with a small logarithmic decrement, amplitudes at intervals of several oscillations. To measure small decrements to a very high accuracy it is, of course, necessary to look at a large number of oscillations, perhaps a few hundred over a period of an hour or so. This makes some kind of automated system highly desireable, particlarly if a large number of experiments are to be performed. While it is quite feasible to measure amplitudes automatically, it is rather inefficient, and so it was decided to take the opposite approach and instead to count the number of oscillations necessary for the amplitude to decay by a fixed amount. With a small logarithmic decrement it is possible to

arrange for the number of oscillations to be large enough that the integral nature of the data is not a limiting factor.

The system developed consists of a laser beam from a Spectra Physics 1mW He/Ne laser, reflected from a 1m focal length, 5mm diameter, galvanometer mirror in the viscometer to a screen about 2m away. This screen has six phototransistors (PT's) set in it, one (PTC) corresponding to the nominal rest position of the system, the others approximately equally spaced in $\ln\theta$ from $\sim 2^{\circ}$ angular amplitude to 10° angular amplitude (see figure 5.13). The outermost PT (PTO), representing the initial amplitude at which measurements are to begin, corresponds to a twist in the wire of ~ 1 rad m^{-1}. The PT's are arranged so that the laser beam passes over them as the disc swings, and the signals from the PT's are used to control a specially developed digital electronic circuit. This records the number of swings, n , necessary for the amplitude to decay through amounts determined by the spacing of PT's 0 to 4. We therefore obtain a five point graph of $\ln\theta$ vs n and can obtain the logarithmic decrement from the slope of a best straight line. The amplitudes were chosen to give of the order of one hundred counts per section and this leads to an intrinsic resolution of the order of ± 0.1% in the logarithmic decrement, less than or of the order of the natural variation.

The circuit operates in the following way (see figure 5.14). The central PT triggers a monostable (555) which produces a voltage pulse of a few tenths of a second duration. This drives a light emitting diode (LED) for a visual check on triggering and also a 3 digit BCD counter (3 x 4510 in series) via a divide by 2

(JK flip flop 4027). The data on the BCD counter, corresponding to the number of oscillations of the torsion disc viscometer, are passed in parallel to four separate 3 digit seven segment display drivers, connected to 7 segment LED displays. The other phototransistors (PTO - 4) drive similar triggers and LED's which, when cut on by the laser beam, latch the data onto the display drivers. PTO is used to reset the count to zero. Thus each display records the state of the counter when the corresponding PT was last triggered by the laser beam. With PTO resetting the counter we obtain, at the end of a run, four counts corresponding to the number of oscillations taken for the amplitude to decay from x_o to x_1, x_o to x_2 etc.

A "master latch enable" (MLE) output is derived from PT4 and freezes the displays a couple of minutes after the last pulse from PT4 (i.e. at the end of the experiment) so as to prevent any spurious signals causing a loss of data if the system is left for some time. The start button puts MLE high and also triggers the torsion disc starter unit.

In calculating the logarithmic decrement, a least squares regression of n_m on $\ln \theta_m$ is used. θ_m (or, more strictly, $2\theta_m$ although this has no effect on the calculation of the logarithmic decrement) is calculated from

$$\tan(\theta_m + \delta\theta) = \frac{x_m}{d} \qquad (5.57)$$

where $\delta\theta$ is the error in the zero position. With a small logarithmic decrement it is preferable to use some kind of dynamic zero measurement, and this function is performed by a

timer section of circuitry (figure 5.15). In fact, this section can operate in one of two modes, zero position or period. In the period mode, successive periods are displayed to 0.1 ms on alternate 6 digit displays, each display being held for half a cycle and then reset (this might appear to be too short a display time, but it should be realised that successive periods are constant to a few tenths of a millisecond). The timing is obtained by enabling two six decade BCD counters (50395's), driven by a (nominal) 10 kHz clock (555), for appropriate intervals. An output is available for an absolute calibration of the clock frequency using a standard frequency counter.

In the zero position mode, the time spent by the laser beam to the left hand side (T_L) and right hand side (T_R) of PTC during one oscillation is measured using the two 6 decade counters. The amplitude at which the zero position is measured is selected by arranging to reset the counters from any one of PT0 to PT4 (or a "manual" push button). The zero error is then calculated from

$$\frac{\delta\theta}{\theta_m} = \cos\left(\frac{T_R\,\pi}{T_L + T_R}\right)$$

which, with 5.57, gives

$$\delta\theta = \frac{\cos\left(\frac{T_R\,\pi}{T_L+T_R}\right)\tan^{-1}(x_m/d)}{1 + \cos\left(\frac{T_R\pi}{T_L+T_R}\right)} \qquad (5.58)$$

Usually PT2 is used to reset the counters. The clock frequency is constant to $\lesssim$ 1 part in 10^5 during zero position measurement, and the zero position is accurate to < 0.1 mm on the screen.

In order to calculate the logarithmic decrement a Hewlett-Packard 41CV programmable calculator with a non-volatile memory was used. A program was written which, given four counts and two times, will correct for the zero error and perform a linear regression of n on $\ln\theta$, also calculating the regression parameter r^2 as a check for bad data. The details of the counter and timer sections are shown in figures 5.16 and 5.17, and an IC list and pinouts are given in an appendix.

The circuit details of the displays are essentially trivial and repetitive and have been omitted. It suffices to note that all of the displays were constructed from single seven segment TIL313 LED displays, the counter displays being driven through 470Ω resistors by the 4 display drivers, the common cathodes being connected to a BC441 which is strobed by one of the timer strobes to give a comparable brightness to the timer displays. The timers have multiplexed displays driven from the 7 segment outputs on the 6 decade counter/timers through BC182 buffer transistors.

The complete system is shown in figure 5.18.

Various error sources must be considered in determining the logarithmic decrement in this way. Firstly, of course, there is the accuracy with which we know the amplitude of oscillation when the phototransitors last trigger. Although they have lenses of 3mm diameter, they trigger if the edge of the laser spot (∿ 1-2 mm diameter) reaches the edge of the PT, whose distance from PTC is known to ∿ ± 0.25 mm to ± 0.5 mm. At large amplitudes in fact, the logarithmic decrement is usually the limiting factor, since the amplitude changes by a few mm (in ~ 750 mm) over one oscillation.

It can be seen that random errors from this and systematic errors in the measured triggering amplitudes are not appreciable. Note that a small correction, δx_m, is made to x_m to allow for refraction through the perspex front of the housing (see figure 5.19). The error due to refraction is

$$\delta x_m = t\,(1 - \frac{1}{N})\,\sin\theta_m$$

where t is the thickness of the perspex (6 mm) and N is the refractive index (N = 1.495). For x_o, $\delta x_o \sim 0.7$ mm which is just significant. Small errors arise from the curvature of the mirror and its displacement from the axis of rotation, but these are normally negligible. Note that the screen and perspex front can be aligned to be perpendicular to the stationary laser beam, using the various reflected beams from the viscometer, to an accuracy of $\sim 1^o$, so this is not a significant error.

The path of the laser spot on the screen is non-linear, the height on the screen compared with that at the centre being

$$H - H_o = ((d^2 + x^2)^{\frac{1}{2}} - d)\tan\varepsilon \qquad (5.60)$$

where ε is the vertical inclination of the incoming beam. Under normal circumstances ε is kept small and the path is a shallow parabola:

$$H - H_o \simeq \frac{1}{2}\,\frac{x^2\varepsilon}{d} \qquad (5.61)$$

This could give small errors due to triggering at points other than the edge of the phototransistors and due to any mean inclination of the screen. However, the maximum deviation is

AD-A137 740 STUDIES OF AERODYNAMIC DRAG(U) CAMBRIDGE UNIV (ENGLAND) CAVENDISH LAB W A WILBY ET AL. DEC 82 AFOSR-TR-84-0071 AFOSR-79-0057 3/3

UNCLASSIFIED F/G 20/4 NL

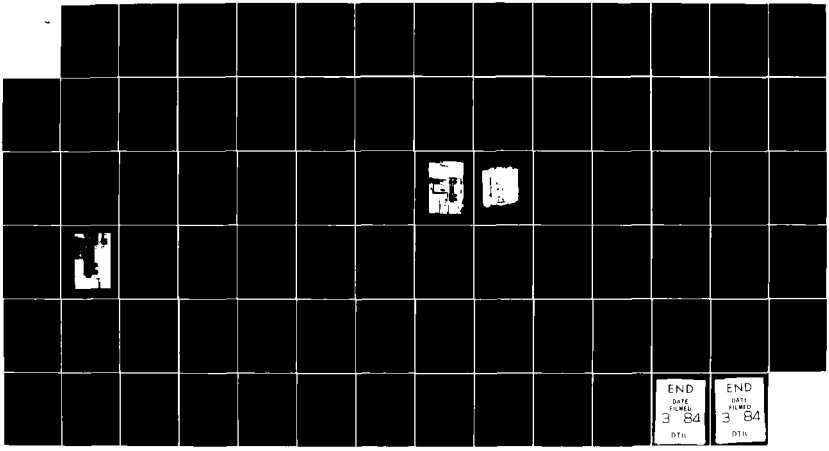

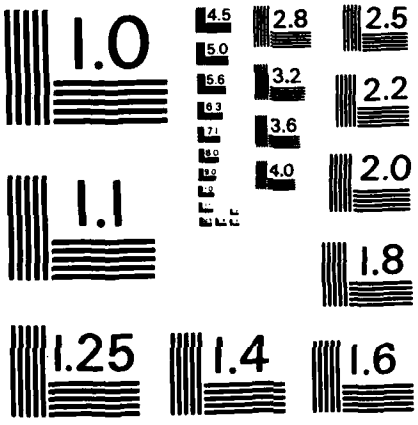

MICROCOPY RESOLUTION TEST CHART

NATIONAL BUREAU OF STANDARDS-1963-A

normally only a few mm, and since the extreme phototransistors can be adjusted vertically by this amount the errors are negligible.

The main potential cause of error is, in fact, vibration, since erroneous counts will be recorded if the "wobble" of the disc is large enough to cause the beam to miss PTC (the other PT's are less critical, since they only need one in two attempts to "succeed" on each swing and are unlikely to lead to errors of more than one or two counts). This has not been a significant problem as it is usually possible to keep the amplitude of vertical vibrations at the screen to $\lesssim$ 1 mm, although occasionally at low pressure (when the logarithmic decrement for pendulum oscillations is much reduced) severe building vibrations have caused trouble. In circumstances where there was frequently a prohibitively high level of vibration it would, of course, be possible to use small vertical arrays of phototransistors connected in parallel to detect the position of the laser beam.

There will be negligibly small errors in the zero position, due to the change in amplitude during measurement and the finite sizes of PTC and the laser spot. The first error arises since we assumed that θ is constant over one period in equation 5.58. At most, it will change by $\sim \frac{1}{2}\%$, giving a $\frac{1}{2}\%$ error in $\delta\theta$ or δx. As $\delta x \lesssim 10$ mm typically, this essentially systematic error is not significant. It is interesting to note that the zero position usually shows a systematic drift of $\sim$ 0.1 mm in the negative x direction between runs. The effect of the finite PT size can be seen by considering the timing sequence, shown in figure 5.19.

The timing error due to the difference in velocities over different parts of a PT of width w is, neglecting the change in amplitude over one oscillation which has already been considered,

$$\delta t \sim \frac{\delta x \; w^2}{x_m^3 \; \omega} \tag{5.62}$$

which will be no more than a few μs. The effect of the finite size of the laser spot will be of a similar magnitude.

Examples of results obtained with the torsion disc viscometer and data logging circuitry are given in the next section.

5.6 Preliminary Experiments

The results of two preliminary experiments performed with air at atmospheric pressure are given in table 5.1, to illustrate the method by which the logarithmic decrement is determined. The corresponding graphs of $\ln \theta$ vs n are shown in figures 5.20 and 5.21. There is no detectable deviation from linearity and it follows that the motion can be treated as damped simple harmonic motion to a very good approximation. It can be seen that the logarithmic decrement is obtained in a very simple and accurate fashion.

The data with the Cu/Be wire were taken with the specification of the viscometer as given in table 5.2. These can be taken as constant throughout the work except for small changes in ℓ (and corresponding changes in D_1 and D_2), when the wire was changed for another from the same source. For the radioactive measurements, d was increased to 1840 ± 10 mm and the wire length was nominally 16.8 mm (Note that the moment of inertia of the disc has not been

corrected for the pinchuck and mirror, but this corresponds only to a systematic error of ~ 0.05 %. This error is also offset to some extent by the comparable error due to the viscous torque on the pinchuck and mirror (also neglected) as can be seen from considering the form of the principal damping term in equation 5.30). The period was observed to be 11.27 s, while that calculated from equation 5.6 is 11.5 ± 0.3 s. The period is expected to be independent of amplitude, and this is observed to within experimental accuracy (< 0.005%). The dependence of the period on the logarithmic decrement is rather different to that for simple harmonic motion, and is predicted to be of the form

$$\frac{T}{T_o} \simeq 1 + \frac{\Delta}{2\pi} \tag{5.63}$$

(Mariens & van Paemel 1956, Kestin & Wang 1957)

rather than the more usual

$$\frac{T}{T_o} \simeq 1 + \tfrac{1}{2}\left(\frac{\Delta}{2\pi}\right)^2 \tag{5.64}$$

The latter variation would not be detectable, whereas the period does, in fact, change with damping. It is, of course, difficult to measure small changes in the period accurately, but the changes seem to agree with equation 5.63 within experimental error. For example, the ratio of the periods for logarithmic decrements of 0.00530 and 0.00206 was observed to be 1.0004 ± 0.0001 compared with a predicted 1.0005. Kestin & Wang (1957) also found equation (5.63) to be a good approximation to their experimental results.

Measurements of the logarithmic decrement were made with various gases and at various pressures to test the theory of the viscometer and to get some idea of the reproducibility. Figures 5.22 and 5.23 show the logarithmic decrement as a function of pressure for air and argon, together with the curve corresponding to equation 5.30. Since it was not possible to achieve a high enough vacuum to measure the damping due to the wire, Δ_o, directly, this has been determined by optimising the fit with equation 5.30 at atmospheric pressure. This gives a value of $\Delta_o = 0.00045 \pm 0.00005$ for the preliminary experiments with air, for example. With the choice of this parameter (which is small enough that relative measurements of viscosity will be insensitive to the value chosen) it can be seen that the agreement is excellent for small boundary layer thicknesses, and still useful up to $\lambda/R \sim 0.5$ (i.e., for air, the pressure range 100-1000 mbar). At low pressures the logarithmic decrement is independent of pressure to within the experimental error.

Figure 5.24 shows data for several gases in the "universal" from $(\Delta-\Delta_o)/\mu$ vs λ/R, which essentially reduces data for all of the gases to the same curve. Note that of the data for large penetration depths, those for helium are the most reliable since the data for air are taken at such a low pressure that the leak rate of the viscometer is appreciable The low pressure behaviour can be described by $\Delta-\Delta_o \approx (125\ \mathrm{kg}^{-1}\ \mathrm{ms})\mu$. Of the two semi-empirical formulae, 5.42 and 5.43, the former is actually in very good agreement with this result, predicting a numerical factor of ≈ 130. The latter is not quite as good, giving a factor of

≈ 75. (Note that both formulae predict a second order dependence on the damping through the period).

Figures 5.22-24 show that the use of the simplified equations 5.30 and 5.44 is entirely adequate for the measurement of small changes in viscosity, and the changes observed on irradiation are discussed in the next section.

5.7 The Effect of Irradiation on Gas Viscosity

To study the effect of irradiation, two ^{147}Pm sources (total activity ∿ 150 mCi) were placed below the disc, giving comparable ionisation levels to the drag balance work at atmospheric pressure. At reduced pressures, the fractional ionisation will increase approximately inversly with pressure. This can be seen by considering the form of equation 4.31. With q and r both being approximately proportional to density, the number density of ions will remain constant with reducing pressure, while the number density of neutral species will fall. The fractional ionisation therefore increases, giving, for example, a fractional degree of ionisation of ∿ 10^{-8} for air at 1 mbar. The ^{210}Po was not used as it was considered unsafe for use in a vacuum. Since the drag on the two halves of the disc is essentially independent, any changes in apparent viscosity correspond approximately to one half of the changes which would be expected with a uniform irradiation of the gas around the disc from a total of ∿ 300 mCi. The results will therefore differ by a factor of two from those for a situation comparable to that of Kestin & Shah's experiments, but this approach is preferable in view of the corresponding simplicity in the experimental proceedure.

A typical set of measurements took the form of several measurements of the damping with the dummy plates in position, several with the active plates in place, followed by a repeat of the null measurements to guard against any shift in calibration. It is also possible to obtain a reliable estimate of the random error. It is essential to avoid any change in calibration during the measurements, and therefore great care is taken to avoid disturbing the alignment of the laser, the perspex front and the phototransistor screen during a series of measurements. With all gases (including zero grade air) the system was vac/purged two or three times before a series of measurements and also on each occasion that the end plate was removed to change the radioactive plates.

The emphasis in the experiments was naturally on zero grade air at low pressure and argon at atmospheric pressure, so that the largest changes reported by Kestin & Shah could be investigated, but some measurements at other pressures and with other gases have been made.

The data obtained are given in tables 5.3-5.9 and a summary of the observed changes in apparent viscosity is given in table 5.10 (in the experiment codes the third letter signifies active (A) measurements with irradiation, or inactive (I) measurements). The errors have been calculated by combining the standard errors for the active and inactive measurements in quadrature and expressing them as a percentage of the null measurements, unless very few data points are available in which case an "educated" estimate is used. (Note that biased and unbiased estimates of

the population standard deviation have been used somewhat indiscriminately, but this does not make an appreciable difference to the error estimates). At high pressure the viscosity has been calculated from equation 5.30, with Δ_o chosen to give good agreement with the nominal viscosity, i.e. that obtained from standard references (Kaye & Laby 1966, Tennent 1971) and extrapolated to the appropriate temperature using Sutherland's law (5.2). Values of Δ obtained at atmospheric pressure are assumed to apply at low pressure, and the viscosity is then calculated using equation 5.44 and the nominal viscosity (note that all low pressure measurements are carried out in the pressure independent regime).

The results show that all changes are consistent with zero change in viscosity, except possibly for the experiments with nitrogen saturated with water vapour. It was thought that clustering might be important in explaining the changes reported by Clark, Kestin & Shah, and these experiments were intended to enhance any such process. However, it can be seen that, if anything, the drag has increaseed. (The results for nitrogen may be slightly less reliable than the others, due to problems with condensation). Some experiments with air/water vapour mixtures were made at low pressure, but it was difficult to control the composition and pressure accurately. In fact, the experiments seemed to be very much more sensitive to slight changes in the partial pressure of the water vapour than to irradiation. It should be noted that no significant changes (< 1%) were observed in preliminary experiments with room air having a signficant humidity.

5.8 Discussion

The torsion disc viscometer and digital circuitry developed have enabled a simple and accurate investigation of the effect

of irradiation on gas viscosity. During the course of the work the equipment functioned extremely reliably, with only two minor malfunctions occuring towards the end of the work. In the first case, one set (of several) of the relay contacts of the temperature digital trip unit failed. In the second, one segment of a seven segment display in the data logging system began to operate intermittently, probably as a result of a dry solder joint in the circuit. This did not, however, lead to any ambiguity in the recorded data. It should also be noted that on two occasions during the particularly violent thunderstorm this summer, the lightning flashes were sufficiently intense to trigger all of the phototransistors, thus resetting the system in mid-experiment.

The results suggest that there are no significant changes in viscosity due to irradiation. If we look at the reported precision of Kestin & Shah's experiments, we can see that in comparable experiments we get precisions of 1% and 1.8% in C. This presumably means that the precision in the changes of viscosity is $\sim$ 1.4% and $\sim$ 2.5% and comparing with the present work (allowing for the factor of two difference) we can see that the precision has been improved in all cases, and for the most important experiments the precision has improved by a factor of $\sim$ 3 (argon, 1 atmosphere) to $\sim$ 11 (low pressure air).

There are obviously several anomalies when we compare the two sets of data, and in chapter 7 an attempt will be made to account for the discrepancies.

5.9 Conclusion

The present work represents the most accurate and reliable investigation to date on the effect of irradiation on gas viscosity. With the viscometer and data logging circuit it has been possible to make simple determinations of the relative viscosity, minimising the possibility of systematic errors in the changes of viscosity and allowing reliable estimates of the random error. No significant reductions in viscosity were observed with radioactive irradiation of the gas.

Table 5.1

Sample Calculations of Logarithmic Decrement

Experimental Results

	36 SWG Piano Wire	38 SWG Cu/Be Wire
n_1	96	74
n_2	192	149
n_3	289	223
n_4	387	297
T_L	2.3255	5.5289
T_R	2.3810	5.6082

Calculated Parameters

δx/mm	-6.04	-3.62
Δ	0.004099	0.005341
r^2	0.999985	0.999996

Table 5.2

Specifications of Torsion Disc Viscometer

(precision as indicated by significant figures unless stated otherwise.)

Disc

mass = 47.15 g

R = 42.49 mm

h = 1.00 mm

centre hole 3 mm radius (OBA clearance)

$I = 4.28 \times 10^{-5}$ kg m^2

Wire

Copper/Beryllium 38 SWG nominal diameter 0.152 mm

$d_w = 0.148 \pm 0.001$ mm

l = 16 cm

$E = 1.17 \times 10^{11}$ Pa

$\sigma = 0.35$

Viscometer

B = 4.9 cm

$D_1 = 9.5 \pm 0.5$ cm

$D_2 = 21$ cm

Data Logging System

$d = 1820 \pm 10$ mm

$x_0 = 750.0 \pm 0.2$ mm

$x_1 = 488.5$ "

$x_2 = 323.0$

$x_3 = 214.5$

$x_4 = 143.0$

Table 5.3

ZERO GRADE AIR - ATMOSPHERIC PRESSURE

Δ_o = 0.00033 T = 11.582 s ρ = 1.184 kgm^{-3}
at 25°C and 1013 mbar. Test temperature = 25.05 ± 0.05 °C.
(Nominal viscosity $\mu = 1.86 \times 10^{-5}$ $kgm^{-1}s^{-1}$)

Expt. Code	P/mbar	Δ	r^2	$10^5 \mu$ /($kgm^{-1}s^{-1}$)
AAI0171	1020	0.005295	0.999985	1.850
AAI0172	1020	5292	57	1.848
AAI0173	1020	5301	91	1.853
AAI0174	1020	5317	83	1.862
AAI0271	1013	5285	73	1.851
AAI0272	1013	5296	75	1.857
AAI0273	1013	5309	82	1.864
AAI0471	1018	5291	77	1.849
AAI0472	1018	5299	63	1.854
AAI0473	1018	5301	64	1.855
AAA0475	1018	5315	67	1.863
AAA0571	1021	5314	94	1.859
AAA0572	1021	5317	83	1.861
AAA0573	1021	5312	83	1.857
AAA0574	1021	5285	91	1.843
AAA0575	1021	5295	62	1.849
AAA0576	1021	5290	60	1.846
AAI0671	1018	5308	81	1.859
AAI0672	1018	5316	71	1.863
AAI0673	1018	5297	66	1.853
AAI0674	1018	5301	67	1.855
AAI0675	1018	5309	67	1.859
AAI0676	1018	5326	48	1.869
AAI0677	1018	5281	43	1.844

Table 5.4

ZERO GRADE AIR - 10 mbar PRESSURE

Δ_o = 0.00033 at 25°C. Test temperature = 25.05 ± 0.05 °C.

Test pressure = 10.0 ± 0.5 mbar.

(Nominal viscosity $\mu = 1.86 \times 10^{-5} kgm^{-1}s^{-1}$)

Expt. Code	Δ	r^2	$10^5\ \mu/(kgm^{-1}s^{-1})$
AMI0772	0.0026195	0.999986	1.8554
AMI0773	26211	82	1.8567
AMI0871	26240	64	1.8590
AMA0872	26302	73	1.8641
AMA0873	26235	73	1.8586
AMA0874	26281	76	1.8624
AMA0971	26242	87	1.8592
AMI0972	26286	75	1.8628
AMI0973	26323	69	1.8658
AMI0974	26257	84	1.8604

Table 5.5

ZERO GRADE AIR - 2 mbar PRESSURE

Δ_o = 0.00025. Test temperature = 25.05 ± 0.05 °C.

Test pressure = 2.0 ± 0.2 mbar.

Nominal viscosity $\mu = 1.86 \times 10^{-5} kgm^{-1}s^{-1}$.

Expt. Code	Δ	r^2	$10^5\ \mu/(kgm^{-1}s^{-1})$
ALI1471	0.0025687	0.999961	1.8560
ALI1472	25761	85	1.8613
ALI1473	25810	72	1.8648
ALI1571	25651	53	1.8534
ALI1572	25710	58	1.8576
ALI1671	25788	72	1.8633
ALA1771	25720	82	1.8583
ALA1971	25814	63	1.8651
ALA2072	25711	35	1.8577
ALA2073	25673	28	1.8549
ALA2171	25702	67	1.8570
ALA2172	25712	84	1.8578
ALI2173	25695	70	1.8565
ALI2174	25806	82	1.8646
ALI2271	25780	41	1.8627

Table 5.6

ARGON - ATMOSPHERIC PRESSURE

Δ_o = 0.00050 T = 11.625 s ρ = 1.633 kgm^{-3}

at 25°C and 1013 mbar. Test temperature = 25.05 ± 0.05 °C.

(Nominal viscosity $\mu = 2.22 \times 10^{-5} kgm^{-1}s^{-1}$)

Expt. Code	P/mbar	Δ	r^2	$10^5\ \mu/(kgm^{-1}s^{-1})$
RAI2842	1035	0.006846	0.999997	2.245
RAI2843	1035	6808	96	2.224
RAI2844	1035	6794	93	2.216
RAI2845	1035	6793	93	2.216
RAI2846	1035	6802	97	2.221
RAI0351	1001	6785	74	2.254
RAI0352	1001	6761	90	2.240
RAI0353	1001	6733	91	2.224
RAI0354	1001	6758	89	2.238
RAI0452	1005	6757	81	2.232
RAI0453	1005	6755	89	2.230
RAA0652	1013	6795	93	2.243
RAA0653	1013	6791	92	2.241
RAA0654	1013	6804	88	2.248
RAA0655	1013	6800	87	2.245
RAA0752	1020	6771	98	2.222
RAA0753	1020	6787	83	2.230
RAA0754	1020	6781	90	2.227
RAA0755	1020	6797	86	2.236

Table 5.7

ARGON - 8 mbar PRESSURE

Δ_o = 0.00025. Test temperature = 25.05 ± 0.05 °C.

Test pressure = 8.4 ± 0.2 mbar.

Nominal viscosity $\mu = 2.22 \times 10^{-5} kgm^{-1}s^{-1}$.

Expt. Code	Δ	r^2	$10^5\ \mu/(kgm^{-1}s^{-1})$
RLI2873	0.003096	0.999981	2.219
RLI2874	3097	67	2.220
RLI2972	3094	79	2.218
RLI2973	3098	72	2.221
RLA2974	3119	52	2.237
RLA3071	3070	81	2.199
RLA3072	3099	38	2.222
RLA3171	3104	70	2.225
RLI3172	3107	54	2.228
RLI3173	3106	65	2.227
RLI0181	3087	96	2.212
RLI0182	3090	69	2.215

Table 5.8

CARBON DIOXIDE - 6 mbar PRESSURE

Δ_o = 0.00033. Test temperature = 25.05 ± 0.05 °C.

Test pressure = 5.9 ± 0.3 mbar.

Nominal viscosity $\mu = 1.48 \times 10^{-5} kgm^{-1}s^{-1}$.

Expt. Code	Δ	r^2	$10^5\ \mu/(kgm^{-1}s^{-1})$
CLI0281	0.0021982	0.999982	1.479
CLI0282	22007	84	1.481
CLI0381	21999	84	1.480
CLA0383	22062	91	1.485
CLA0481	22185	56	1.495

Table 5.9

NITROGEN SATURATED WITH WATER VAPOUR - ATMOSPHERIC PRESSURE

Δ_o = 0.00033. Test temperature = 25.05 ± 0.05 °C.

ρ = 1.145 kgm^{-3} at 1013 mbar. T = 11.581 s .

Nominal viscosity $\mu = 1.79 \times 10^{-5} kgm^{-1}s^{-1}$.

Expt. Code	P/mbar	Δ	r^2	$10^5\ \mu/(kgm^{-1}s^{-1})$
WAI1182	1020	0.005222	0.999983	1.840
WAI1183	1019	5207	79	1.832
WAI1184	1019	5193	98	1.825
WAI1185	1018	5193	81	1.826
WAI1186	1018	5189	80	1.823
WAI1282	1012	5148	1.000000	1.805
WAI1283	1012	5187	0.999991	1.828
WAA1284	1012	5185	97	1.826
WAA1382	1009	5208	85	1.843
WAA1383	1008	5206	84	1.843
WAA1384	1008	5230	72	1.857
WAA1385	1007	5194	99	1.836
WAA1386	1007	5204	65	1.842
WAA1481	1015	5205	96	1.839
WAI1482	1012	5188	92	1.828
WAI1681	1011	5176	90	1.822
WAI1682	1011	5182	70	1.826

Table 5.10

Summary of Results

Gas	Pressure	Viscosity (10^5 $\mu/kgm^{-1}s^{-1}$) Inactive	Active	% Change in Gas Viscosity
Air	1 Atmosphere	1.8556±0.0016	1.8540±0.0030	-0.09 ± 0.18
Air	10.0±0.5 mbar	1.8600±0.0016	1.8611±0.0026	+0.06 ± 0.11
Air	2.0±0.2 mbar	1.8600±0.0014	1.8585±0.0014	-0.08 ± 0.11
Ar	1 Atmosphere	2.2309±0.0036	2.2365±0.0033	+0.25 ± 0.22
Ar	8.4±0.2 mbar	2.2200±0.0019	2.2208±0.0079	+0.04 ± 0.37
CO_2	5.9±0.3 mbar	1.480 ±0.002	1.489 ±0.005	+0.6 ± 0.4
N_2(sat)	1 Atmosphere	1.8267±0.0028	1.8412±0.0041	+0.79 ± 0.27

Appendix

IC List and Pinouts

TIL 313	7 Segment LED display
555	Timer
4001	Quad 2i/p NOR
4002	Dual 4i/p NOR
4011	Quad 2i/p NAND
4016	Quad Switch
4027	Dual JK Flip Flop
4069	Hex NOT
4070	Quad 2i/p EX-OR
4510	BCD Counter
4511	BCD 7 Segment Display Driver
50395	Six Decade Counter/Display Driver

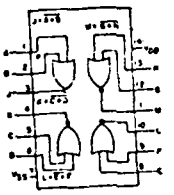

4001BE

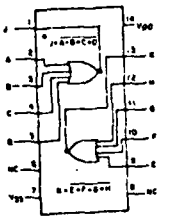

4002BE

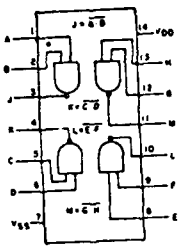

4011BE

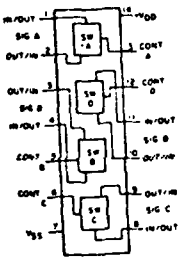

4016BE

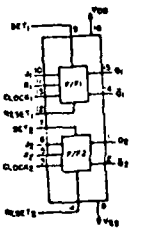

4027BE

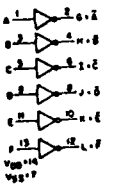

4069UBE

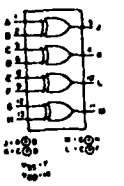

4070BE

555 timer

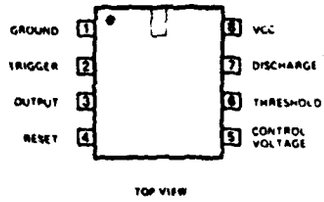

TIL 313 DISPLAY

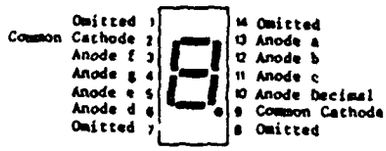

4510

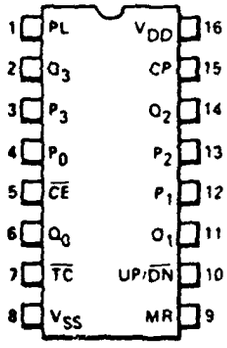

PL	Parallel Load Input (Active HIGH)
P_0-P_3	Parallel Inputs
$\overline{CE}$	Count Enable Input (Active LOW)
CP	Clock Pulse Input (L → H Edge-Triggered)
$U_D/\overline{D_N}$	Up/Down Count Control Input
MR	Master Reset Input
$\overline{TC}$	Terminal Count Output (Active LOW)
Q_0-Q_3	Parallel Outputs

4511

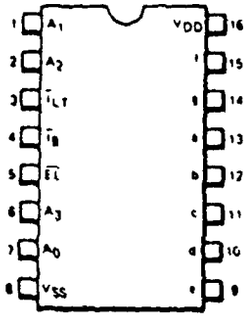

A_0-A_3	Address (Data) Inputs
$\overline{EL}$	Latch Enable (Active LOW) Input
$\overline{I_B}$	Blanking (Active LOW) Input
$\overline{I_{LT}}$	Lamp Test (Active LOW) Input
a-g	Segment Outputs

MK50395 SIX DECADE COUNTER/DISPLAY DRIVER

A six decade synchronous up/down counter and display driver with a compare register and storage latches. The counter features look-ahead carry or borrow and multiplexed BCD and seven segment outputs with direct LED segment drive and leading zero blanking. Connect a 330pF capacitor between pins 21 and 1, +12V DC to pin 1 and ground to pin 22.

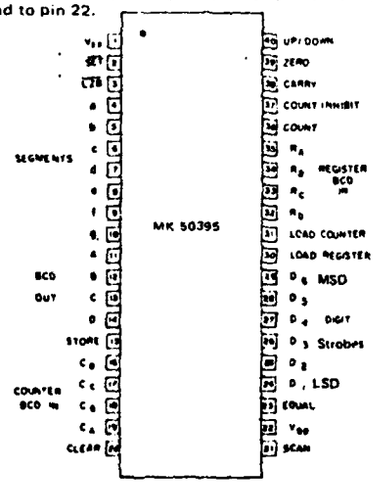

Supply current:	30mA max
Output current digit strobes:	3mA max
segment outputs:	10mA max
Count input frequency:	1MHz max

555 timer

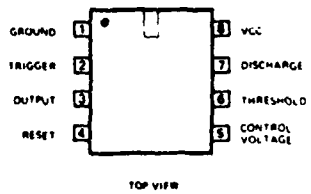

TIL 313 DISPLAY

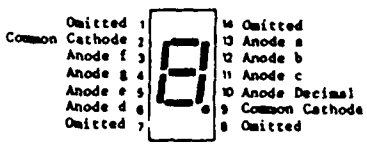

4510

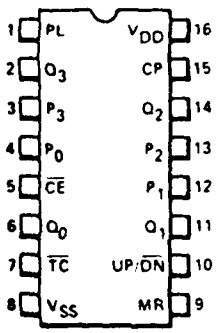

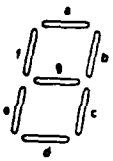

PL	Parallel Load Input (Active HIGH)
P_0-P_3	Parallel Inputs
$\overline{CE}$	Count Enable Input (Active LOW)
CP	Clock Pulse Input (L → H Edge-Triggered)
Up/$\overline{Dn}$	Up/Down Count Control Input
MR	Master Reset Input
$\overline{TC}$	Terminal Count Output (Active LOW)
Q_0-Q_3	Parallel Outputs

4511

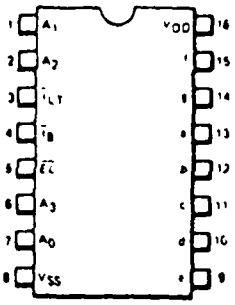

A_0-A_3	Address (Data) Inputs
$\overline{EL}$	Latch Enable (Active LOW) Input
$\overline{I_B}$	Blanking (Active LOW) Input
$\overline{I_{LT}}$	Lamp Test (Active LOW) Input
a-g	Segment Outputs

MK50395 SIX DECADE COUNTER/DISPLAY DRIVER

A six decade synchronous up/down counter and display driver with a compare register and storage latches. The counter features look-ahead carry or borrow and multiplexed BCD and seven segment outputs with direct LED segment drive and leading zero blanking. Connect a 330pF capacitor between pins 21 and 1, +12V DC to pin 1 and ground to pin 22.

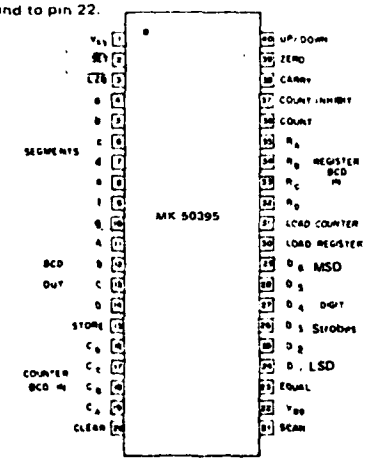

Supply current:	30mA max
Output current digit strobes:	3mA max
segment outputs:	10mA max
Count input frequency	1MHz max

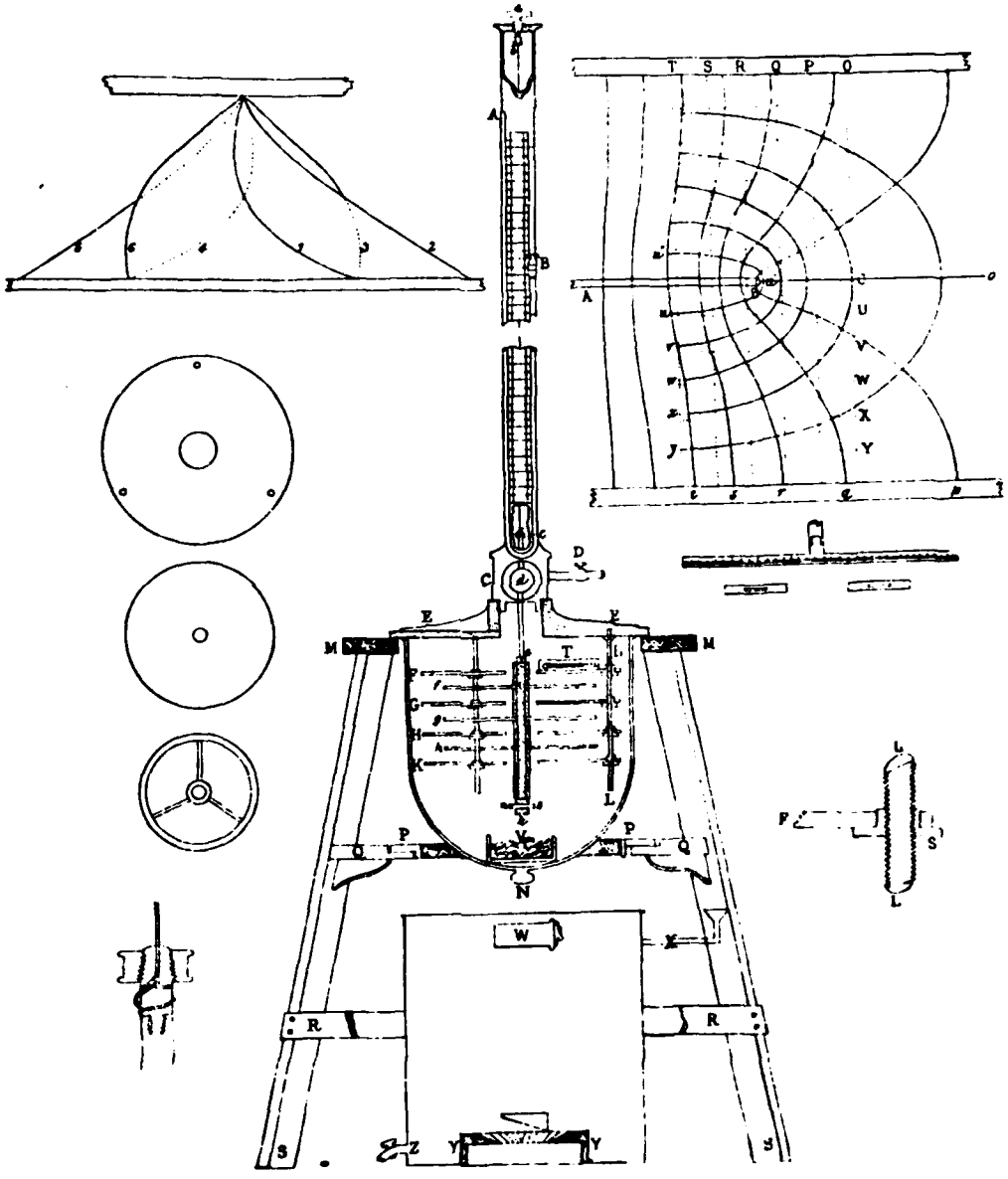

Figure 5·1. Maxwell's Viscometer.

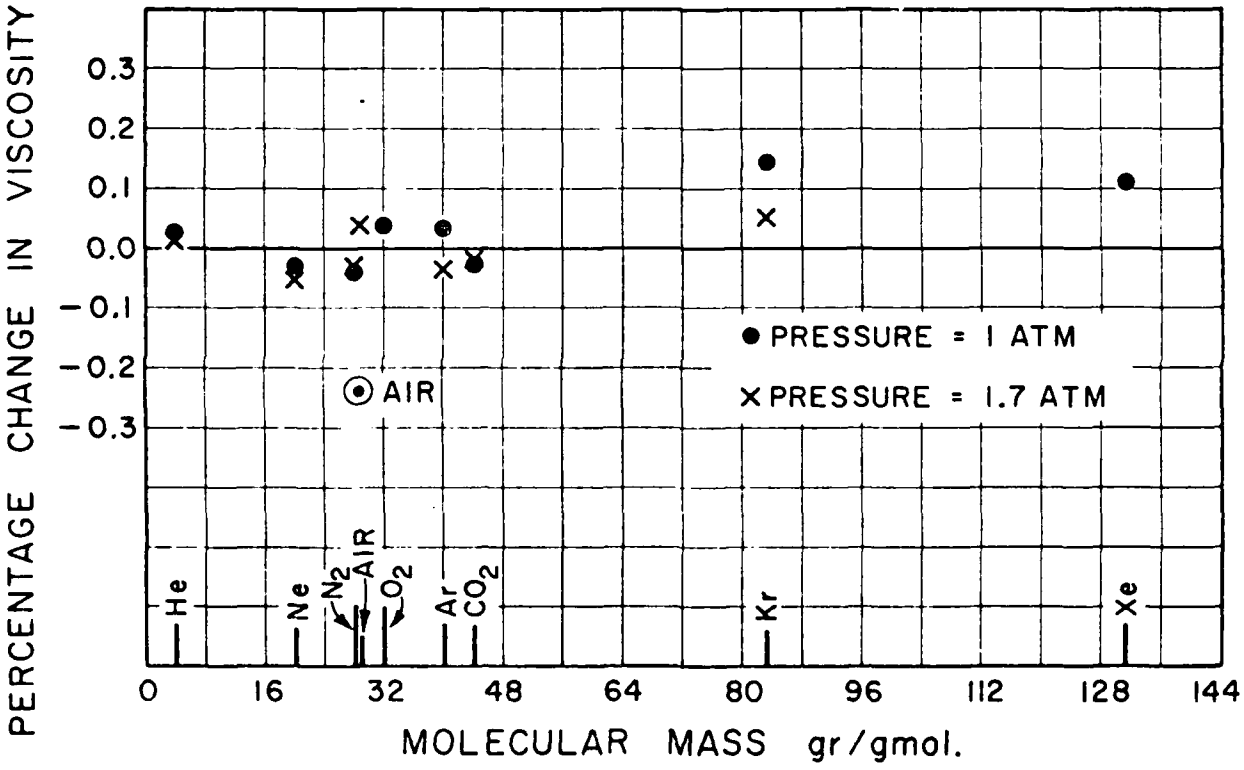

Figure 5·2. PERCENTAGE CHANGE IN THE APPARENT VISCOSITY DUE TO EXTERNAL IRRADIATION WITH CESIUM SOURCE (Cs−137)—SERIES 2 (after Kestin & Shah 1968).

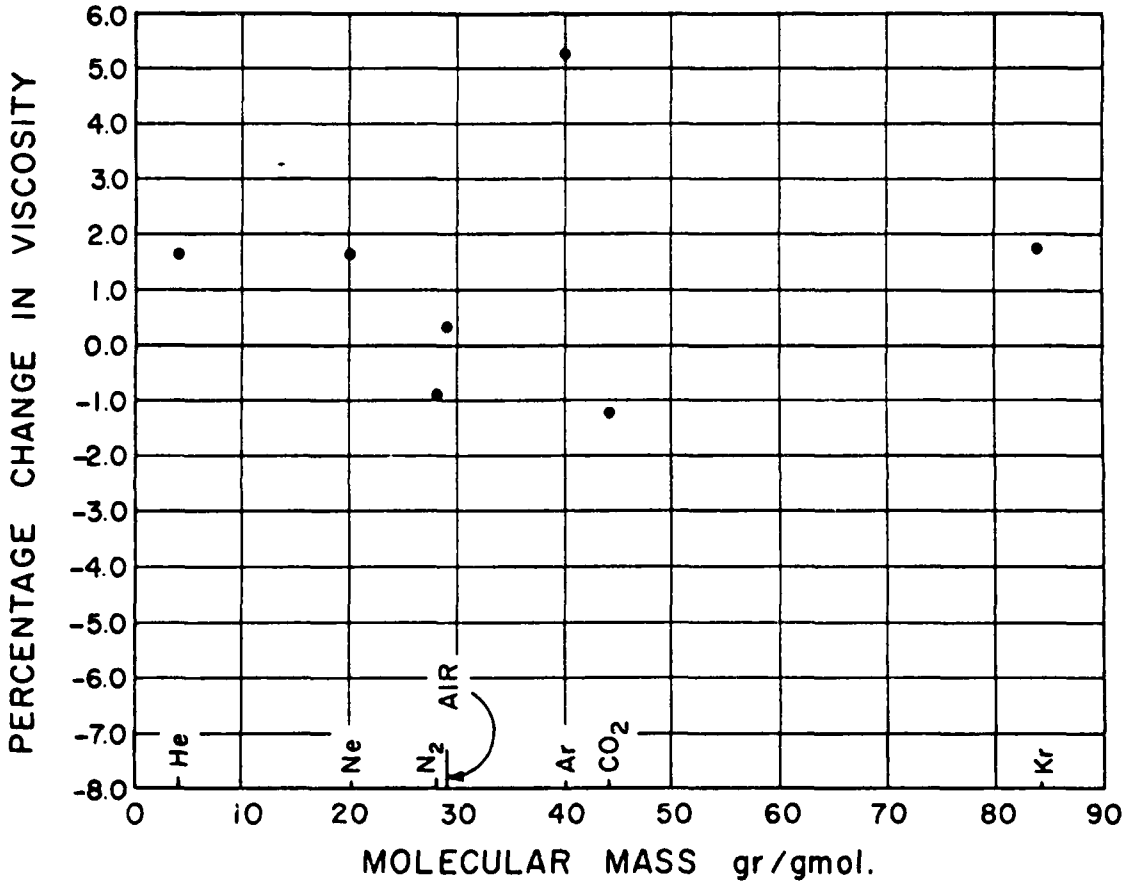

Figure 5·3. PERCENTAGE CHANGE IN THE APPARENT VISCOSITY DUE TO IRRADIATION AT THE GAS–SOLID INTERFACE FROM Po–210 COATING (1ATM)–SERIES 3 (after Kestin & Shah 1968).

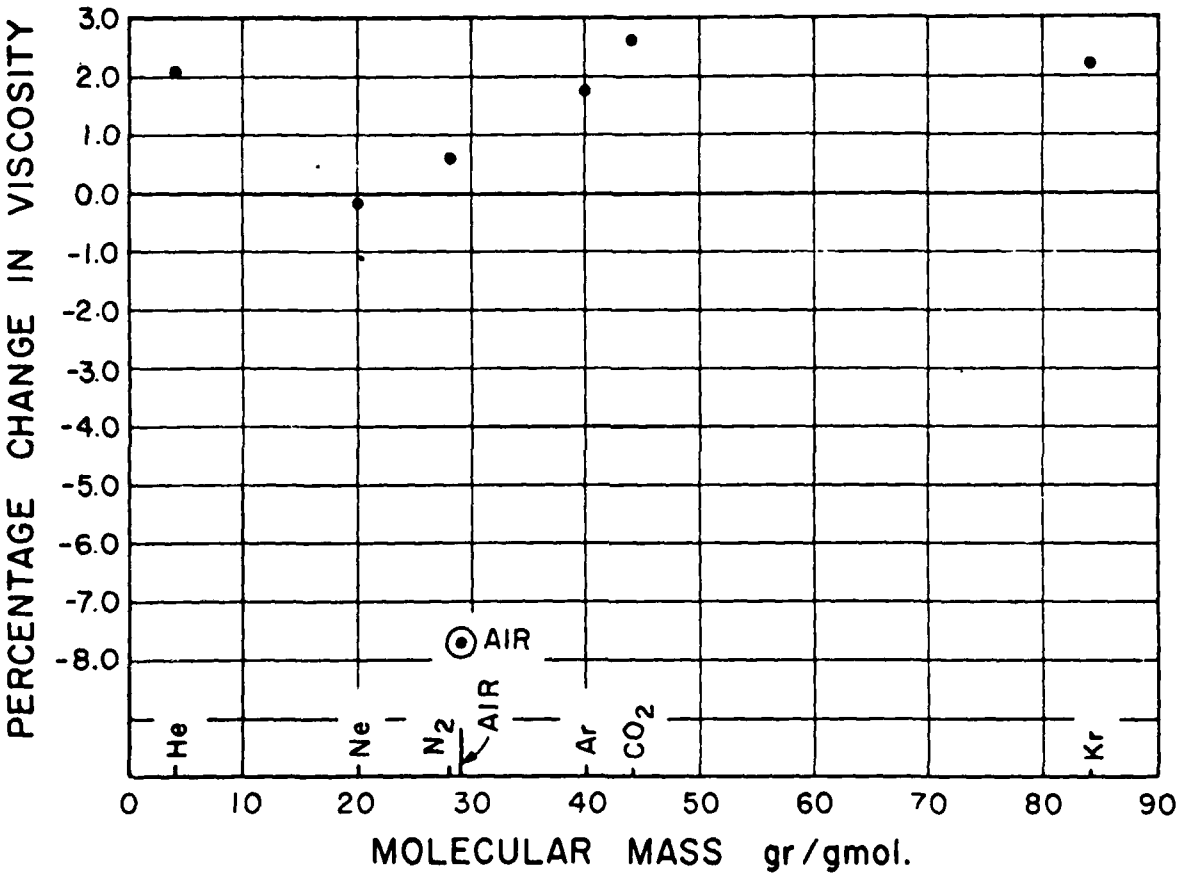

Figure 5·4. PERCENTAGE CHANGE IN THE APPARENT VISCOSITY DUE TO IRRADIATION AT THE GAS—SOLID INTERFACE FROM Po—210 COATING (1 mm Hg.) SERIES 4 (after Kestin & Shah 1968).

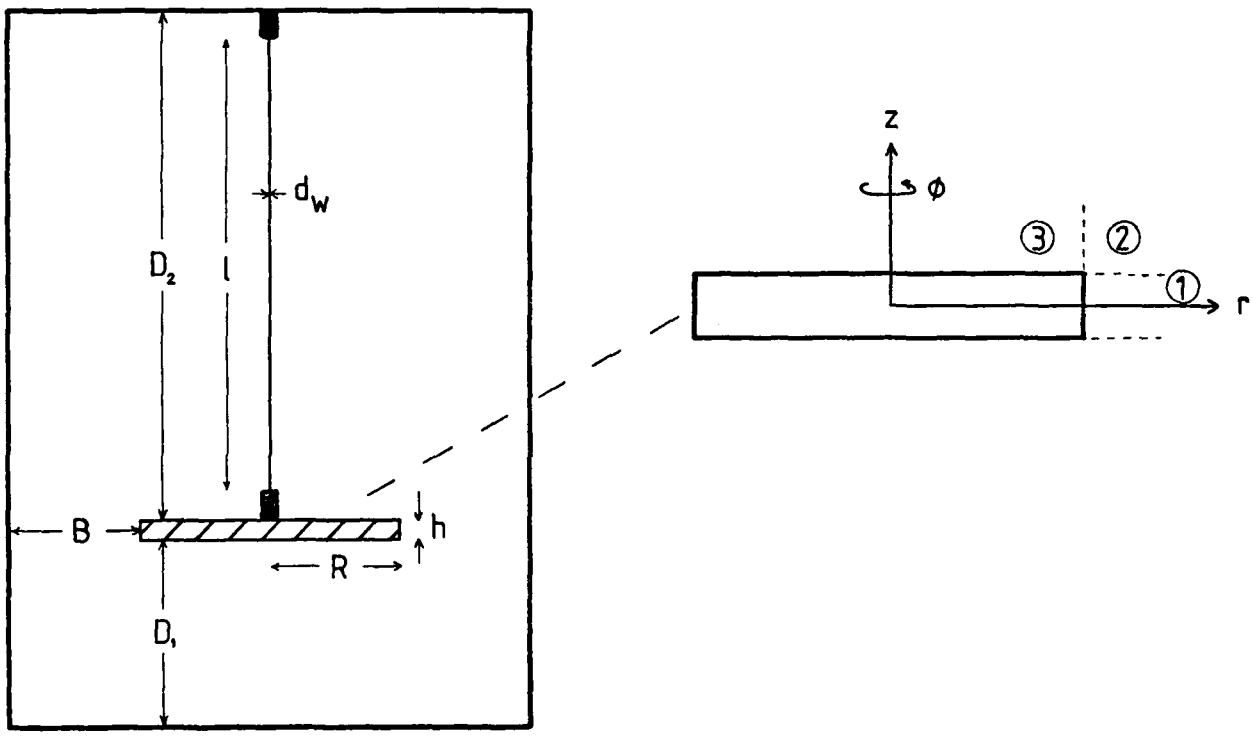

Figure 5·5. Schematic Diagram and Co-ordinate System of Viscometer.

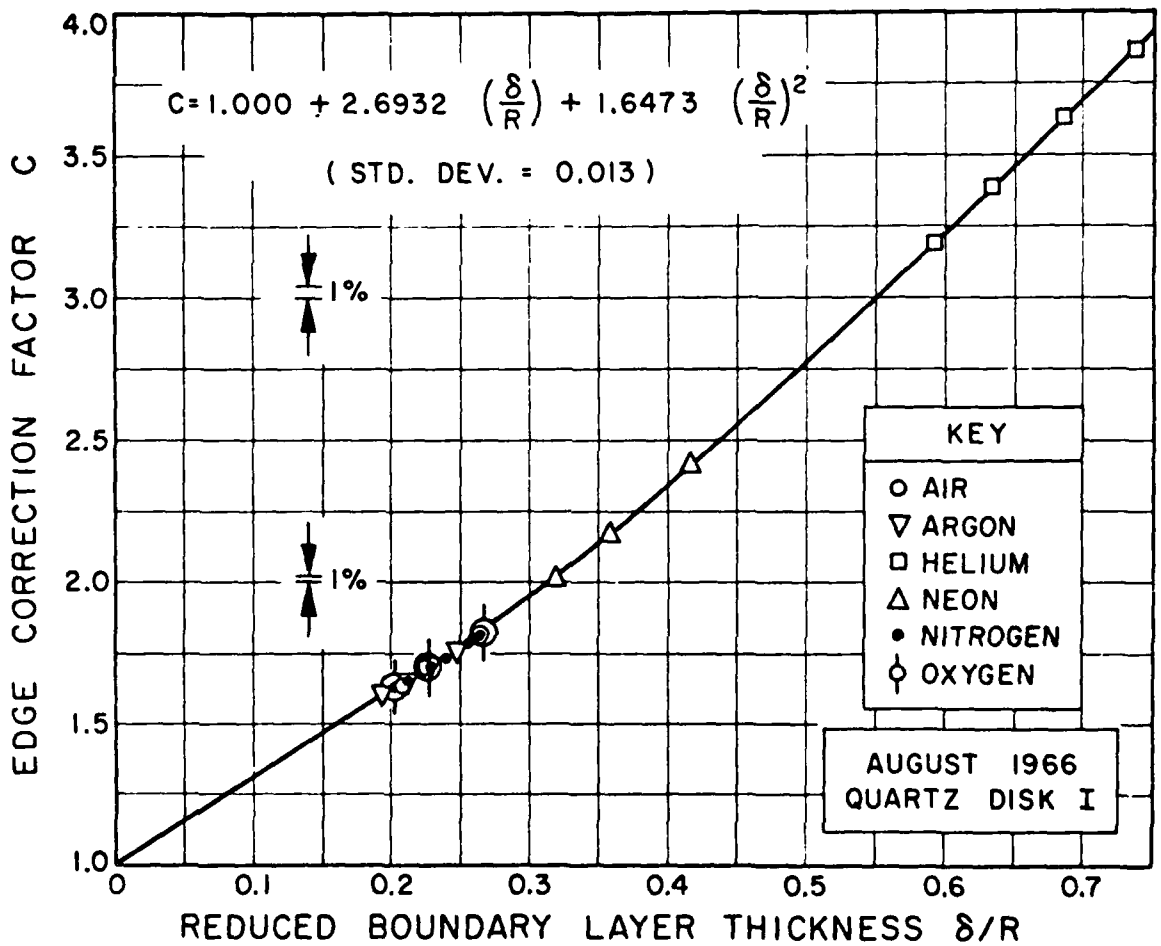

Figure 5·6. CORRECTION FACTOR AS A FUNCTION OF REDUCED BOUNDARY-LAYER THICKNESS — SERIES I (after Kestin & Shah 1968).

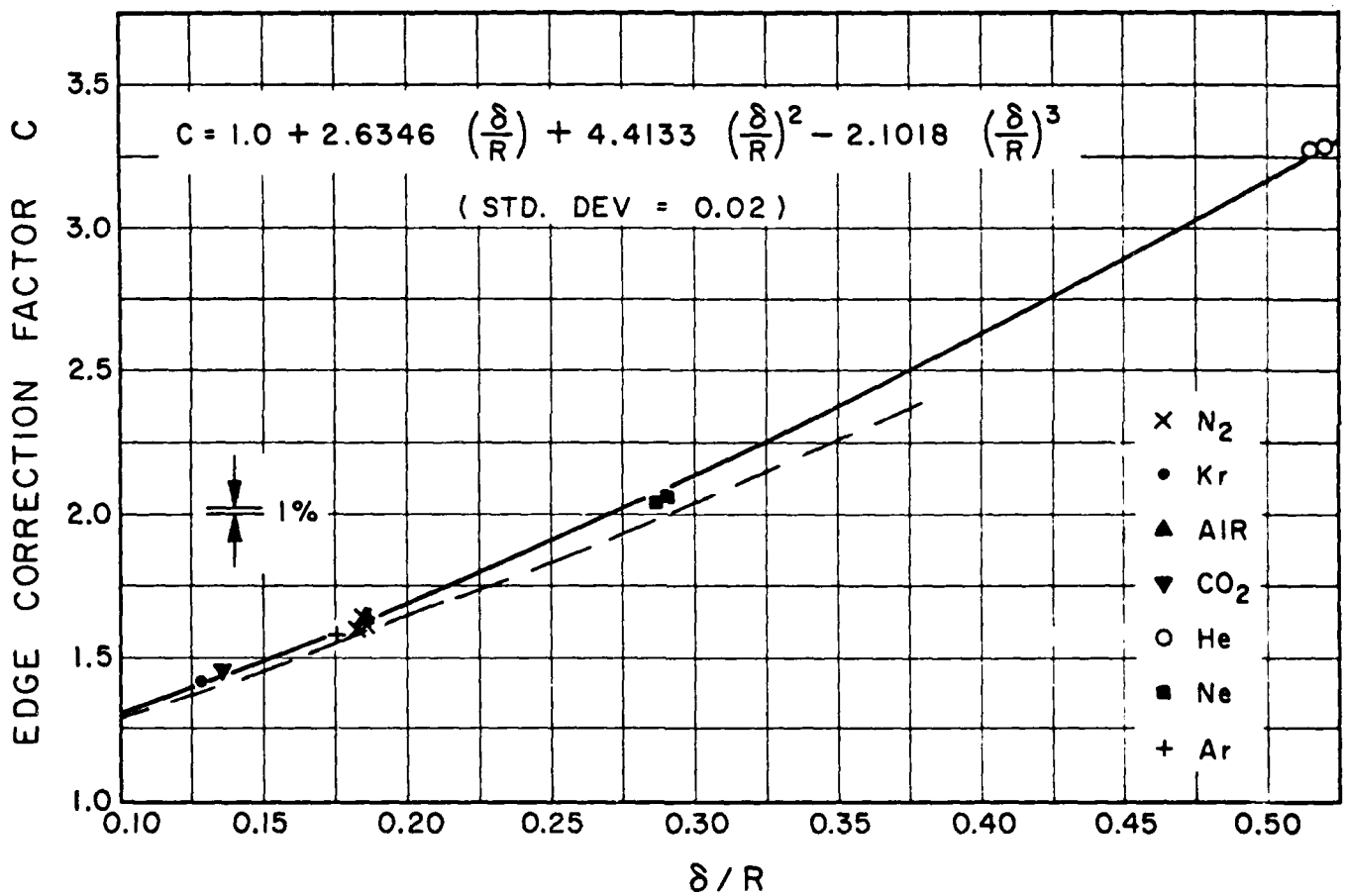

Figure 5·7. CORRECTION FACTOR C AS A FUNCTION OF RATIO OF BOUNDARY-LAYER THICKNESS TO DISK RADIUS (1 ATM.) — SERIES 3 (after Kestin & Shah 1968, broken line - correction factor predicted by equation 5·30).

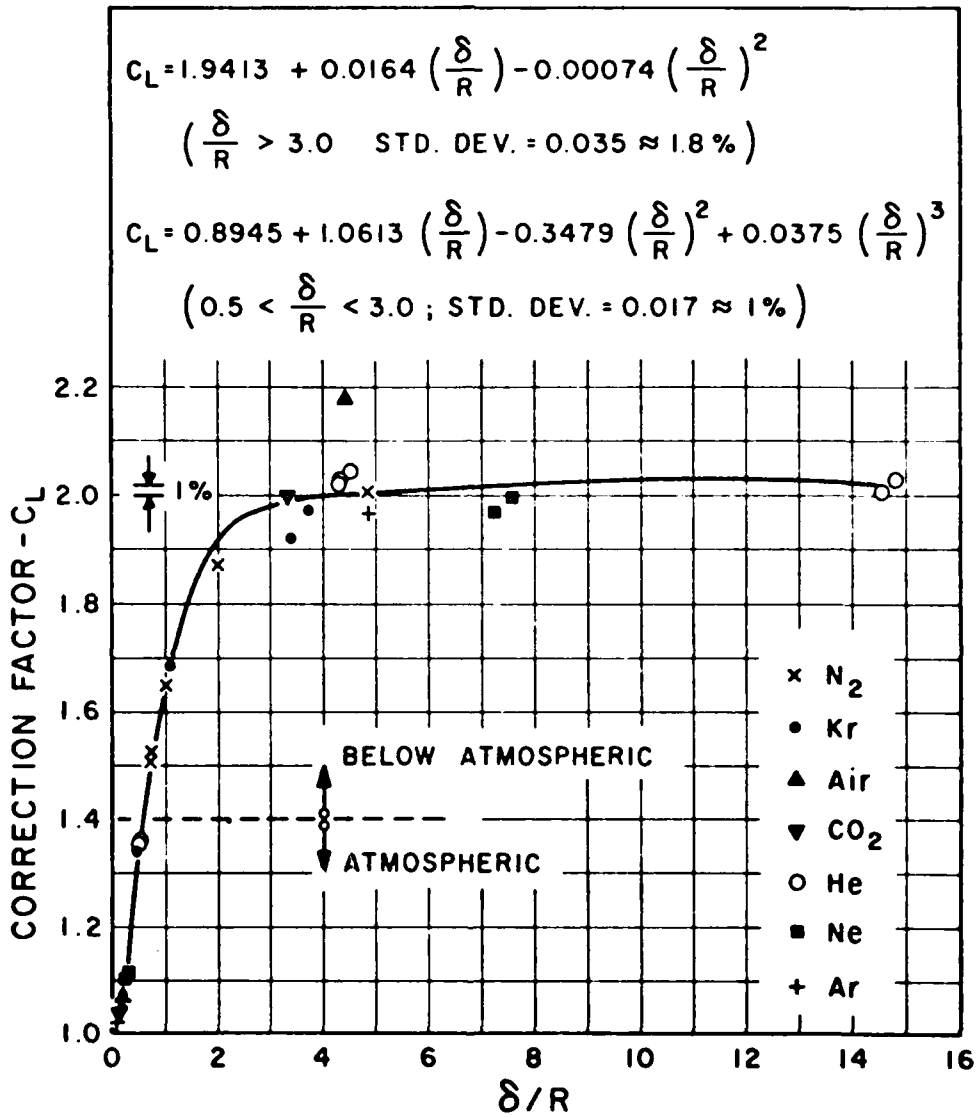

Figure 5·8. CORRECTION FACTOR - C_L AS A FUNCTION OF RATIO OF BOUNDARY—LAYER THICKNESS TO DISK RADIUS — SERIES 4 (after Kestin & Shah 1968).

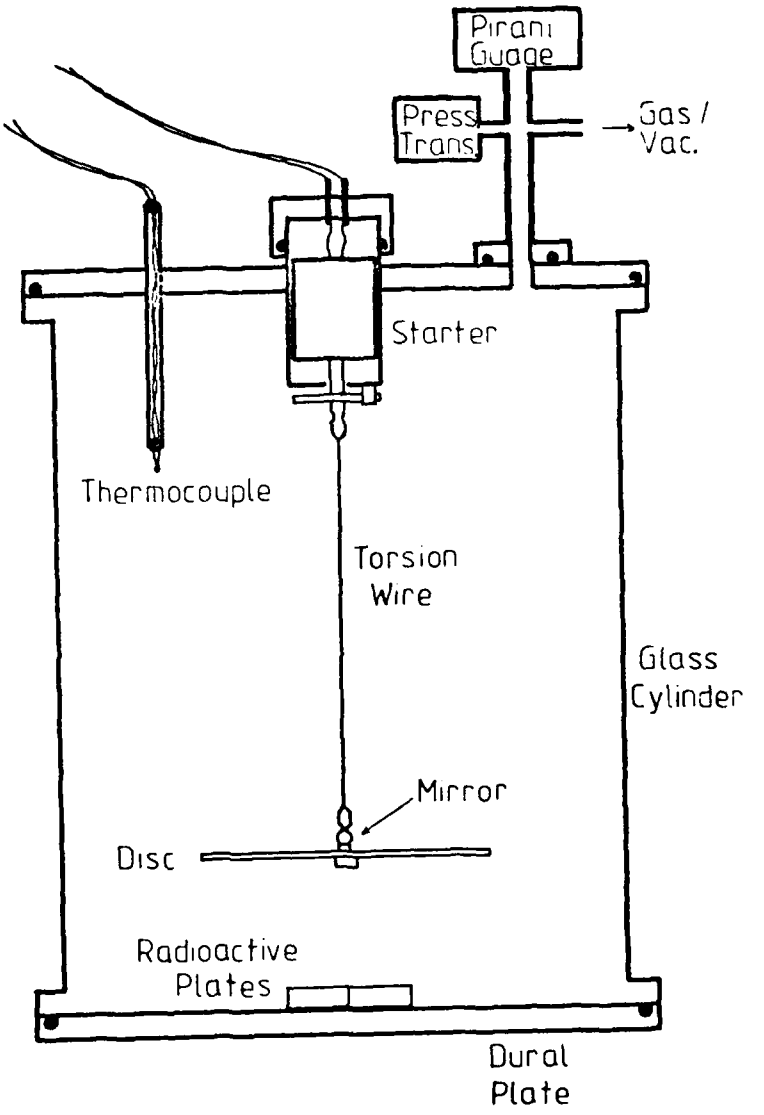

Figure 5·9. Torsion Disc Viscometer.

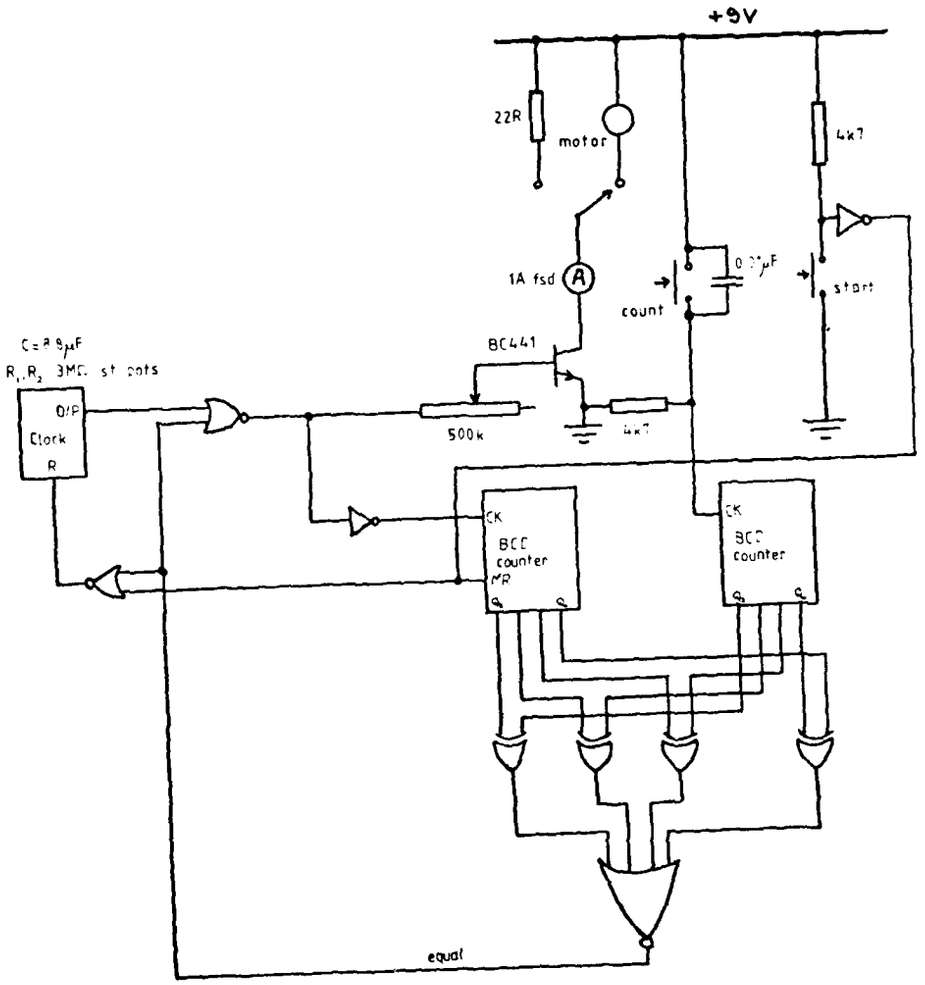

Figure 5·10. Schematic Diagram of Starter Circuit.

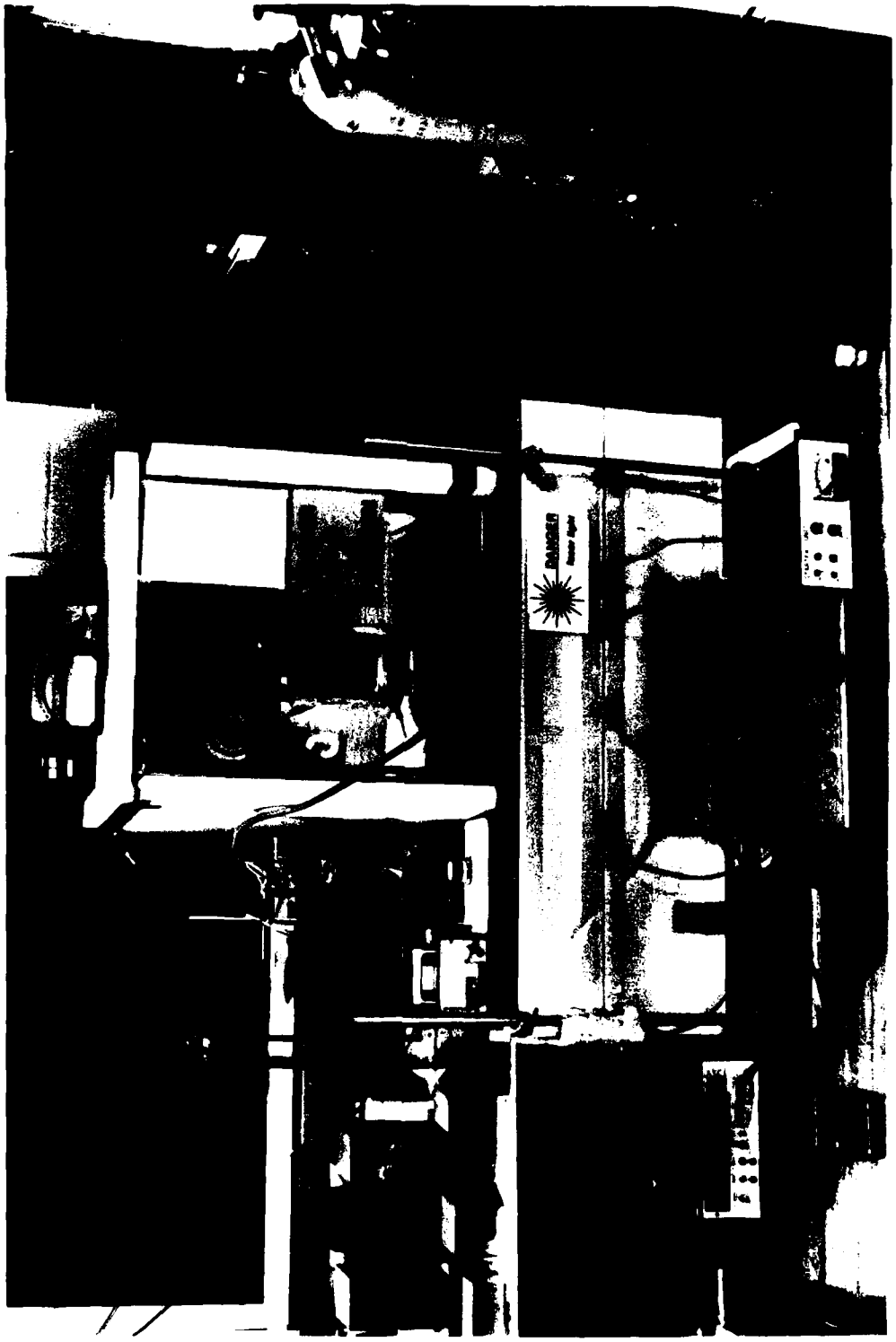

ure 5.11 Torsion Disc Viscometer: This photograph shows the torsion disc viscometer in its ystyrene and dexion constant temperature enclosure. The gas cylinders and vacuum pump used be seen to the right, with the data logging circuitry at the front.

Figure 5.12 Close up of Torsion Disc: This close up shows the disc wire in the glass housing. The contrast is not particularly good, but the disc, mirror and pinchuck can be seen with the two radioactive sources (^{147}Pm) below the disc.

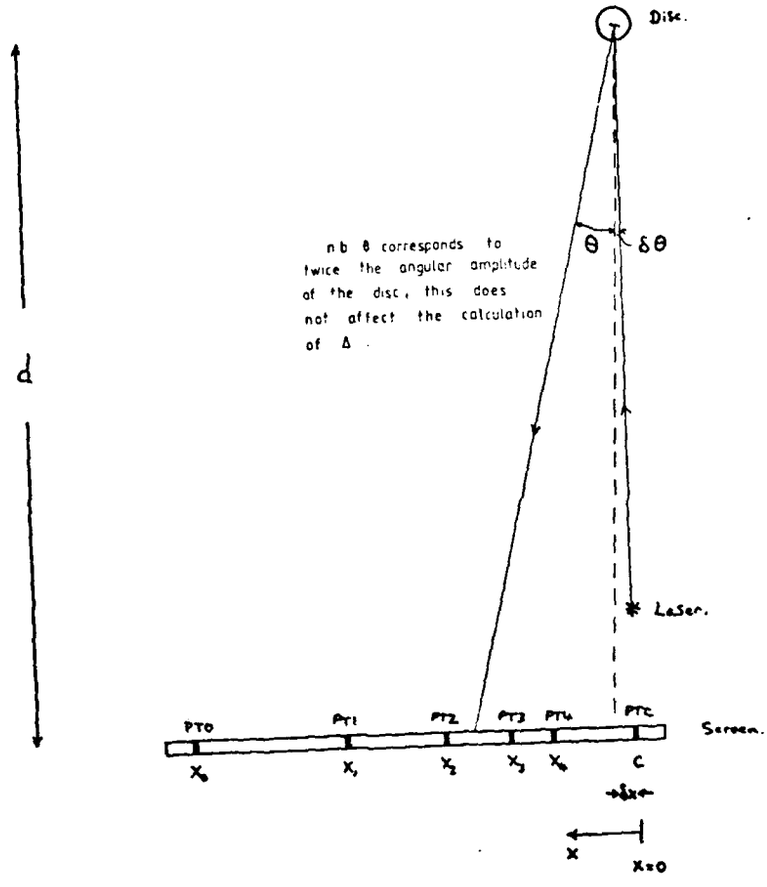

Figure 5·13. Experimental Configuration.

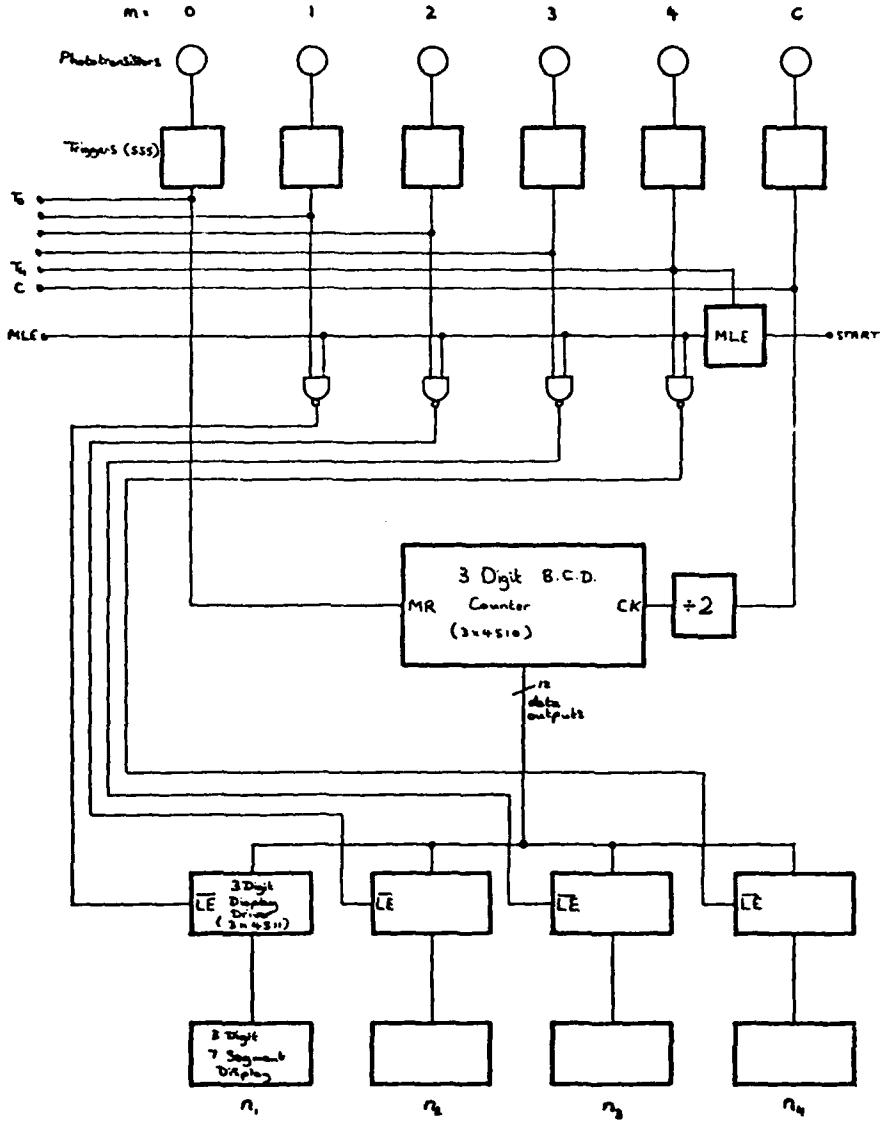

Figure 5·14. Schematic Diagram of Data-Logging Circuit :- Counters.

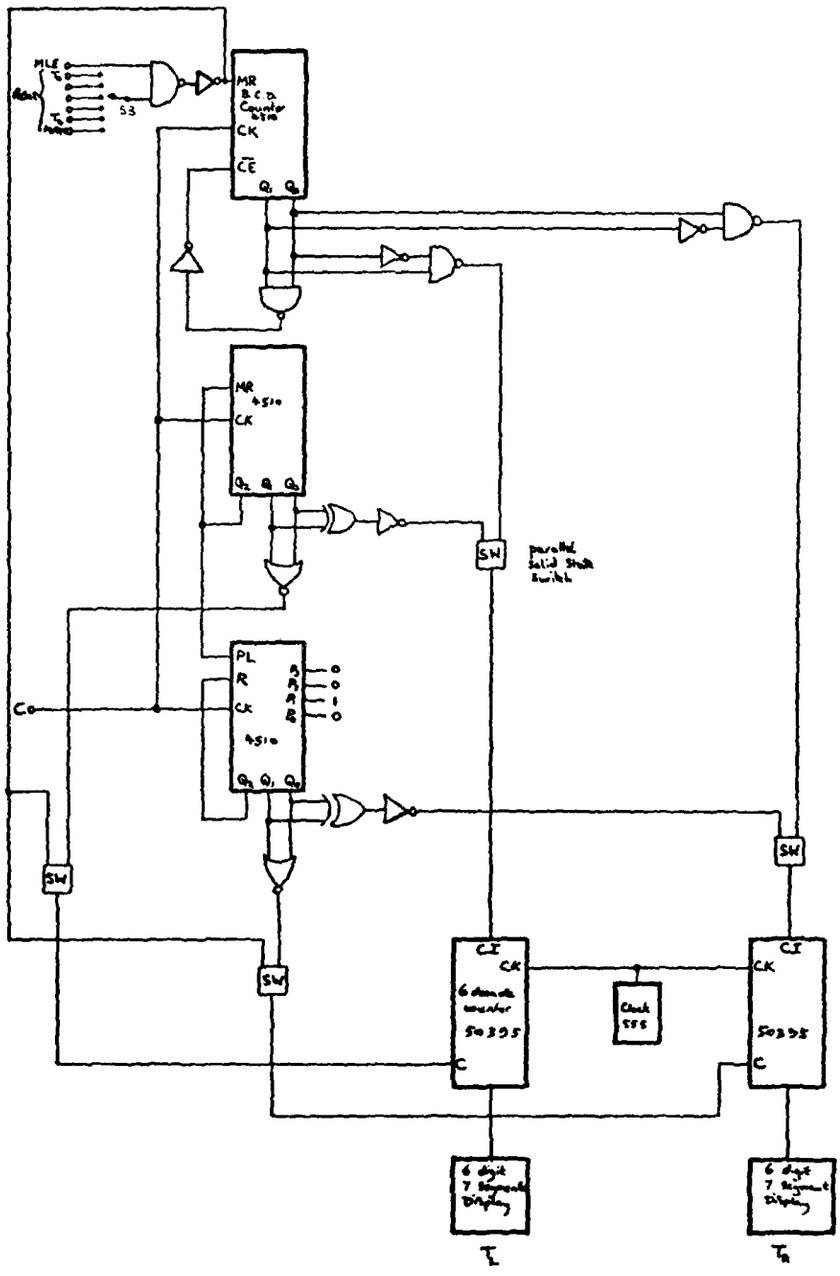

Figure 5·15. Schematic Diagram of Data - Logging Circuit :- Timers .

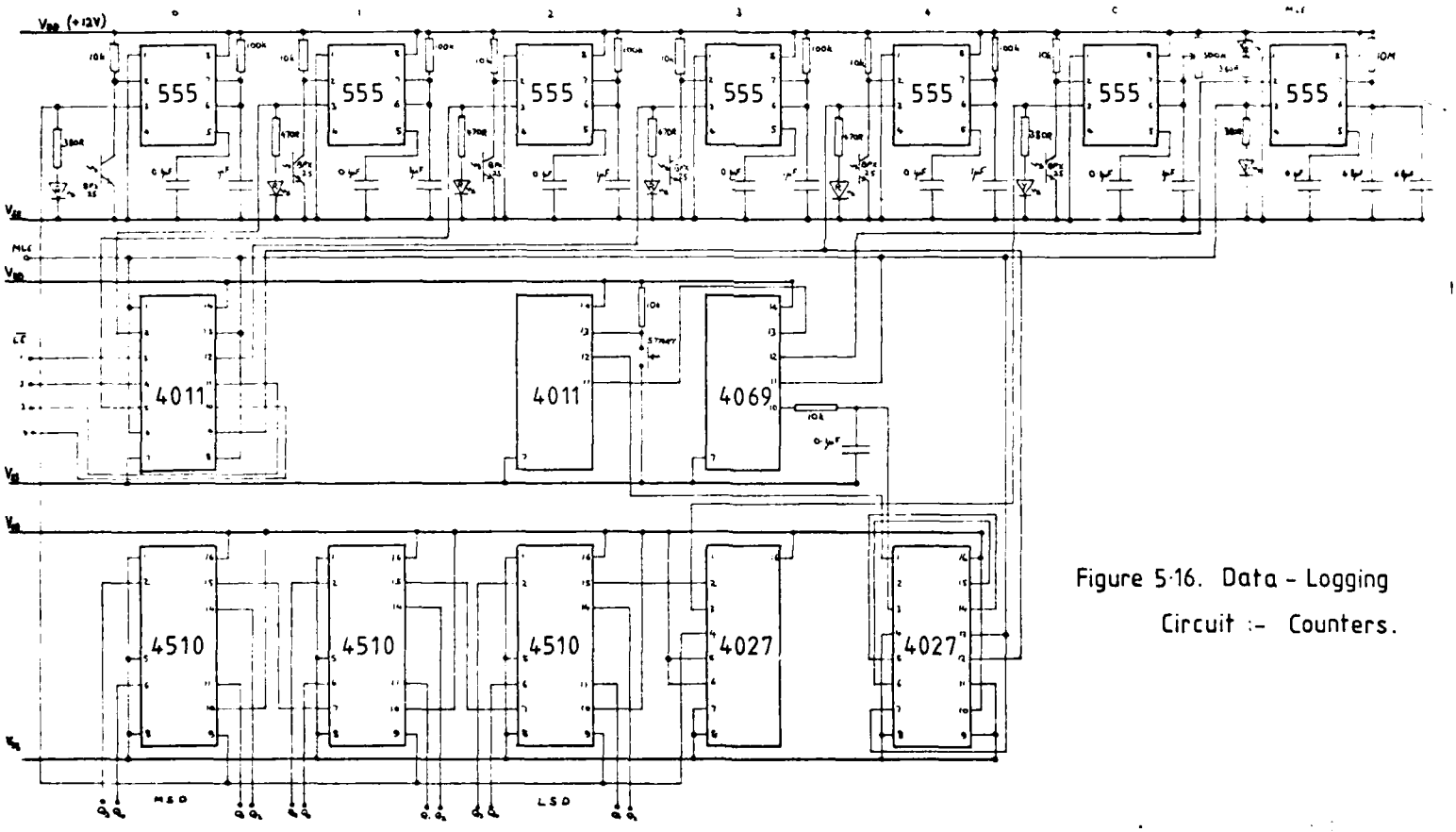

Figure 5·16. Data - Logging Circuit :- Counters.

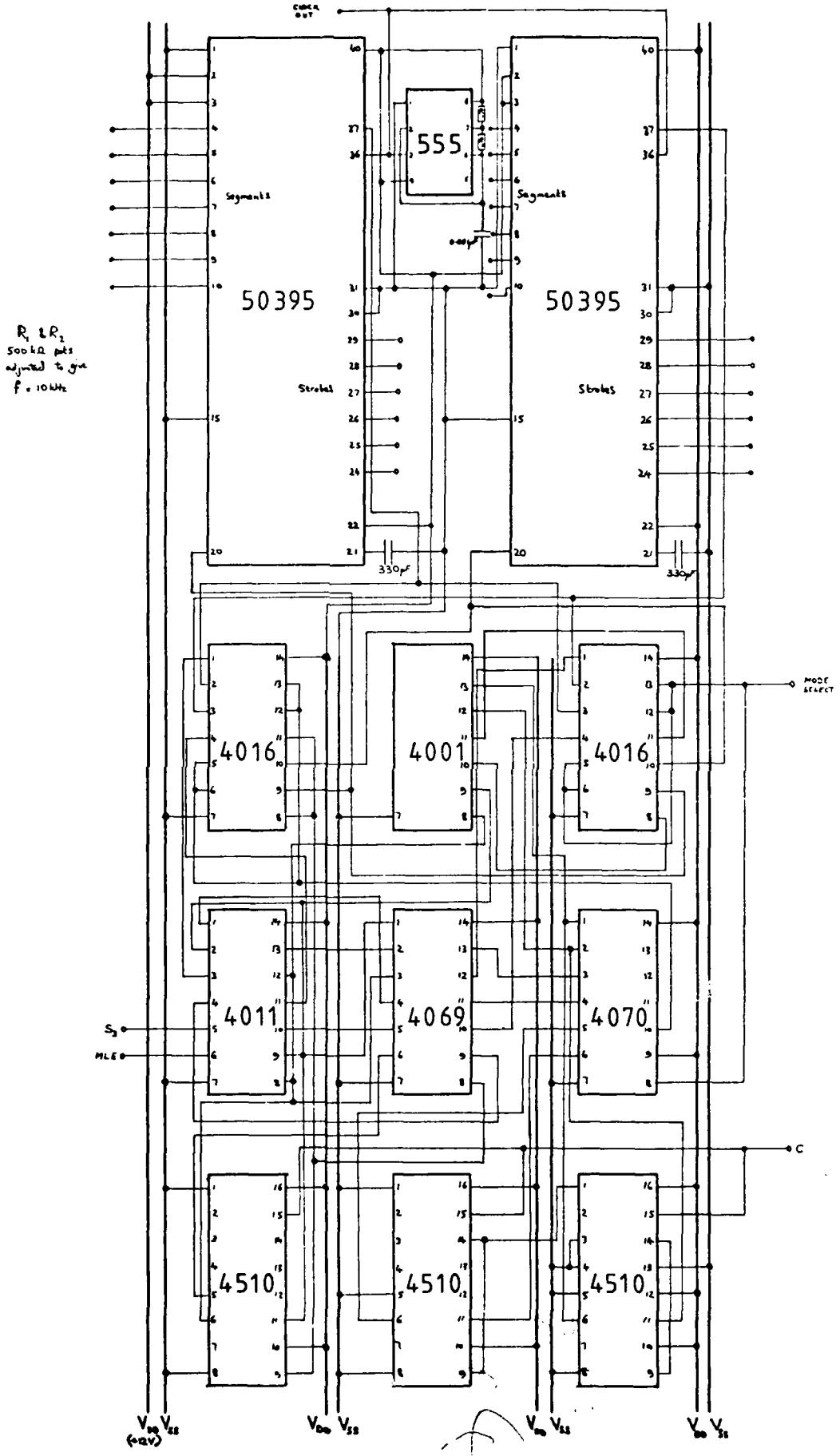

Figure 5·17. Data - Logging Circuit :- Timers.

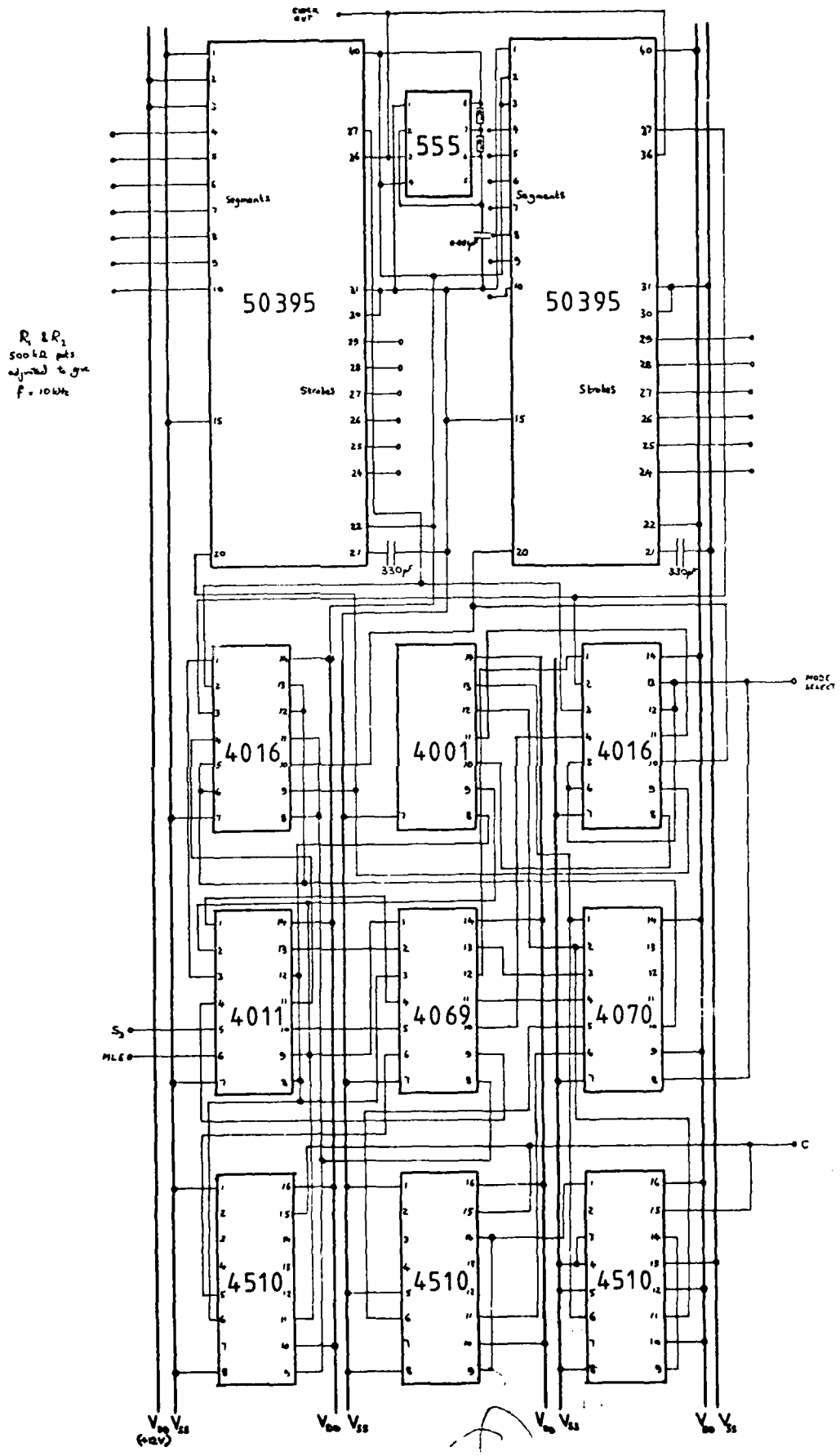

Figure 5·17. Data - Logging Circuit :- Timers.

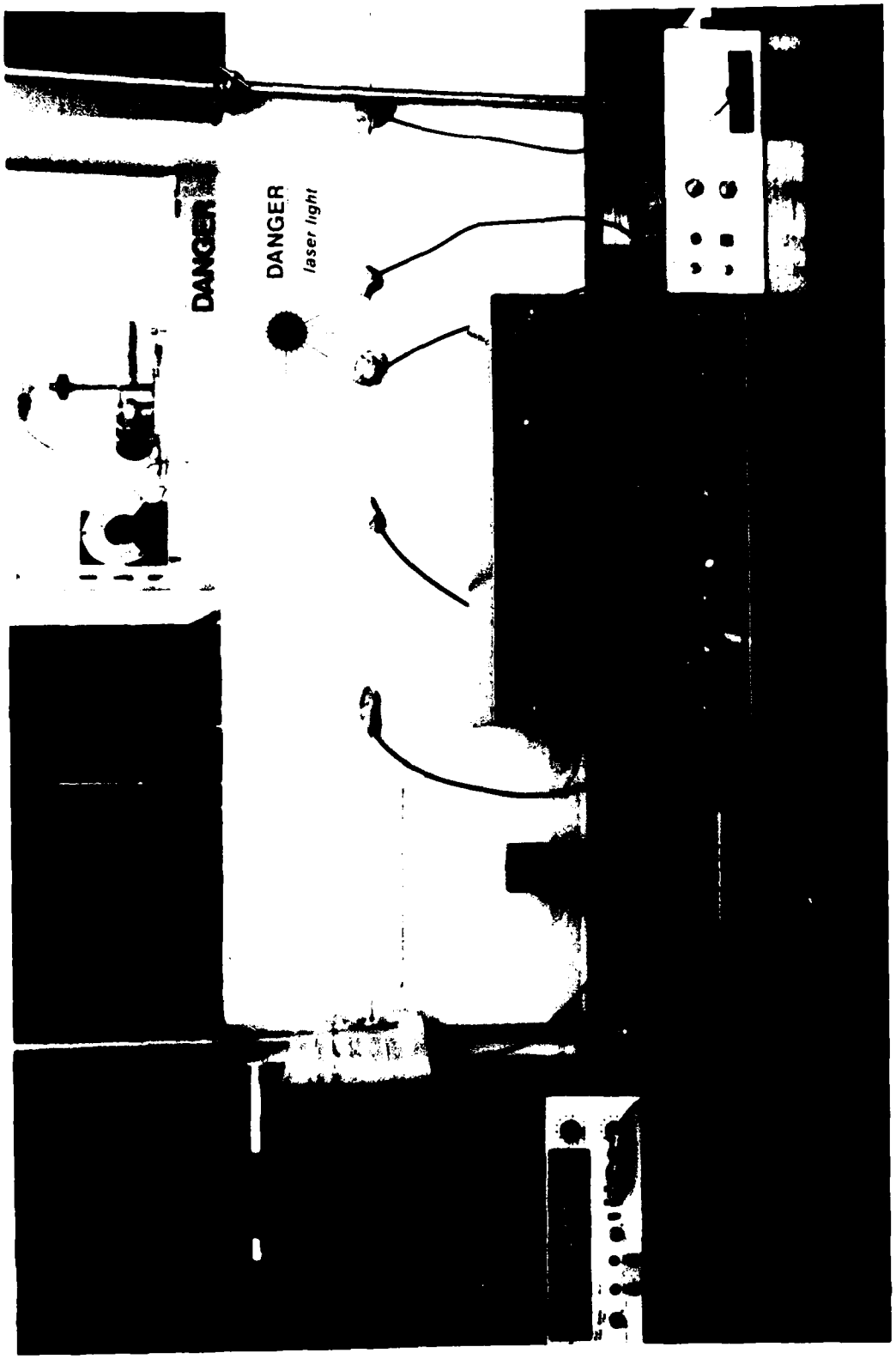

Figure 5.18 Data Logging Circuit: This photograph shows the phototransistor screen and data logging circuit, with a typical set of experimental results displayed.

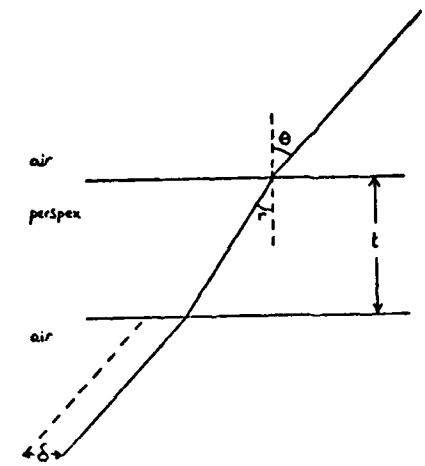

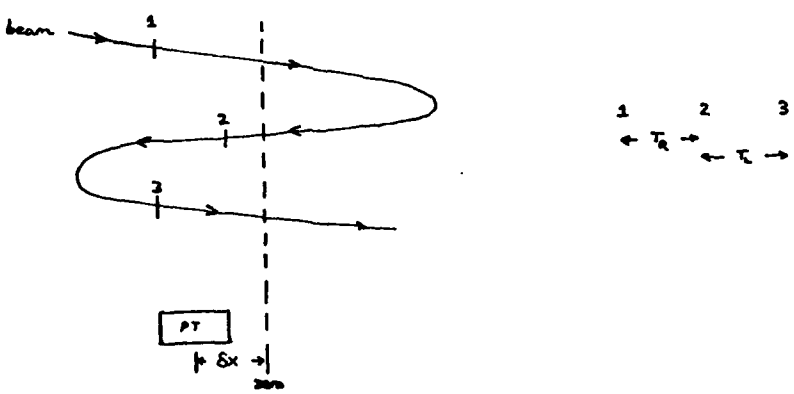

Figure 5·19. Effect of Refraction and Finite Size of Phototransistor / Laser Spot.

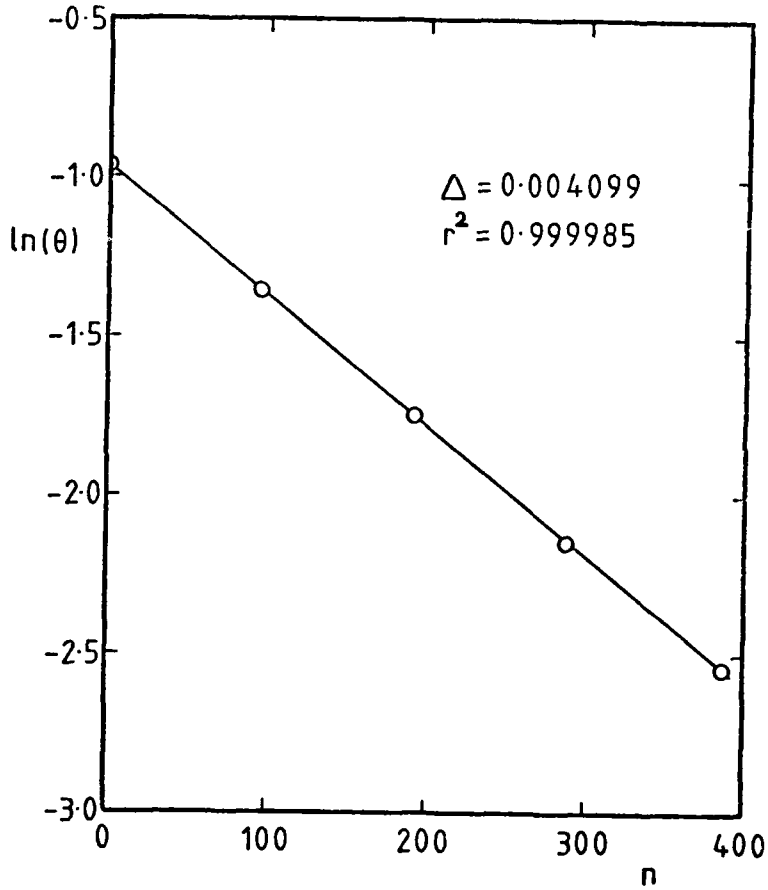

Figure 5·20. Typical Decay Curve, Steel Torsion Wire.

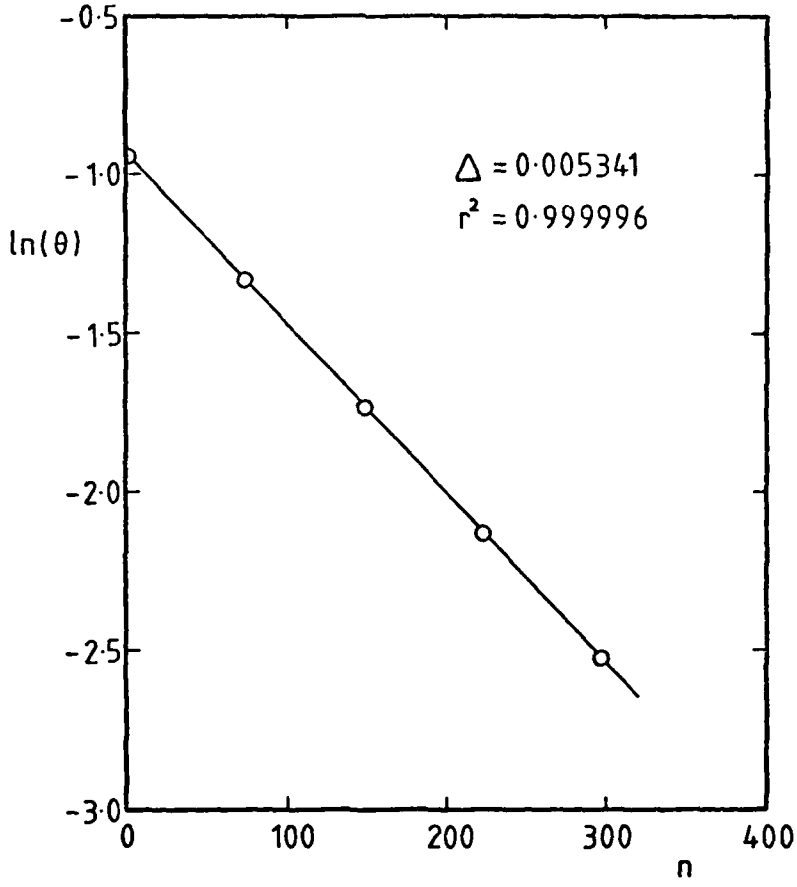

Figure 5·21. Typical Decay Curve,
Cu/Be Torsion Wire.

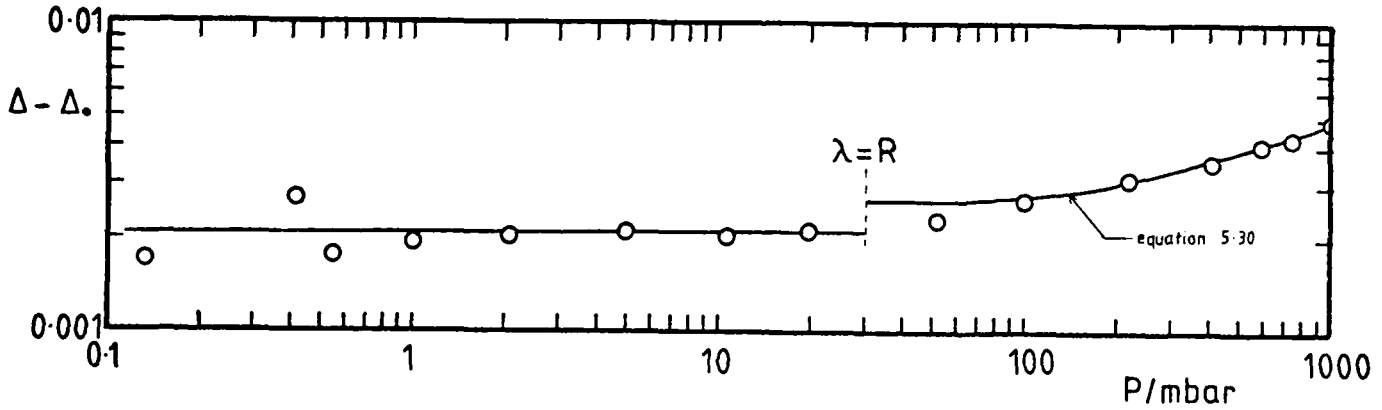

Figure 5·22. Logarithmic Decrement vs Pressure for Air.

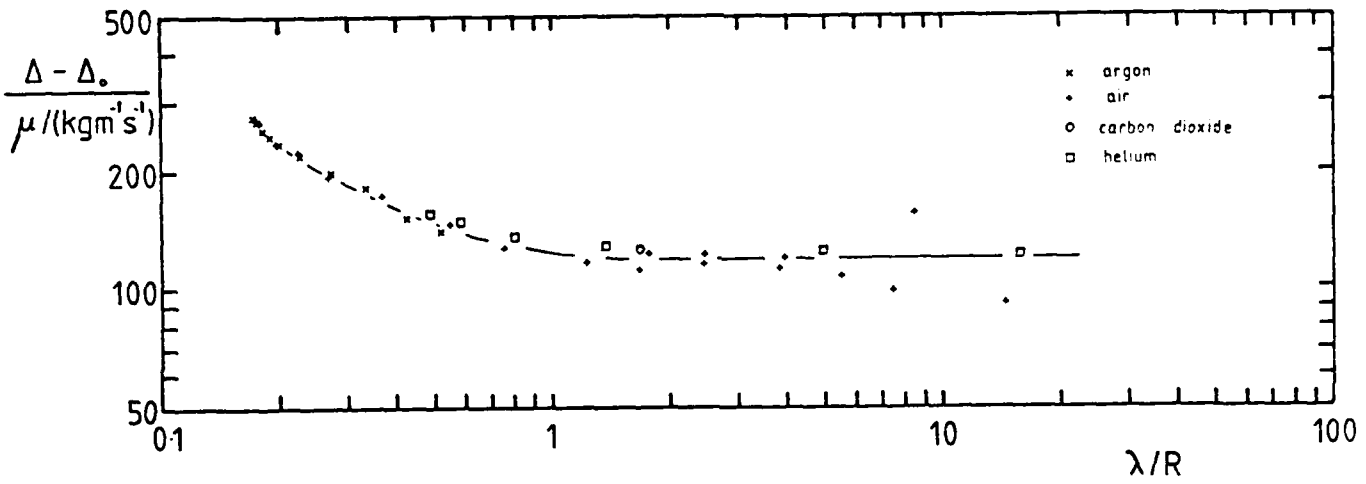

Figure 5·24. Universal Plot of Logarithmic Decrement as a function of Penetration Depth .

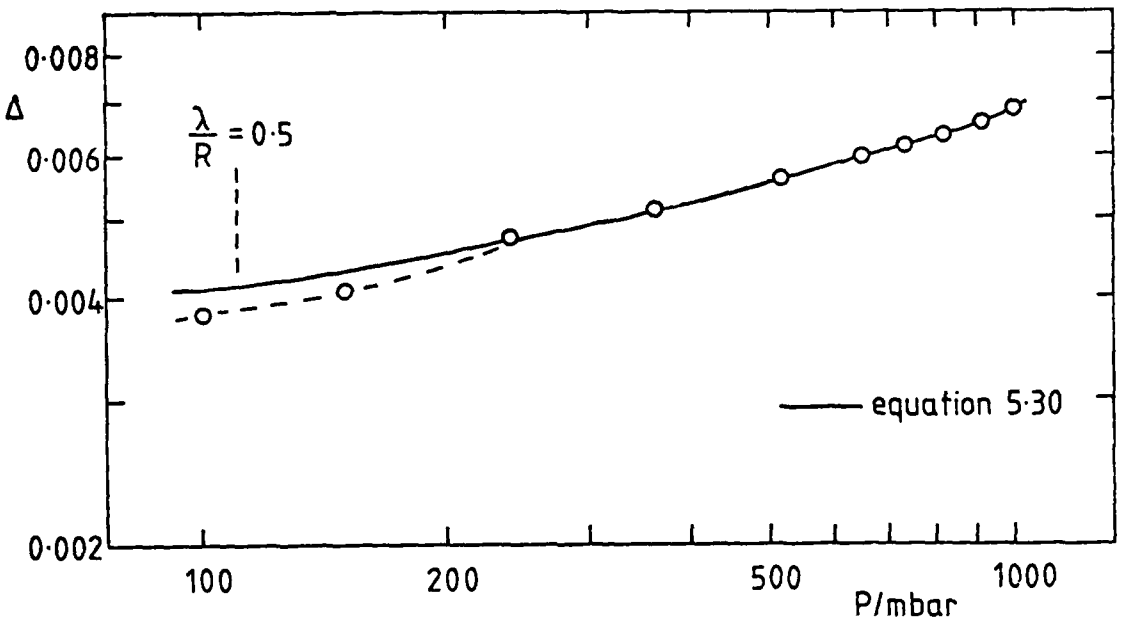

Figure 5·23. Logarithmic Decrement vs Pressure for Argon.

SUMMARY OF EXPERIMENTAL RESULTS

6.1 Electromagnetic Radiation from Turbulent Gas Flows

The experimental results presented in chapter 2 show that there is no detectable (i.e. $< 10^{-11}$ T) electromagnetic radiation from un-ionised gas flow on a small scale. The probes used in previous work on this topic (Clark 1958, 1975, 1980a, 1981) are, however, seen to respond very significantly to vibration caused by mechanical vibration or sound.

6.2 The Effect of Blockage on Vortex Shedding Frequencies

For low Reynolds numbers, windtunnel blockage is seen to increase the stability of the flow, causing an increase in the critical Reynolds number at which vortex shedding begins, as well as a reduction in the Strouhal number after vortex shedding has commenced. In the intermediate Reynolds number range, blockage is seen to exaggerate the natural variation of the Strouhal number, with the Strouhal number rising to a maximum at $Re \approx 3 \times 10^3$.

6.3 Drag Balance Experiments

The results of the experiments performed with the drag balance are summarised in figures 6.1 - 6.4, which show the percentage changes in drag observed an irradiation. It is clear that in both sets of experiments (i.e. perspex shield, low ionisation level and aluminium shield, high ionisation level) the changes are consistent with no change in drag. The errors are such that it can be concluded that no practically signficant changes in drag were caused by irradiation.

6.4 Torsion Disc Viscometer Experiments

The torsion disc viscometer experiments are summarised in figure 6.5, showing the percentage changes in viscosity observed. The figures have been multiplied by two to cast them into a form comparable with Clark, Kestin & Shah's results. The relevant data from these experiments have also been presented, and it can be seen that there is rather less scatter in the present work.

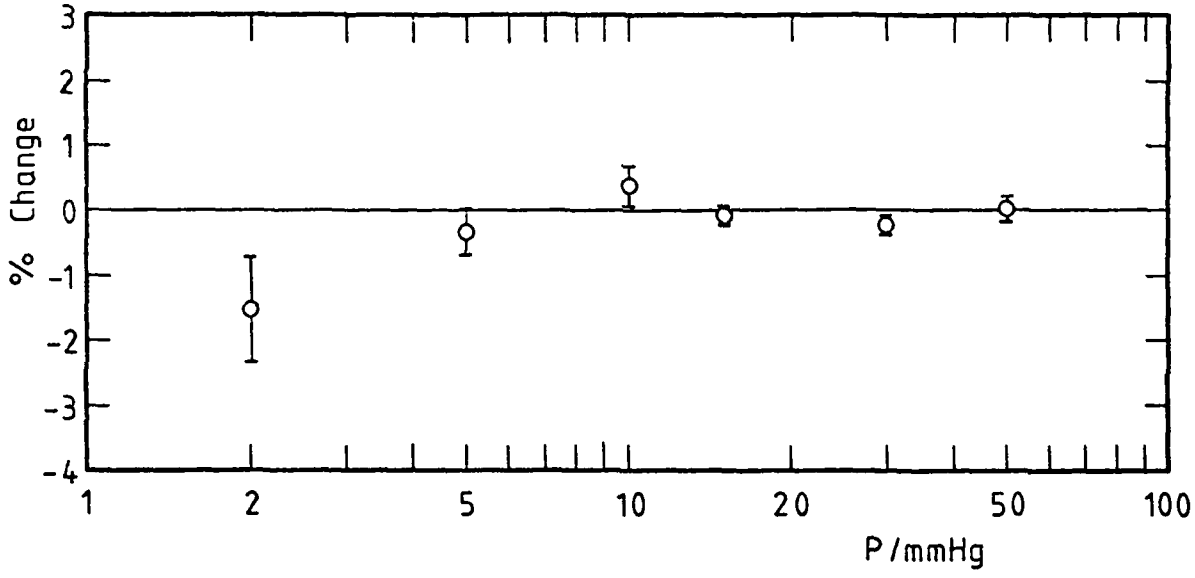

Figure 6·1 . Drag Change on Irradiation
(fully turbulent flow ,
perspex shield).

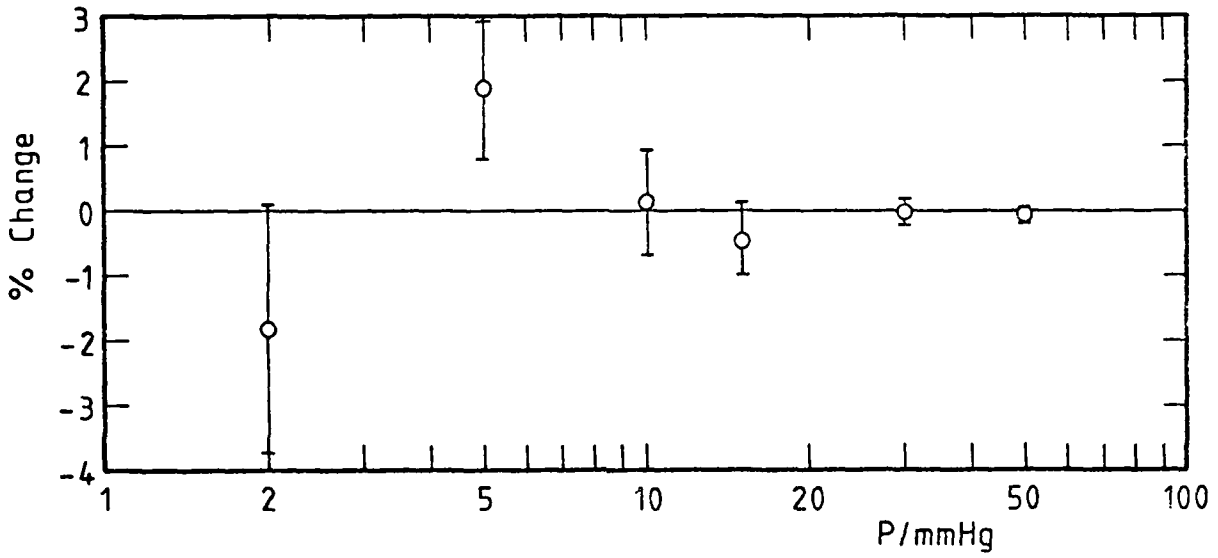

Figure 6·2 . Drag Change on Irradiation
(laminar / transitional flow ,
perspex shield) .

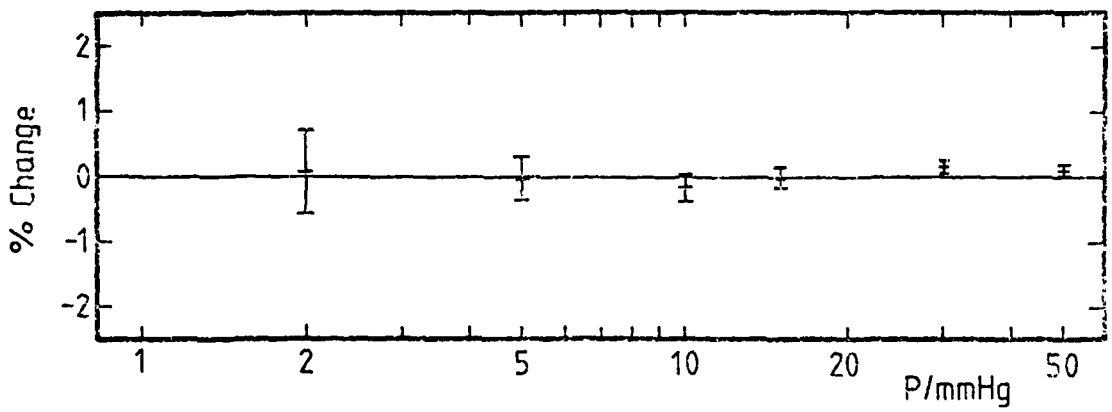

Figure 6·3. Drag Change on Irradiation
(fully turbulent flow, aluminium shield).

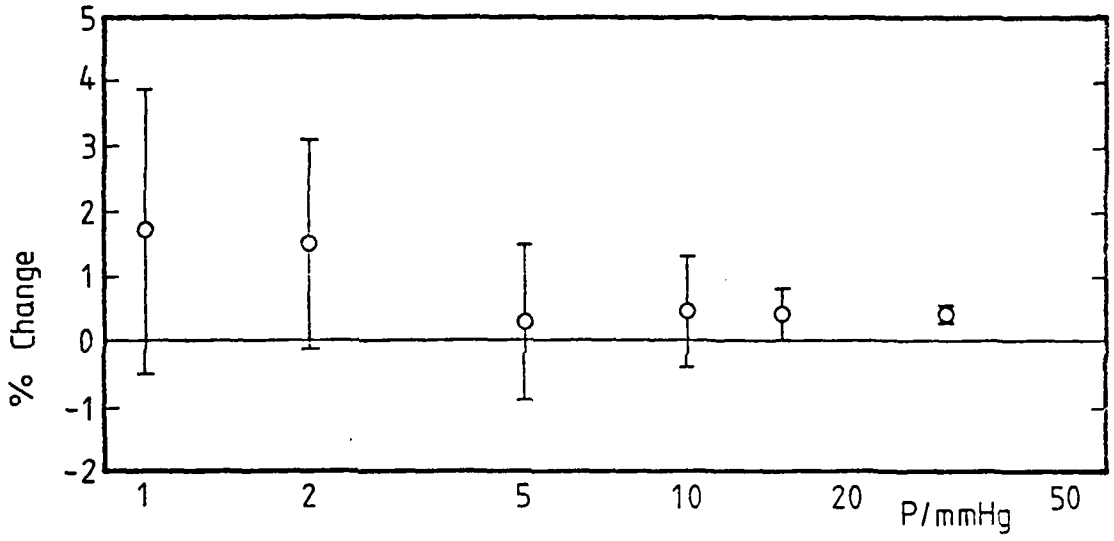

Figure 6·4 . Drag Change on Irradiation (laminar / transitional flow , aluminium shield) .

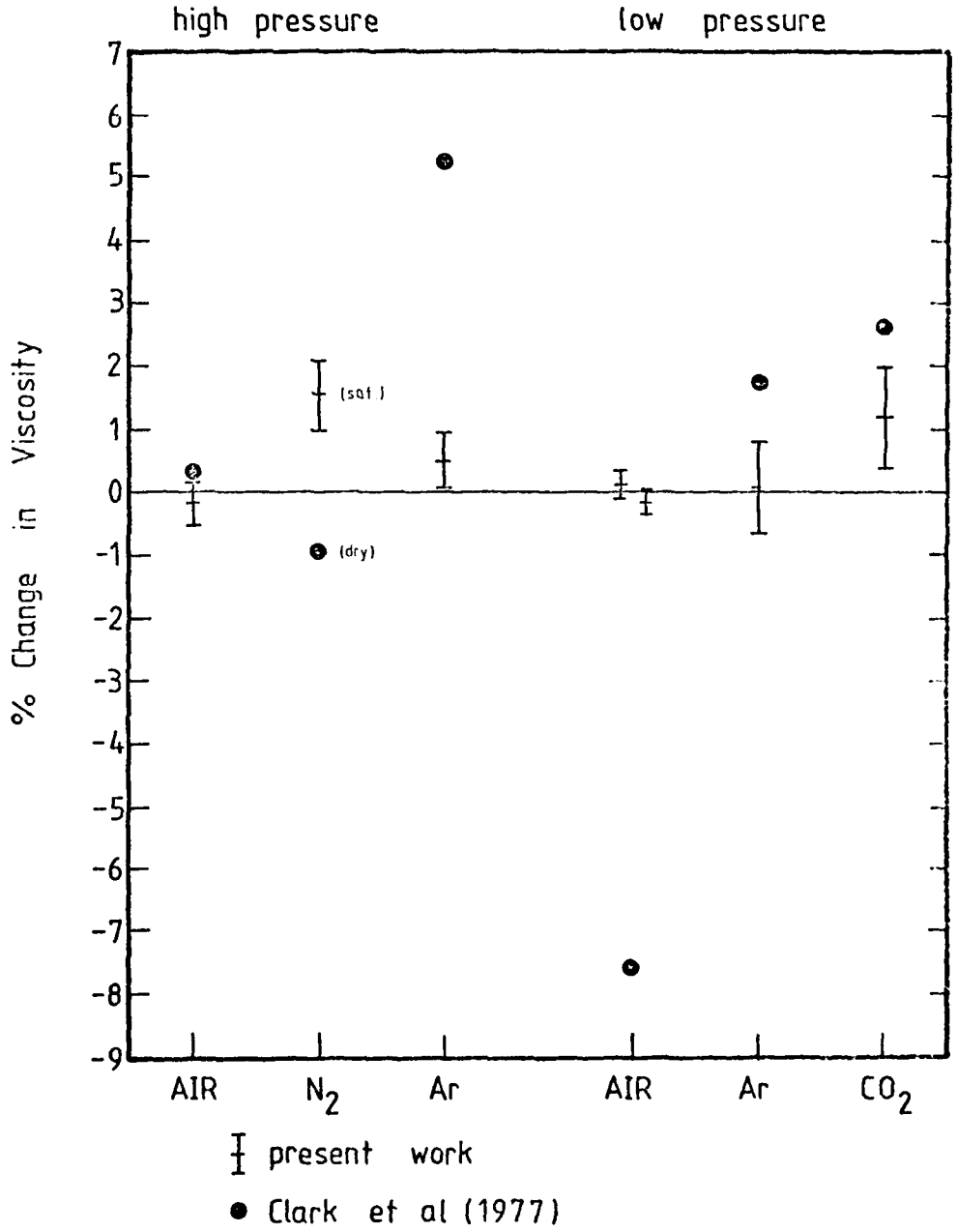

Figure 6·5 . Effect of Irradiation on Viscosity .

DISCUSSION

7.1 Electromagnetic Radiation from Turbulent Gas Flows

In view of the problems experienced with vibration in the most recent work on the phenomenon described by Clark, little credibility can be given to the earlier work in which no precautions were taken to avoid such effects. Even making rather ambitious approximations, theory would seem to suggest that any such effect will be so small as to be undetectable, and it seems certain that the signals detected by Clark were not due to electromagnetic radiation. Since only extremely small vibration amplitudes are needed to give a significant response from the probes used, it is obviously essential in any experiments of this nature, whether on turbulent gas flows or sound and shock waves, to take rigourous precautions to eliminate spurious vibration signals and microphonics. With ionised flows, or intense shock waves with ionisation in the shock front, it is, however, well known that electric and magnetic fields are produced.

7.2 The Effect of Blockage on Vortex Shedding Frequencies

This work has provided some data on an area of fluid mechanics which merits further study. The subject is, however, one of some complexity, and more work is needed to gain a better understanding of vortex shedding in confined flows. The data given in chapter 3 constitute, therefore, only a preliminary investigation of the effect of blockage on vortex shedding frequencies at low and intermediate Reynolds numbers.

7.3 Drag Balance Work

Before dealing with the present investigation; it is appropriate

to mention again the earlier work by August (1972). It has not been possible to assess the experimental work directly, as no details were given. However, the analysis is questionable. The idea which seems to underly the irradiation approach in this case (and which may have figured in Clark, Kestin & Shah's work) is the observation that, at high temperatures, the viscosity of a thermally ionised plasma decreases with increasing temperature, i.e. with an increasing ionisation level. It is suggested that if the ionisation were to be induced by other means (such as radio-active irradiation) with air at room temperature, it might be possible to achieve significant drag reductions (August 1967). This is, superficially, not unreasonable. However, in the work reporting measurements of such drag reductions (August 1972) the drag reductions were explained in terms of an analogy with long chain polymers in liquids. The factors interpreted as important in both cases were linearity, solubility, high molecular weight, low concentration and, in the case of irradiation, ionisation along the "long chain molecule". The track of an α particle in air is considered to be a "chain of linked ionised air particles" acting like a long chain polymer molecule.

There are so many errors in the work that it is difficult to present a coherent analysis, but an attempt will be made to highlight the major fallacies.

The linearity (length divided by diameter) is calculated by imagining the ionised molecules side by side in a chain, and therefore corresponds only to the total number of particles in the track. The linearity calculated in this way is similar to that of a long chain

polymer molecule. This calculation has no real physical significance or relevance and, in any case, the linearities calculated in this fashion must be inconsistent by a factor of the average interionic separation (discussed below) compared with the C-C bond length in the polymer. Not suprisingly, the "molecular weights" in the two cases are also calculated as being similar.

The α tracks are considered to be "completely dissolved" since they are composed of air.

The weight concentrations and ionisation levels of the α particle tracks are also calculated, incorrectly in both cases. This is presumably because it is assumed that the α particle tracks are confined within the laminar sub-layer, a most unlikely assumption.

Let us now look at the concept of an α particle as a chain of linked ionised air particles. (Calculations will be made for atmospheric pressure, but since the average ionic separation along a track and the intermolecular separation of neutral molecules both increase with decreasing pressure, the conclusions are valid at lower pressures as well). We remember that we get $\sim$ 30,000 ip cm^{-1} for a 5 MeV α particle (figure 4.18), and so the average pair separation is $\sim$ 0.3 μm. This compares with a mean free path of $\sim$ 0.07 μm and a mean separation of neutral molecules of $\sim$ 0.003 μm, a hundred times smaller than the mean distance between ion pairs. If we look at the Coulomb interaction energy between two ions at such a separation, neglecting the effect of the other ions and any screening by neutral molecules, we get an energy of $\sim$ 0.1 kT. This would be smaller at lower pressures. It seems likely, then, that the random thermal motion of the gas molecules and ions, and the large ionic separation, will ensure that the track has no coherent identity.

It seems unlikely that the "chain of linked ionised molecules" could interact in any sensible way with the turbulent boundary layer, since there is no obvious way in which turbulent energy can be accommodated in the "chain", and the length of the track, probably very much larger than the boundary layer thickness, obviously bears no relation to any turbulent length scales.

The work of August, therefore, presents no convincing evidence for an irradiation effect analagous to the effect of long chain polymers in hydrodynamics.

The present work on drag, described in chapter 4, while restricted to experiments at atmospheric pressure, shows that irradiation from the ^{147}Pm sources has no detectable effect on skin friction drag (with either turbulent or laminar flow) or on transition.

As the results obtained with the drag balance are very precise, the changes in drag being consistent with zero change to within a precision of $\sim 0.1\%$, and as the radiation level corresponded to a specific activity of 100 Ci m^{-2}, we can see that there is no prospect of achieving significant drag reduction at atmospheric pressure with reasonable radiation levels.

7.4 Torsion Disc Viscometry

The work described in chapter 5 is not in good agreement with the earlier work by Clark, Kestin & Shah, particularly in the case of low pressure air, and in this section an attempt will be made to account for the discrepancies. It would be useful to be able to assess the reliability of the two sets of results, but in the case of Clark, Kestin & Shah's work the problem is complicated

by the inconsistent assessments of the work given in different references. To illustrate this point let us first look at the abstract and conclusion of Kestin & Shah (1968)*

"The viscosity of air in the boundary layer of an aerodynamic body has been reduced by bombarding the air with α particles ... The maximum reduction in viscosity obtained was 7.6% at a pressure of 1.0 mmHg abs... This work has opened up a new field of aerodynamic research in the reduction of skin friction"

and

"The diagrams in Figs. [5.3] and [5.4] can be interpreted to indicate that the introduction of long-range intermolecular forces at the interface produces qualitatively different effects at atmospheric pressure as compared with that of 1 mmHg. At normal pressures there are no significant changes in the torque exerted on the disk. We may either assert that the apparent viscosity changes by an amount which is comparable with the resolution of the experiments or that the damping torque increases by amounts that only slightly exceed the quantities which can be detected. The reduction of the pressure to 1 mmHg preserves the same conclusion with respect to all gases but with the signficant exception of air. In it, a considerable reduction in both quantities was measured, even though the level of confidence of the result was reduced compared with that observed in the presence of external bombardment with cesium - 137 (Series 2).

In Clark, Kestin & Shah (1977) we find

"... there is a very small change in the skin friction experienced by the disk"

---

* my italics and square brackets.

and

"The diagrams in Figs [5.3] and [5.4] * can be interpreted to indicate that the introduction of long range intermolecular forces at the interface induced by bombardment with alpha particles *did not* produce significant changes in the torque exerted on the disk"

More recently, we have the opinion of Clark (in Field & Clark 1978):-

"...in the first set of experiments [series 2] Kr and Xe showed very small (but statistically signficant) increases in viscosity of 0.15 and 0.1% respectively at atmospheric pressure. Air ... gave a reduction of 0.2 to 0.3%.

In the second experiment [series 4] ... all the gases tested ... except air and Ne showed increases in viscosity of up to 2.5% (CO_2) ... With air the decrease was large and 18 experiments gave a mean value of $\Delta\mu$ = -7.6%"

and the conflicting opinion of Kestin (1981)

"I still am of the opinion that we have performed enough experiments to convince ourselves that radiation at the levels of ionisation that we created by the thin layer of ^{210}Po *did not* produce a consistently measureable reduction in drag. Had this been the case, we would have noticed it."

Despite Clark's confidence (which extends to a patent (Clark 1968) on the control of radioactive emissions into a fluid, for the purposes of drag reduction, using reverse biased surface pn

---

* note that in the paper the figures referred to are actually of the changes in C_L, rather than μ.

junctions) it seems that Kestin (who is probably the leading exponent of torsion disc viscometry in the world) is less convinced about the conclusions originally expressed in Kestin & Shah (1968).

A closer analysis of the experimental results does, in fact, appear to justify this reticence. One anomaly which is immediately apparent is that the +5.2% increase for argon was dismissed while the -7.6% change for air was considered significant. In fact, with the quoted precisions, the result for argon should be statistically much more signficant. As a general comment, one might also point out that the use of generalised error estimates* in an investigation of this nature is quite reprehensible, and makes a statistical analysis of the results almost worthless.

Factors which may have introduced errors are the pressure and temperature corrections (the method used is described in Kestin & Shah 1968) and the use of different wires, with one wire apparently being used predominantly for the calibration and another for the active measurements. Complete sets of raw data are not available, and a direct comparison of the data available for air at low pressure is not particularly illuminating. For three calibration points at 1.37 mmHg a viscosity of 1.833×10^{-5} $kgm^{-1}s^{-1}$ was obtained, while with the ^{210}Po coated disc with a pressure of 1.3 mmHg two data points gave 1.851×10^{-5} $kgm^{-1}s^{-1}$ (with a different wire), an increase of 1%. These results do not need significant pressure or temperature corrections, and are therefore inconsistent with the reported change of -7.6%. We do notice, however, that the calibration point for low pressure

* i.e. a single value for the precision of several different experiments.

air in figure 5.8 is 8% above the calibration curve.

Taking a general view of the results of Kestin & Shah we can see that there is no systematic trend to the data, except perhaps that the average of the results might suggest an average change of 1% in viscosity. The experience of the present work has been that it is very easy to cause a systematic error of this magnitude on changing discs or wires. If, as seems possible, the precision is rather less than that quoted, the results might be accountable for as a combination of random and systematic errors.

It follows that the work of Clark, Kestin & Shah does not contain any compelling evidence to support the conclusion that this level of irradiation causes significant changes in viscosity.

In the case of the present work, a systematic investigation of the effect of irradiation was made, with a great deal of care being taken to avoid systematic errors and to get an accurate assessment of the random errors. The significance of any changes in viscosity can then be properly determined. At both high and low gas pressures, no statistically significant changes in viscosity were observed. The very accurate experiments made for air show conclusively that it is not possible to obtain practially significant drag reductions at atmospheric or reduced pressure with this level of irradiation.

To conclude this discussion, we can look briefly at some theoretical estimates of the effect of ionisation on viscosity.

7.5 Theoretical Estimates of the Effect of Irradiation

In principle, it should be possible to calculate the viscosity of a partially ionised gas exactly, using the Fokker-Plank theory or, as a first approximation, the Chapman-Enskog expression for the viscosity of a multicomponent gas mixture, given values for the ionic and molecular viscosities (see Chapman & Cowling 1970 and Hirschfelder et al 1954 for example).

Exact solutions are difficult but with such a small degree of ionisation an elaborate analysis is out of place. A simplified expression for the viscosity of a partially ionised thermal plasma has been given (Mathers 1978) which gives some insight into the problem. With α representing the fractional ionisation we get

$$\mu = \frac{\mu_a(1 + \alpha(1-\alpha)S_1')}{\{(1-\alpha)^2 + \alpha(1-\alpha)S_2 + \alpha^2 s_3\}} \tag{7.1}$$

with

$$S_1' = \left(\frac{3}{5+3A}\right)\left[\frac{(\Omega_{ii}^{(2,2)} + \Omega_{aa}^{(2,2)})}{\Omega_{ia}^{(1,1)}} - 4A\right] \tag{7.2}$$

Where the subscripts i and a refer to ions and atoms (or molecules) respectively. The definitions of the collision integrals (Ω's) and ratios of collision integrals (S's) are detailed in Mathers (1978) and Chapman & Cowling (1970) and, although they are not known precisely, we can assume that S_1', S_2 and S_3 are not appreciably different from unity. A first approximation to 7.1 is then

$$\mu \simeq \mu_a\,(1 + \alpha(S_1' + 2 - S_2)) \tag{7.3}$$

While the sign of the change in viscosity depends in principle on the magnitude of S_1' and S_2, we can say that the fractional

change is of the order of the fractional ionisation, α, where, of course, we have assumed $\alpha << 1$.

A similar result follows from the Chapman Enskog theory if $\alpha << 1$, i.e.

$$\mu = \mu_a (1-\alpha) + \alpha\mu_i \qquad (7.4)$$

and so the maximum fractional reduction in viscosity is again $\sim\alpha$. (In these crude estimates we need not worry about the presence of more than one type of ion, or about free electrons which will play only a very small part in the transport properties of the gas).

Looking at the explicit data in Mathers (1978) for ion and atom viscosities for hydrogen, it can be shown that the fractional decrease in viscosity is likely to be $\lesssim 10\alpha$.

It seems, therefore, that the presence of a small fraction of ions in a gas should not, as such, cause an appreciable change in the viscosity. It is, of course, possible that ionisation might initiate some other processes in the gas which could have a bearing on the transport properties. The problem of clustering has attracted some interest. However, even if a significant fraction of ions form clusters with a much longer lifetime than the ions, it seems unlikely that the maximum change in viscosity would be substantially greater than that suggested by equation 7.4. The probability of clustering is generally quite low. Hirschfelder et al (1954) give the following expression for the concentration of simple clusters at room temperature in hydrogen, assuming a fundamental vibration frequency of $\sim 100\ cm^{-1}$ for the cluster,

considered as a diatomic molecule:

$$\frac{[H_2 \cdot H_2^+]}{[H_2^+]} = 0.186\ (P_{H_2}/\text{atmospheres}) \qquad (7.5a)$$

$$\frac{[H_2 \cdot H_3^+]}{[H_3^+]} = 0.173\ (P_{H_2}/\text{atmospheres}) \qquad (7.5b)$$

The equilibrium concentration of small clusters is significant, but the probability of two molecules clustering about an iron is estimated to be the square of the probability for one molecule. The probability of a large cluster forming is then expected to be very small. With polar molecules rather more clustering might be expected but again it is difficult to envisage any conditions which would lead to a perceptible change in viscosity. In nitrogen with traces of water vapour, for example, ion molecule reactions can lead to clusters of the form $H_3O^+(H_2O)_n$, but usually $n \lesssim 4$ (McCrumb & Warneck 1977). (Allied to this problem is the nucleation of water droplets. It is conceivable that ion induced nucleation might form droplets of a sufficient size to influence the drag, but this can only occur under conditions of saturation. However, in the experiments described in chapter 5 for saturated N_2 there was, if anything, an increase in drag).

It is also possible to introduce short chains of molecules into a gas, with the possiblity of causing an analagous effect to that of polymers in liquids (I believe that some experiments have been made with polyox dust in air, but this is, of course, pointless from the point of view of the properties of individual polymer molecules).

Kebarle & Hogg (1965a) have observed ion induced polymerisation of ethylene, in ethylene irradiated by α particles at pressures up to 200 Torr (a later paper, Kebarle & Hogg 1965b, considers clusters of water and ammonia in irradiated ammonia). The ethylene chains produced, however, have masses of only a few hundred amu and are present in a low concentration, and so should not influence the viscosity appreciably. It might be possible to introduce larger polymer chains by dispersing finely divided catalyst particles through the gas, but since most of the Ziegler-Natta catalysts used for ethylene and propylene polymerisation are based on Ti/Al chloride and alkyl aluminium activators, they are extremely sensitive to air and moisture and would not be of any practical use for drag reduction in flight.

It seems likely then, that the fractional change in viscosity due to irradiation will be no more than of the order of the fractional ionisation. This is also in general agreement with the calculations of Kestin & Shah (1968).

To obtain a significant change in drag it follows that we would need an extremely high ionisation level, which would be impractical even from the point of view of the energy necessary to sustain such an ionisation level.

8. Conclusions

Earlier workers have reported that the viscosity of gases can be changed appreciably by radioactive irradiation, offering a possible means of achieving drag reduction in flight. A precision skin friction drag balance and torsion disc viscometer have been developed in order to investigate this effect. It has been shown that, with practical radiation levels, irradiation has a negligibly small effect on viscosity and skin friction drag (both laminar and turbulent). In the sense that an analysis based on a small fractional ionisation would predict only indetectable changes, all of the experimental results of chapters 4 and 5 can be said to be in complete agreement with theory. A critical analysis of the earlier work highlights several inadequacies, and the present work is considered to be the most reliable to date. The prospects of achieving significant drag reduction by this method must be viewed with some pessimism.*

It has also been reported that turbulent gas flows align polar or polarisable molecules, whose motion then gives rise to detectable electromagnetic radiation. A study was made of this phenomenon, with a view to applications in monitoring the structure of turbulent gas flows during drag reduction experiments. The previous work was erroneous, with the probes used responding to vibration rather than to electromagnetic radiation. Calculations suggest that any such electromagnetic signal would have been at least 120 dB below the background noise level.

The equipment and electonics developed in the cause of this work can be used for accurate, relative, measurements of skin friction drag and viscosity. The operation of the torsion disc viscometer

* It is possible, however, that under more initial flow conditions, in which compressibility or heat transfer were more important for example, that irradiation might have some effect.

has been made particularly straightforward, with the logarithmic decrement being determined automatically, and the system could be of general use as a simple but accurate viscometer.

The results obtained with the viscometer and drag balance suggest that radioactive irradiation does not offer a practical means of reducing drag in flight.

References

Abramowitz, M. & Stegun, I.A. (eds.)	1970	"Handbook of Mathematical Functions" Dover Publications.
Allen, J.M.	1977	"Experimental Study of Error Sources in Skin-Friction Balance Measurements" J. Fluids Eng. (Trans. ASME) March 1977 pp 197-204.
Allen, J.M.	1980	"Improved Sensing Element for Skin-Friction Balance Measurements" AIAA Journal 18 pp 1342-1345.
August, H.	1967	"Trends in Viscosity of a Gas Ionised by Radioisotope Emissions" Eighth Int. Conf. on Phenomena in Ionized Gases, Vienna, Austria. August 1967.
August, H.	1969	"Alteration of Shock Waves by Radio-isotope Emissions" Tenth Int. Conf. on Phenomena in Ionized Gases, Oxford, England. September 1969.
August, H.	1972	"Similarities in Characteristics and Effects between Alpha Tracks and Long Chain Molecules" TFD-72-363, Los Angeles Division, North American Rockwell. March 1972.
Azpeitia, A.G. & Newell, G.F.	1958	"Theory of Oscillation Type Viscometers III: A Thin Disk" Z. angew. Math. Phys. 9 pp 97-118.
Azpeitia, A.G. & Newell, G.F.	1959	"Theory of Oscillation Type Viscometers IV: A Thick Disk" Z. angew. Math. Phys. 10 pp 15-34.
Barker, S.J. & Gile, D.	1981	"Experiments on Heat Stabalised Laminar Boundary Layers in Water" J. Fluid Mech. 104 pp 139-158.
Bearden, J.A.	1939	"A Precision Determination of the Viscosity of Air" Phys. Rev. 56 pp 1023-1040.
Beckwith, D.A. & Newell, N.F.	1957	"Theory of Oscillation Type Viscometers: The Oscillating Cup, Part II" Z. angew. Math. Phys. 8 pp 450-465.

Bellhouse, B.J. & Schultz, D.L.	1968	"The Measurement of Fluctuating Skin Friction in Air with Heated Thin-Film Gauges" J. Fluid Mech. 32 pp 675-680.
Blick, E.F.	1969	"The Theory of Skin Friction Reduction by a Compliant Coating in a Turbulent Boundary Layer" in "Viscous Drag Reduction" ed. C.S. Wells, Plenum, pp 409-425.
Boas, F.	1971	"Streaming Birefringence in CO_2 and N_2" Phys. Lett. 36A pp 107-108.
Boothroyd, R.	1966	"Pressure Drop in Duct Flow of Gaseous Suspensions of Fine Particles" Trans. Inst. Chem. Eng. 44 pp 306-313.
Boyer, G.R. Lamouroux, B.T. & Prade, B.S.	1975	"Air Flow Birefringence Measurement" J. Opt. Soc. Am. 65 pp 1319-1320.
Bradshaw, P.	1971	"An introduction to Turbulence and its Measurement" Pergamon.
Brown , K.C. & Joubert, P.N.	1969	"The Measurement of Skin Friction in Turbulent Boundary Layers with Adverse Pressure Gradients" J. Fluid Mech. 35 pp 737-757.
Cary, A.M. Jr. Weinstein, L.M. & Bushnell, D.M.	1980	"Drag Reduction Characteristics of Small Amplitude Rigid Surfaces Waves" in "Viscous Flow Drag Reduction" Vol. 72 Prog. Astronautics and Aeronautics, AIAA, ed. G.R. Hough, pp 144-167.
Chalmers, S.A.	1949	"Atmospheric Electricity" OUP.
Chapman, S. & Bartels, J.	1940	"Geomagnetism" OUP.
Chapman, S. & Cowling, T.G.	1970	"The Mathematical Theory of Non-Uniform Gases" (3rd. ed.) CUP
Clark, J.	1958	"A New Method for Detecting Cavitation and Turbulence in Cryogenic Fluids" Proc. 1958 Ann. Cryogenic Eng. Conf. (AiResearch Mfg. Co., Phoenix, Arizona), pp 203-217.

Clark, J.	1968	"Utilizing Energy of Radiations" UK Patent No. 1, 258, 407, 10th Dec. 1968.
Clark, J.	1975	"Electromagnetic Fields Generated by Turbulent Air Flow and Shock Waves" AIAA Journal 13 pp 1382-1384.
Clark, J. Kestin, J. & Shah, V.L.	1977	"The Effect of Long-Range Intermolecular Forces on the Drag of an Oscillating Disk and on the Viscosity of Gases" Physica 89A pp 539-554.
Clark, J.	1980a	"Electromagnetic Radiation from Turbulent Gas Flows" Departmental Report, Physics and Chemistry of Solids Group, Cavendish Laboratory, Cambridge. March 1980.
Clark, J.	1980b	private communication.
Clark, J.	1980c	private communication.
Clark, J.	1981	"Verification of the Electromagnetic Radiation from Shock Waves in Air" Departmental Report, Physics and Chemistry of Solids Group, Cavendish Laboratory, Cambridge. May 1981.
Clauser, F.H.	1954	"Turbulent Boundary Layers in Adverse Pressure Gradients" J. Aeronaut. Sci. 21 pp 91-108.
Clifford, A.A. Kestin, J. & Wakeham, W.A.	1981	"The Viscosity of Mixtures of Hydrogen with Three Noble Gases" Ber. Bunsen Gesell. Phisik Chem. 85 pp 385-388.
Corke, T.C. Guezennec, Y. & Nagib, H.M.	1981	"Modification in Drag of Turbulent Boundary Layers Resulting from Manipulation of Large Scale Structures" NASA-CR-3444.
Davey, K.R. & Melcher, J.R.	1980	"Electromagnetic Precipitation and Ducting of Particles in Turbulent Boundary Layers" in "Viscous Flow Drag Reduction" Vol. 72 Prog. Astronautics and Aeronautics, AIAA, ed. G.R. Hough pp 90-107
Davies, B.	1978	"Integral Transforms and Their Applications" Springer-Verlag.

Dhawan, S.	1953	"Direct Measurement of Skin Friction" NACA Report 1121.
Drescher, H.	1956	"Messing der auf querangeströmte Zylinder ausgeübten zeitlich veränderten Drücke" Z. Flugwiss. 4 pp 17-21
Everett, H.U.	1958	"Calibration of Skin Friction Balance Discs for Pressure Gradient" Univ. Texas DKL-426.
Field, J.E. & Clark, J.	1978	"Reduction of Aerodynamic Drag" Research Proposal, Physics and Chemistry of Solids, Cavendish Laboratory, Cambridge. Jan. 1978.
Frei, D. & Thomann, H.	1980	"Direct Measurement of Skin Friction in a Turbulent Boundary Layer with a Strong Adverse Pressure Gradient" J. Fluid Mech. 101 pp 79-95.
Frenkiel, F. Landahl, M. & Lumley, J. eds	1977	Proc. IUTAM Symposium on Structure of Turbulence and Drag Reduction, Phys. Fluids 20 No.10, part II.
Froude, W.	1872	"Experiments on the Surface-Friction experienced by a Plane moving through Water" 42nd Report of the British Association for the Advancement of Science, pp 118-124.
Gad-el-Hak, M. Blackwelder, R.F. & Riley, J.J.	1981	"On the Growth of Turbulent Regions in Laminar Boundary Layers" J. Fluid Mech. 110 pp 73-96.
Graham, T.	1846	"On the Motion of Gases - Part I" Phil. Trans. 1846 pp 573-631.
Graham, T.	1849	"On the Motion of Gases - Part II" Phil. Trans. 1849 pp 349-631.
Hefner, J.N. Weinstein, L.M. & Bushnell, D.M.	1980	"Large-Eddy Break-up Scheme for Turbulent Viscous Drag Reduction" in "Viscous Flow Drag Reduction" Vol. 72 Prog. Astronautics and Aeronautics, AIAA, ed. G.R. Hough, pp 110-127.
Hirschfelder, J.O. Curtiss, C.F. & Bird, R.B.	1954	"Molecular Theory of Gases and Liquids" Wiley.

Hoffman, A.W. Douglass, D.H. Gram, R.Q. & Lam, D.	1976	"Flux Gradient Accelerometer: Tests on a Working Model" Rev. Sci. Instrum. 47 pp 1441-1444.
Kaye, G.W.C. & Laby, T.H.	1966	"Tables of Physical and Chemical Constants" (13th ed.) Longmans.
Kebarle, P. & Hogg, A.M.	1965a	"Mass-spectrometric Study of Ions at Near Atmospheric Pressures. I. The Ionic Polymerisation of Ethylene" J. Chem. Phys. 42 pp 668-674.
Kebarle, P. & Hogg, A.M.	1965b	"Mass-spectrometric study of Ions at Near Atmospheric Pressures. II. Ammonium Ions Produced by the Alpha Radiolysis of Ammonia and their Solvation in the Gas Phase by Ammonia and Water Molecules" J. Chem. Phys. 43 pp 449-456.
Kennard, E.H.	1938	"Kinetic Theory of Gases" McGraw-Hill.
Kestin, J. & Wang, H.E.	1957	"Corrections for the Oscillating Disk Viscometer" J. Appl. Mech. 24 pp 197-206.
Kestin, J. & Newell, G.F.	1957	"Theory of Oscillation Type Viscometers: The Oscillating Cup, Part I" Z. angew. Math. Phys. 8 pp 433-449.
Kestin, J. & Leidenfrost, W.	1959	"An Absolute Determination of the Viscosity of Eleven Gases over a Range of Pressures" Physica 25 pp 1033-1062.
Kestin, J. & Shah, V.L.	1968	"The Effect of Long-Range Intermolecular Forces on the Drag of an Oscillating Disk and on the Viscosity of Gases" AFFDL-TR-68-86.
Kestin, J. & Shankland, I.R.	1981	"A Re-evaluation of the Relative Measurement of Viscosity with Oscillating-Disk Viscometers" Z. angew. Math. Phys. 32 pp 533-545.
Kestin, J.	1981	private communication.
Klein, E.J. & Margozzi, A.P.	1970	"Apparatus for the Calibration of Shear Sensitive Liquid Crystals" Rev. Sci. Instrum. 41 pp 238-239.

Kovásznay, L.S.G.	1949	"Hot Wire Investigation of the Wake behind Cylinders at Low Reynolds numbers" Proc. Roy. Soc. Lond. A198 pp 174-190.
Landau, L.D. & Lifshitz, E.M.	1959a	"Fluid Mechanics" Pergamon Press.
Landau, L.D. & Lifshitz, E.M.	1959b	"Theory of Elasticity" Pergamon Press.
Lebedev, N.N.	1965	"Special Functions and Their Applications" Prentice-Hall.
Leuchtag, H.R.	1978	"Polymer Additives Reduce Fluid Drag in Turbulent Flow" Physics Today 31 no. 3 pp 17-19.
Ling, S.C. & Ling, T.Y.	1974	"Anomalous Drag Reducing Phenomena at a Water/Fish Mucus or Polymer Interface" J. Fluid Mech. 65 pp 499-512.
Ludwieg, H.	1950	"Instrument for measuring the Wall Shearing Stress of Turbulent Boundary Layers" NACA TM 1284.
McCrumb, J.L. & Warneck, P.	1977	"On the Mechanism of Water Cluster-Ion formation in Nitrogen" J. Chem. Phys. 67 pp 5006-5011.
Malkus, W.V.R.	1979	"Turbulent Velocity Profiles from Stability Criteria. J. Fluid Mech. 90 pp 401-414.
Mariens, P. & van Paemel, O.	1956	"Theory and Experimental Verification of the Oscillating Disc Method for Viscosity Measurements in Fluids" App. Sci. Res. 5 pp 411-424.
Mathers, C.D.	1978	"Simplied Expression for the Calculation of the Viscosity of Partly Ionised Gases" Phys. Lett. 69A (1978) pp 119-121.
Mathews, J. & Walker, R.L.	1970	"Mathematical Methods of Physics" 2nd ed. W.A. Benjamin, Inc.
Maxwell, J. Clerk-	1866	"On the Viscosity or Internal Friction of Air and other Gases" Phil. Trans. CLVI pp 1-25.
Meyer, O.E. & Jahde V. a.d.	1861	"Ueber die Reibung der Flussigkeiten" Pogg. Ann. der Physik and Chemie CXIII pp 55-86, 193-238, 383-425.

Meyer, O.E.	1865	"Ueber die innere Reibung der Gase" Pogg. Ann. der Physik und Chemie CXXV pp 177-209, 401-420, 564-599.
Meyer, O.E.	1887	"Ueber die Bestimmung der inneren Reibung nach Coulomb's Verfahren. Wied. Ann. der Physik und Chemie XXXII pp 642-659.
Millikan, R.A.	1947	"Electrons (+ and -), Protons, Photons, Neutrons, Mesotrons and Cosmic Rays" (Revised ed.) Univ. Chicago Press, Chicago, Illinois.
Mitry, R.T.	1977	"Wall Confinement Effects for Circular Cylinders at Low Reynolds Numbers" MSc. Thesis, Univ. British Columbia.
Modi, V.J. & El-Sherbiny, S.	1971	"Effect of Wall Confinement on Aerodynamics of Stationary Circular Cylinders" Proc. Third. Int. Conf. Wind Effects on Buildings and Structures, Tokyo, pp 369-375.
Mohanty, A.K. & Asthana, S.B.L.	1978	"Laminar Flow in the Entrance Region of a Smooth Pipe" J. Fluid Mech. 90 pp 433-447.
Monchick, L. & Mason, E.A.	1961	"Transport Properties of Polar Gases" J. Chem. Phys. 35 pp 1676-1697.
Morgan, K.Z. & Turner, J.E. (eds.)	1967	"Principles of Radiation Protection" Wiley
Morsy	1974	"An Instrument for the Direct Measurement of the Local Wall Shear Stress on Circular Cylinders" J. Phys. E 7 pp 83-86.
Mysels, K.J.	1949	"Flow of Thickened Fluids" U.S. Pat. 2, 492, 173 Dec. 27, 1949.
Newell, G.F.	1959	"Theory of Oscillation Type Viscometers V: Disk Oscillating Between Fixed Plates" Z. angew. Math. Phys. 10 pp 160-174.
O'Donnel, F.B. & Westkaemper, J.C.	1965	"Measurement of Errors caused by Misalignment of Floating Element Skin Friction Balance" AIAA Journal 3 pp 163-165.
Okamoto, T & Takeuchi, M.	1975	"Effect of Side Walls of Wind-Tunnel on Flow around Two-Dimensional Circular Cylinder and Its Wake" Bull. JSME 18 No. 123 pp 1011-1017.

Patel, V.C.	1965	"Calibration of the Preston tube and limitations on its use in Pressure Gradients" J. Fluid Mech. 23 pp 185-208.
Patel, V.C. & Head, M.R.	1969	"Some observations on Skin Friction and Velocity Profiles in fully developed Pipe and Channel Flows" J. Fluid Mech. 38 pp 181-201.
Phillips, O.M.	1969	"Shear Flow Turbulence" Ann. Rev. Fluid Mech. 1 pp 245-264.
Polymeropoulos, C.E. & Gebhart, B.	1967	"Incipient Instability in Free Convection Laminar Boundary Layers" J. Fluid Mech. 30 pp 225-240.
Preston, J.H.	1954	"The Determination of Turbulent Skin Friction by means of Pitot Tubes" J. Roy. Aeronaut. Soc. 58 pp 109-121.
Rees, W.G. & Wilby, W.A.	1982	"A Determination of the Drag Coefficient of an Arrow" Report prepared for P.N. Jones, R.A.R.D.E., April, 1982; also H.M. Tower of London Records.
Reif, F.	1965	"Fundamentals of Statistical and Thermal Physics" McGraw-Hill.
Reshotko, E.	1979	"Drag Reduction by Cooling in Hydrogen-Fueled Aircraft" J. Aircraft 16 pp 584-590.
Richter A. & Naudascher, E.	1976	"Fluctuating Forces on a Rigid Cylinder in Confined Flow" J. Fluid Mech. 78 pp 561-576.
Rosenhead, L. & Schwabe, M.	1930	"An Experimental Investigation of the Flow behi Circular Cylinders in Channels of Different Breadths" Proc. Roy. Soc. Lond. A129 pp 115-135.
Roshko, A.	1954	"On the Drag and Shedding Frequency of Two-Dimensional Bluff Bodies" NACA-TN-3169.
Rossetti, S.J. & Pfeffer, R.	1972	"Drag Reduction in Dilute Flowing Gas Solid Suspensions" AIChE Journal 18 pp 31-39.

Saffman, P.G.	1962	"On the Stability of Laminar Flow of a Dusty Gas" J. Fluid Mech. 13 pp 120-128.
Schlichting, H.	1979	"Boundary Layer Theory" McGraw-Hill (7th ed. 1979).
Shah, V.L.	1970	"Extension of the Theory of the Oscillating - Disk Viscometer for Large Boundary - Layer Thicknesses encountered at Low Pressures" Physica 49 pp 217-228.
Shair, F.H. Grove, A.S. Petersen, E.E. & Acrivos, A.	1963	"The Effect of Confining Walls on the Stability of the Steady Wake behind a Circular Cylinder" J. Fluid Mech. 17 pp 546-550.
Smith, A.M.O.	1960	"Remarks on Transition in a Round Tube" J. Fluid Mech. 7 pp 565-576.
Sparrow, E.M. & Gregg, J.L.	1960	"Mass Transfer, Flow and Heat Transfer about a Rotating Disc" Trans. ASME J. Heat Transfer 82 pp 294-302.
Suzuki, T. & Hirano, T.	1979	"Effects of the Channel Height on the Flow Past a Circular Cylinder (on the Nearcritical Flow)" Bull. JSME 22 no. 167 pp 661-668.
Tanner, L.H.	1977	"A Skin Friction Meter, using the Viscosity Balance principle, suitable for use with Flat or Curved Metal Surfaces" J. Phys. E. 10 pp 278-284.
Tennent, R.M. (ed)	1971	"Science Data Book" Oliver & Boyd.
Toms, B.A.	1948	"Some Obervations on the Flow of Linear Polymer Solutions through Straight Tubes at Large Reynolds Numbers" Proc. First Int. Congr. Rheology, Vol. II, North Holland, Amsterdam. pp 135-144.
Townsend, A.A.	1976	"The Structure of Turbulent Shear Flow" CUP (2nd ed. 1976).
Tritton, D.J.	1977	"Physical Fluid Dynamics" Van Nostrand Reinhold.

Virk, P.S. Merrill, E.W. Mickley, H.S. Smith, K.A. & Mollo-Christensen, E.L.	1967	"The Toms Phenomenon: Turbulent Pipe Flow of Dilute Polymer Solutions" J. Fluid Mech. 30 pp 305-328.
Virk, P.S.	1975	"Drag Reduction Fundamentals" AIChE Journal 21 pp 625-655.
Whitehouse, W.J. & Putman, J.L.	1953	"Radioactive Isotopes" OUP.
Wilby, W.A. Rees, W.G. & Field, J.E.	1982	"Studies of Turbulent Gas Flows using Electric and Magnetic Probes" J. Phys. E. 15 pp 916-918.
Winter, K.G.	1977	"An Outline of the Techniques Available for the Measurement of Skin Friction in Turbulent Boundary Layers" Prog. Aerospace Sci. 18 pp 1-57.
Zakin, J.L. & Hunston, D.L.	1980	"Effect of Polymer Molecular Variables on Drag Reduction" J. Macromol. Sci. - Phys. B18 pp 795-814.

END

DATE
FILMED

3 84

DTIC

END

DATE
FILMED

3 84

DTIC